UNIVERSITÀ
DEGLI STUDI
DI PADOVA

UNIVERSITÁ DEGLI STUDI DI PADOVA

DIPARTIMENTO DI INGEGNERIA INDUSTRIALE

CORSO DI DOTTORATO DI RICERCA IN
INGEGNERIA INDUSTRIALE
CURRICOLO IN INGEGNERIA MECCANICA
CICLO XXIX

Design and development of the target-ion source system for the SPES project

Coordinatore: CH.MO PROF. PAOLO COLOMBO
Supervisore: CH.MO PROF. GIOVANNI MENEGHETTI
Co-Supervisore: CH.MO DR. ALBERTO ANDRIGHETTO

Dottorando : ALBERTO MONETTI

A Irene

Ai miei genitori

Alla mia famiglia

Ai miei amici

Contents

List of abbreviations

LNL	Laboratori Nazionali di Legnaro
INFN	Istituto Nazionale di Fisica Nucleare
RIBs	Radioactive Ion Beams
PB	Proton Beam
STIS	SPES Target Ion Source
ISOL	Isotope Separator On-Line
CERN	Conseil Européen pour la Recherche Nucléaire
FE	Front-End
FEA	Finite Element Analysis
DB	Diagnostic Box
BP	Beam Profiler
FC	Faraday Cup
PCB	Printed Circuit Board
WF	Wien Filter
SPIS	SPES Plasma Ion Source

Introduction

During the last century, many efforts have been spent by the nuclear physics community in order to improve the knowledge about the behaviour and the stability of the nucleus. For this purpose, very challenging equipment and technologies have been designed and produced leading to important applications even in the industry, applied physics and medicine.

Europe is surely the leader in the field of nuclear physics as the world's largest particle physics laboratory proves: CERN. On the other hand, one of the most important organization, which supports CERN, is surely INFN, the National Institute of Nuclear Physics, founded in 1951, which has four main Laboratories in Italy. One of them is LNL, the National Laboratories of Legnaro, close to Padova. The most important project of LNL financed by INFN is the SPES project, now at the construction phase. The aim of this new facility is to produce Radioactive Ion Beams in the neutron rich side of the so-called "valley of stability". This is a very challenging project since it requires a lot of knowledge and studies from physical, chemical, engineering points of view. In fact, the core of the facility is a uranium carbide target which produces by fission radioactive atoms by means of an energetic and powerful proton beam. Moreover, most of the equipment has to be internally designed and tested in order to safely manage the accelerator. An important network of collaborations, both national and international, has been constituted to complete the project, among which University of Padova, LENA, ISOLDE (CERN), HRIBF (ORNL - US), iThemba LAB (South Africa) etc.

In this thesis, both the target and some of the most delicate devices which have to be installed inside the bunker where the nuclear reactions occur are presented. In particular, Chapter 1 provides a general overview of the ISOL facility, its application and a brief description of the SPES project with the main devices which compose it. Then, in Chapter 2 the design phase of the target and the tests performed at iThemba LABS in South Africa will be presented. Chapter 3 describes the design of all the diagnostics that have to be installed inside the SPES bunker to safely manage and control the production of the radioactive beams, whereas in Chapter 4 a very comprehensive description and the design phases of a Wien Filter are presented. Finally, Chapter 5 provides the conclusions of the work with some important ideas in order to improve the devices to be installed in the SPES bunker.

Chapter 1

The SPES project at the LNL

1.1. Introduction

The atom is the fundamental component of the matter. Its mass is essentially concentrated in its nucleus at the atom centre since the electrons are much lighter (almost 1/2000 the proton mass). It is composed by the positively charged protons and the neutral neutrons and the nucleus stability is assured by the Strong Interaction, which is one of the four fundamental interactions of nature. In fact, it permits to bind the nucleons together (general name for protons and neutrons) contrasting the electrostatic repulsions between positively charged protons. In order to break the atomic nucleus, a lot of energy is generally required to overcome the Strong Interaction.

The nucleus is not a simple agglomerate of nucleons but it is a balanced combination of protons and neutrons. The stable nuclei are positioned on the "valley of stability", the black squares in the chart of the nuclides (Fig. 1.1) that gathers together all the discovered nuclides. The isotopes which are not placed in the "valley of stability", are unstable and they stochastically decay into different elements. Each isotope has his own typical half life, which is the time required to reduce to the half of an initial number of isotope. Longer is the half-life, longer is the usual life of this atom. The most unstable atoms are usually far from the stability valley and they can be very interesting for nuclear physics research.

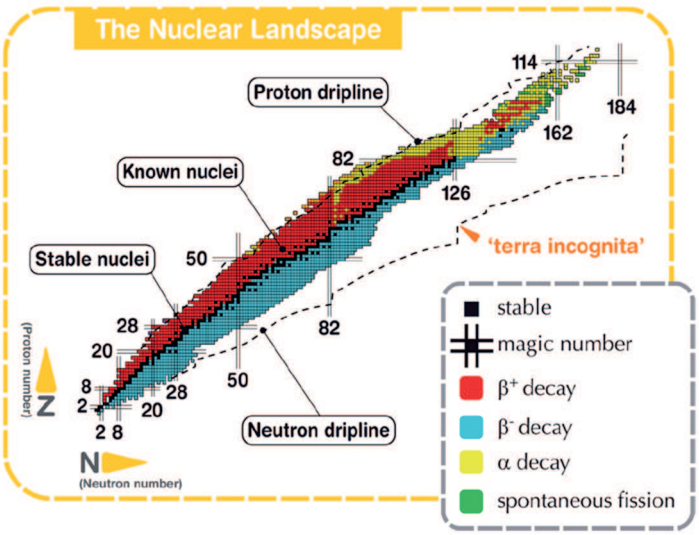

Fig. 1.1. Chart of the nuclides, after [1.1].

The most important types of decay are essentially four [1.2]:

- The alpha decay represented in yellow squares in Fig. 1.1, which characterizes the heavy isotopes over the Pb. It is an emission of a ^{4}He nucleus (called α particle). In this way, the new atoms will have a variation of both the number of protons (Z) and mass (A) according to: $Z_N = Z_0 - 2$, $A_N = A_0 - 4$ (subscript N: new atom; 0: old atom).
- The beta decay, which is divided in β^+ and β^-, presented respectively by the red and blue squares in Fig. 1.1. Essentially, in the first reaction, a proton becomes a neutron with the emission of a positron and a neutrino, whereas in the second one, a neutron changes to a proton with the emission of an electron and an antineutrino. In both reactions, there is the emission of the energy. In this decays, the mass of the new atom does not change ($A_N = A_0$), whereas the number of protons decreases of one for the β^+ decay ($Z_N = Z_0 - 1$), or increases of one for the β^- decay ($Z_N = Z_0 + 1$).
- Spontaneous fission represented in green squares in Fig. 1.1. By this reaction, the heaviest nuclei tend to spontaneously break forming two large fragments. As example, the common source of both fission fragments and neutrons is the ^{252}Cf.
- Gamma ray emission, which are not represented on the nuclide chart in Fig. 1.1. The isotope, which decays by this reaction, does not change its position in the nuclide chart and, consequently, it remains the same isotope. It was in an excited status, called metastable, and tend to lose the excess energy emitting high frequency electromagnetic radiation due to the internal re-arrangement of the nucleons.

The nuclear properties of approximately 3600 radioactive nuclei, called “exotic nuclei”, have been studied and they can be more or less easily produced in several facilities all over the world. However, the existence of more than 6000 unstable nuclei is predicted by theoretical calculations until the neutron and proton dotted line showed in Fig. 1.1. Beyond this boundary, the nucleus is so unstable that it tends to immediately decay emitting nucleons.

The use of Radioactive Ion Beams (RIBs) is one of the technique to study the properties of the nuclei far from the “stability valley”. A large number of species can be produced and the beams can be used in different fields of science. As an example, the next paragraph will summarize the most important applications for the RIBs.

1.2. The applications for the RIBs [1.3]

1.2.1. Nuclear physics

The most of the knowledge of the atomic nucleus structure is based on the study performed on the nuclei positioned very close to the "valley of stability" in the chart of nuclides or in the proton rich side, since they were the most simple to produce and, consequently, to be studied. The models implemented based on these studies have been extrapolated to describe the neutron-rich region of the nuclide chart and, inevitably, errors and wrong suppositions have been introduced. For this reason, some of the bases of the nuclear physics have to be revised and modified.

As an example, the Halo effect is the clear deviation of the common accepted rules described by the one of the most significant model: the "liquid drop model", developed by Bohr and Wheeler. This model describes the radius of an atomic nucleus according to $R=R_0A^{1/3}$, where R_0 is a constant and A the atomic mass. The Halo nuclei have a very bigger atomic radius due to the presence of two or more external nucleons orbiting around the core that contains all the other nucleons. A clear example is ^{11}Li, which has two neutrons orbiting around a core of ^{9}Li.

Other typical nuclear physics research topics using exotic nuclei RIBs are, for example, physics of super heavy elements, one or two proton radioactivity, nuclear spectroscopy, nuclear reactions mechanisms, nuclear shell description, isospin symmetry.

1.2.2. Physics of solid state

Radioactive ion beams can be used as a tool to detailing diagnostic the environment where they are implanted [1.4]. As an example is the technique of the Emission Channeling used to study the properties of the semiconductors. Their function is strongly influenced by defects and impurities due to the change of their structure. During the study, the position occupied by the radioactive isotopes inside the structure where it has been implanted, can be determined with a good accuracy measuring the anisotropic intensity distributions of the emitted radiation. In fact, the radiation intensity depends on the orientation of the host crystal because the emitted particles (both α or β) move through a single crystal and are then revealed by a 2-dimension position sensitive detector.

1.2.3. Nuclear astrophysics

The nuclear astrophysics is the most important physics branch concerning the study of the structure and composition of the Universe. One of the major goal of this science is to describe the stellar cycles [1.5] where nuclear reactions produce energy and atoms from the reaction

between other atoms. In order to model some steps of these processes, nuclear astrophysics needs some specific characteristics of exotic nuclei and, if no experimental information are present, extrapolations of the nuclear models have to be performed. The use of radioactive ion beams can provide this experimental information or, as said in the previous paragraph, can test the applicability of the nuclear models themselves.

1.2.4. Nuclear medicine

Nuclear medicine is a branch of medicine that uses the radioactive decay of the unstable isotope in the diagnostics and the treatment of diseases. A clear example is the Positron Emission Tomography (PET) that produces 3D images of functional processes undergoing in the human body detecting the emission of the energy due to the nuclei decay. It is mainly used in clinical oncology for the imaging of tumours or metastases and for neuroimaging.

The isotopes with β^+ decay (typically ^{11}C, ^{13}N, ^{15}O, ^{18}F) are dissolved into compounds involved in the functional process of interest and, in their decays, a positron is emitted. In the sudden annihilation with a surrounding electron, two γ-ray photons are emitted in the exact opposite directions. Using an opportunely designed set of scintillators, the photons are revealed and the consequently position where the decay happened is reconstructed.

1.3. The ISOL technique for the production of the RIBs

1.3.1. Introduction

In general, the three characteristics which determine the goodness of a technique for the production of the RIBs are:

- The yield, determined by the cross section of the reaction to produce the desired isotopes.
- The contamination of the desired beam from unwanted species.
- The isotopes half-live which could zero the beam intensity for the most exotic nuclei due to the time needed to for the various process from the isotope production to the experiment.

Currently, two main technique can be used in order to deliver to the users RIBs:

- The “In-Flight” Separation technique is based on a light target impinged by a primary beam in order to produce a secondary beam of radioactive ions. The fragmentation reaction of the primary beam determines the range of produced nuclei which are ejected without limitations due to lifetimes or chemical properties. On the contrary, the contamination of the products and from the primary beam is a

disadvantage respect to other methods. Finally it can be implemented in existing heavy-ion accelerators.

- The Isotope Separation On-Line technique [1.6], [1.7]. Isotope are produced by an imping primary beam on a target. The atoms constituting beam and target and the beam energy determines the produced atoms which later have to diffuse from the target, effuse to the ion-source, be ionize, be extracted and finally separated and delivered to the experiment. The various process has been designed to be:
  - Efficient, to avoid loss of interesting isotopes
  - Fast, in order to accelerate the most exotic nuclei
  - Selective, to deliver only the desire beam to the users
  - Highly productive, to increase as much as possible the secondary beam intensity

The most important ISOL facilities in the world are:

- ISOLDE at CERN, where a high energetic beam (1 or 1.4 GeV) could imping several targets, but especially the UC_x version. The proton beam is delivered by the PS synchrotron booster, which is the first accelerator that delivers the beam to the very famous LHC. The estimated number of fissions per second is about $2.5 \cdot 10^{12}$ for a 1 GeV 2 μA of proton beam.
- ISAC @ TRIUMF in Vancouver: a 500 MeV proton beam delivered by a high energy cyclotron could imping various target, such as U, Th, Si, Ta etc. For the UC_x target the maximum beam current delivered is about 10 μA [1.8], for a total power of 5 kW.
- ALTO in Paris: a 50 MeV electron beam impinges a converter which produces photons in the range of gammas. These photons fission an UC_x target for an expected rate of $1.2 \cdot 10^{11}$ fissions per second for a 10 μA of electron beam.
- HRIBF at ORNL: this facility has been closed few years ago. A 50 MeV and maximum 20 μA of proton beam was delivered to various target. The UC_x version could provide about $4.8 \cdot 10^{11}$ fissions per second.

The description of the ISOL technique is the object of this paragraph.

1.3.2. The isotope production with the ISOL technique

In general, the isotope production is obtained by nuclear reactions between the primary beam and the target. Various beams and target can be used according to the production of the various beam for the experiments. Usual primary beams are:

- Low energy protons, neutrons or deuterons (between 30 to 100 MeV): as example SPES at LNL (protons at 40-70 MeV)
- High energy protons ranging from 500 MeV to 1500 MeV (as ISOLDE with 1-1.4 GeV protons or TRIUMF with 500 MeV protons)
- Heavy ions from 4 to 100 MeV/u
- Thermal neutrons
- Electron beams (as ALTO with 50 MeV electrons)

The intensity of the products in the target, called *I*, can be easily calculated by the following formula [1.7]:

$$I = \Phi \, \sigma \, N \qquad (1.1)$$

Where Φ is the intensity of the primary beam, σ is the reaction cross section and N is the number of target atoms per surface area. From a nuclear physics point of view, the cross section σ is the probability of the interaction between the target nuclei and the primary beam. Integrating the cross section over the primary beam energy range which impinges the target, the final products intensity can be easily found without taking into account any losses.

The types of nuclear reactions that essentially occur in the target are:

- Fission: it occurs on typical targets of ^{238}U, ^{232}Th or other long lived actinides target. The nucleus splits into two species with similar masses between the range of 80 and 150 amu with the emission of few neutrons.
- Spallation: here a large number of proton, neutrons and α particles are expelled from the target nucleus. The new nucleus will have a mass slightly lower than the target atom but in the very proton-rich side of the nuclides chart.
- Fragmentation: this reaction can happen both for target fragmentation (if a proton beam energy of 50 MeV or more impinges a heavy target) or for primary beam fragmentation (if a heavy-ion beam is sent against a light target). This reaction produces a wide variety of species but close to the projectile and target nucleus.
- Light- and Heavy-Ion Fusion Evaporation reactions or direct reactions: these reactions does not involve fissile material, consequently the number of products is very limited compared to the three other reactions. The Light-Ion Induced Fusion Reaction produces proton rich nuclei close to the valley of stability, whereas the Heavy-Ion version produces neutron deficient nuclei very far from the stability line.

1.3.3. The isotope release from an ISOL target

The characteristics of the ISOL technique compared to the In-Flight method is that for the second one the particle are ejected from the target, whereas in the first one they have to diffuse. This process is governed by the Fick's laws and it has to be as fast as possible in order to provide to the users the lower half-lives isotopes beams. This process is promoted by:

- High temperatures
- Reduction of the target material grain size
- Reducing the target thickness
- Reduction of number of collisions of the isotope with the target surface properly designing the system geometry (ex. inserting material porosity)
- Using a material with a low adsorption enthalpy relative to the particle-surface-interaction

During the functioning, the only parameter which can be adjusted is the target temperature which has to be maintained as high as possible because, probably it is one of the most influencing parameter as reported in [1.10]. The upper limit is defined by considering the vapour pressure of the target material [1.9]. Anyway, since the target is surely in contact with other materials and this could change its properties [1.9], the specific case has always to be analysed.

For these reasons, the most common material for an ISOl target is the made of carbide, as, for example, Uranium carbide or Silicon Carbide. In fact, these materials couple very high maximum temperatures (over 2000°C), high porosity and high emissivity, which lets to dissipate the high beam power.

Finally, temperature, that has always to be maintained as high as possible, and chemical properties of both the produced isotopes and the target assembly govern the effusion of the products to the ion-source.

1.3.4. The ionization process of the radioactive isotopes, the separation and the production of the RIBs

Most of the ISOL facilities in the world use essentially three types of sources depending on the RIB requested by the user. Essentially the three sources correspond to three different ionization mechanisms:

- The Surface Ionization: it is most simple way to ionize the isotopes in an ISOL facility due to the very small number of components required. When an atom interacts with the source surface it can lose an electron becoming a positive ion if

the ionization potential is smaller than 7 eV, or it can became a negatively charged if the electron affinity of the atom is greater than 1.5 eV. This process is deeply governed by the temperature which greatly increases the efficiency at high values and typical working temperatures are of the order of 2000°C. Moreover, also the material working function, a chemical properties of the material constituting the surface of the ion source, determine the possibility and the efficiency process. In particular, the working function has to be higher than the ionization potential for positive ions or has to be lower than the electron affinity for negative ions. Typical materials used for a standard Surface Ion Source are tantalum, tungsten and rhenium for positive ion beams, LaB_6 and BaO for negative ion beams.

- The Laser Ionization: this method is one of the last implemented successfully at the ISOL facility but probably now is the most used. In fact, the atoms are stepwise excited by different laser photons (usually from 1 to 4) at precise energy levels corresponding to a precise element, that lets the atoms be ionized. It is an efficient ionization and, above all, very selective, leading to an extremely pure ion beam. The only contaminants in the beam are essentially due to the unwanted surface ionization.
- Electron Impact Ionization: it is often used to create multiply charged ions or ionize the elements which require high ionization energy (typically noble gases and halogens). The technique is based on the atoms bombardment by electrons which cause the emission from the isotope of one or more outer electrons. According to the cross section for electron impact ionization of the wanted element is determined the optimum electron energy to accelerate. It is a very unselective method and, in general, it does not offer any chemical selectivity, but, on the other hand, it is the only method available to efficiently ionize some elements.

After the ionization process, the ion has to be extracted by a certain potential, usually on the order of tens of kV. The beam has in general good properties which are essentially only dependent on the source used. Then a very important step has to be performed: the desired mass has to be selected in order to provide the requested mass to the users. This process is, on the other hand, typical of other type of accelerators and, for this reason, it will be discussed in the next paragraph.

1.3.5. Conclusion

To conclude, it is cited a very explicative sentence found in [1.11] concerning the ISOL technique: "*The ISOL technique is complicated by high-temperature physics, chemistry, metallurgy, diffusion, and surface adsorption processes which take place in the target-ion source; all of these processes add to the delay times which result in losses of the short-lived radioactive species of interest*". For this reason, the design of an ISOL facility, and especially the various devices involved on the RIB production is one of the best challenge from an engineering point of view.

1.4. The ISOL facility at the LNL: the SPES project

1.4.1. Introduction

The SPES project has the aim to develop and to install an ISOL facility with the primary goal of produce intense exotic beams and it is now at the construction stage in Italy at INFN-LNL (Fig. 1.3). The primary driver is the 70p commercial cyclotron [1.12] of the BEST Cyclotron Systems Inc., a member of TeamBest™, able to provide an intense and energetic proton beam (max 70 MeV – 49 kW). A multi-cusp ion source delivers a maximum of 15-20 mA of negative hydrogen beam current, which is then accelerated by an RF systems consisting of two half cavities and providing up to 70 kV of accelerating voltage [1.13]. The RF operates in 4th harmonic mode at a frequency of 56 MHz, whereas the maximum magnetic field has been fixed to 1.6 T. The total magnet weight is about 200 tons. The vacuum inside the tank is maintained by 7 cryogenic pumps able to reach vacuum levels of less than $3 \cdot 10^{-7}$ mbar.

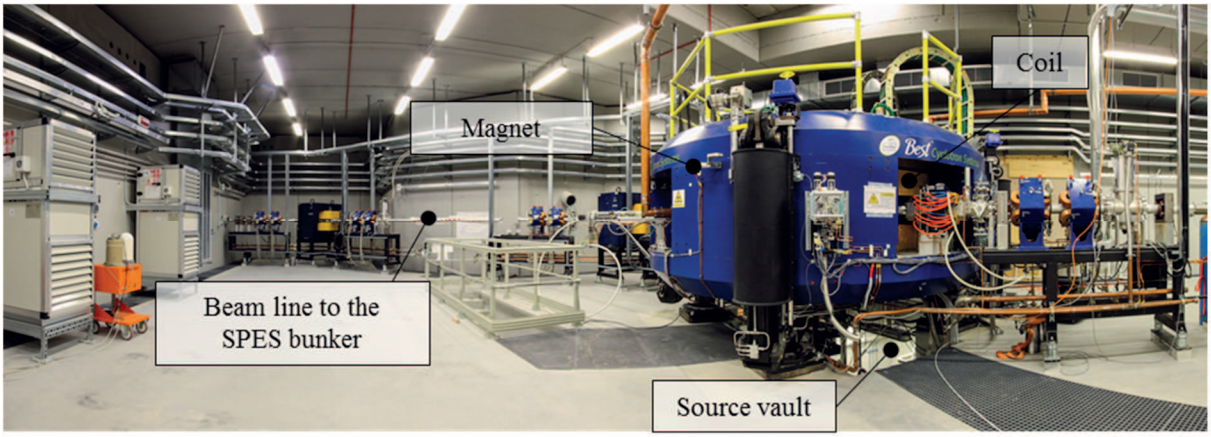

Fig. 1.2. Cyclotron during the phase installation in the SPES building.

The primary beam (40 MeV – 200 μA – 8 kW) travels along the beam line and, after entering inside the SPES bunker, is delivered to an UC_x target, housed in an opportunely designed vacuum chamber installed in the SPES Front-End. Here the exotic species are produced,

ionized, accelerated and separated by means of a dedicated ion source, extraction potential and a Wien Filter, which constitutes the first stage mass separation.

The beam is later delivered out of the bunker and it is injected into a Beam Cooler (BC), a device which is used to decrease the longitudinal and transversal emittance, then a High-Resolution Mass Separator (HRMS) is foreseen to purify the beam from the unwanted isobar masses. Now the RIBs could be delivered to the users for the low energy experiment or it can be injected into a Charge Breeder (CB), which is able to increase the beam charge state. Another mass separator will be installed to select the most intense charge state and finally, the beam is injected into a Radio Frequency Quadrupole (RFQ) and the following ALPI Linac already functioning in Legnaro. The total accelerator assembly is able to deliver ion beams at energies of 10 AMeV and, for the 130 amu mass in the neutron rich region, the expected rate at the users is above 10^8 pps.

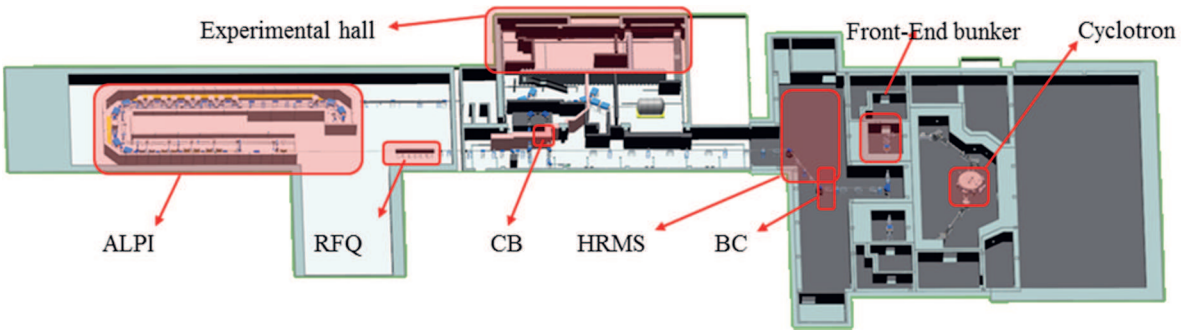

Fig. 1.3. The layout of the SPES facility

In this paragraph, particular attention will be dedicated to the description of the components installed inside the SPES bunker, which is the heart of the project, the facility first stage under installation and the object of this thesis.

1.4.2. The SPES bunker

The SPES bunker is the local indicated in Fig. 1.4 set in the new SPES building at the underground level. The dimensions are 7.12 x 6.2 m, for a total area of 44.1 m^2. The wall thickness are ranging from 1 to 4 meters according to the dose rate tolerated in the adjacent room. The proton beam enters in the bunker through a beam pipe coming directly from the cyclotron vault.

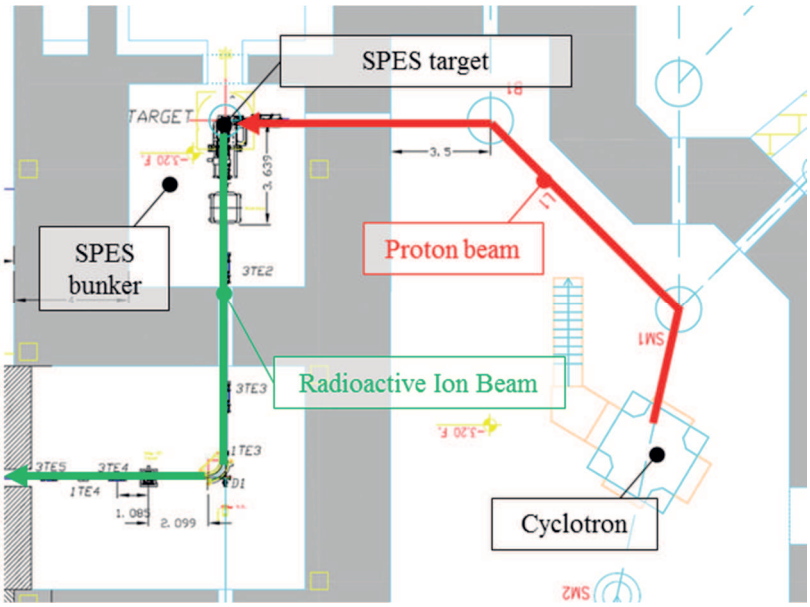

Fig. 1.4. Map of the SPES building – underground level.

The bunker is isolated by a 1 meter thick concrete door which rolls into rails and is air tight. Moreover during the irradiation, a depression of 40 Pa is maintained between the two rooms in order to control the air flow to avoid uncontrolled release of radioactive air in the adjacent locals. This is very important to plan the auxiliary systems feedthrough such as water, compressed air, electrical power, electrical signals and control cables because the air losses have to be decrease as much as possible.

1.4.3. The Protonic Front-End

Since the proton beam is the most concentrate power of the overall facility, the control has to be very accurate in order to avoid the perforation of the beam pipe. This is not so uncommon but in this specific case, it could be quite catastrophic: the fresh air entering in the beam line and, consequently, into the SPES chamber, could cause the burn of the UC_x disks with the consequent release of radioactive gases into the bunker. This event can be provoked by a power supply fail if it is not promptly detected, a bad management of the proton beam or an insufficient control of the beam characteristics.

For these reasons, it is important to foreseen a safe and efficient proton beam diagnostic system in order to be able to properly manage the beam. The block diagram of the architecture developed for the SPES Front-End is presented in Fig. 1.5.

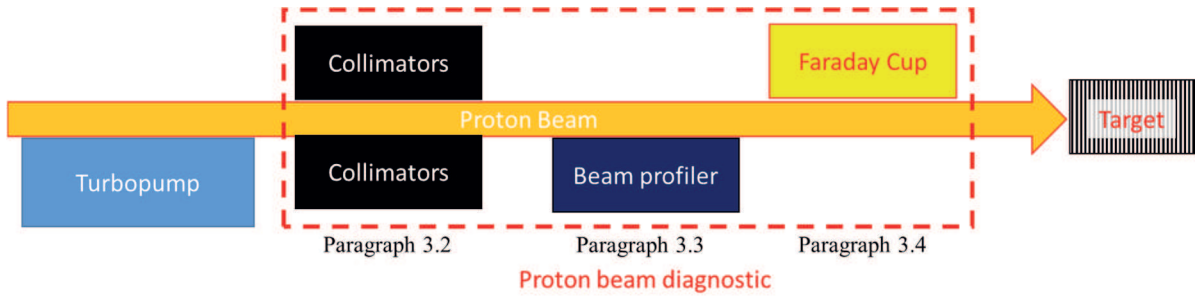

Fig. 1.5. Block diagram of the proton beam line

The collimators are the first elements foreseen in the proton beam diagnostic because they prevent and detect a beam misalignment during operation. In addition, they are essential to determine the proton beam size and to avoid that the beam impinges other elements on the beam pipe. Substantially they stop the outer particles of the proton beam, defining its shape. Their design will be presented in paragraph 3.2.

Then, as usual, a beam profiler and a Faraday cup are installed. The first evaluates the beam profile, whereas the second measures the beam intensity. They are always used to prepare and tune the beam before the target irradiation. Their design will be presented in paragraph 3.3 and 3.4.

Often, and when was possible due to its simplicity, the proton beam power was modelled with the classical Gaussian distribution:

$$p(x,y,t) = \frac{P}{2\pi\sigma^2} \cdot exp\left(-\frac{((x - r_w \cdot cos(\omega t))^2 + (y - r_w \cdot \sin(\omega t))^2)}{2\sigma^2}\right) \qquad (1.2)$$

Where σ is the proton-beam mean-square deviation (assumed identical on the x and y planes), P the power delivered, r_w and ω the sweeping radius and its angular frequency, t the time, x and y the position, P the total beam power (assuming zero losses) and p the power density per area. An example of the beam shape is presented in Fig. 1.6.

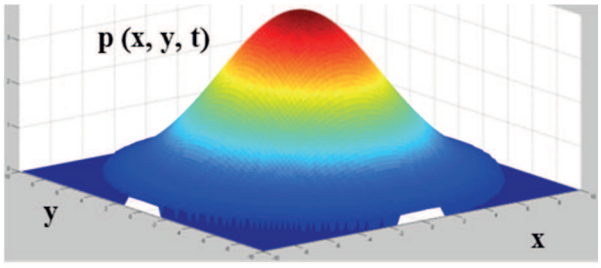

Fig. 1.6. Example of a Gaussian distribution used to model the proton beam power (r_w = 0).

Assuming stationary conditions of the proton beam, the power can be obtained numerically integrating (1.2), as in (1.3).

$$p(r) = \iiint p(x,y,t) = \int_0^{2\pi} \int_{t_1}^{t_2} p(r,\theta,t) \cdot r \, dt \, d\theta = \\ = \int_0^{2\pi} \frac{P}{2\pi\sigma^2} \cdot exp\left(-\frac{((r\cdot\cos(\theta) - r_w)^2 + (y\cdot\cos(\theta))^2)}{2\sigma^2}\right) \cdot r \tag{1.3}$$

If a collimation of the proton beam occurs, the formula can be changed as:

$$p(r) = \frac{P_{TOT}}{P} \int_0^{2\pi} exp\left(-\frac{((r\cdot\cos(\theta) - r_w)^2 + (y\cdot\cos(\theta))^2)}{2\sigma^2}\right) \cdot r \, d\theta \tag{1.4}$$

Where P and P_{TOT} are respectively the beam power after and before the collimation, as expressed below.

$$P_{TOT} = \int_0^{\infty} \int_0^{2\pi} exp\left(-\frac{((r\cdot\cos(\theta) - r_w)^2 + (y\cdot\cos(\theta))^2)}{2\sigma^2}\right) r \, dr \, d\theta \tag{1.5}$$

These equations will be used to model the proton beam power in the design of the protonic beam diagnostic, which will be presented in Chapter 3.

1.4.4. The Target-Ion Source unit

The SPES Target-Ion Source unit (STIS) is the core of the facility: here the radioactive nuclei, mainly n-rich isotopes, will be produced by the fission interactions of a 40 MeV proton beam, at currents up to 200 μA, with a uranium carbide target [1.14]. The spectra yield is presented in Fig. 1.7. The target is composed by 7 uranium carbide disks, all characterized by a diameter and a thickness of 40 and 0.8 mm respectively, with a density of about 4 g/cm^3 for the Uranium Carbide manufactured. This system will produce a rate of about 10^{13} fissions per second of 42 different elements (Fig. 1.7), which are then ionized by the ion source. The importance of choosing the specific ion source is primarily dictated by the efficiency optimization and secondarily by its capability of selective ionization. Three standard SPES ion-source types are currently being investigated (Fig. 1.8): the surface ionizing (SSIS) [1.15], which constitutes also the base of the laser ion source SLIS if three different lasers are delivered to the hot cavity, and the plasma ionizing source (SPIS) [1.16]. The most of the species will be produced by the laser ion source which is able to efficiently ionize the isotopes, but, at the same time, it delivers very pure ion beams: the only contaminants of the desire element will be constitute by the first and second element groups which are inevitable. The ionization mechanism has already been reported in paragraph 1.3.4.

The ions produced with the aforementioned sources are then accelerated towards the ion extraction electrode by a potential up to 40 kV.

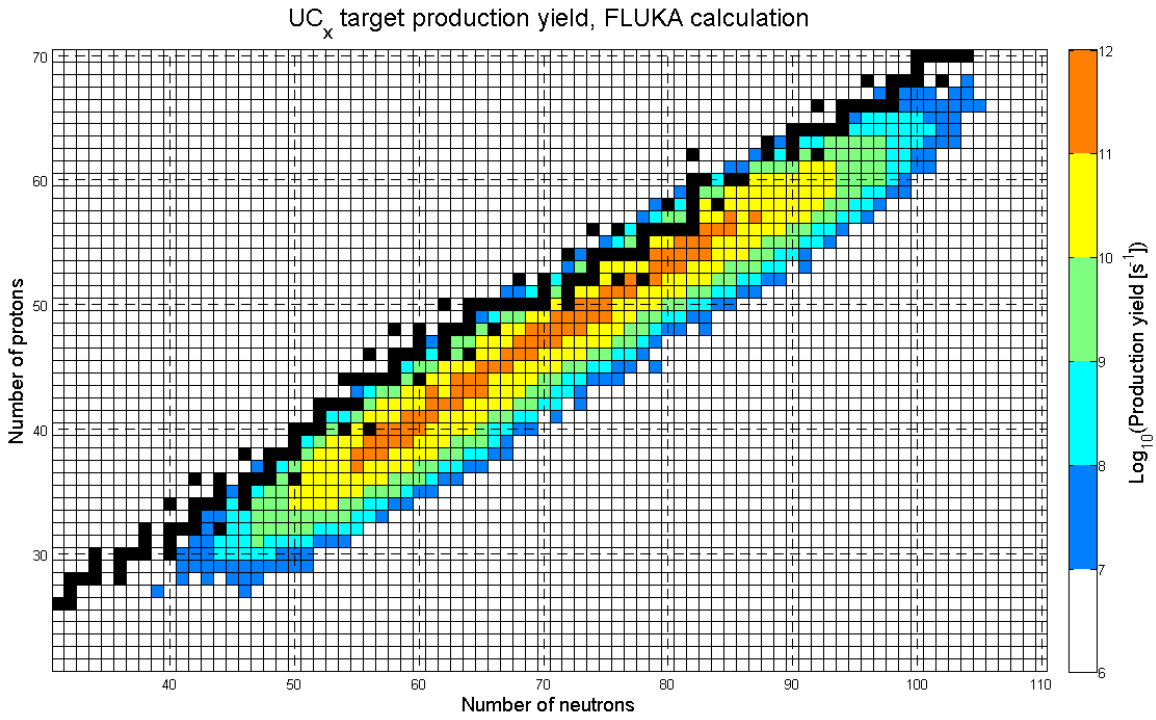

Fig. 1.7. UC_x target yield production for a 40 MeV, 8 kW of beam power, for a production rate of about 10^{13} fissions per second, calculated by FLUKA.

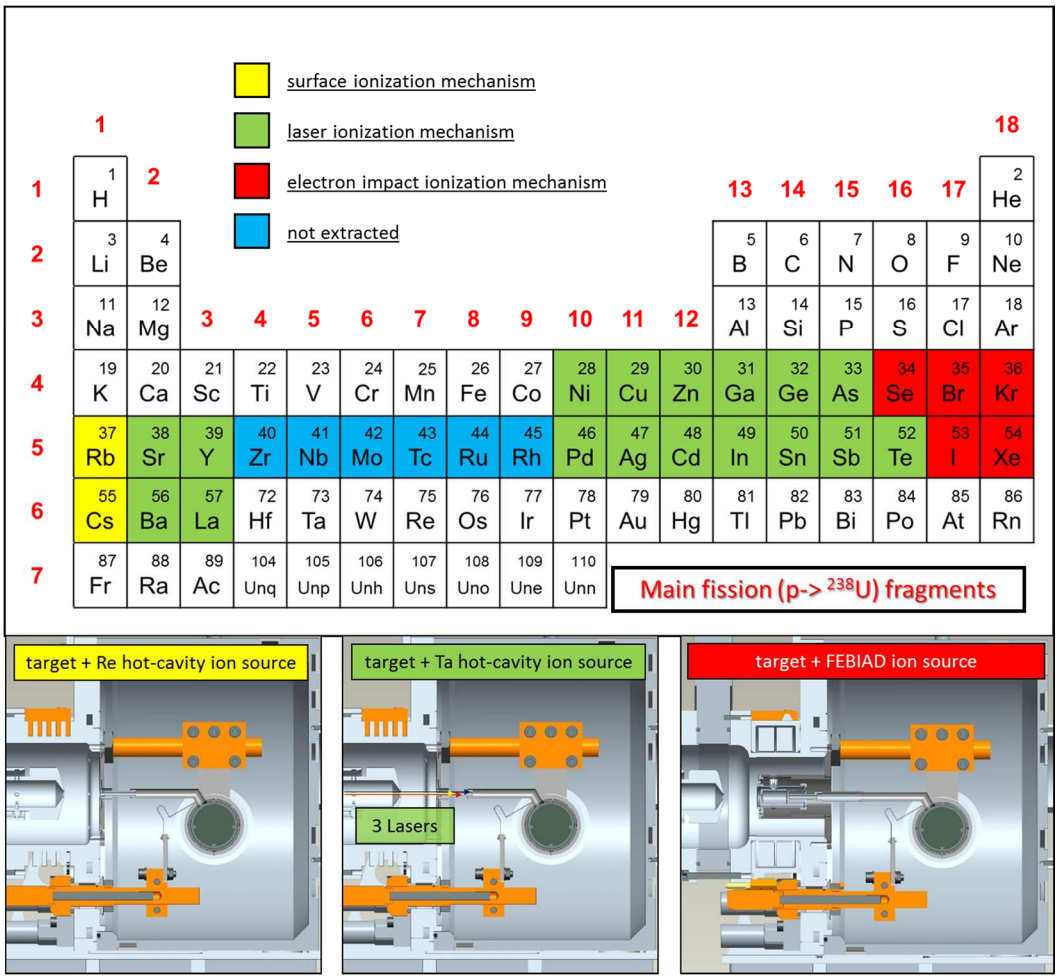

Fig. 1.8. Elements produced by the SPES target for an UC_x target and sources used to ionize them.

The target preliminary design was already performed in [1.17] for an ideal flat power beam profile and Uranium Carbide properties, but in Chapter 2 the Target design will be fully presented for the actual characteristics. In particular, the definition of the proton beam profile is very important since it characterizes the design of the protonic Front-End.

It is underlined that during the conditioning phase and at beam power lower than the maximum value (8 kW), the target is heated by Joule effect in order to perform the outgassing process and to increase the temperature of the target to promote isotopes release from the disks. The heater and all the connections used to provide the sufficient electrical current have been already studied in [1.17] and [1.18].

1.4.5. The Radioactive Front-End

The Radioactive Front-End is the part of the accelerator which houses the Target-Ion Source Chamber, supplies all the power and signals needed, extracts, separates and transports the radioactive ion beam out of the bunker. It is composed of several sub-apparatus visible in Fig. 1.9. Its design is essentially not critical from the thermal or structural point of view as the Protonic Front-End, but the number of devices here installed makes it very complex. In particular, three main elements are responsible for the beam transport:

- The deflectors: they are used to correct beam misalignment induced by inevitable imprecisions on the manufacturing process, assembling, controlling, etc. The design of the second deflectors will be presented in paragraph 4.8, but a short description will be presented in paragraph 1.4.6.
- The triplets: they are one of the most used devices to transport a beam, especially for low energy beam as in the Front-End. They are composed of three quadrupoles. Two triplets will be installed in the SPES bunker: the first one is used to provide the correct beam to the WF, whereas the second will transport the beam out of the bunker. A short description of the working principle will be presented in paragraph 1.4.6
- The Wien Filter: it is a velocity separator, but in the SPES bunker it is used as a mass separator. Its study, redesign and tests will be presented in Chapter 4.

The “eyes” of the operators on the final beam are the RIB beam diagnostics housed in DB1 and DB2. The first one is used to check the beam properties size and alignment in order to provide the best beam to the WF. The second one is fundamental to correctly set the Wien Filter, to intercept the unwanted beam and measures its dimension. Both are provided by a Faraday Cup, a device which measures the beam intensity, and a Beam Profiler, used to

estimate the beam size. Their design and working principle are described in the second part of Chapter 3.

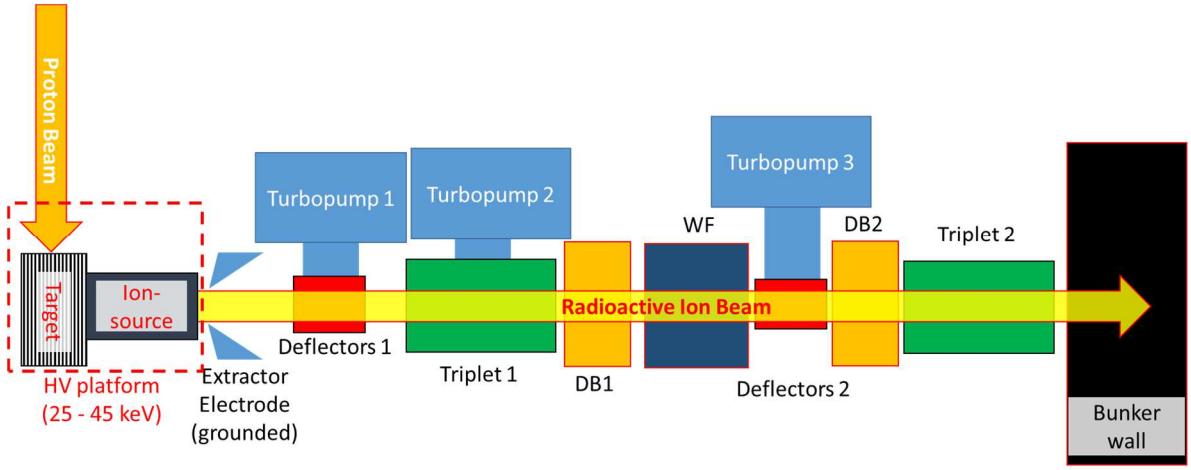

Fig. 1.9. Block diagram of the radioactive beam line

1.4.6. The device for the beam transport: steerers and triplets

The beam transport can be constituted by electrostatic or magnetic devices: the first are based on the change of the particle trajectories due to a certain electric field, the second one due to a certain magnetic field. Due to the low extraction potential (maximum 45 kV for the SPES project), the best way to transport the beam is by using electrostatic devices, since they are:

- Simpler: the shape of the electrodes controls the electric field uniformity that, consequently, can be very well reproduced by a good study, manufacturing and assembly process.
- Cheaper: the devices can be manufactured in an ordinary workshop, as the internal INFN workshops. Moreover, most of the cost reduction is assured by the electrostatic power supply instead of high current power supply.
- Radiation harder: the insulation of the magnet coil is usually made of epoxy resins, whereas the insulator material for the electrodes are ceramic, typically MACOR or Alumina, which assure one order of magnitude more of radiation hardness.
- Easier to tune: the electric field to set depends only on the extraction potential and not on the beam particle mass and charge of state. This is very helpful especially for the very first part of the accelerator, where the beam is composed of all the various masses ionized by the ion source.

Two of the main components which have to be installed in the SPES Front-End and all along the beam line are deflectors (or steerers), and triplets. The deflectors are essentially composed

by two plates, with an opportune shape, maintained at a certain potential. Usually, one of the electrodes is at a positive potential, the other at a negative, as presented in Fig. 1.10, in order to create the best uniform and constant electric field. Using two couple of steerers, it is possible to completely remove beam misalignment (variable to change: position and angle): the first deflector corrects the beam trajectory, the second align the beam to the axis centre, as it will be presented in paragraph 4.8.

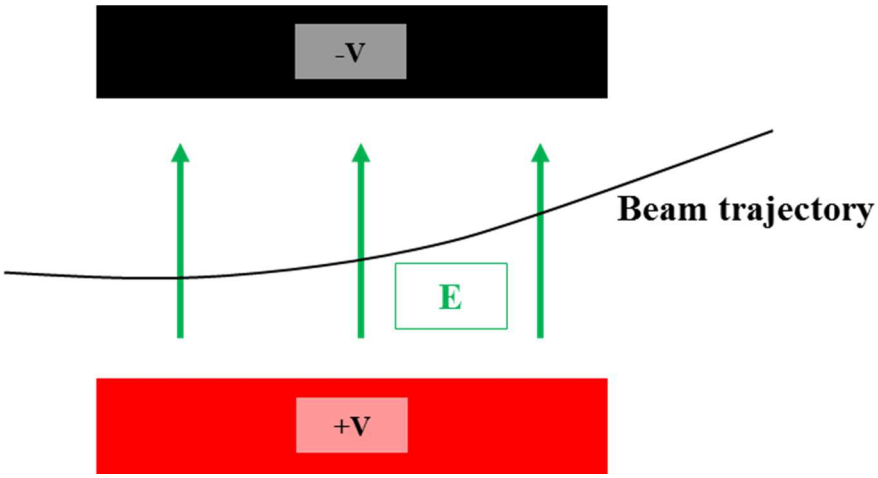

Fig. 1.10. Sketch of a typical example of deflectors.

On the other hand, the triplet is a device which lets to control beam size along the beam line. It is constituted of a triplet of quadrupoles, which ideal section is presented in Fig. 1.11. Here the ideal hyperbola profile of an infinite quadrupole creates isopotential hyperbola lines.

Along the Cartesians axis x and y of the quadrupole, it is possible to demonstrate that the potential is essentially a parabola, as presented in Fig. 1.12. The consequent electric field, which is essentially its derivative, is a straight line. This is very important since the electrical force acting on a particle is proportional (linear) to the particle position.

For simpler manufacturing process, the quadrupole shape is approximated by a circle, in order to create the pole by a simple cylindrical rod. This profile changes the electric field distribution inserting to the function non-linear terms. This could be very bad for the beam transport since the beam emittance could significantly increase. The problem of “non-linear effects” will be only introduced in paragraph 4.1 in order to provide to the reader all the tools to understand the Wien Filter design phase.

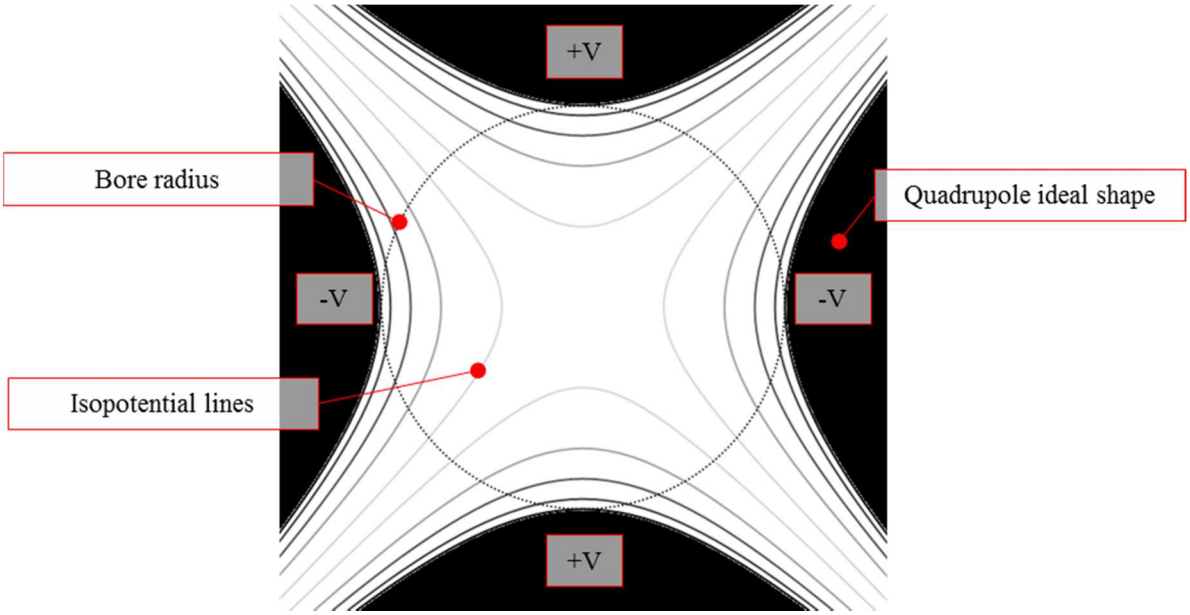

Fig. 1.11. Section of an ideal quadrupole

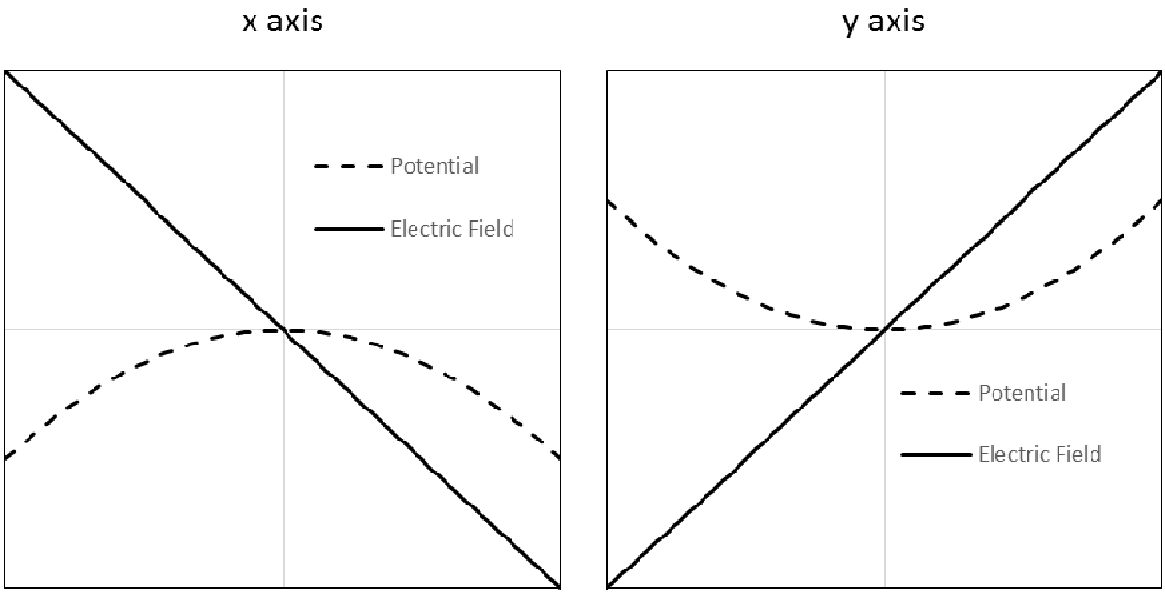

Fig. 1.12. Potential and consequently electric field created in a quadrupole.

References of Chapter 1

[1.1] Eurisol Design Study, www.eurisol.org.

[1.2] G.R. Gilmore, *Practical Gamma-ray Spectrometry*, 2nd Edition (John Wiley & Sons., Chichester, West Sussex, UK, 2008).

[1.3] M. Huyse, The Why and How of Radioactive-Beam Research in J. Al-Khalili and E. Roeckl (Eds.), *The Euroschool Lectures on Physics with Exotic Beams*, Vol. I, Lect. Notes Phys. 651 (Springer, Berlin Heidelberg, Germany, 2004).

[1.4] H. Hoffsass, Hyperfine Interactions 97-98 (1996) 247-283.

[1.5] K. Langanke *et al.*, *Nuclear Astrophysics and Nuclei Far From Stability in J. Al-Khalili and E. Roeckl (Eds.)*, *The Euroschool Lectures on Physics with Exotic Beams*, Vol. I, Lect. Notes Phys. 651 (Springer, Berlin Heidelberg, Germany, 2004).

[1.6] U. Köster, Eur. Phys. J. A **15**, 255-263 (2002).

[1.7] P. Van Duppen, *Isotope Separation On Line and Post Acceleration in J. Al-Khalili and E. Roeckl (Eds.)*, *The Euroschool Lectures on Physics with Exotic Beams*, Vol. II, Lect. Notes Phys. 700 (Springer, Berlin Heidelberg, Germany, 2006).

[1.8] http://mis.triumf.ca/science/planning/yield/target/U.

[1.9] Y. Zhang, G.D. Alton, Nuclear Instruments and Methods in Physics Research A **521**, 72-107 (2004).

[1.10] S. Corradetti et al., Eur. Phys. J. A **47**, 119 (2011).

[1.11] G. D. Alton, *Post-Accelerator Issues at the IsoSpin Laboratory*, Proceedings Post-Accelerator Issues at IsoSpin Laboratory,LBL-35533, CONF-9310290, UC-413.

[1.12] Best Cyclotron System Inc, www.bestcyclotron.com.

[1.13] V. Sabaiduc et al., "Resonator System for the BEST 70 MeV Cyclotron", CYC'13, Vancouver, Sept. 2013, (2013); http://www.JACoW.org.

[1.14] A. Monetti *et al.*, *The RIB production target for the SPES project*, Eur. Phys. J. A **51**, 128 (2015).

[1.15] M. Manzolaro et al., Nucl. Instrum. Meth. B **317**, 446 (2013).

[1.16] M. Manzolaro et al., Rev. Sci. Instrum. **83**, 02A907 (2012).

[1.17] M. Manzolaro, *Engineering of the INFN SPES target – ion source system* (LAP Lambert Academic Publishing, 2012).

[1.18] M. Ballan, *Progettazione e test di componenti e sistemi di misura per l'operazione e la sicurezza del sistema target - sorgente del progetto SPES*, Tesi di Laurea Magistrale, Università degli Studi di Padova (2014).

Chapter 2

The target: study, redesign and tests

2.1. Introduction

The SPES production target is composed by 7 uranium carbide disks, characterized by a diameter and a thickness of 40 and 0.8 mm respectively, with a density of 4 g/cm^3 for the Uranium Carbide manufactured [2.1]. In the previous study, the disks thicknesses was higher due to the lower Uranium Carbide density assumed there (2.5 g/cm^3). On the other hand, the target heating system consists of a thin tantalum tube, with a length of about 170 mm, a thickness and an external diameter of 0.2 and 50 mm respectively.

The most common type of uranium carbide produced, used and tested in ISOL facilities, is commonly referred to as UC_x, indicating it is composed of different phases: uranium dicarbide (UC_2), graphite (C), and a minor amount of uranium monocarbide (UC) [2.3] [2.4]. In recent years, the synthesis and the characterization of uranium carbide thin disks (SPES target prototypes) have been successfully carried out [2.5] [2.6], and the production methodology can be considered mature.

The synthesis is based on the reaction between a proper uranium source, typically uranium dioxide, and graphite:

$$UO_2 + 6C \rightarrow UC_2 + 2C + 2CO \qquad (2.1)$$

Which is made to occur at high temperature (up to 1800 °C) in high vacuum (~10^{-6} mbar).

The production route for the disks to be used as SPES targets consists of the following steps:

- Mixing of the precursors powders by means of a planetary ball mill or using an agate mortar. A small quantity of a phenolic resin binder, usually 2% wt., is used to provide the pressed green pellet with sufficient mechanical stability to be handled without damage and loss of powder.
- Then uniaxial cold pressing of the mixed powders into pellets, making use of a hydraulic press and a specifically designed die.
- After extraction of the pressed pellet from the die, its thermal treatment is carried out in a high vacuum furnace developed to reach very high temperatures (~ 2000°C).

The performances of the UC_x target in terms of both isotopes production and thermal stability have been successfully evaluated during two low power irradiation tests at HRIBF facility of the Oak Ridge National Laboratory (ORNL) [2.5], [2.7]. During these tests, a good

correspondence between the electro-thermal simulations and the on-line behaviour of the target-ion source system was obtained [2.5]. Moreover a SiC target has been tested under high power density conditions (0.5 kW - 650 W/cm^3) demonstrating a good structural and thermal stability during the test [2.8].

In this thesis, particular attention has been paid to the definition of the proton beam characteristics. This is crucial since, as it will be possible to see later, the temperature and thermal stresses could be very critical and causes the rupture of the disks and the consequently stop of the RIBs.

In the first paragraph, the presentation of the final configuration of the 40 MeV UC_x target is presented, in nominal conditions, varying beam properties and simulating some failure scenarios. In particular, this is the first time that the effect of different beam properties has been taken into account for this target. After that study, it was possible to give the constraints to the cyclotron group in order to safely manage the target irradiation.

In the second paragraph, a new 70 MeV UC_x target is described, applying the same methodology used on the first. It is a very important description since it could be used at a later time even in the SPES facility, but also in a new facility at iThemba LABS now in the planning stage. Finally, the last three paragraphs are focused on the test performed to validate all the previous calculus and, in particular, to validate the SPES target simulations. In fact, in these paragraphs, it is described the preparation, the design and the measures performed at iThemba LABS during the irradiation of the 70 MeV target, with SiC disks, by means of a 4 kW, 66 MeV proton beam delivered by the cyclotron.

2.2. The final design of the 40 MeV UC_x target

A lot of work has been already done on the 40 MeV UC_x target in Fig. 2.1, especially described in [2.2]. The previous studies were more dedicated to the development of a target prototype, whereas this work will be focused on the final definition of the disks configuration. Consequently, the main boundary conditions of final design have been already defined by the previous preliminary works and they are:

- Target material: UC_x with a density of about 4 g/cm^3
- 40 MeV, 200 μA (8 kW) of proton beam
- 40 mm disks
- Tantalum heater length: 170 mm
- Graphite container length: 200 mm

- Graphite container inner container diameter: 45 mm

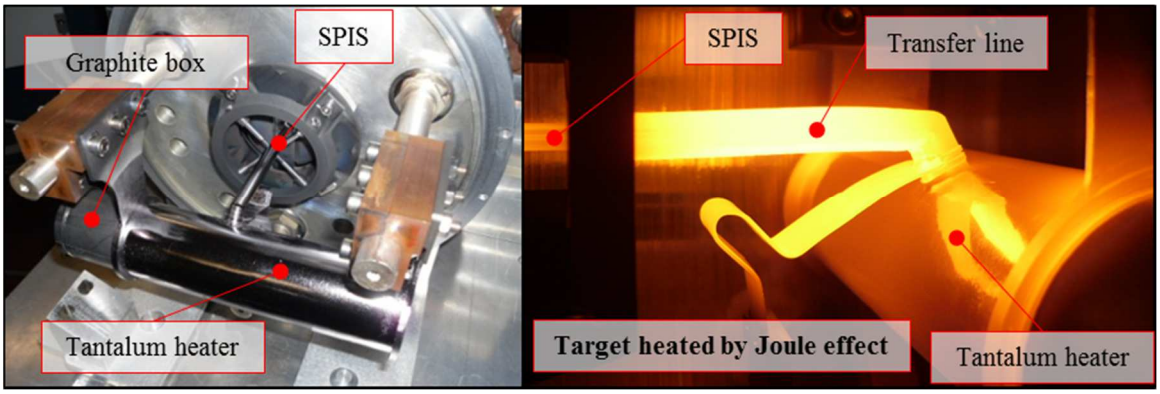

Fig. 2.1. Target-ion source assembled and heated by Joule effect (not maximum power).

2.2.1. Verification of the codes for the power deposition

The beam particles, when impinges the target material, release their kinetic energy to the target atoms. This energy can be thought as an internal power generation and it depends on:

- Beam energy and particle (mass and element)
- Target composition (elements, masses and density)

The physical quantity which describes the power deposited by the beam is the stopping power, defined as the retarding force acting on charged particles due to the interaction with matter. Essentially, it is the loss of the beam energy per unit path length. The integration of this function along the particle path gives the power deposition of the beam particles in the target. Moreover, the stopping power can provide the minimum target thickness to statistically stop the beam: essentially the beam penetration inside the target. This quantity is called projected range. Finally, the beam particles, during the penetration inside the target, are subjected to the straggling, the deviation of the particles respect to their straight path.

Since the power deposition is the most critical boundary condition on the target design, particular attention has been paid to its definition. Various codes can be used to simulate the power deposited onto the material. In particular, three are the fully integrated Monte Carlo packages adopted for the simulation of the transport and interaction of particles and nuclei with matter, which can provide the power deposition:

- MCNPX 2.7e [2.9] and FLUKA [2.10] [2.11]: in these two codes, the nuclear interactions generated by ions are treated through interfaces with external event generators since cross-section libraries are not available for all materials, energies and reactions.
- SRIM [2.12]: this code allows determining the trajectory and the power deposition by an ion in different materials. The number of protons with SRIM is much less (0.1%) of the

particles simulated with the other two codes and this reflects on the more irregular trend compared to the other codes.

In the previous target design [2.2], a uniform proton beam profile and a 2.5 g/cm^3 UC_x density were assumed. The comparisons between the various codes power deposition is presented for a flat beam profile.

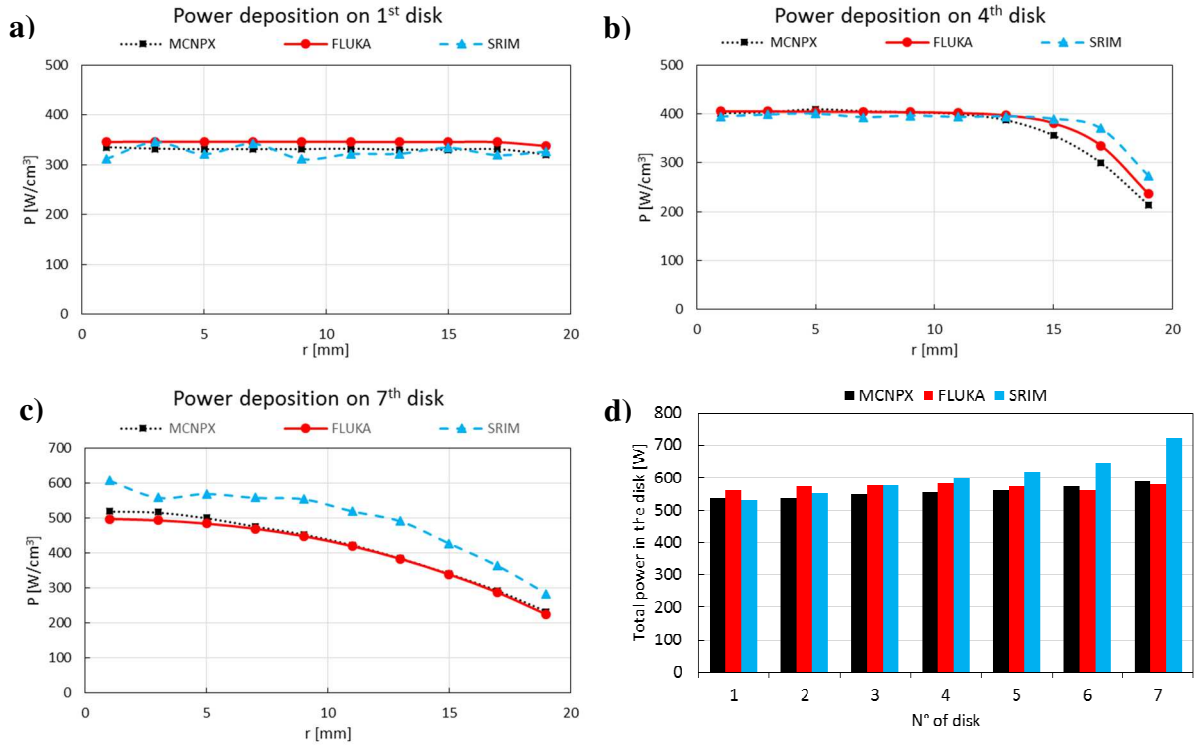

Fig. 2.2. Power deposition in some UC_x disks (1st, 4th, 7th) of the target and total power released in the disks (d) according to different Monte Carlo codes.

Slight differences can be observed for the 1st and 4th disks, due to a different treatment concerning the straggling of the protons by the codes: the highest is in MCNPX, the lowest in SRIM. On the contrary, in the 7th disk, SRIM predicts a power density of about 20% higher. A higher beam straggling has two main effects:

- Higher scattering of protons decreasing the efficiency of the isotopes production.
- Lower power deposition on the last disks.

Therefore, the maximum temperatures of a thermal simulation with the results given by SRIM are more conservative than those obtained by FLUKA or MCNPX, which on the contrary are probably the most reliable.

The actual production of the UC_x disks fixes the density of about 4.0 g/cm^3, leading to a thickness for all the disks to 0.8 mm, for a total mass of 28 g, in order to maintain the product between disk thickness and density. These values are sufficient to efficiently utilize the Uranium cross-section since the mean proton energy exiting the last disk is about 15 MeV

(after this energy, no fissions happen in the uranium). The beam shape is assumed to be Gaussian as presented in 1.4.3. For a safer condition due to a simpler control, the shape of the proton beam has been chosen to be a wobbled Gaussian around the disk axis, with a fixed standard deviation. The wobbler, the device which allows to rotate the beam, is fundamental to spread the proton beam power on the disk surfaces. As an example, two different beam profiles have been presented in Fig. 2.3 with the same amount of power (15%) out of the target due to the Gaussian tails. Without wobbling, the power peak in the centre of the disk is approximately 50% higher, leading to a consequent increase of the temperature difference between the centre and the edge of the disk, and then higher stresses. In addition, a smaller proton beam spot, focused on the disks edge due to the wobbler, decreases the maximum temperature of the disks in the centre and, consequently, decreases the stresses on it.

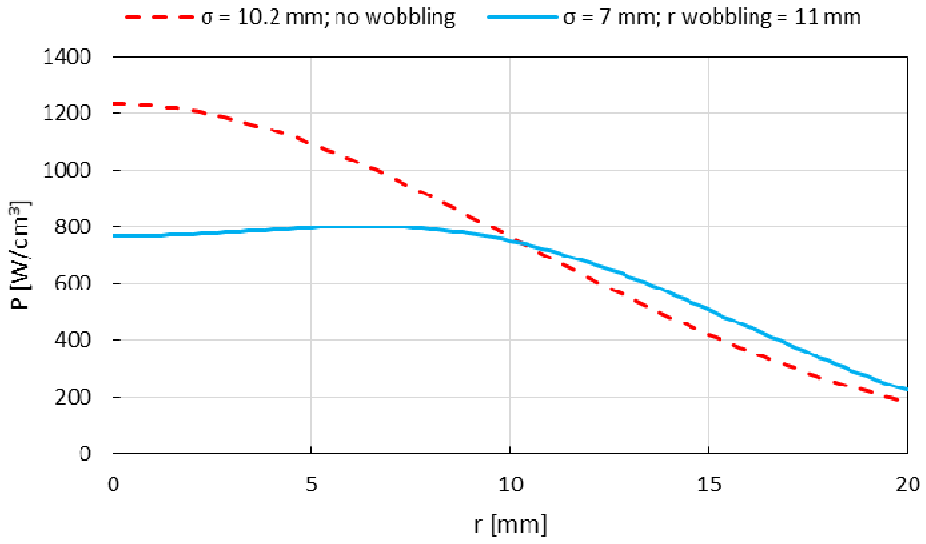

Fig. 2.3. Power density in the first disk with and without wobbling.

Until reasonable bound, it is clear that the highest the sweeping radius and the smallest beam spot are the best working conditions mixing. This limit is essentially due to the beam size, which directly depends on the beam emittance and the transport line. In our case, the BEST Company confirms a maximum 7 mm RMS radius for the beam onto the target.

The power beam losses out of the target onto the collimators increase with a higher sweeping radius, leading to higher activation levels and radiation doses especially at the collimators. It is essential, for this cause, to decrease as much as possible the sweeping radius for a fixed RMS radius.

A compromise between losses and working conditions is a sweeping radius of 11 mm, with about 15% of power dropped on the collimators.

2.2.2. *Thermal and structural simulations of the 40 MeV target in stationary and nominal conditions*

The proton beam properties depend on the emittance of the beam, on the transport lines and on the wobbling system, which strongly influences the reached temperatures. For the thermal simulations, the temperatures of the disks must be kept below 2300°C, which is the typical melting point of Uranium Carbide [2.13] [2.14] [2.15], the conductivity has been assumed to be 8 W m^{-1} K^{-1} [2.16] [2.1], the emissivity 0.85 [2.1] [2.3]. For the structural simulations, the maximum stress has been assumed below 200 MPa [2.17], the thermal expansion coefficient $12.4 \cdot 10^{-6}$ $°C^{-1}$ [2.17] (with the same procedure used in [2.18]), the elastic modulus 176 GPa, whereas the Poisson's ratio 0.269 [2.2]. Especially for the structural properties of the Uranium Carbide, the data are extrapolated for 2000°C from properties evaluated at 1300-1500°C. All the assumption and simplifications are already well described in [2.2]. A campaign of simulations has been implemented to estimate the new temperatures on the disks with the new boundary conditions. For this purpose, FLUKA has been chosen to simulate the power distribution, considering also the good agreement with MCNPX shown in the previous analysis. The power deposition has been used as input for ANSYS [2.19] for the simulation of the target thermal and structural distributions.

The geometry of the target has been simplified to axial-symmetric volumes. For example, only the tube of the tantalum heater has been simulated, without the tantalum connectors and the water cooled electrical feed-through, which is a strong simplification when the Joule effect is predominant. On the other hand, at the maximum beam current, goal of this study, the power is only due to the beam power.

To complete the geometry, the chamber is introduced in the simulation. In particular, the temperature of the chamber has been fixed to 50°C, since its value does not affect the temperature of the target and of the dump [2.20] because the chamber is sufficiently large, while the emissivity of the internal walls has been fixed to 0.1. Some iterations between FLUKA power deposition and ANSYS thermal simulations was performed in order to get the best disks configurations. In fact, the increase of the distances between the disks is a compromise between the two main effects:

- Decrease temperatures and stresses on them - good effect
- Increase of the target length and decrease of number of fission due to the increase number of proton which do not impact with the last disks - bad effect

The power density calculated by FLUKA deposited into the various disks at the final configuration is presented in Fig. 2.4.

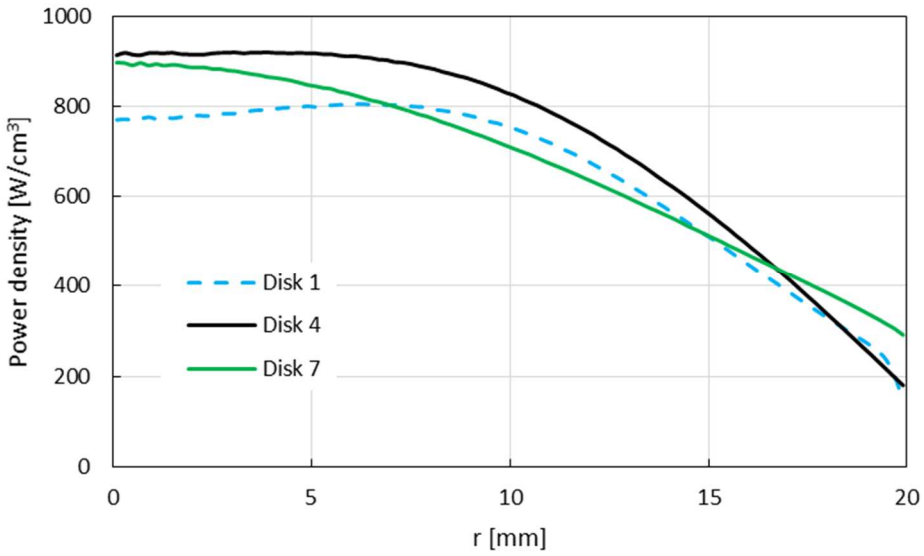

Fig. 2.4. Power density in several disks of the target calculated by FLUKA.

Then the power deposition has then given as boundary conditions to the thermal FEA as shown in Fig. 2.5.

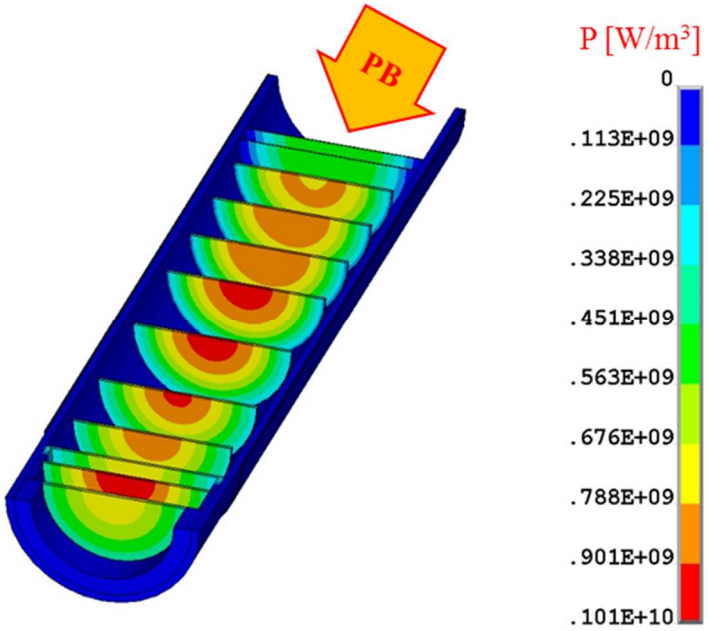

Fig. 2.5. Power deposition for the nominal case - 8 kW, 7 mm RMS radius, 11 mm wobbling radius.

Finally, the thermal results are the boundary conditions for the consequent structural FEA. A sum of the main results of the process is presented in Table 1.

N° disk	P [W]	$N_{FISSION}$ [s^{-1}]	Distance between disks [mm]	T_{mean} [°C]	ΔT_{max} [°C]	T_{max} [°C]	$\sigma_{von\ Mises}$ [MPa]
1	553	$1.7 \cdot 10^{12}$		2060	174	2127	198
2	572	$1.6 \cdot 10^{12}$	15.5	2169	158	2230	186
3	589	$1.5 \cdot 10^{12}$	16.5	2238	151	2297	181
4	604	$1.4 \cdot 10^{12}$	16.5	2274	139	2330	169
5	597	$1.2 \cdot 10^{12}$	24.5	2288	122	2342	139
6	573	$9.0 \cdot 10^{11}$	25.5	2276	120	2333	125
7	568	$6.3 \cdot 10^{11}$	18.5	2226	160	2299	164

Table 1. Power, temperature and highest stresses for the disks in the SPES target impinged by a 40 MeV, 200 μA proton beam.

The highest fission number, aim of the target, is concentrated to the first disk even if the most of the power is deposited in the 4th disk, effect due to the higher cross-section of the uranium at the energy of 40 MeV.

The conclusions for the nominal conditions are summarize below:

- The highest temperatures are concentrate in the last disks, which could be suffered of material evaporation.
- The highest Von Mises stresses are presented in the first disks.

Probably the second point is the most critic since a break of the disk will be instantaneous, whereas the evaporation process effects are visible only at longer time. Anyway, just as a first information, very high values of difference of temperature on the UC_x disks have been applied to measure the material conductivity in [2.1]. No evidences of damage on the disk were observed for a 30 mm, 1.4 mm thick UC_x disk: here a maximum of 300°C of difference of temperature at 1500°C has been measured.

Anyhow, if the temperatures and stresses turn out not to be fully sustainable by the disks, a reduction of the beam power of 10% from 200 to 180 μA of beam current can decrease the temperatures by about 70°C and the stresses of about 5%, as Fig. 2.6 shows.

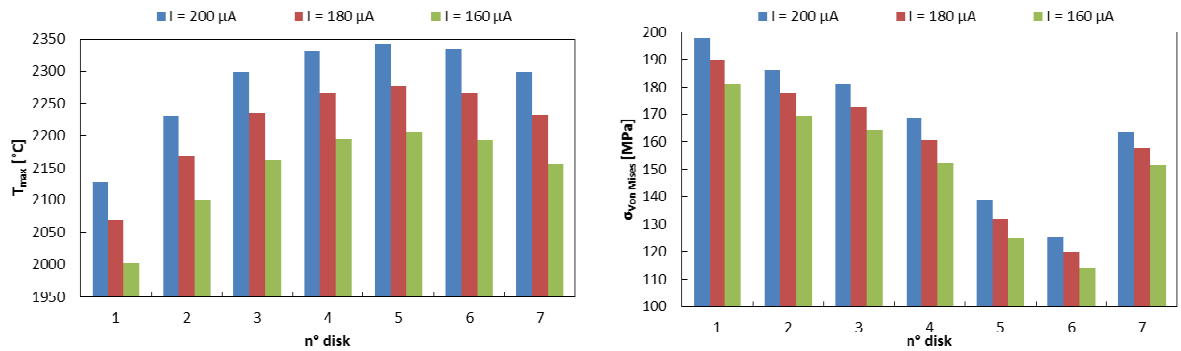

Fig. 2.6. Variation of the temperature peak and the maximum von Mises stresses on the disk according to different beam power.

To complete the analysis, a sensitivity study for the UC_x emissivity and conductivity has been implemented, in order to evaluate the effect of the assumed properties. The conductivity is expected to be in the range between 6 and 15 W m^{-1} K^{-1}, whereas the emissivity between 0.70 and 0.95. Fig. 2.7 shows that a variation of the 25% of the conductivity expected value does not influence the maximum temperature of the disks (about 10°C), whereas the von Mises stresses can change of about 10%. The same considerations were obtained concerning the emissivity: the decrease of about 10% from the assumed value (from 0.85 to 0.75) increases the maximum temperature of few degrees (about 20 °C), while it increases the von Mises stresses of about 9%. This is very important since just the stresses on the disks are effected by the variance of the UC_x properties.

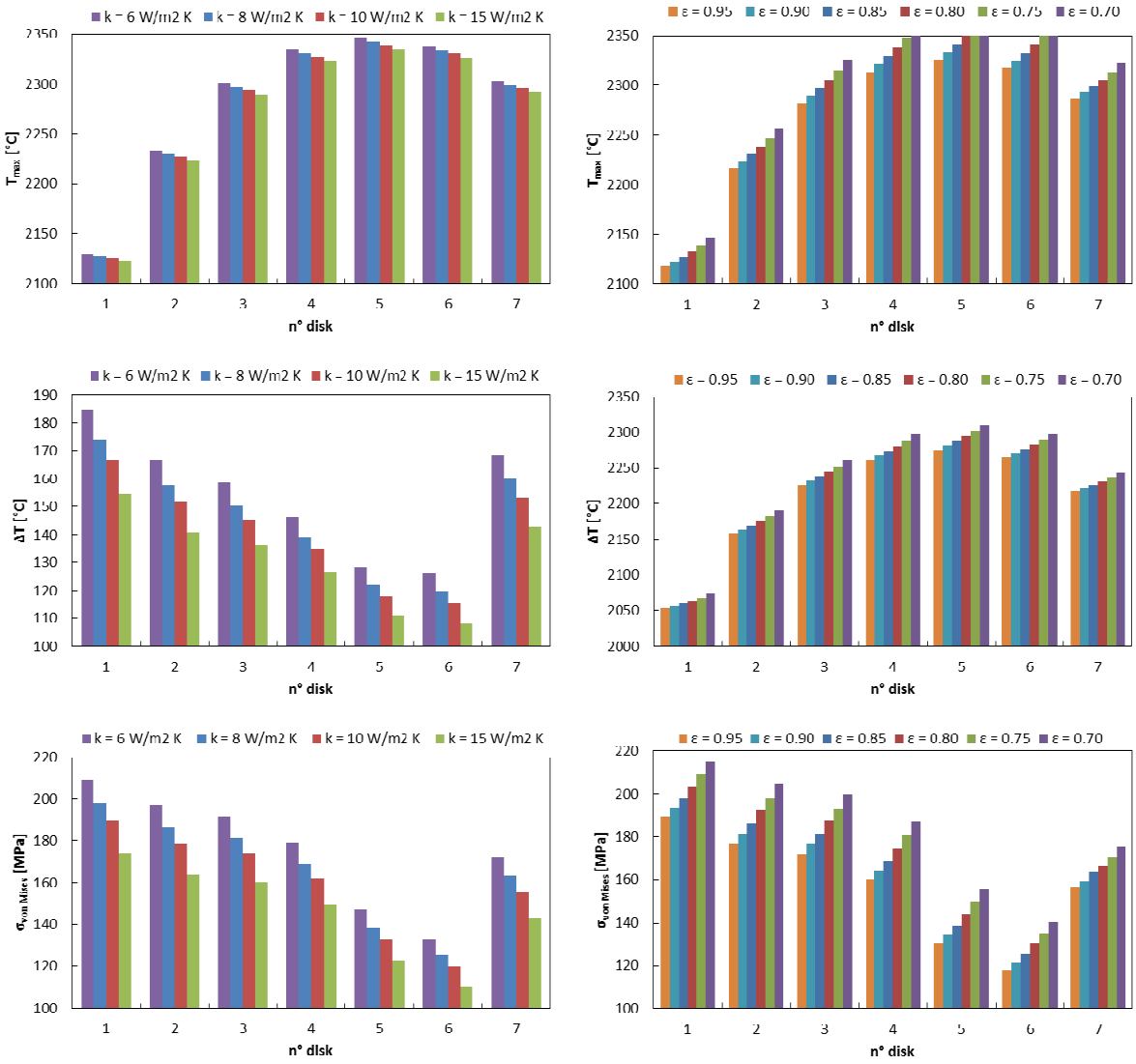

Fig. 2.7. Variation of the temperature peak, the maximum difference of temperature and the relative von Mises stresses on the disk according to different conductivity and emissivity.

In the overall paragraph and sometimes even in the later, the Von Mises stresses has been used, but it is not very significant since:

- In literature, for what it is known, there are not criteria to describe which is the limit on multiaxial stress fields at high temperatures.
- The point where the Von Mises stresses are the highest is at the edge of the disk, which is extremely thin. Consequently the stress distribution is essentially uniaxial.

2.2.3. Thermal and structural simulations of the 40 MeV target with different beam profiles

A sensitivity study has been performed in order to evaluate the effect of a change of the beam size. As said previously, the beam characteristics are defined by:

- RMS size
- wobbling radius

assuming axis-symmetric and Gaussian beam profile.

As shown later in 3.2, the beam radius is defined by the collimators, where it is possible to measure the beam current impinging on them and, consequently, to check the beam properties. Fig. 2.8 represents the percent power out of the target with combination of r_{RMS} and $r_{wobbling}$ during the target irradiation.

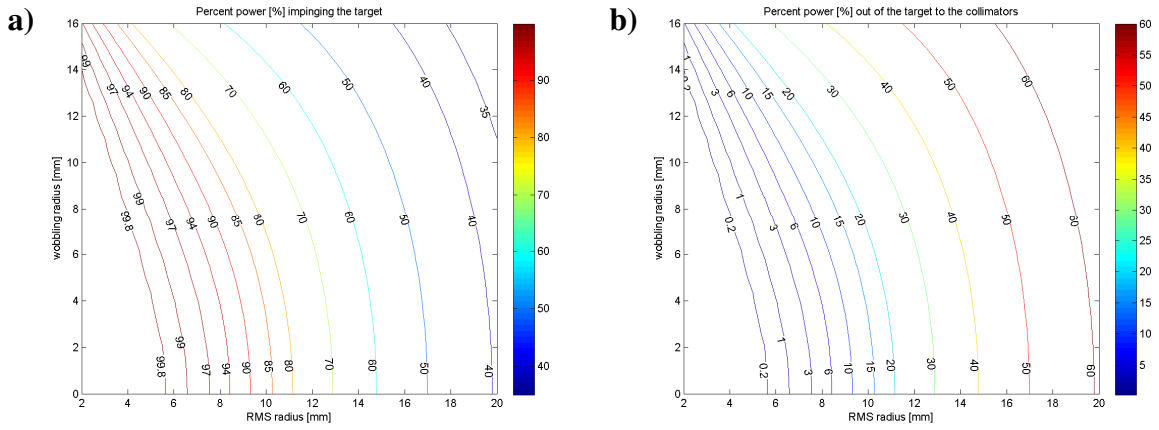

Fig. 2.8. Power in (a) and out (b) the target depending on RMS and wobbling radius

Since the nominal case is r_{RMS} = 7 mm and $r_{wobbling}$ = 11 mm, the consequent beam power loss on the collimators is about 15%. As it would be possible to see in chapter 3.2, one of the requirements imposed on the collimators design is the possibility to measure the total beam intensity dropped on them. This diagnostic will be essential from the target point of view since it will be possible to monitor the beam properties during the target irradiation. The dependence of the wobbling radius against the RMS beam radius is plotted in Fig. 2.9 with a 15% of beam lost out of the target.

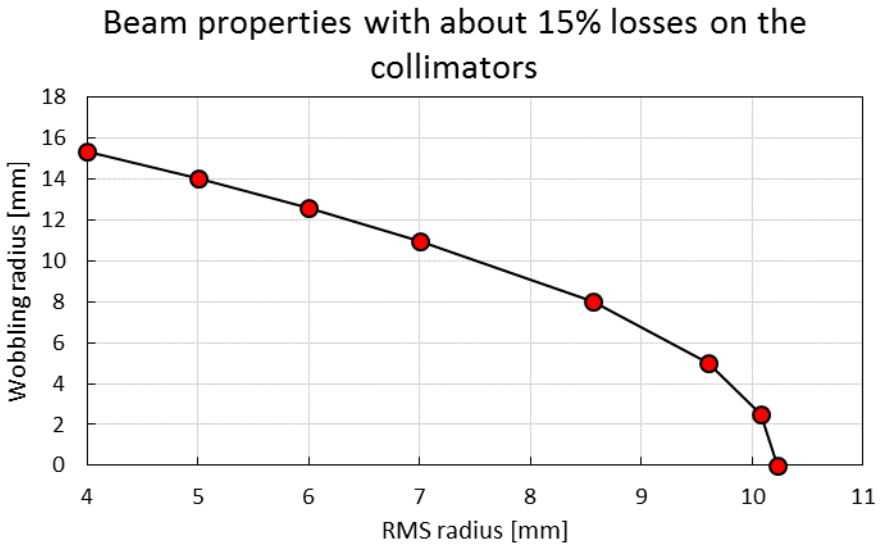

Fig. 2.9. Beam properties with about 15% of beam losses on the collimators

The various cases in red dot, which have in common the total amount of beam losses in the collimators, have been then study in order to complete the analysis of the target under stable conditions. For each beam properties, the power deposition have been calculated by FLUKA and then given as a boundary condition to ANSYS. The results are presented in Fig. 2.10.

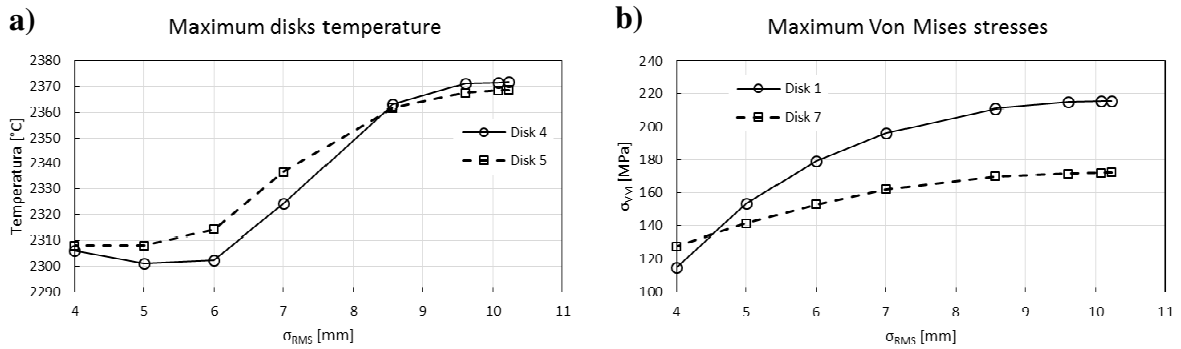

Fig. 2.10. Effect of beam variation on the maximum temperatures and stresses for the target.

It is clear that the variation on the maximum temperature is limited to few tens of degrees, whereas the Von Mises stresses could increment of about 5%. Moreover, as already said, the rupture of the disks will be immediate, without letting the use of the target to produce RIBs for the users.

Since the wobbler inserts, anyway, a complication on the beam managing, the beam profiler without wobbler has been simulated for lower beam currents, maintaining the power dropped onto the collimator constant to 15% of the total beam. The results are presented in Fig. 2.11 for the most critical disks.

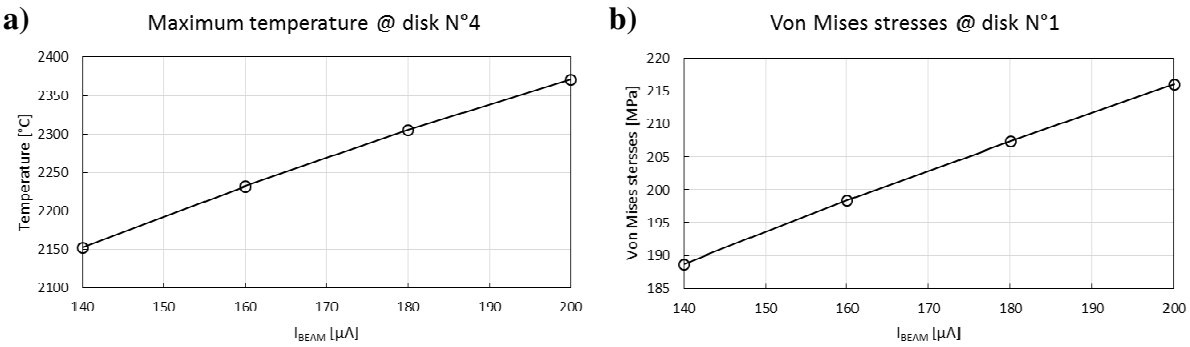

Fig. 2.11. Maximum temperatures and stresses for different beam current without wobbler.

It is clear that, according to the aforementioned mechanical properties of the UC_x, the use of the wobbler could be surely avoided at proton beam current lesser than 160 μA. Moreover, in the simulation, heater power was not added as boundary condition and, essentially, it can contribute on decreasing the stresses and increase the temperature in order to avoid sticking of radioactive isotopes. This last contribution will be very important in order to increase the efficiency of the target for the most exotic nuclei. To complete the study, the minimum temperature of the target is presented in Fig. 2.12. At 160 μA, the minimum temperature is about 1820°C which is quite low for the release of the most refractory elements.

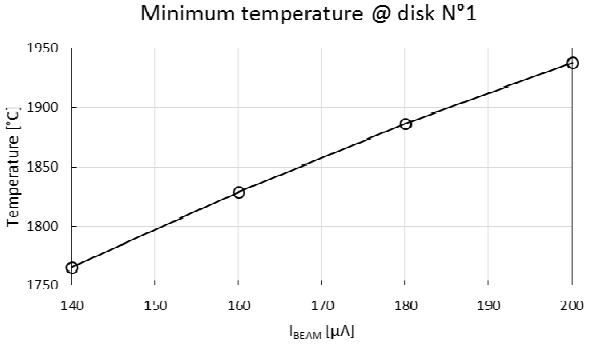

Fig. 2.12. Minimum temperature of the target disks

2.2.4. The effect of wobbling rotation to the target

As showed in the previous paragraph, the wobbling is a fundamental device in order to spread the beam and to decrease temperatures and stresses in the target. Due to the low conduction coefficient of the Uranium Carbide and the high power density of the beam, it is important to evaluate the effect of the beam wobbling. For this purpose, a time-variant simulation has been performed. The temperature of the nominal case has been applied as initial temperature and a rotating heat generation rate has been applied for the various substep. The size of the substep was set to 1/32 of the wobbling time revolution (0.02 s, 50 Hz), leading to an amplitude of 0.625 ms. The main results are summarized in Table 2 and in Fig. 2.13.

Disk N°	ΔT_{centre} [°C]	ΔT_{edge} [°C]	$T_{mean\ edge}$ [°C]	$\Delta\sigma_{VM}$ [MPa]	$\sigma_{VM,\ mean}$ [MPa]
1	0.077	2.1	1944	13	209
2	0.054	1.9	2078	14	184
3	0.090	2.1	2159	14	177
4	0.060	2.3	2206	13	165
5	0.071	2.6	2235	10	135
6	0.067	2.5	2232	6.6	122
7	0.081	2.3	2167	4.8	158

Table 2. Main results concerning the wobbling simulation

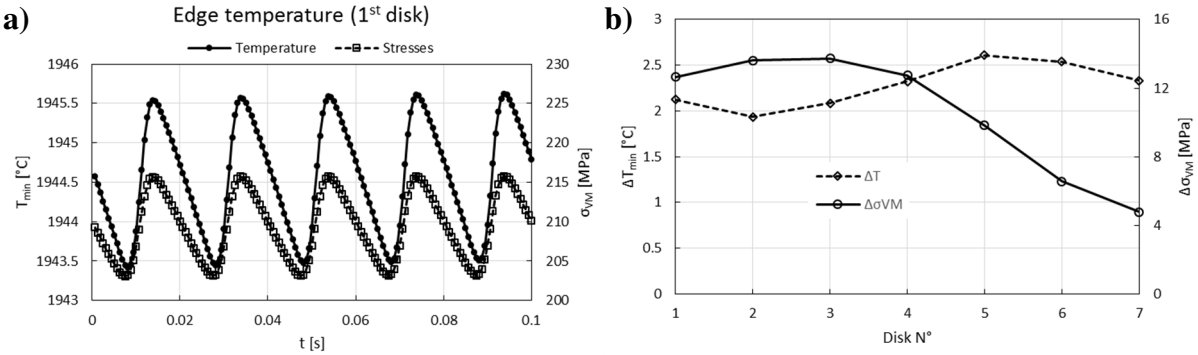

Fig. 2.13. Effect of the wobbling on the first disk concerning the temperature and stresses at one edge; b) Maximum temperature variation and relative stresses amplitude for the various disks

The values of ΔT_{centre} not presented, which is the temperature variation of the centre disks, provides the error of the numerical calculations, which has been found on the order of one tenth of degree. The maximum variation in temperature is found on the fifth and sixth disks, which are the hottest. On the other hand, the maximum stress amplitude is in the first disks. It is clear that there is not a correlation between temperature and stress amplitude since the temperature amplitude is quite constant, whereas the stress not. As a first approximation, it seems that the stress amplitude is correlated to the maximum stresses.

In conclusion, a wobbling of 50 Hz leads to variation of about 14 MPa on the mean stresses of 200 MPa. This value seems quite high and, thanks to this simulation, a 100 Hz wobbling radius has been requested.

2.2.5. The effect of the wobbling stop to the target

In the previous paragraphs, the effects of the beam during nominal conditions have been characterized, but two failure scenarios concerning the proton beam delivery have to be taken into account:

- The wobbling stop
- The beam stop

Here, the first one will be discussed, whereas the second one will be analysed in the next paragraph.

The wobbling stop could be caused by a failure on one of the magnets which is in charge of steering the beam or a failure of the power supply which feeds the coils. The worst scenario has been study that is the stop of the beam in one of the position relative to the target. In this case, the beam has the RMS radius equal to the nominal case, but it is move from the centre with a fixed position equal to the wobbling radius. This has very low probability to happen but it gives the highest constraint to the safety system of the cyclotron.

In particular, the highest temperature is localized in the fourth disk as it is presented in Fig. 2.14a. In 0.1 seconds, the temperature increases of more than 100°C, which could lead to the disk evaporation beginning. Anyhow, the thermal shock is more present on the first disk because after 0.1 s, the Von Mises stresses more than double, until values of approximatly 450 MPa, for a difference of temperature of about 325°C. Almost sure, the disk can not sustain this stresses and the beam stop is needed in order to avoid successive damage of the target or of the scattering chamber. Probably the wobbling fail has to be detected within 0.01 s in order to be sure of the target integrity.

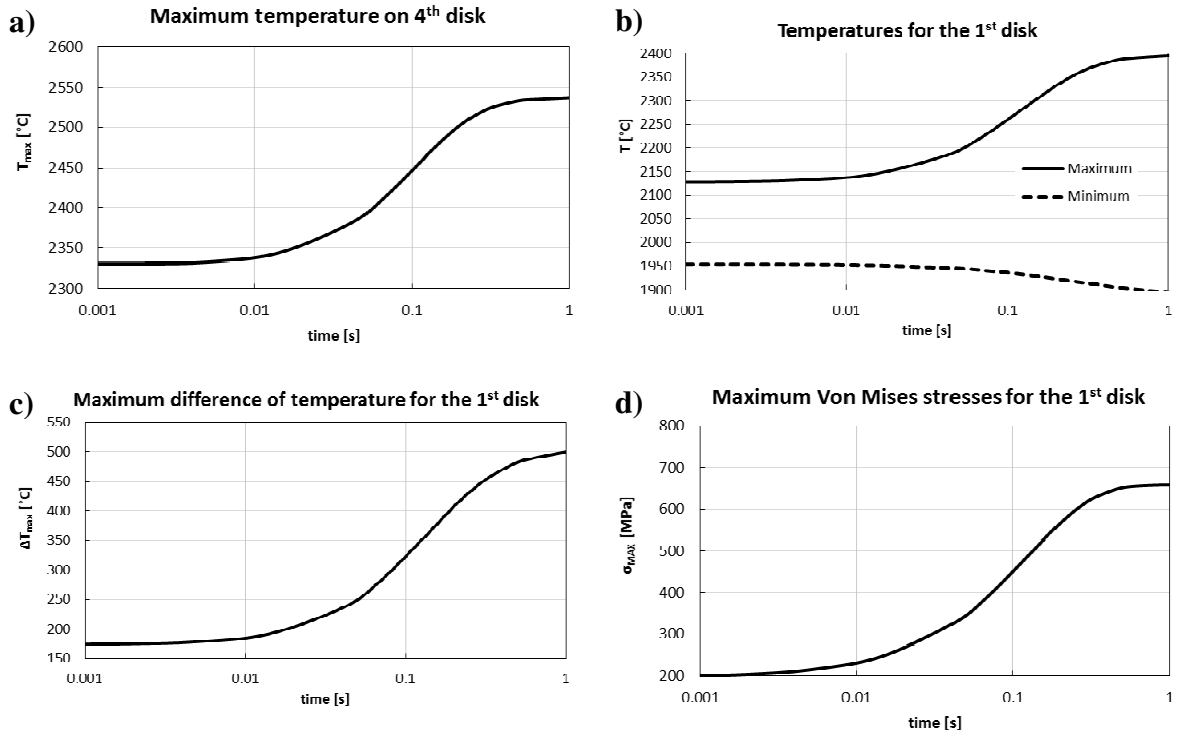

Fig. 2.14: a) Maximum temperature on the 4th disk; b) Maximum and minimum temperature for the 1st disk; c) maximum difference of temperature for the 1st disk; d) maximum Von Mises stresses for the 1st disk.

2.2.6. *The effect of the beam stop to the target*

This is the last effect which has to be evaluated in order to complete failure scenarios. The stop of the beam delivery to the target could happen in case of problems to the cyclotron RF system which is in charge of accelerating the protons, or in case of safety interlocks intervened for other various reasons (power supply malfunctioning, cooling circuit failure, etc.).

The main results are presented below in Fig. 2.15. It is clear that the beam stop do not increase stresses on the disks since the cooling process is very homogenous, probably due to the low thickness of the disks compared to the diameter (factor of 50). Anyway, the temperature are initially very steep since in 1 second it drops of about 200°C for the fourth disk. In order to reduce the cooling process and avoid shocks, it is suggested to turn on the heater current. In addition, during some tests [2.21], no evidences of damage on the heater integrity have been showed during a ramp of 1 second from zero to the maximum current.

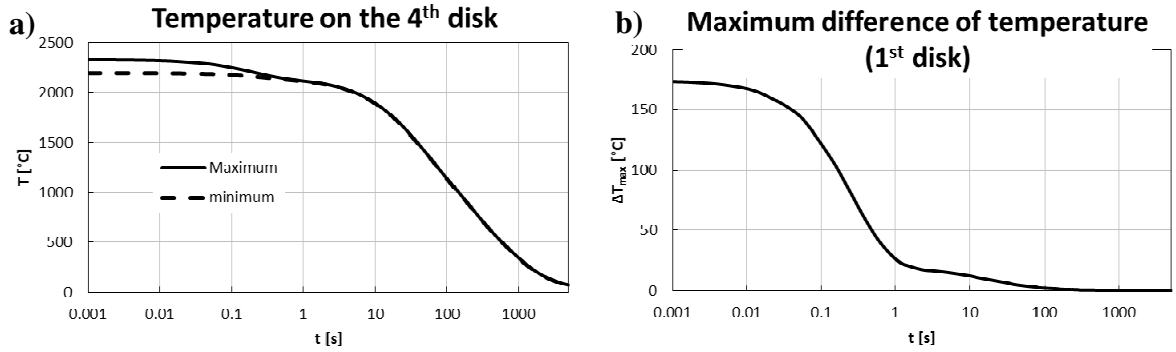

Fig. 2.15. Maximum and minimum temperature for the fourth disks and maximum difference of temperature for the first disks

2.3. The design of the 70 MeV UC_x target

2.3.1. *Initial conditions for the target design*

In a collaboration between INFN and iThemba LABS, an UC_x target has been adapted to a 70 MeV energy beam. IThemba LABS is a group of multi-disciplinary research laboratories especially involved for Accelerator-Based Sciences. The centre is placed 50 km far from Cape Town in South Africa, where a Separated Sector Cyclotron was designed, installed and operational since late ’80.

The boundary condition of the target are different from the previous study:

- The beam energy has been fixed to 70 MeV
- The target must fit inside the SPES scattering chamber: maximum target total length of 230 mm
- The maximum power lost in the collimators must be lower than 150 W.

The second point was important since, in this way, this target could be used even at an eventual upgrade of the SPES facility. In the design, in order to reduce the degree of freedom of the study, the relative dimension of the SPES 40 MeV UC_x target has been maintained:

- Disk diameter: 40 mm
- Box section: 45 inner diameter, 49 outer diameter
- Heater section: 50 outer diameter, 0.2 thickness
- Geometry of tantalum heater connections

During the dimensioning process, the power deposition was calculated by SRIM, which is less reliable than FLUKA, especially for the bad statistic due to the lower number of particle run, but its use was more simple and user-friendly. Then all the results on the final configuration have been obtained coupling FLUKA to Ansys as in the previous paragraph.

It is underline that just the target disks and dumps configuration has been changed, whereas the heater has just been adapted to the configuration of the 40 MeV target.

2.3.2. Definition of the main dimensions

The most important parameters which have to be fixed are:

- Disks thickness
- Number of disks (and consequently total target thickness)
- Beam power

These parameters influences:

- Number of fissions (and consequently isotopes yields)
- Release time
- Disks spaces
- Maximum temperatures and stresses

First of all, the number of fissions has to be increased as much as possible, in order to provide to the users the highest beam intensity. Simultaneously, the isotopes have to be released as fast as possible since the release time could affect of various order of magnitudes the isotopes available at the ion source, as already described in [2.22]. This is the reason why the dimension of the target and especially its thickness has to be maintained short.

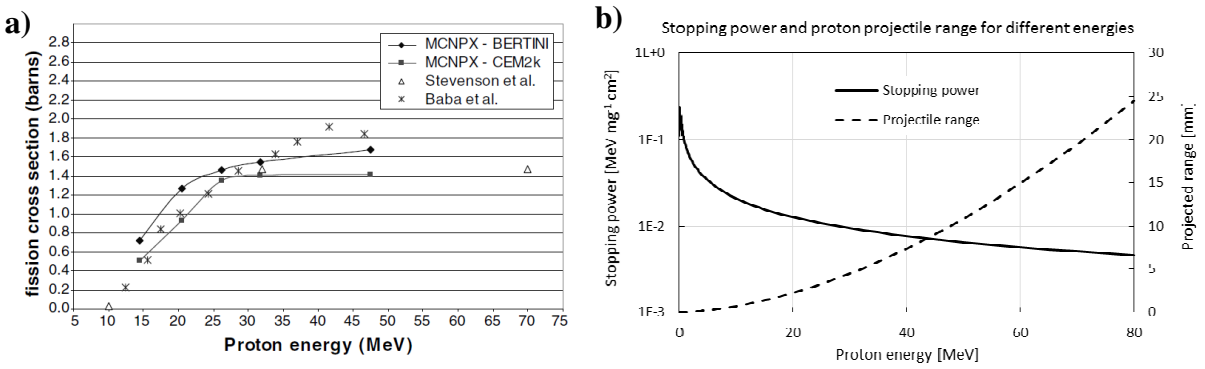

Fig. 2.16: a) Fission cross section, after [2.22]; b) stopping power and projected range for different proton energies.

Fig. 2.16a shows that at higher energies the cross section is higher, this means that the protons are more efficient to fission Uranium. On the other hand, raising the energy from 40 MeV to 70 MeV, the projected range, which is plotted in Fig. 2.16b and describes the UC_x thickness needed to fully stop protons, increases of a factor 2.6 (from 7.5 mm to 19.5 mm). Since 10 MeV is the minimum energy to fission Uranium atom, a thickness of 19 mm is needed to fully use the target, corresponding to 24 disks of 0.8 mm thickness. The number of disks in this target will be surely higher than the 40 MeV version and the space between them lower to maintain approximately the same length.

As presented in paragraph 2.2, the two engineering constraints for the design of the target are the maximum temperature and the maximum stresses reached by the disks. Both of them are extremely influenced by power profile and space between disks. In particular, a reduction on the disks distance will for sure increase both the temperature and stress.

In order to dimension the target, the normalized cumulative number of fission F_N has been used:

$$F_N = \frac{\sum_{i=1}^{j} F_i}{\sum_{i=1}^{N} F_i} \qquad (2.2)$$

Where F_i is the number of fission of the disk i and N is the total number of disks which could generate fissions. In order to get fast results, the number of fissions has been estimated post-processing the power deposition obtained from SRIM and assuming that the protons were stopped just by the interaction with the Uranium atoms, causing its fission. This is not fully true since Carbon has not a negligible effect, but for the aim of this part, the assumption is fine.

This index is presented in Fig. 2.17a according to different disks thickness, fixing a constant distance between the various disks of about 18 mm. It is clear that, for all the configurations, the 80% of the fission available are obtained for beam energies between 70 and 40 MeV. The number of disks necessary to stop the beam until this energy is observable in Fig. 2.17d.

Another important aspect is the beam losses, which decreases with the increase of the disk thickness (Fig. 2.17b) due to minor particle scattering. This leads to an increase of 15% of the total number of fission from the thicker disks (1.5 mm) to the thinnest version (0.8 mm) - Fig. 2.17c. On the other hand, thicker disks could double the release time causing a drop of various order of magnitude for the efficiency of the most exotic species (which probably are the most interesting). For this reason, it is better to avoid a significant increase of the disk thickness even if to increase the total fission number.

The particle scattering causes the decrease of the normalized beam current impinging the last disks at lower beam energy, presented in Fig. 2.17b. Moreover it concentrates the beam at the disks centre. This effect is observable in Fig. 2.18 where the power deposition at the centre of the 13th disk is almost three time than at the edge. Proceeding with the further disks, where beam energy is lower, the particle dispersion is so high that the power deposition decreases even if the stopping power increases. This preliminary consideration has to be taken into account since, for this target, the stresses at the last disks could significantly increase. Anyhow, the power dissipated per disk is approximately constant (Fig. 2.19a) with a reduction of less than 25% from the maximum power (dropped in the first disk), but the number of fission is reduced of about 50% for the 15th disk (Fig. 2.19a).

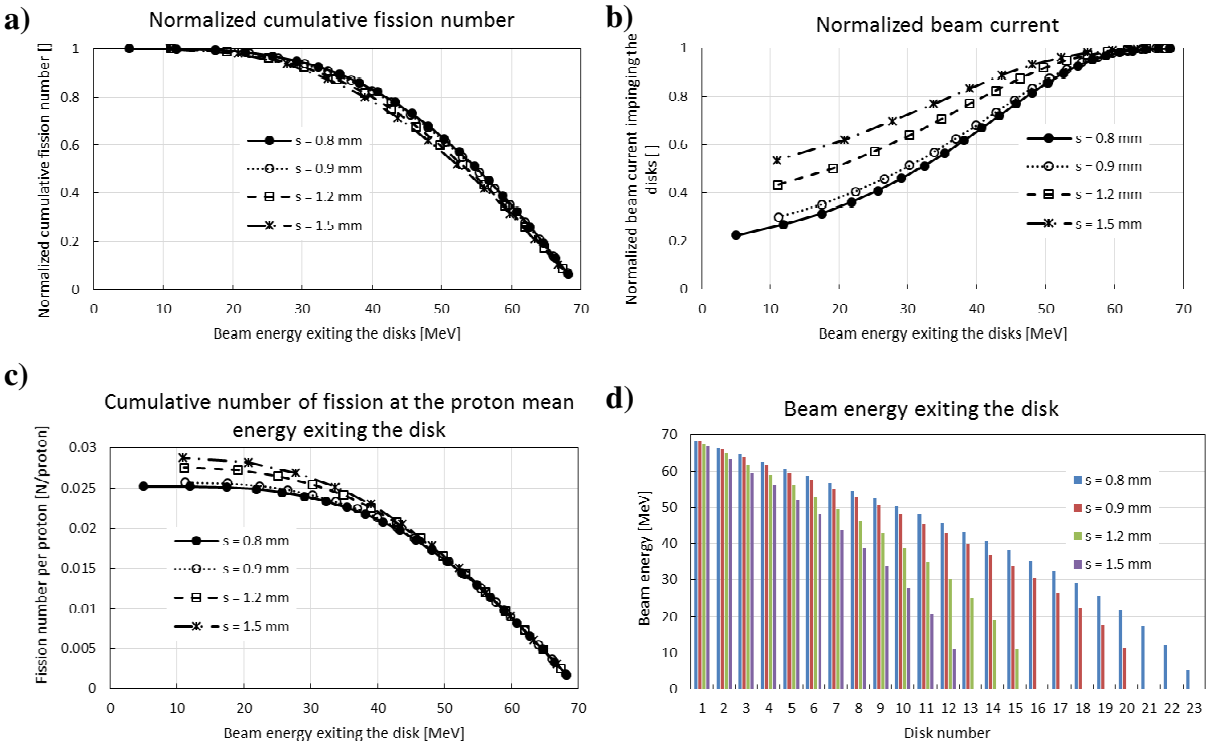

Fig. 2.17. For a distance of 18 mm between all the disks: a) normalized cumulative number of fission (F_r); b) normalized beam current; c) cumulative number of fission per proton at the proton mean energy exiting the disk; d) beam energy exiting the disk.

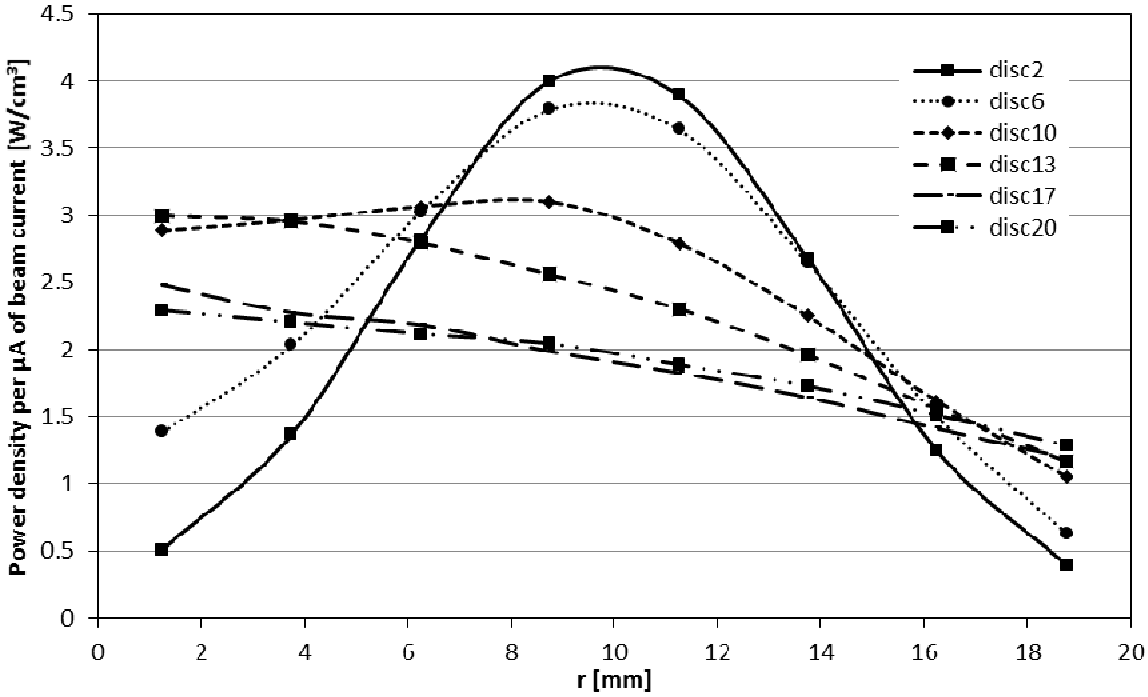

Fig. 2.18. Power deposition per µA of beam current for a disk thickness of 0.9 mm and distance of 18 mm

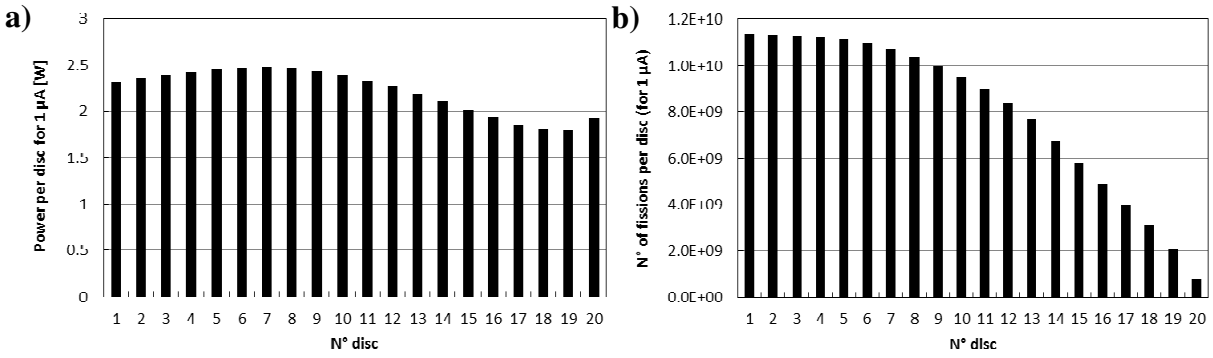

Fig. 2.19. Power and number of fission per disk for a disk thickness of 0.9 mm and distance of 18 mm

In conclusion, the disks thickness has been chosen to be 0.9 mm because:

- The release time will be slightly incremented compared with the standard 40 MeV version (0.8 mm). This aspect will alters the yield for the very short alf-lives.
- Even if probably the total UC_x thickness would not be sufficient to completely use the proton beam energy, the first 30 MeV would generate the 80% of the total number of fission, and this will be the goal of the target design.

In particular, the last reason is not trivial: graphite would be then used to completely stop the beam. In fact, graphite is much more efficient to dissipate power due to higher conductivity (more than five times) compared to UC_x and the amount of prompt radiation and activation generated by the impinged proton is definitely lower. The reduction of the number of disk could leave more space available between the disks, leading to the possibility to increase the beam

power. For the chosen disk thickness, to reach the 80% of the available fission number, the minimum number of disks is 13 and this is the value assumed.

The maximum beam power impinging the target will be fixed in the further paragraph by means of the structural and thermal analysis.

In order to complete the study, the effect of the increase of the disk distances is presented in Fig. 2.20. It is clear that higher is the distance, higher is the proton scattering and the loss of beam current to the graphite box (a). In particular, the losses become very significant decreasing with the beam energy (b). As a preliminary information, if the distance double, the beam losses approximately double. The general effect is the reduction of the cumulative number of fission (b-c): assuming as reference the case with distance of 6 mm, the reduction is maximum of 25% for the case with distance of 24 mm (Fig. 2.20d). The conclusion is that to increase as much as possible the number of fission avoiding beam losses, it is important to decrease the disk distance where it is possible.

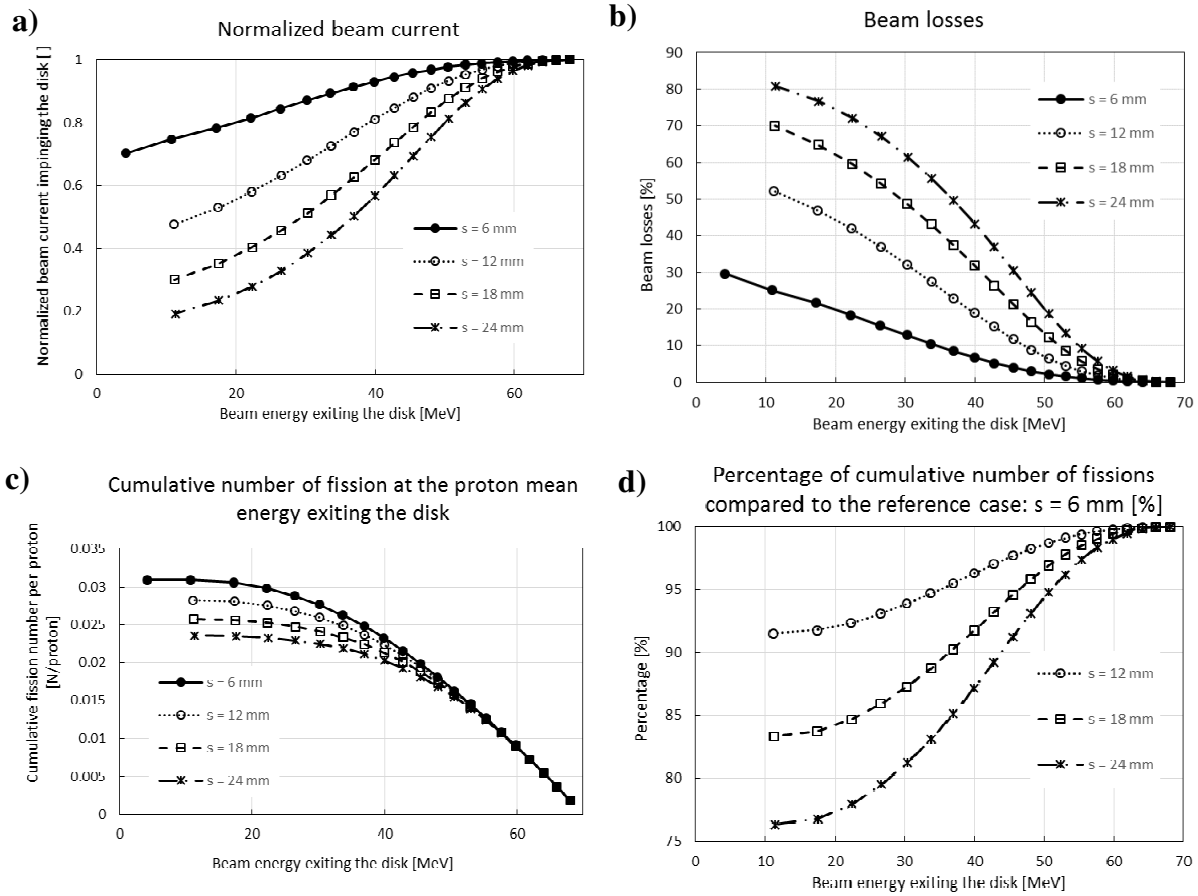

Fig. 2.20. For a disk thickness of 0.9 mm: a) normalized beam current. b) Beam losses. c) Cumulative number of fission per proton. d) Percentage of cumulative number of fissions compared to the reference case: s = 6 mm.

2.3.3. Preliminary study of the 70 MeV target

In the previous paragraph, the disk characteristics has been decided:

- 40 mm of diameter
- 0.9 mm of thickness
- N° of disks: 13

The mass per disk used is about 4.75 g (in the 40 MeV version is 4.02 g), leading to a density of 4.2 g/cm^3. This is in the error range of the disk manufacturing procedure but it is not so important: the disk is defined by the total mass used in their production and, if the density decreases, the disk thickness simply will slightly increase.

The final target design was performed by means of some iterations between SRIM output for power deposition and Ansys® in order to homogenise the maximum temperatures on the disks and reduce as much as possible the thermal gradient and the consequently structural stresses on the first disks. The results of the final version, presented below, are obtained using FLUKA coupled with Ansys, and, in the simulation, the following characteristics were applied:

- Scattering chamber emissivity: 0.1 (temperature fixed to 50°C)
- Heater Power: 2.5 kW
- 150 µA for a 70MeV, 10.5 kW of proton beam power (maximum power deliverable obtained by thermal and structural results)
- RMS radius of 5 mm, wobbling radius of 10 mm: power released to the collimators 100 W

		66 MeV beam energy					70 MeV beam energy				
N° disk	D [mm]	P [W]	$N_{FISSION}$ [s^{-1}]	ΔT_{max} [°C]	T_{max} [°C]	σ_{vM} [MPa]	P [W]	$N_{FISSION}$ [s^{-1}]	ΔT_{max} [°C]	T_{max} [°C]	σ_{vM} [MPa]
1		335	$1.2\cdot10^{12}$	158	2055	207	321	$1.2\cdot10^{12}$	155	2033	202
2	12.1	341	$1.2\cdot10^{12}$	159	2158	175	326	$1.2\cdot10^{12}$	156	2134	172
3	10.1	347	$1.2\cdot10^{12}$	157	2235	178	331	$1.2\cdot10^{12}$	154	2209	174
4	9.1	353	$1.2\cdot10^{12}$	151	2278	176	336	$1.2\cdot10^{12}$	148	2250	173
5	9.6	358	$1.2\cdot10^{12}$	138	2293	165	341	$1.2\cdot10^{12}$	134	2264	162
6	12.6	362	$1.2\cdot10^{12}$	121	2294	145	343	$1.2\cdot10^{12}$	119	2263	143
7	14.6	361	$1.2\cdot10^{12}$	110	2298	129	342	$1.2\cdot10^{12}$	108	2265	128
8	15.6	356	$1.1\cdot10^{12}$	102	2306	114	338	$1.1\cdot10^{12}$	100	2271	113
9	17.6	344	$1.0\cdot10^{12}$	92	2312	97	328	$1.1\cdot10^{12}$	92	2277	98
10	17.6	329	$9.3\cdot10^{11}$	83	2309	85	313	$9.8\cdot10^{11}$	83	2275	86
11	16.6	312	$8.4\cdot10^{11}$	77	2285	76	298	$8.9\cdot10^{11}$	77	2253	76
12	17.1	292	$7.3\cdot10^{11}$	80	2231	74	280	$8.0\cdot10^{11}$	80	2202	75
13	12.1	282	$6.6\cdot10^{11}$	68	2141	87	269	$7.2\cdot10^{11}$	67	2112	86

Table 3. Power, temperature and highest stresses for the disks in the 70 MeV target impinged by a 66 MeV, 150 µA proton beam (D is the spacing between disks).

The results of the nominal case is presented below in Table 3 for a 66 and 70 MeV beam energy. This has been done to demonstrate the possibility to test the target at iThemba LABS

in Cape Town, where a cyclotron delivering a 66 MeV proton beam is functioning. The test on the same target in SiC is presented in paragraph 2.6. The total power dissipated into the disks is respectively about 4.4 and 4.1 kW (about 44% and 40% of the beam power) for a $1.4 \cdot 10^{13}$ number of fission estimated by FLUKA for both cases.

The results for the two beam energies are very close even if the temperatures and stresses are slightly higher for the 66 MeV beam due to a 6% higher power on the disks, whereas the number of fission per second are more or less the same.

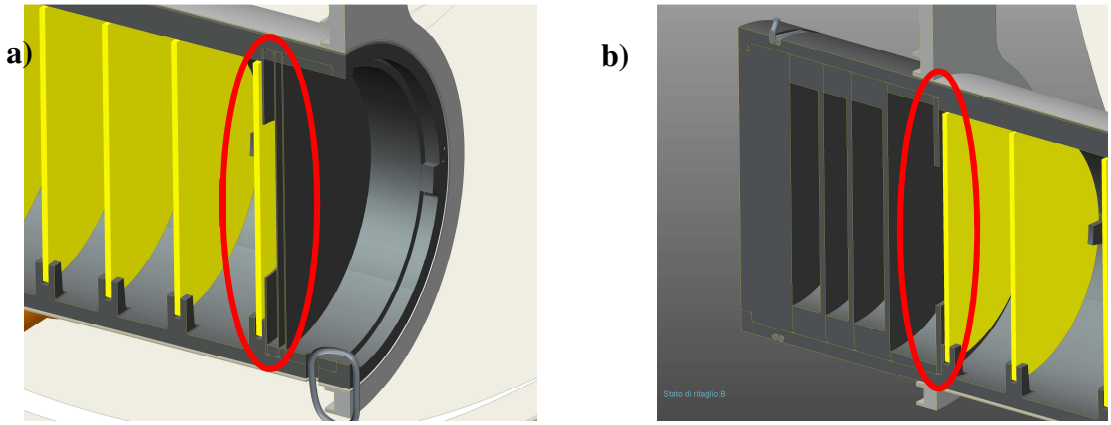

Fig. 2.21. Graphite annulus introduced to decrease stresses on the target disks: a) 0.3 mm thick after the two graphite windows before the first disk; b) 1 mm thick after the last target disk.

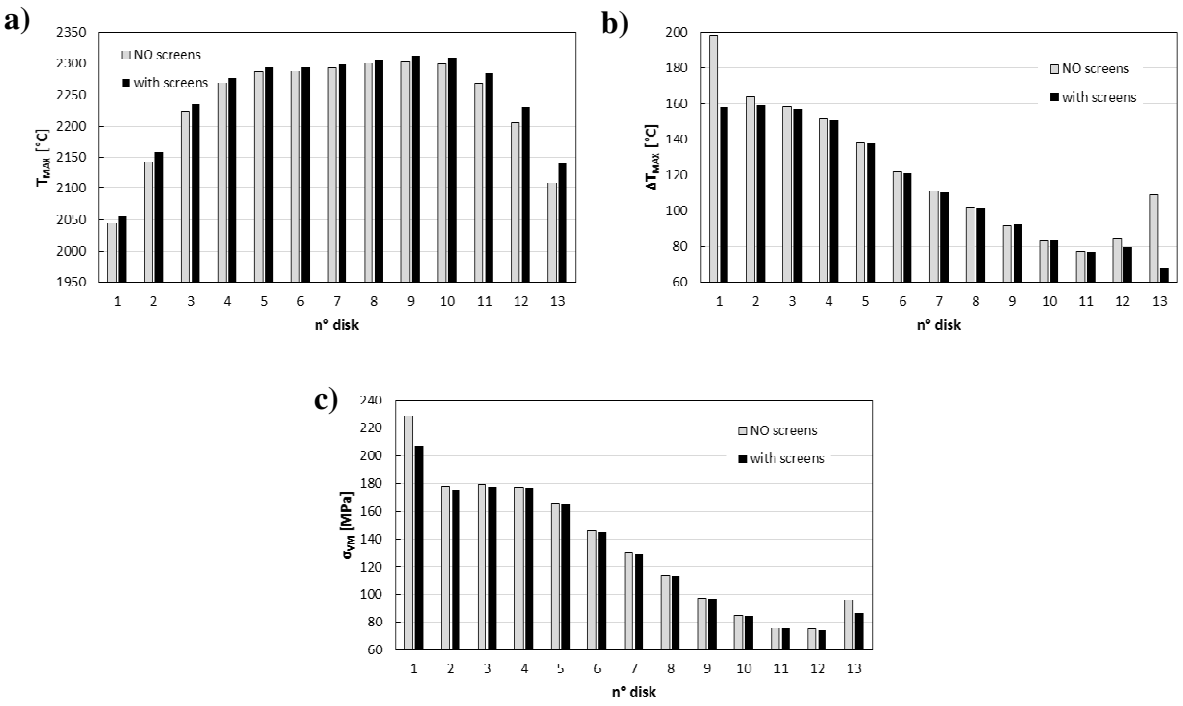

Fig. 2.22. Effect of the presence of the graphite screens for a 66 MeV, 150 μA of proton beam on the: a) maximum temperature; b) maximum difference of temperature; c) Von Mises stresses.

A 0.3 mm and 1 mm thick graphite annulus, called screens, have been introduced respectively after the two graphite windows and the target disks (Fig. 2.21) in order to reduce

stresses on them. The effect is presented in Fig. 2.22 for a 66 MeV, 150 μA of proton beam. The maximum temperature is slightly higher with the screens, but the maximum difference of temperature is significantly lower and this reflects to a decrease of the Von Mises stresses (about 10%). For this reason, they are strongly suggested and its implementation can be inserted even for the SPES target if necessary.

As for the SPES target, the decrease of the beam current has been simulated in Fig. 2.23. The reduction of the 13% of the beam power (from 150 μA to 130 μA) leads to a decrease of the maximum temperature of about 80°C (decrease of 3.5%) and stresses of 16 MPa (decrease of 7.8%). Summarizing, the decrease of the beam power is more significant for decrease of the stresses on the disks respect to the maximum temperature.

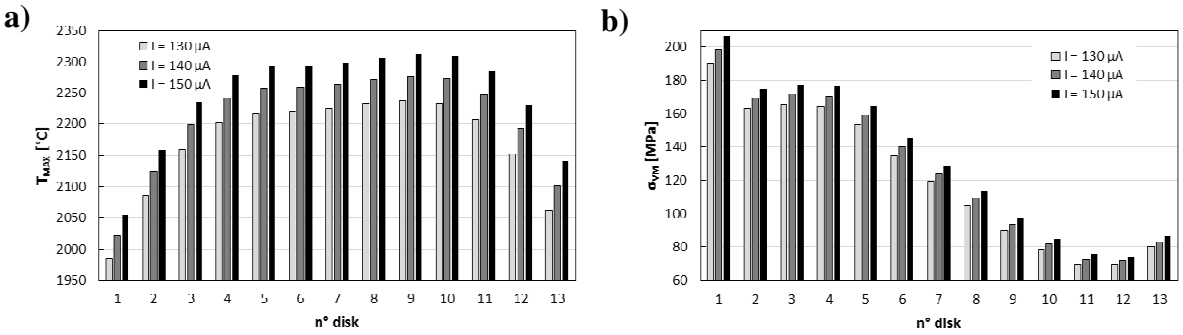

Fig. 2.23. Maximum temperature (a) and stresses (b) for different beam currents

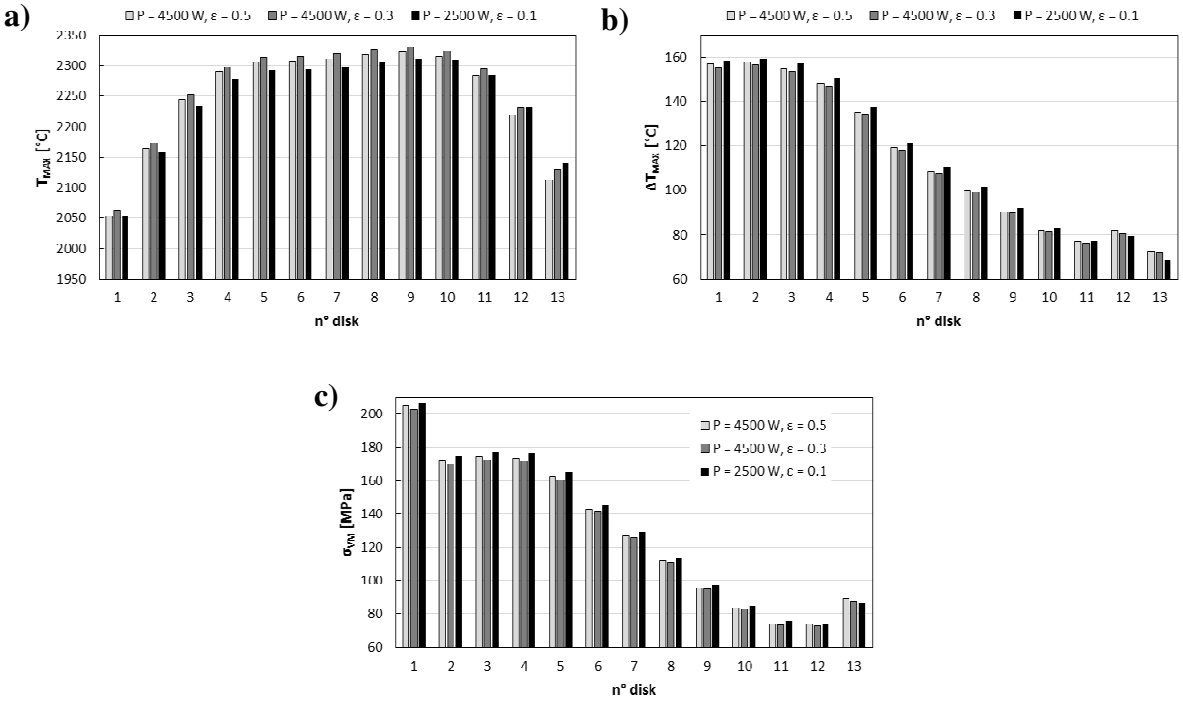

Fig. 2.24. Effect of the chamber surface emissivity and uniform power on the heater for a 66 MeV, 150 μA of proton beam on the: a) maximum temperature; b) maximum difference of temperature; c) Von Mises stresses.

Finally, to complete the study, the effect of the chamber emissivity and power on the heater is presented in Fig. 2.24. It seems that the best compromise is with a wall surface of 0.3 and power on the heater of 4.5 kW. In fact, this will cause a slight decrease of the target stresses with a slight increase of the maximum temperature, but with a much better control of the target temperature: the power released to the heater can efficaciously compensate the proton beam instabilities.

It is underlined that it is very important to study with a much more detail the tantalum heater coupled with the graphite container during Joule heating. In fact, this target has an increased length compared to the 40 MeV version and it can increase problems of parallel circuit already reported in [2.24].

2.4. The design of the iThemba scattering chamber

2.4.1. Preliminary description

A very important step was the definition of a test to validate the calculation process implemented to simulate the thermal and structural distribution of the target. A collaboration with iThemba LABS has been established to test the target since a powerful cyclotron is currently in use. The proton beam energy deliverable is about 66 MeV with a maximum intensity of 350 μA. Moreover, the experience matured on the proton beam control during the various years of operation was surely of great advantage.

For this reason, it has been chosen to test the 70 MeV target, measuring the temperature and validating the numerical results obtained by the FEAs. Previous tests were already performed on a prototype of 13 mm in [2.25], but neither the temperature was measured to compare with the numerical results, nor it was tested the full-scale target with 40 mm diameter disks at high power.

For this purpose, a scattering chamber was design to test a target. Due to the beam energy deliverable by the cyclotron, the choice was to test the 70 MeV target with SiC disks in order to reduce as much as possible the radioactivity of the system after the irradiation process. Moreover, no volatile elements are foreseen to be released, reducing the contamination of the beam line. Preliminary results lead to a maximum of about 60 μA, 4 kW proton beam deliverable, whereas the maximum power released by the heater to the chamber is approximately 11 kW (maximum power load). The overall boundary condition assumed for the design are:

- Maximum power to absorb: 11 kW

- 4 temperature measuring point to foreseen: first disk, graphite container, tantalum heater and dump chamber
- Beam current to read on the chamber dump (in case of target rupture)
- Vacuum measure

Main dimension of the vacuum chamber were fixed to 320 mm of inner diameter and 220 mm of height. In this way, various devices could eventually be tested and not only the 70 MeV target.

2.4.2. The mechanical design

The vacuum chamber is made of three different components: the base, the lateral cylinder and the head. They are removable in order to simplify the assembly procedure of the targets. All three parts have its own water cooling circuit to decrease temperatures and an additional simple cooling circuit on the chamber dump seat has been foreseen. The mechanical design is showed in Fig. 2.25.

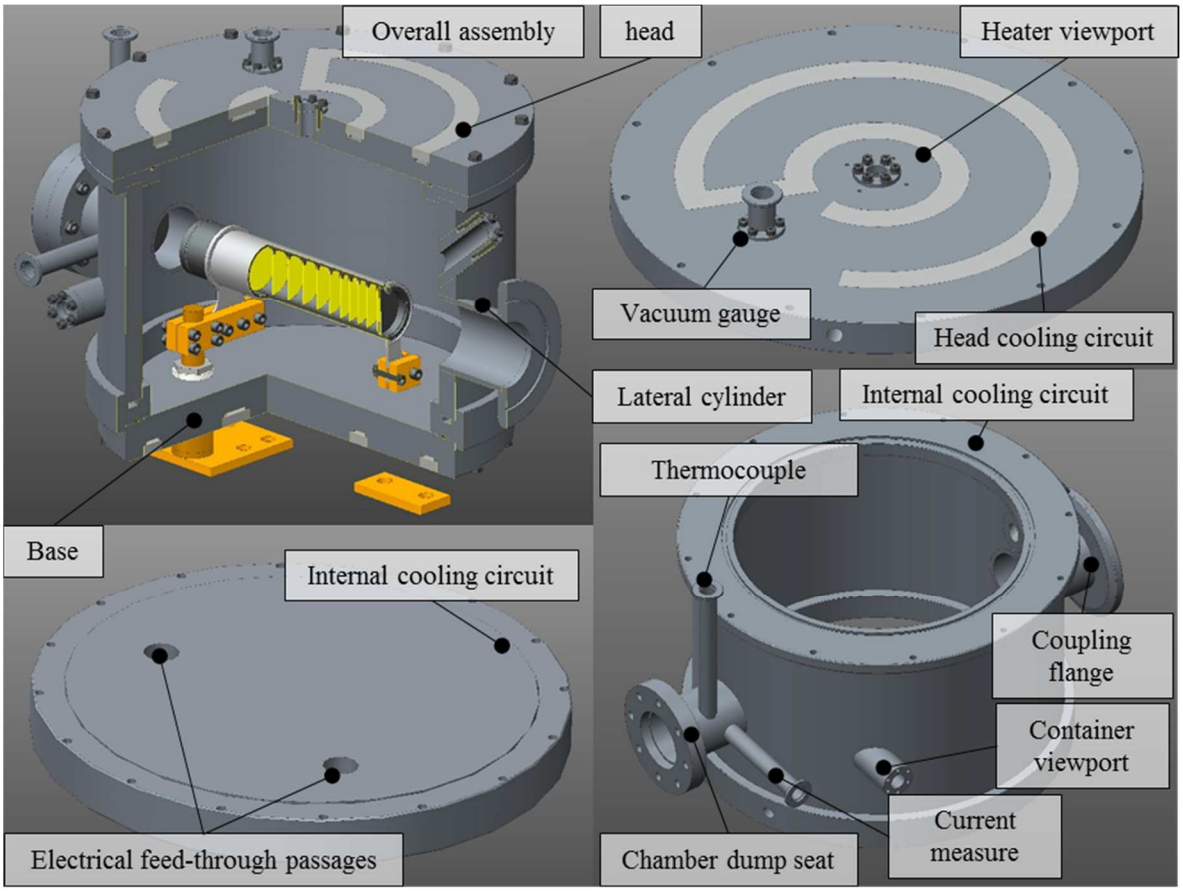

Fig. 2.25. Mechanical design of the scattering chamber used for the test

New type of electrical feedthroughs have been designed to increase their performances (Fig. 2.26a and Fig. 2.26b). They are composed by two concentric copper tubes where water flows and they are maintained in position by some MACOR insulators, feeding the electric power

from the chamber base. An additional dump (called chamber dump) is housed in the chamber after the target in order to protect the chamber in case of target failure: if the target breaks, the dump is impinged and could support beam power. This device is equipped with a thermocouple to measure the temperature, as already planned in [2.2], but it is also insulated: by means of an electrical feed-through, the eventual fast measure of the proton beam current could be the first signal of the target failure and the slow increase of the temperature just a double check to confirm it.

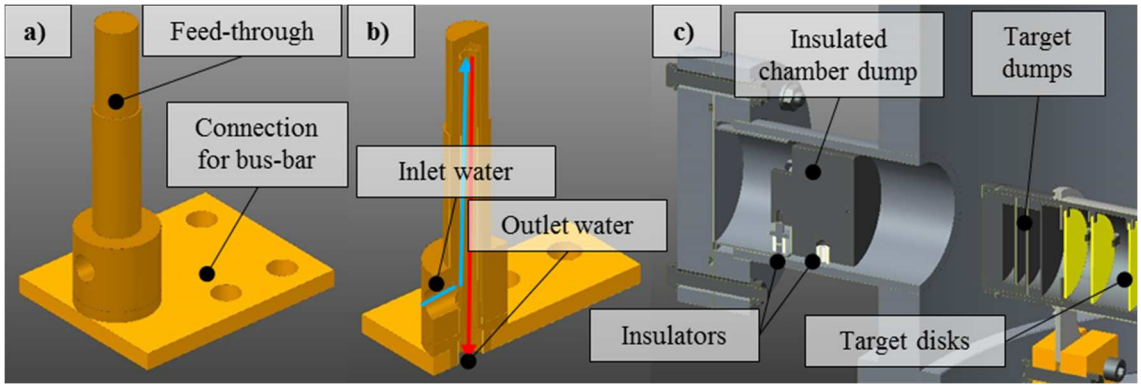

Fig. 2.26. Particular of two components: electrical feedthrough with section (a,b) and chamber dump (c)

2.4.3. *Thermal simulation*

As already said, the maximum power load is foreseen during the conditioning phase of the target when it is heated by the Joule effect with 1300 A of electrical current (as for the SPES target). The heater dimensions are the same of the SPES target, except for the length that has been incremented to 169 mm. Considering the ideal case, where the current just flows along the heater, the potential difference has been evaluated to be about 8.4 V (Fig. 2.27), for a power deposited of 11 kW.

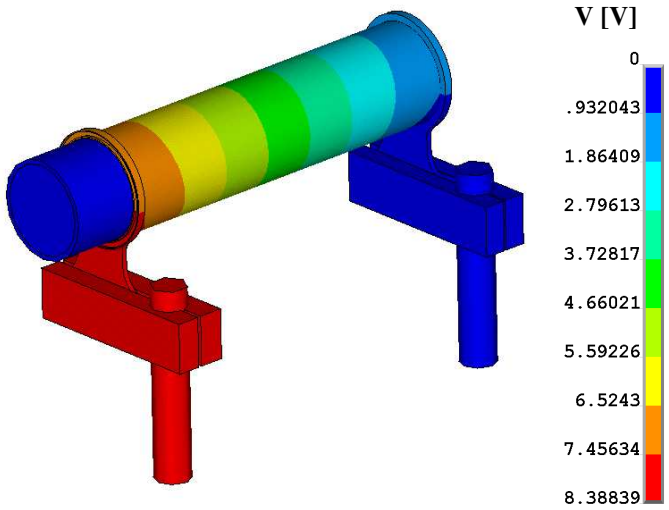

Fig. 2.27. Potential distribution for the 70 MeV target at the maximum electrical current of 1300 A.

The emissivity of the wall surfaces was fixed to 0.1, whereas the convection coefficient applied are showed in Fig. 2.28.

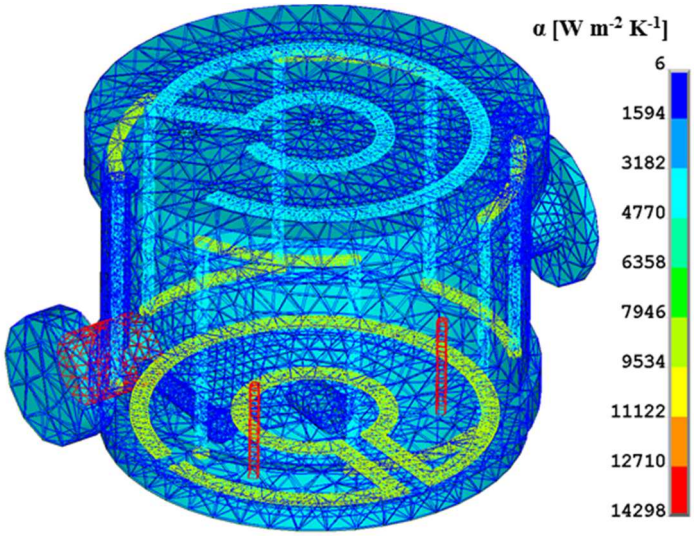

Fig. 2.28. Film coefficient applied on the various cooling circuits. The natural convection coefficient has been assigned to 6 W m^{-2} K^{-1}

The thermal results are presented in Fig. 2.29. Each component of the aluminium vacuum chamber does not exceed the temperature of 90°C, which is very important especially for the polymeric seal. The maximum is reached on the flange where the chamber is coupled to the overall beam line. Anyway, with such a temperature level, no problems are evidenced. The feedthroughs are efficiently cooled since its maximum temperature is about 50°C, whereas the copper connectors increase their temperature to 220°C due to their significant length. Finally, the target seems well heated with temperatures of the order of 1800°C. In particular, it is underlined that the temperature of the graphite chamber dump in Fig. 2.29d is about 950°C and it is quite uniform: an increase of the chamber dump temperature has not immediately to be related to a target failure due to the influence of the target temperature distribution.

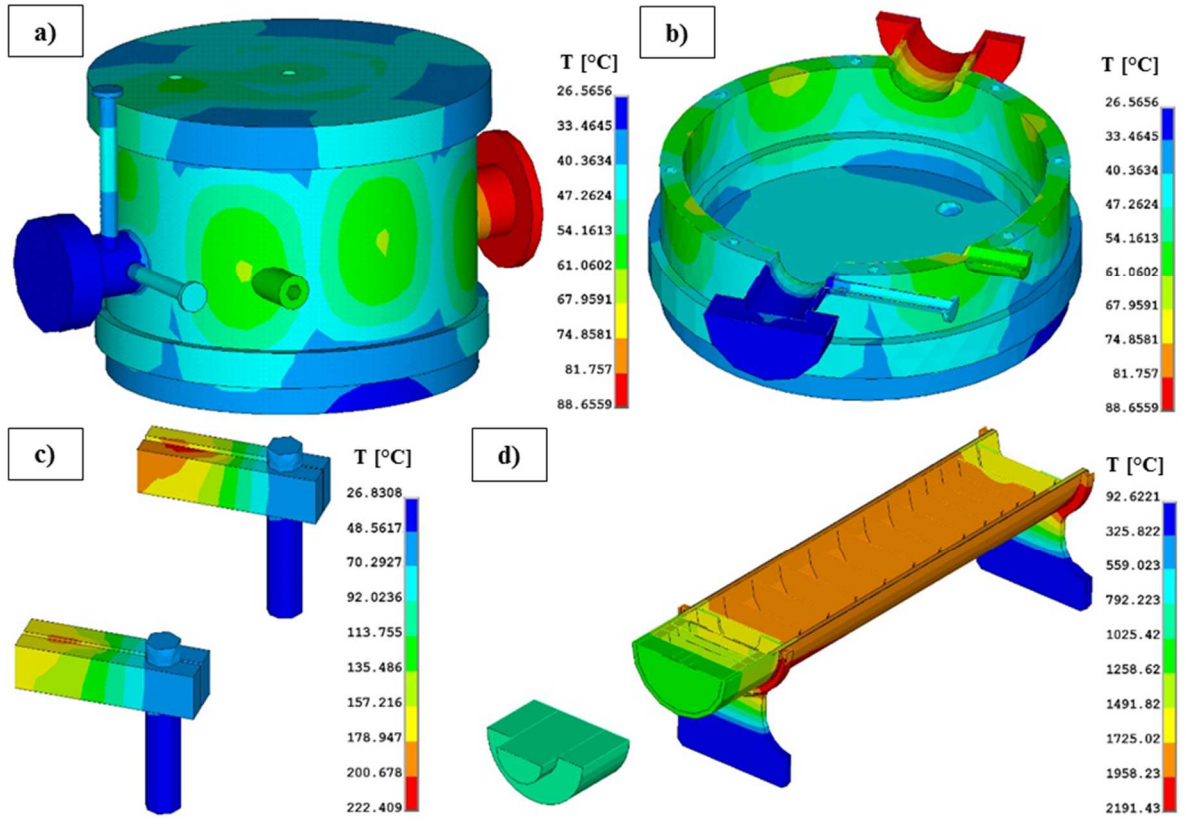

Fig. 2.29. Thermal results on the scattering chamber with 11 kW dissipated on it.

2.5. Off-Line test at iThemba LABS

2.5.1. Preliminary description

Off-Line test is intended the heating of the target using Joule effect created by electrical current flowing on the tantalum heater.

As already said, to confirm the validity of the various simulations performed, SiC target disks were chosen: its relatively low activation after irradiation with the proton beam reduces the radioprotection issues and do not require special permissions. To establish the main characteristics of the SiC, the SPES target group performed many experiments [2.27]-[2.28] and the main properties assumed in the numerical calculation are below summarized:

- Thermal conductivity: 30 W m^{-1} K^{-1} [2.27]
- Maximum temperature: 2000°C [2.27]
- Maximum difference of temperature for a diameter of 40 mm: 200°C at 1000°C (increase with the temperature) [2.27]
- Emissivity: 0.85 [2.27], [2.28]
- Density: 3.05 g/cm^3 [2.27]

The maximum temperature accepted was fixed at 1800°C to have a reasonable safety margin. This is not a problem during off-line test since it is the maximum temperature reachable

in the ideal case, with all the current flowing in the tantalum heater and not in the graphite container.

A Penning gauge was installed in the test chamber to measure the high vacuum directly in it and three different viewports were present to monitor the temperature at the 1st disk (point 1), at the heater centre (point 2) and at the graphite container (point 3), by means of some pyrometers (Fig. 2.30).

At the end of the chamber, an insulated graphite dump was housed in a port equipped with a type K thermocouple. Then a tantalum wire was here connected in order to take out a current reading used as safety signal, as already said.

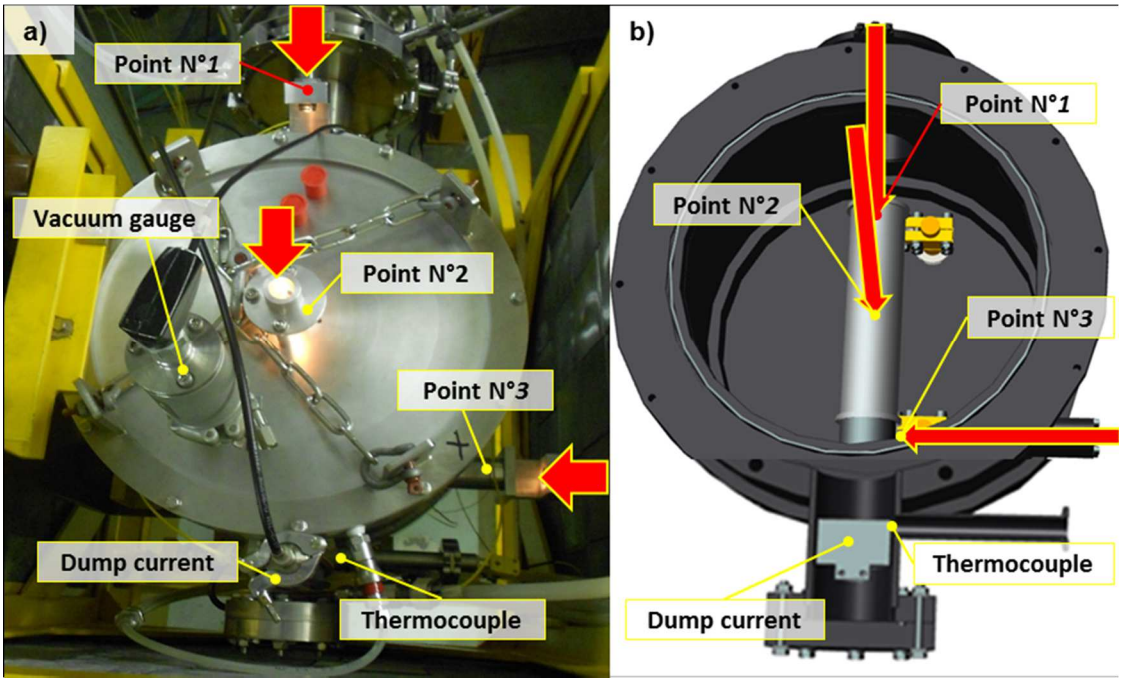

Fig. 2.30. Test chamber with the foreseen measurements point: picture (a), partially sectioned CAD image (b).

Ircon Modline® 6 series pyrometers were used to measure the temperature from the three different viewpoints, composed of the sensor 6R-2565 (range from 1000 to 2500°C), RF Lens and a 22 m long optical fibre cable. In this way, the sensor was placed far enough from the irradiated chamber, in a shielded area, to avoid radiation damage.

The Joule power on the tantalum heater was supplied by two GenesysTM 10kW GEN 12.5-800 connected in parallel. The remote sensing was used in order to measure directly the voltage drop between the electrical feedthroughs close to the chamber.

2.5.2. The first calibration process before irradiation test

Before the in-beam test, two optical fibre cables were initially installed in the vault in order to monitor the temperature during the target heating and out-gassing. This procedure was

performed some weeks before the tests when, on a nearby beam line, regular isotope production was taking place. This inadvertently exposed the optical fibre cables to neutron irradiation causing a significant damage to the fibre visible for a faulty temperature readings. Fortunately, a spare short optical fibre was already available and it was used to re-calibrate the damaged ones. Fig. 2.31 clearly shows the difference between undamaged and damaged optical fibre cables: as a light source, a filament bulb was used and the pictures show the big difference between the two fibres; in fact in Fig. 2.31a the light is brightened, whereas in Fig. 2.31b only a very small red spot is observable. This confirms the extremely low transmission due to neutron damage.

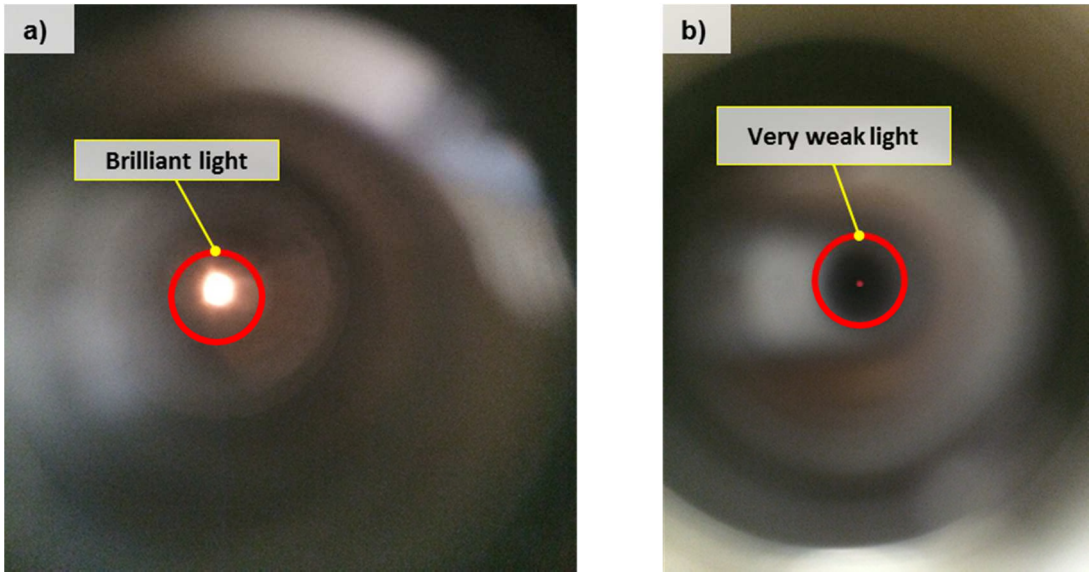

Fig. 2.31. Picture of the intact (a) and damaged (b) optical fibre cables.

The first calibration was performed in two steps:

1. Measure the temperature at all three monitoring points with the pyrometer in two colour mode by means of the fully functional fibre.
2. Repeat the measurements with the two damaged fibres and the pyrometer in one colour mode. The emissivity has to be set to obtain the same temperature as read by the undamaged fibre.

The emissivity setting was fairly constant over the range of temperatures measured, whereas the error due to this procedure can be assumed to be a maximum of 30°C.

2.5.3. The off-line test results

To simulate the target during the conditioning phase, a simple FEM model has been implemented with Ansys® [2.19] (Fig. 2.32).

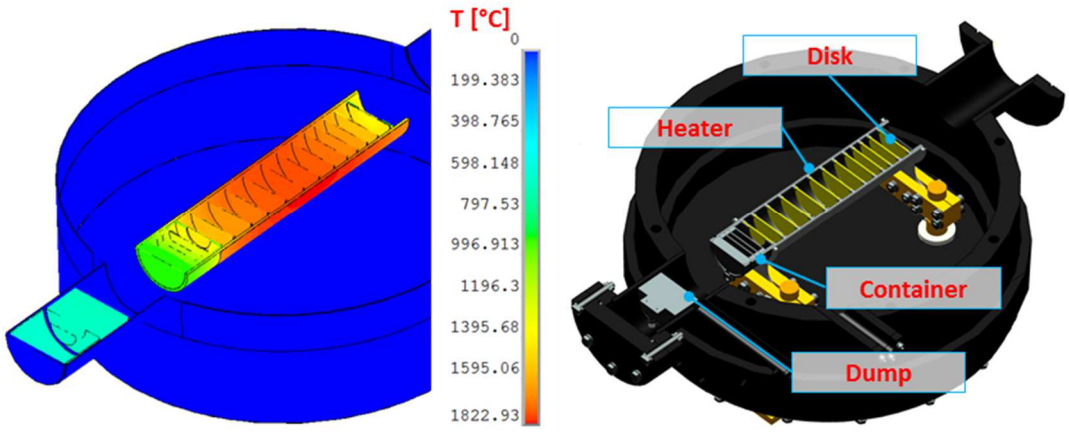

Fig. 2.32. Plot of the temperature distribution with a uniform power load of 8 kW assigned to the Ta heater, calculated using the FEM model.

Concerning the main boundary conditions, the chamber temperature has been fixed to 0°C, since its value does not affect the target and dump temperature [2.20], while the emissivity of the internal walls has been fixed to 0.1, which is a reasonable value for a cleaned aluminium alloy. In general, its value does not affect the target temperature (maximum 10-20°C) since the chamber is sufficiently large. On the other hand, this is not true for the chamber dump temperature, as it sits in a tight-fitting slot that protrudes from the chamber. The comparison between the FEA model and the experimental results is presented in Fig. 2.33 as a function of the net power dissipated in the heater by the Joule effect. In particular, the voltage drop due to the feedthroughs and the power cables, that was not taken into account on the remote sensing, has been estimated by a FEA analysis. The inconsistencies at the contact interface between the tantalum tube and the graphite container are surely the causes of the variance of the experimental data at high temperatures.

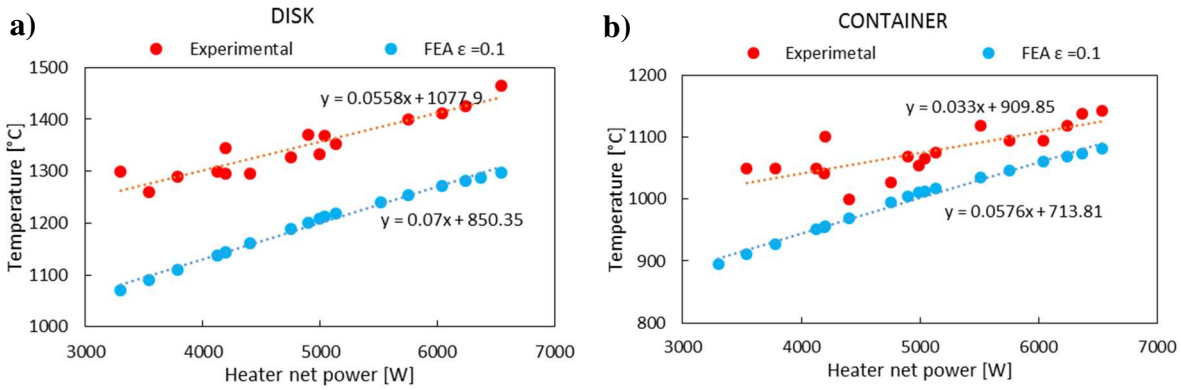

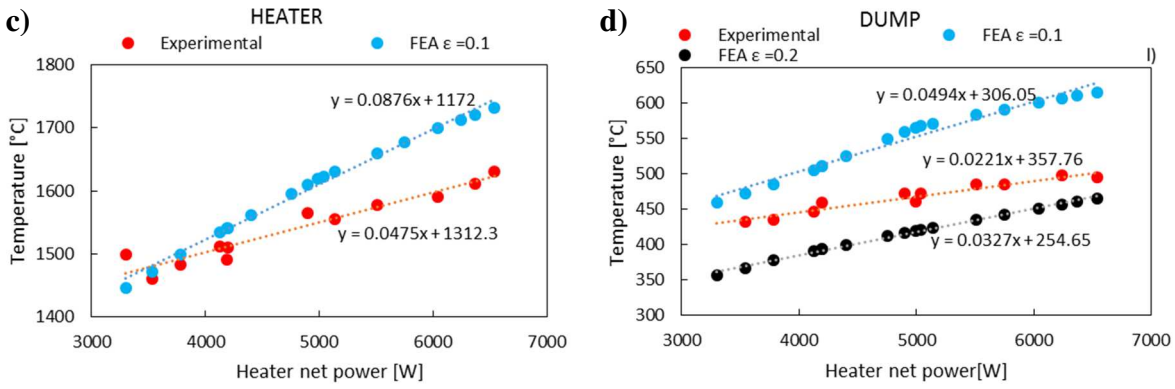

Fig. 2.33. Comparison between experimental measures and FEA results for the off-line test.

The FEA temperatures of the container and the disk are clearly low compared to the measurements, whereas on the heater the FEA temperature is higher. The main simplifications introduced in the FEA causing these effects are probably:

- The elements, especially graphite container and tantalum heater, exchange heat only by radiation.
- The power on the heater is distributed uniformly on the volume in the FEA.

The most drastic simplification is the second. In fact, the power dropped by the Joule effect is higher at the extremities because:

1. Since the current flows in the upper part of the heater, the resistance at the extremities is higher
2. A decrease of the total resistance of the heater is caused by the parallel current flowing into the graphite container

The same two effects have already been presented in [2.2] where the heater connections had the higher temperature registered and the FEA results were significantly higher with respect to the experimental measures.

On the other hand, the chamber surface emissivity strongly influences the dump temperature since its housing on the chamber is just a little bigger than the diameter of the dump. Looking to Fig. 2.33d, the emissivity value can be set between 0.1 and 0.2.

2.5.4. The second calibration process after the irradiation

After the in-beam test, the target was cooled down and a new pyrometer calibration was performed to check if any further radiation damage had occurred.

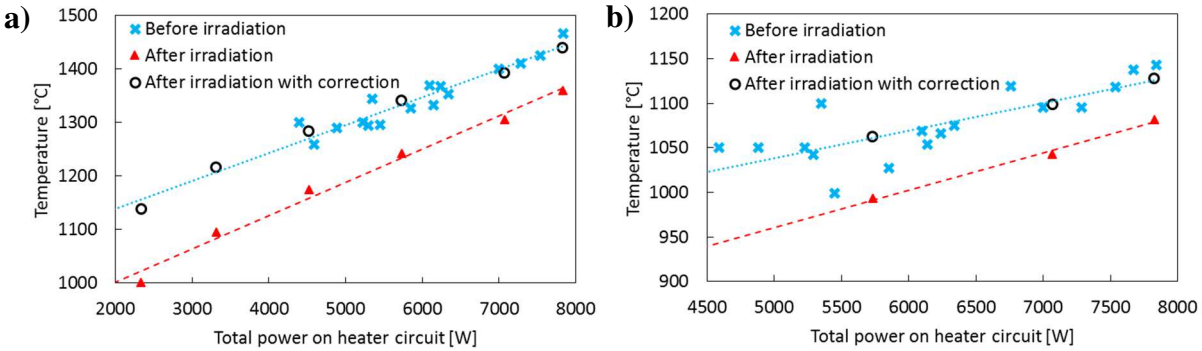

Fig. 2.34. Temperatures on the disk (a) and the container (b) before and after irradiation in relation to the total power on the heater circuit.

The results, shown in Fig. 2.34, point out a change in calibration. Another correction of the temperatures has been performed assuming three reasonable hypotheses:

1. The damage to the optical fibre is proportional to the integral of the beam current
2. The temperature is approximately linear with the power on the heater circuit
3. The decrease of the temperature read by the pyrometer is proportional to the damage

The 1st assumption leads to the definition of the cumulative factor of the fibre damage *f*:

$$f(t^*) = \frac{\int_0^{t^*} I_{BEAM}(t)dt}{\int_0^{t_{FIN}} I_{BEAM}(t)dt} \tag{2.3}$$

Where t^* is the time when *f* is evaluated, t_{FIN} is the total time of the on-line experiment and I_{BEAM} is the proton beam current at the time *t*. The consequence of the 2nd and 3rd hypothesis lets to find the coefficient *m* (2.4) and *q* (2.5) of the straight line at the irradiation time *t* according to the notation used in Fig. 2.35.

$$m(t^*) = m_b - (m_b - m_a)f \tag{2.4}$$

$$q(t^*) = q_b - (q_b - q_a)f \tag{2.5}$$

In particular, equation (2.4) can be demonstrated applying (2.5), directly consequence of the 3rd hypothesis, to the arbitrary temperatures T_{M1} and T_{M2} of Fig. 2.35.

$$T_b = m_b P + q_b \tag{2.6}$$

$$T = mP + q \tag{2.7}$$

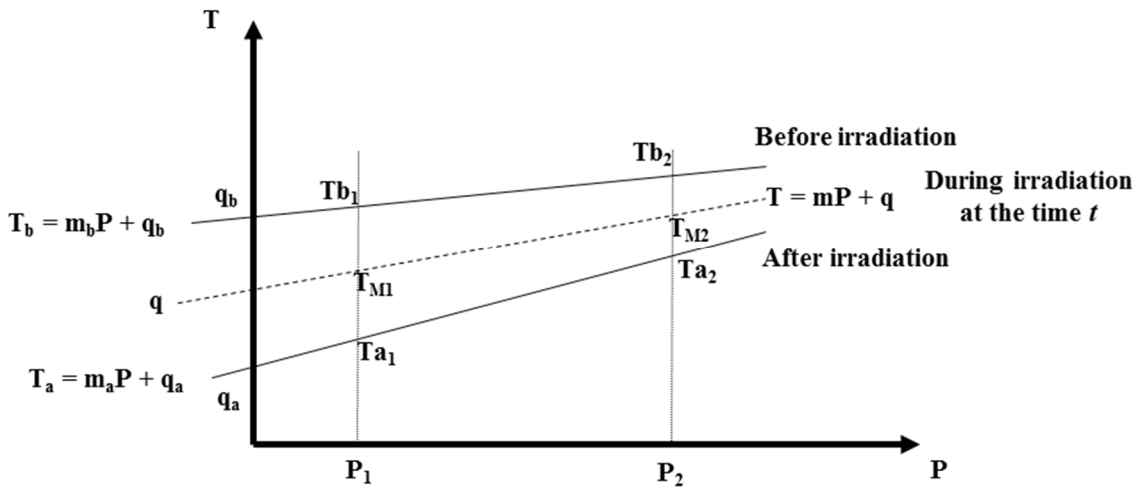

Fig. 2.35. Notation used to find the correction on the temperature read by the pyrometer

Finally, substituting (2.4), (2.5), (2.6), into (2.7), the temperature during the on-line measurements can be corrected according to the following equation:

$$T_C = \frac{1}{1 + f \cdot \frac{m_a}{m_b}} \cdot T_M + \frac{q_b \cdot \frac{m_a}{m_b} - q_a}{1 + f \cdot \frac{m_a}{m_b}} \cdot f \qquad (2.8)$$

Where T_C and T_M are respectively the temperature corrected and measured (the "old" T_b and T), m_a and m_b the slope of the straight line after and before the irradiation, q_a and q_b the intercepts after and before the irradiation. As an example of the accuracy of the process, the temperatures (with corrections) in Fig. 2.34, measured after the irradiation, clearly show that the two measurements are within the error band of the measurements taken before the irradiation.

2.6. On-Line test at iThemba LABS

2.6.1. Setup description

The iThemba LABS Separated Sector Cyclotron (SSC), a K=200 machine, optimized with flat-topping in order to supply a 66 MeV proton beam up to a maximum of 350 μA intensity, was used to test the 70 MeV SiC target. The proton beam is extracted from the SSC and transported to the last three quadrupole magnets placed about 3 meters before the target. After the quadrupole magnets, a wobbler was installed to sweep the beam around its axis. Then, a concrete wall of 1.5 m thickness protects these devices from the radiation produced by the interaction between the proton beam and the target (see Fig. 2.36).

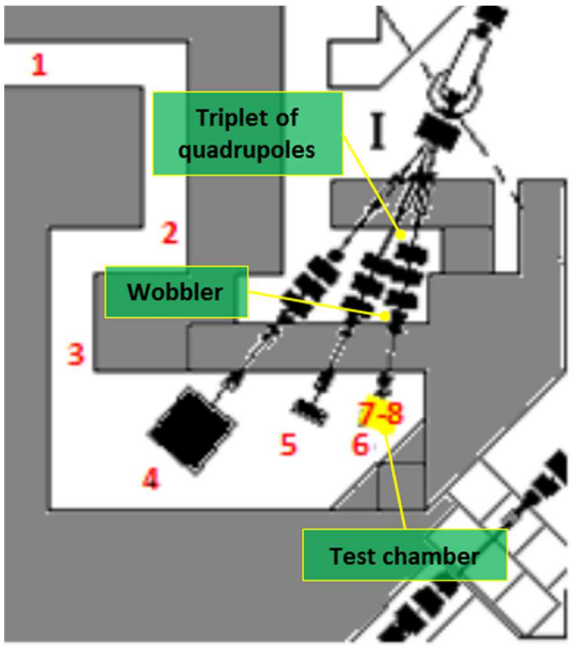

Fig. 2.36. Vaults surrounding the test chamber at iThemba LABS. The positions where the dose rates were measured are numbered. The yellow square is the test chamber.

The proton beam line was equipped inside the vault by, in sequence, a Beam Profiler and a Faraday Cup (maximum current 10 μA), then a Turbo molecular pump to optimize the chamber vacuum, a 4 segment collimator (max total current 1.6 μA) and, after about 0.8 m, the test chamber with the target (Fig. 2.37). In particular, the scattering chamber was set inside a 5 cm thick lead wall to reduce during the cooling time the gamma dose rate after the test, in order to let people free to work on the closed isotope production target.

It was possible to monitor during the on-line test:

1. The temperatures of the 1st disk, container and chamber dump
2. The current of the chamber dump
3. The temperature of two different points at the chamber
4. Temperatures of the water for all the 3 cooling circuits
5. The vacuum level in the chamber
6. Currents dropped on each of the four segments composing the collimators

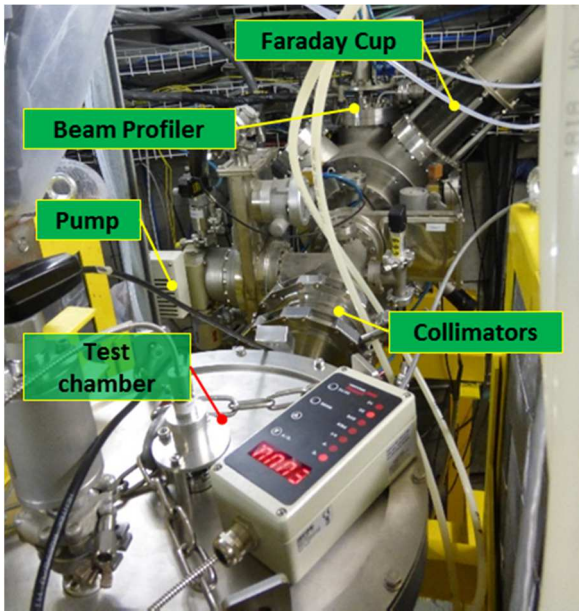

Fig. 2.37. Proton beam line inside the vault where are visible in succession: beam profiler, faraday cup, pump, collimators and test chamber.

2.6.2. The ramp up

For the online test, it was decided to use the two re-calibrated 22 meter long optical fibre cables to monitor the temperatures at the first disk and on the container (points 1 and 3).

In order to have the most uniform temperature distribution within the target system, many efforts were made to provide to the target the right beam profile. In fact, as presented in 2.2.3, the most diffuse proton beam has to be supplied to decrease stresses and temperatures in the disks and avoid any rupture. For this reason, the wobbler rotates the beam of about 5 mm radius around its un-deflected axis with a frequency of 100 Hz. The four segment collimator could sustain a maximum of 1.6 μA at 66 MeV of proton beam current on each of the four segments and they were installed just before the chamber entrance. Assuming that the proton beam shape is a Gaussian with the same characteristics in the x and y planes, as already done in 2.2, the current, I_c on the collimator could be derived using

$$I_c = I_{TOT}\frac{1}{\sigma^2 2\pi}\iint_A exp\left(-\frac{((x - r_w \cdot cos(\omega t))^2 + (y - r_w \cdot \sin(\omega t))^2)}{2\sigma^2}\right) dxdy \quad (2.9)$$

Where σ is the proton-beam mean-square deviation (assumed identical on the x and y planes), A is the area of the collimator, r_w and ω the sweeping radius and its angular frequency and finally I_{TOT} the maximum current delivered. The integration of equation (2.9) gives a beam mean-square deviation of approximately 6.5 mm.

The emittance measured before the vault was 26.5 and 5.24 π mm mrad, respectively for the horizontal and vertical plane, with a 4.5 μA of beam current. This was possible inserting attenuators on the beam line before entering the SSC and reducing the beam current from the nominal value of 60 μA. A safety interlock system monitors the four segments of the collimator in order to trip the beam in the event of a sudden increase in the beam spot size. Moreover, balancing the amount of current intercepted by each of the four collimator segments, the beam alignment was checked during the on-line test and beam preparation. Finally, the focus of the beam was placed between the collimators and the target to avoid unexpected beam spot increase.

The irradiation time was limited to 1 h with the highest power deliverable, 60 μA 66 MeV (3.960 kW) proton beam, to minimize the final activation of target and test chamber.

The on-line test was divided in three main phases. Firstly, 0.8 μA of beam current was supplied to the target for 1 h for the checking of the system, in order to establish that all components worked to specification. A slight increase in temperature of a few °C was detected by the three measuring points (1st disk, container and dump) as expected. After the first evaluation of the radiation level in the chamber, the proton beam current was increased stepwise, waiting for the stabilization of the temperature read by the two pyrometers. On the contrary, the temperature on the dump was not so fast to stabilize due to its high thermal capacity. This was a good point since it confirmed that there were no power directly disposed on it, but just thermal radiation heated it up. Anyway, the maximum value of 60 μA was reached in about 40 minutes. Finally, the beam current was maintained on the target for about 20 minutes (see Fig. 2.38). During this period, the increasing radiation damage of the fibres slightly and continuously decreased the temperature read by the pyrometers. On the other hand, the value of the dump temperature slightly increased due to its large thermal inertia, but the vacuum gauge on the chamber registered decreasing vacuum values, confirming stable target function. At the end of the 20 minutes, the proton beam current was turned off.

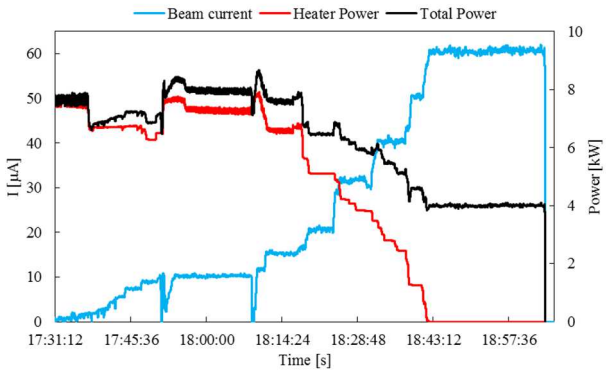

Fig. 2.38. Beam current, heater and total power supplied to the target during the on-line test.

2.6.3. *The numerical model*

As already presented in 2.2 and 2.3, the Monte-Carlo code FLUKA [2.10], [2.11] has been used to evaluate the proton beam power deposited in the disks. The main results obtained by FLUKA are presented below.

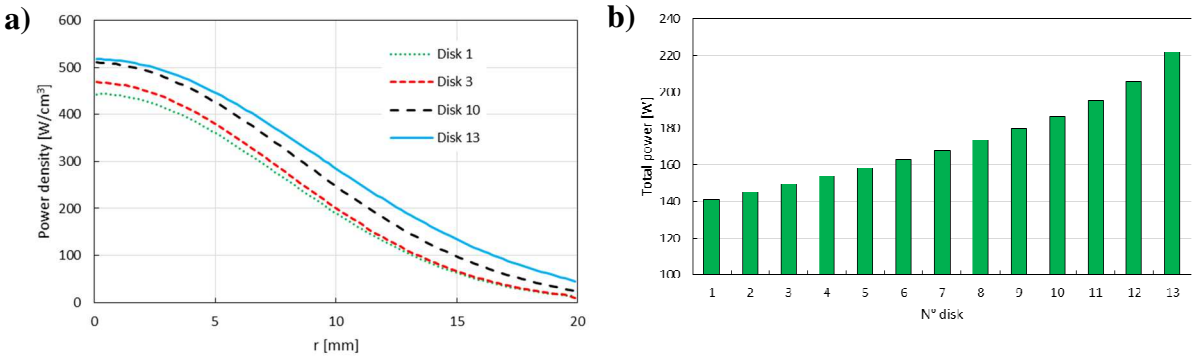

Fig. 2.39. Power density (a) and total power (b) on various disks obtained by FLUKA for a 60 μA, 66 MeV proton beam (5 mm sweeping radius, 6.5 RMS radius).

The power density as a function of disk radius is plotted in Fig. 2.39a for various disks. The proton scattering causes the beam spread, which results into a higher relative increase of power density at the edge of the disk compared with the centre for the last disks in relation to the first ones. Moreover, the increase in power deposition with disk number reflects the increase of the stopping power (and consequently the energy deposited) at lower energies (see Fig. 2.39b).

The temperature distribution during the experiment was simulated by Ansys®. A uniform power distribution on the heater was again assigned to take into account the Joule effect, but for the power deposited by the proton beam, the FLUKA power deposition were assigned for all the components of the target. In Fig. 2.40a is presented the heat generation boundary condition, whereas in Fig. 2.40b the consequent temperature results, for the case of a 40 μA of beam current.

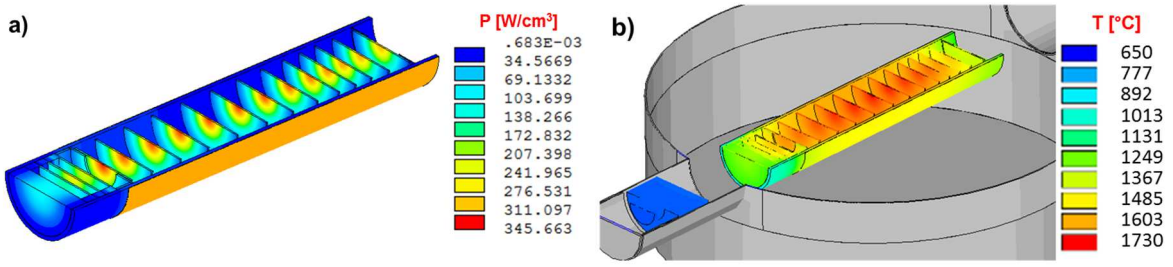

Fig. 2.40. Power deposition a) and temperature results b) for the specific case of 40 μA, 66 MeV proton beam current with 5 mm sweeping radius and 6.5 RMS beam radius.

2.6.4. The comparison between experimental and numerical results

In Fig. 2.41, the temperatures measured by the two pyrometers before and after correction are presented. For 60 µA of beam current, two points are showed corresponding to the initial and final temperature measurements taken during the 20 minutes of irradiation time.

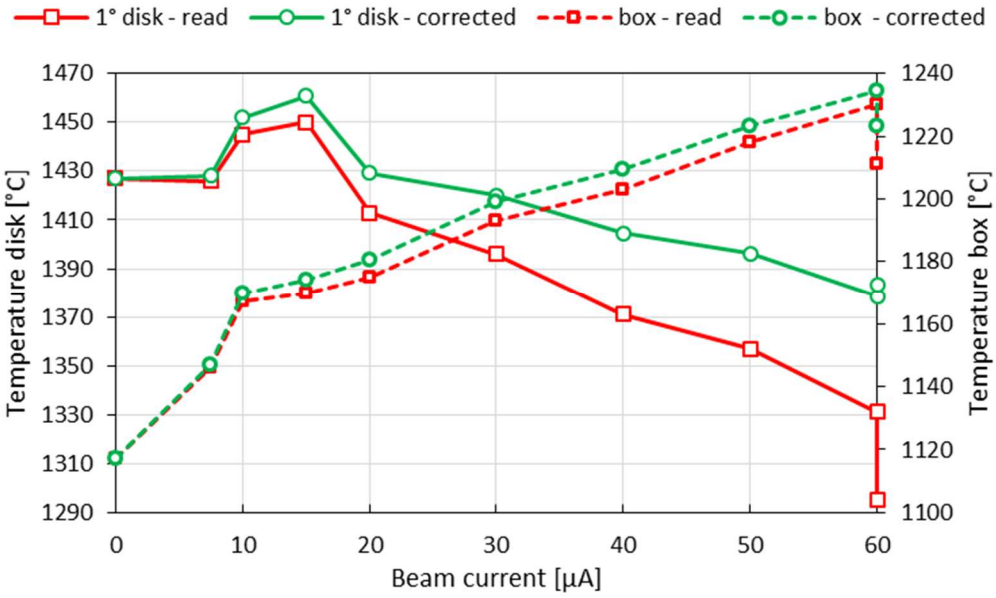

Fig. 2.41. Correction applied to measured temperatures taking into account radiation damage occurs to the optical fibre cables.

The correction performed is satisfactory for the temperature measurement of the first disk, but worst so for the graphite container. Indeed, the difference between the final and initial corrected temperature at 60 µA is negligible for the disk (some degrees) but not for the graphite container. Probably this is because there are not enough measurements at temperatures higher than 1150°C for the container and, moreover, they are affected by a big variance with respect to the regression line.

The comparison between experimental (corrected) measurements and FEM model is presented in Fig. 2.42 for the three points (first disk, container and dump).

The experimental results and the FEA model are in good agreement, especially at high proton beam current, since the simplification used to simulate the power deposited by Joule effect in the heater becomes negligible. This is probably the principal cause of the two different slopes for the FEM and experimental-corrected temperature curves for the first disk. Then, a higher emissivity for the chamber walls (from 0.1 to 0.2) or a change of 0.05 in the SiC emissivity can affect the numerical results by a maximum of 15°C each for the first disk. On the contrary, a change of 0.05 g/cm^3 in the SiC density (range of 3.0-3.1 g/cm^3) could lead to a temperature variation of about 25°C. Finally, the most sensitive parameter for the temperature

is probably the beam profile. Assuming that the beam has a Gaussian shape, a decrease of 0.4 mm in the mean square deviation of the beam, increases the temperature of the disks by about 10°C even if the total power deposited on the disk is approximately the same. For this reason, particular attention was spent in the beam preparation.

Concerning the graphite container, the slope of the measurements and the FEA predictions are very similar, even if the FEA slope is steep, probably for the same reason as for the first disk: the strong simplification introduced to simulate the Joule effect is not negligible.

Finally, the FEA temperature for the chamber dump with an emissivity of 0.1 for the chamber surface is the closest to the measures, except at low proton beam currents, where it approaches the curve with emissivity of 0.2. It is underlined that, if the disk temperature is affected primarily only by the proton beam current and shape, the measurements on the dump and the container are more influenced by the proton scattering and by the power deposited in all of the components that are sit on the last part of the target. Consequently, they are indicative of the quality of the whole target modelling.

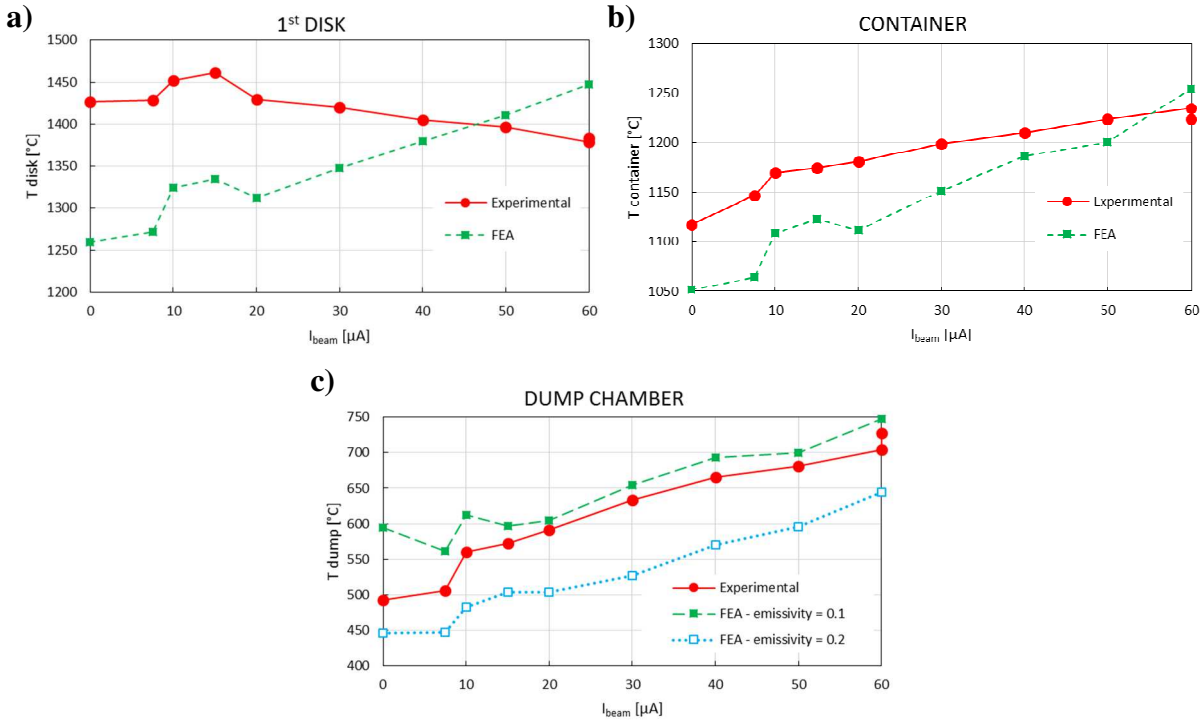

Fig. 2.42. Comparison between temperature measured (corrected) and FEA results for the 1st disk (a), container (b) and dump (c) with a 66 MeV proton beam current.

In conclusion, the maximum difference between the FEA and the temperature measurements at the maximum proton beam current, under stable conditions, are respectively about 60°C, 20°C and 25°C for the first disk, the container and dump, corresponding to a relative error of 4.3%, 1.6% and 3.4%. These are essential results because they confirm the suitability of the

implemented simulation procedure (FLUKA coupled with ANSYS) and, indirectly, all the simulations presented in the previous paragraph.

Finally, it was not possible to measure the stresses on the disks, which have been numerically predicted to complete the analysis. The thermal FEA evaluates at 60 μA of proton beam a maximum difference in temperature of about 170°C for the second and third disks, and 140°C for the last one. Then, the stresses are evaluated to be about 90 MPa at the edge of these disks assuming a mechanical elastic behaviour of the SiC, whereas the variance of the stresses due to wobbler is plotted in Fig. 2.43. The amplitude of the stresses are very small, around 0.5 MPa, due to very small amplitude of the temperature (about 0.1°C), probably because to the small wobbling radius (5 mm) comparing to the 40 MeV target simulations in paragraph 2.2.4.

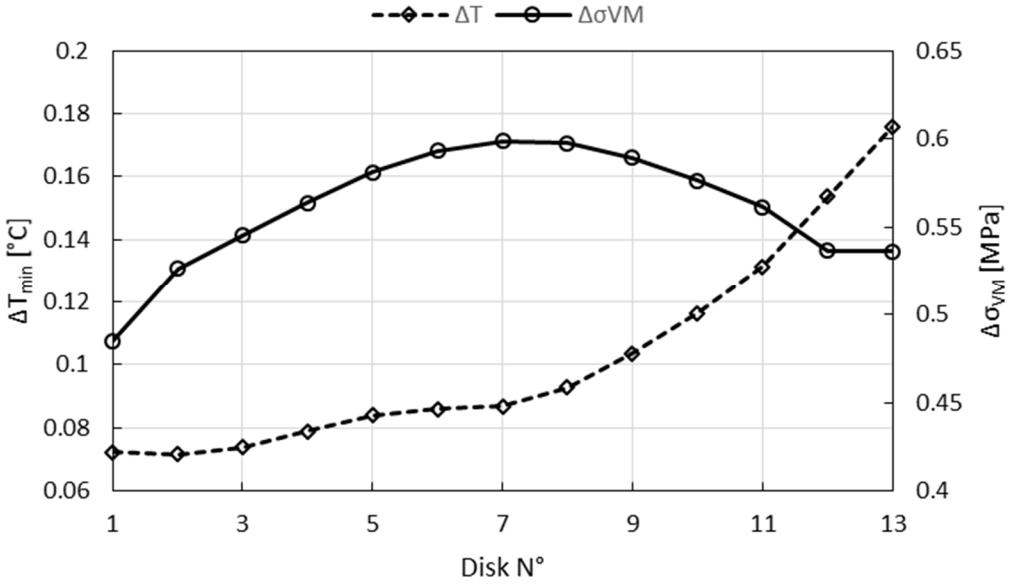

Fig. 2.43. Effect of the wobbled beam on the temperature and stresses at the SiC disks

2.6.5. Post-irradiation measurements

In the irradiation vault, radiation dose levels were taken at the end of the in-beam test at the various locations indicated in Fig. 2.36, by means of a Thermo ESM FH 40G-L10 connected to an FH 40 TG Teleprobe. In particular, the position *6* was behind the 5 cm thick lead wall, *7* and *8* respectively 30 cm above and below in contact with the chamber; these dose measurements were of great interest since the nearest to the target. The results are presented in Table 4 and Fig. 2.44.

Experimental measurements - Time from stopping the beam (about 43 min of cumulative time with 60 µA, 66 MeV beam current)								
Point N°	**Unit**	**19 min**	**16 h 40 min**	**38 h 40 min**	**13 d**	**20 d**	**27 d**	**34 d**
1		9	8.3	4.4	3.5	3.5	4	5
2		6	4	4	4	4	4	4.5
3	µSv/h	13	8	4	4.8	4	3.8	5
4		120	18	13	15	17	16	18
5		750	30	15	15	13	15	18
6		10	0.303	0.113	0.017	0.010	0.010	0.011
7	mSv/h	410	1.10	0.460	0.050	0.023	0.015	0.018
8		1000	6.30	2.60	0.16	0.078	0.043	0.028

Table 4. Various dose rates measured after the irradiation time

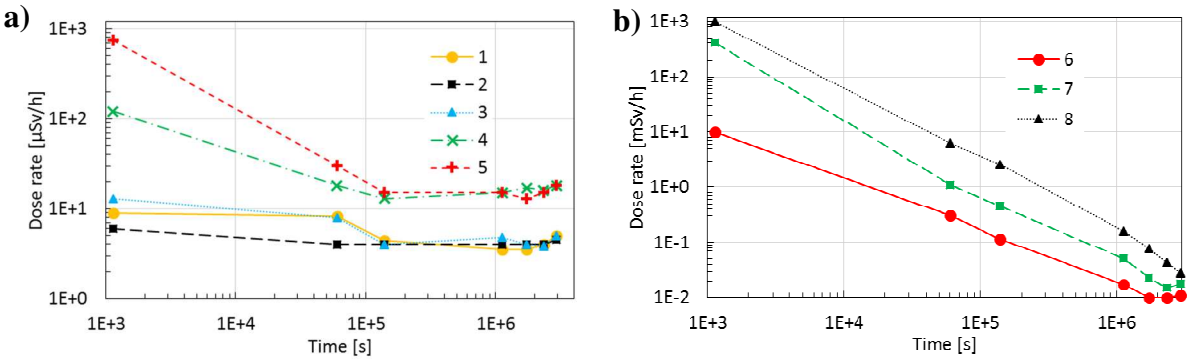

Fig. 2.44. Dose rate measured after the irradiation according to the time in different positions.

The measurements around the vault (positions 1-5, Fig. 2.44a) reach typical background levels for the radioisotope vault after about 1 day. Later dose increases were probably due to the isotope production chamber close to the test chamber used after the irradiation tests. On the contrary, the dose rate from the chamber and the target continued to decrease even after about 1 month (Fig. 2.44b), but a relative low radiation level was detected. After the removal of the chamber lid 34 days after the end of the irradiation, the radioactivity level in contact with the target heater was:

- 210 µSv/h close to the entrance
- 220 µSv/h (maximum value) from 1/3 of heater length from the entrance
- 80 µSv/h at the end of the graphite container

A comparison between these measurements and FLUKA activation calculations has been performed. Here a continuous 60 µA proton beam for 43 minutes (the cumulative irradiation time performed during the test) impinges the target. In the simulation, the main components were taken into account: the various SiC disks, tantalum, graphite container, copper feedthroughs, aluminium irradiation chamber and the 5 cm thick lead shielding. Not all the components were introduced to do not excessively complicate the design: the iron supports,

the copper cables, the concrete walls and the close irradiation target stations. For the measurements closest to the target (point N° 6, 7, 8 and target activation), the comparisons are presented in Fig. 2.45. In fact this position are the less affected by the irradiation history performed on other target stations in the vault.

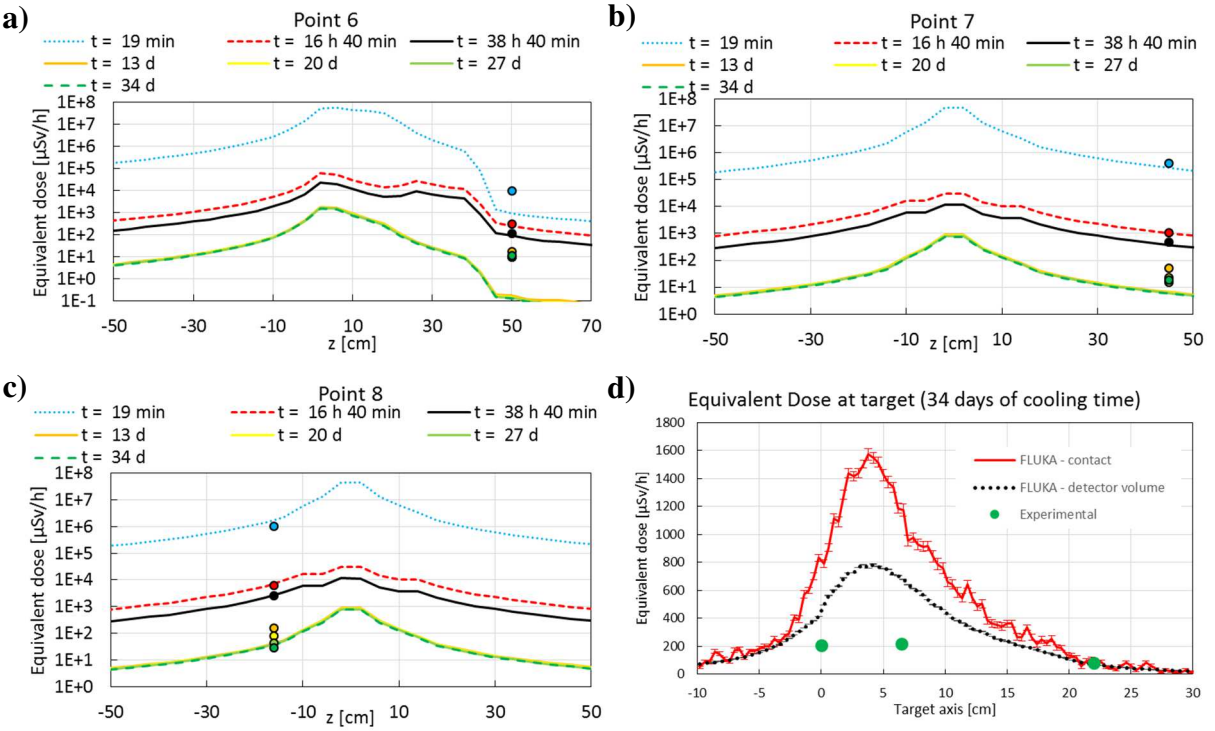

Fig. 2.45. Comparisons between equivalent dose measurements (circles) and FLUKA calculations (lines) at different times.

In general, there is a good agreement between the measurements and the numerical results, especially at short cooling times for the points N°7 and 8. This is probably because the dose rates measured at short cooling times come mostly from the irradiated target, whereas the environment radiation strongly influences the measurements at longer times, which can justify the differences at long cooling times for Fig. 2.45a. On the contrary, the FLUKA calculations are quite different for the irradiated target for the contact dose rate measurements (disks, graphite container and tantalum heater) presented in Fig. 2.45d, where almost a factor 10 is observable. Probably, here the effect size (r^2) is very affective since the detector was just a few millimetres from the source, mostly constituting by the irradiated disks. Just taking into account the detector volume, estimate with 1x5x10 cm, the evaluated dose rate is reduced by a factor of two.

Using a HPGe detector, the observation of the γ-ray line target spectrum confirmed the main activities predicted by FLUKA, that are due to ^{7}Be and ^{22}Na, as listed in Table 5.

Element	Experimental activity [MBq]	FLUKA activity [MBq]
^{7}Be	100	78
^{22}Na	3.6	3

Table 5. Comparisons between measurements and FLUKA results for the main isotopes responsible of the target activity.

In addition, X-rays coming from the tantalum heater activation were observed at low relative intensity (~ 1%), qualitatively in agreement with FLUKA estimates.

2.7. Conclusions

In this chapter, the first part was dedicated to the study performed on the 40 MeV SPES target. The new aspect was the definition of the proton beam characteristics and the effect of various beam profiles on the temperature and stresses distribution. Moreover, a better disk distance has been define in order to work in a safe range. Finally, some specific conditions have been investigated, such as the beam wobbling or a potential beam stop effect on the temperature distribution. These was very important information in the design phase of the beam control system.

Then, the same procedure was adopted to study a new target for a 70 MeV proton beam energy. The goal was the definition of a target with a higher number of fissions per second able to operate in the same vacuum chamber of the 40 MeV target, in order to constitute a future development of the SPES project or a target for the new RIB facility in the design phase at iThemba LABS. The study was focused on the definition of the main dimension of the target (number of disk, spaces, etc.) and it did not concern the heater dimensions that were just adapted, increasing its length, from the 40 MeV version.

Finally, the last part of the chapter was dedicated on the realization of the test on the 70 MeV target, performed at iThemba LABS on SiC disks (much lower activation and no special permission required). Firstly, the design of the water cooled vacuum chamber was presented. Then the tests on the target are showed and explicated. During these tests, the temperature was measured in 3 points and then compared with the numerical results. The match was certainly satisfying, especially with high proton beam current, aim of the tests, validating the procedure adopted to simulate the irradiation of the SiC target and, consequently, even the 40 MeV and 70 MeV UC_x targets. This was the first test performed on the 40 mm target and, in addition, with high power (4 kW), and it is surely promising for the final achievement of the SPES project.

References of Chapter 2

[2.1] S. Corradetti *et al.*, Nucl. Instrum. Meth. B **360**, 46-53 (2005).

[2.2] M. Manzolaro, Engineering of the INFN SPES target – ion source system (LAP Lambert Academic Publishing, 2012).

[2.3] L. Biasetto *et al.*, J. Nucl. Mater. **404**, 68 (2010).

[2.4] L. Biasetto *et al.*, Eur. Phys. J. A **42**, 517 (2009).

[2.5] D. Scarpa *et al.*, Eur. Phys. J. A **47**, 32 (2011).

[2.6] S. Corradetti *et al.*, Eur. Phys. J. A **49**, 56 (2013).

[2.7] S. Corradetti *et al.*, Eur. Phys. J. A **47**, 119 (2011).

[2.8] M. Barbui *et al.*, Nucl. Instrum. Meth. B **266**, 4289-4293 (2008).

[2.9] J.S. Hendricks *et al.*, MCNPX Version 2.5.e, LA-UR-04-0569 (2004).

[2.10] A. Ferrari *et al.*, FLUKA: a multi-particle transport code, CERN-2005-10 (2005), INFN/TC_05/11, SLAC-R-773.

[2.11] T.T. Bohlen *et al.*, Nucl. Data Sheets **120**, 211-214 (2014).

[2.12] J.F. Ziegler, M.D. Ziegler, J.P. Biersack, SRIM The Stopping and Range of Ions in Matter (2008).

[2.13] M.G. Saint-Laurent *et al.*, Spiral Phase-II Final Report (European RTT, 2001).

[2.14] L.C. Carraz *et al.*, Nucl. Instrum. Methods **158**, 69 (1979).

[2.15] S. McLain, J.H. Martens (Eds), Reactor Handbook, (Interscience Publishers, New York, 1964).

[2.16] J. P. Greene *et al.*, Nucl. Instrum. Meth. B **241**, 986 (2005).

[2.17] Hj. Matzke, Science of Advanced LMFBR Fuels, North Holland, Amsterdam (1980).

[2.18] A. Andrighetto et al., Eur. Phys. J. A **30**, 591 (2006).

[2.19] ANSYS® Academic Research, Release 15.0.

[2.20] G. Meneghetti *et al.*, Finite Elem. Anal. Des. **47**, 559-570 (2011).

[2.21] M. Ballan, *Progettazione e test di componenti e sistemi di misura per l'operazione e la sicurezza del sistema target - sorgente del progetto SPES*, Tesi di Laurea Magistrale, Università degli Studi di Padova (2014).

[2.22] A. Monetti *et al.*, *The RIB production target for the SPES project*, Eur. Phys. J. A **51**, 128 (2015).

[2.23] A. Andrighetto *et al.*, Eur. Phys. J. A **25**, 41 (2005).

[2.24] M. Manzolaro, *Study, design and test of the Target – Ion Source system for the INFN SPES facility*, PhD thesis, Università degli Studi di Padova (2011).

[2.25] M. Barbui *et al.*, *Calculations and first results obtained with a SiC prototype of the SPES direct target*, Nucl. Instrum. Methods B **266**, 4289-4293 (2008).

[2.26] *ANSYS Mechanical APDL Basic Analysis Guide*, Release 15.0.

[2.27] L. Biasetto et al., Eur. Phys. J. A **38**, 167–171 (2008).

[2.28] M. Manzolaro et al., Rev. Sci. Instrum. **84**, 054902 (2013).

Chapter 3

The beam diagnostic in the SPES bunker

3.1. Introduction [3.1]

The beam diagnostic is a fundamental equipment for all the accelerators since it could be compared to the apparatus sense essential for a safe and correct use of the machine. It could satisfy three main types of needs [3.2]:

- Fast check of the general efficiency and settings of the relative apparatus
- Daily check of the accelerator performance and the stability
- Commissioning or develop of new parts of an accelerator for the improvement of its performances

The importance of a good diagnostic stands out during the use of the accelerator and even more for the Front-End. In fact, the access to the bunker during on-line operation will be allowed only if strictly necessary and after some days/weeks of radiation cooling.

The main parameters of a beam are:

- Intensity, defined by number of particle per second
- Profile: distribution of the beam intensity on the space
- Position
- Energy and energy spread
- Number of charge state and mass
- Emittance (dimension of the phase space)
- Time structure

The beam diagnostics are based on one of the following physics principles:

1. The electro-magnetic influence of moving charges according to the classical electrodynamic
2. The photon emission from the particles (ex. synchrotron radiation)
3. The Coulombic interaction of the beam particle during the penetration into the matter
4. The nuclear interaction between the particle during collision
5. The particle interaction with the photons

In the cases of the SPES bunker, the diagnostics are based essentially on the third principle and they consist on elements interposed in the beam. In the case of collimators or Faraday Cup, the beam is completely stopped and the signal read by an ammeter is the beam current dropped

on them. For these components, it is essential to suppress the emission of secondary electrons which are ejected when a particle with enough energy (typically few eV) strikes a metal or a conductive surface. The amount of electrons emitted depends upon the energy and ion species, but the maximum electron energy can be assumed approximately of few tens of eV [3.3]. Using an electrode at a negative potential, the electrons emitted can be pushed back to the target. This effect is clearly visible in Fig. 3.1, where the target current reaches stable values for suppressor voltage of about – 90V.

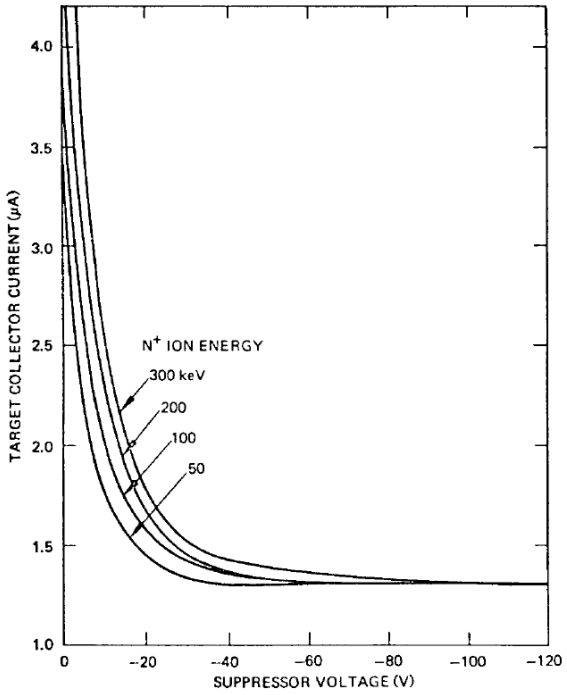

Fig. 3.1. Target collector current function of the suppressor voltage for different N^+ beam energies, after [3.3].

As indicative information:

- The amount of electron per ion increases with ion energy
- The amount of electron per ion increases with ion mass
- The suppressor voltage to apply for sufficient current measure resolution does not increase with ion energy
- The angular emission of electrons change with ion energy

It is important to point out that a very small part of the electrons has energy over the "suppressor voltage", if well designed, since a small fraction of electrons has high energy, which maximum corresponds to the projectile energy. In general, the amount of high energetic particles is negligible for our purpose.

Some preliminary study has been carried out on the current version of the Faraday Cup, with the results presented below in Fig. 3.2 [3.1]. The beam was a mixture of ions from H^+ to Ta^{1+}

with a 25 keV energy. The experimental results are in good agreement with Fig. 3.1 since a maximum electron energy of about 80 eV has been found (corresponding to the bend of Fig. 3.2). The minimum potential along the beam axis was calculated by a FEA to be about 73.4% of the potential applied to the suppressor. It is remarked that for the particular case presented in Fig. 3.2, the unsuppressed signal was only 12% higher than the suppressed version, but, according to different geometries and beam energies, it could be very much higher.

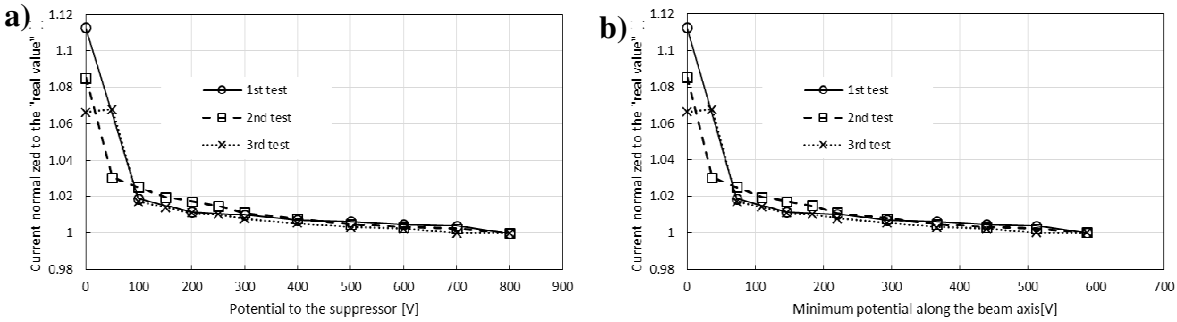

Fig. 3.2. a) Current read by the Faraday Cup (normalized to the "real current") over the suppressor potential. b) Current read by the Faraday Cup (normalized to the "real current") over the minimum potential on the Faraday Cup axis

On the other hand, the beam profiler (designed in paragraph 3.4 and 3.5.3), are usually called Secondary-Emission Monitors (SEM) [3.4], and are well described in [3.3]. This type of devices makes use of the electron emission due to the impact of the beam on wires and measuring on each wire the flow of current recalled to balance the new charges. In this case, an electrode produces a "clearing field" in order to remove the electron cloud over the surface (and so promoting the electron emission). The clearing field of few 100 V/cm is enough in order to remove the electron cloud and let the further emission [3.4]. This is not essential when the beam current is low, as in the case of the SPES RIBs, since the experience in the Front-End do not exhibit this problem.

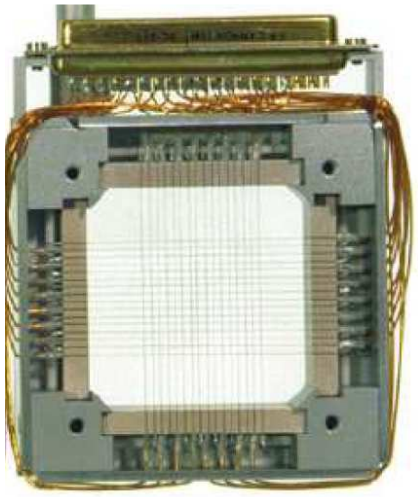

Fig. 3.3. Example of a Secondary Emission Monitor (SEM), after [3.2].

Other type of beam profiler, called wire scanners, are composed by just one or two filament that are moved in order to read the current in various positions. This is the only option available for this type of measurement when the beam current or beam pulse is too intense or when it is very important to decrease as much as possible the beam losses.

During this chapter, the various diagnostics designed are presented. In particular, the collimators (paragraph 3.2), the Faraday Cup (3.3) and the Beam Profiler (3.4) for the proton beam requires a deep study due to the high power beam density. Moreover they are placed in the most activated area due to the fact the 14% of the beam will always impinges here, as specified in paragraph 2.2.

On the other hand, even the RIB diagnostics (paragraph 3.5) require an engineering study, especially focused on decreasing the time for the maintenance procedure. It is underlined that these devices, as it is specified at the beginning of that paragraph, are absolutely not suggested to high power and, consequently, the temperatures will be low.

Finally, the study on the pneumatic motor (3.6), which has to move all the diagnostics, has been performed in order to increase its radiation hardness.

3.2. Design and tests of the PB collimators [3.5]

3.2.1. Preliminary description

In general, the collimator is a device that narrows a beam. It can be used as a way to shape the beam in order to force the beam size into a target, or to monitor the beam size and position thanks to the beam halo. For this reason, the collimator has to be placed as much as possible close to the target.

Until the amount of power dropped on the collimator is not important (few tenths of watts), the cooling circuit on the collimators can be avoided, as in the case of [3.6]. In paragraph 2.2, the power dropped in the collimator, in the nominal case, has been fixed to 15% of the total power, for a value of 1.4 kW. It is a significant part of the beam and it would be very useful to use it as a monitor for the beam size and properties. To be in safer conditions, the collimators will be designed for a 3 kW of beam power (more than twice the nominal value).

In particular, if the beam is modelled as a Gaussian, as it has been presented in Chapter 2, the number of independent variable are two: the RMS radius σ and the wobbling radius m. Since the collimator will be placed about 1.4 meters far from the target, the beam characteristics will not be the same. The cyclotron group fixed the collimators diameter to 32 mm in order to get the wanted beam size into the target [3.7]. Assuming the RMS and wobbling radius proportional to the beam size, the beam properties at the collimators position are:

- σ_{RMS} = 5.6 mm
- $r_{WOBBLING}$ = 8.8 mm

Two independent current values have to be collected from the beam edge to estimate σ and r, like it is presented in Fig. 3.4.

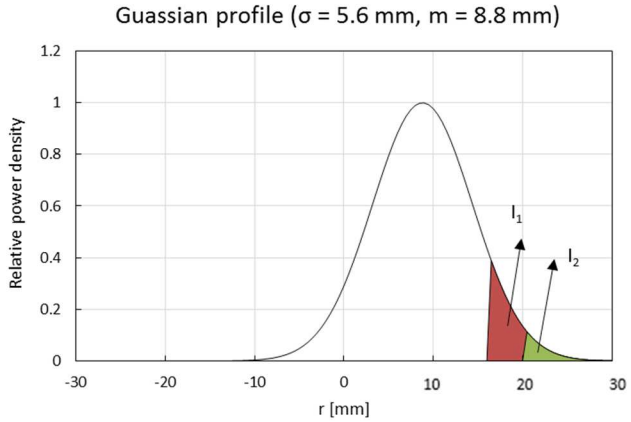

Fig. 3.4. Example of a current read from the collimators

In order to better estimate the beam parameters with a higher confidence, it will be preferable to increase the number of signals of current, anyway limiting the complexity of the instrumentation. The choice has been to split the collimators in 4 segments as presented in Fig. 3.5 in order to collect 4 signals. Moreover, the last segment has been divided in four sectors in order to control:

- Beam alignment, checking that the same amount of beam current is dropped on them
- The wobbling functioning, monitoring that a periodical function of 50 Hz describes the current signals

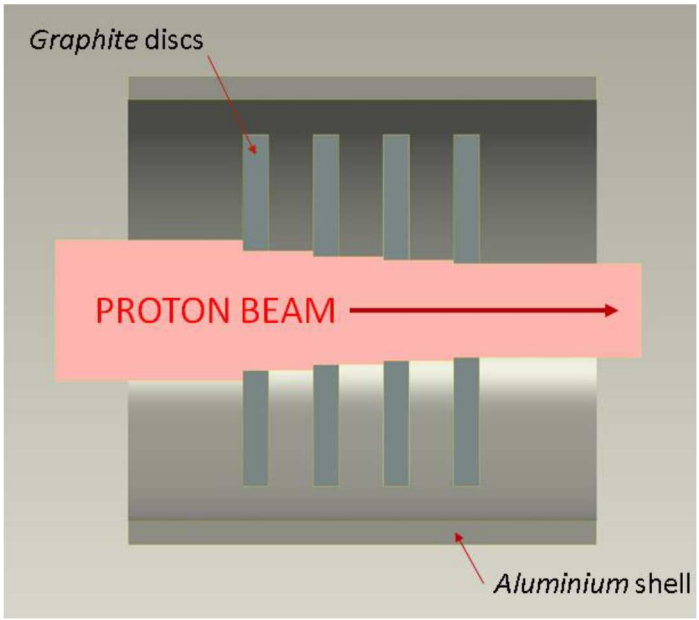

Fig. 3.5. Simple scheme to illustrate the multi-collimator principle

Graphite has been chosen as material for the collimators due to its low activation at these proton energies. According to oral conversation, even at Arronax, a facility in France where an intense cyclotron delivers a high power proton beam, they are substituting their collimators with a graphite version. The thickness needed to fully stop the 40 MeV proton beam has been evaluated with SRIM and it is about 10 mm for a 1.76 g/cm^3 density [3.8]. The thickness has been increased of 20% to 12 mm.

Due to its importance, the last segment has been designed to increase the power dropped on it of about 30%, to assure a significant amount of read current. Assuming a Gaussian profile with the nominal condition for the target, for a 3 kW proton beam, the current, power density and the inner diameter of the collimator disks has been calculated and presented in Table 6.

	Disk 1	Disk 2	Disk 3	Disk 4	Total disks	UC_x disks
Inner radius [mm]	40.8	36.8	34.4	32		
Power percentage [W]	0.0312	0.0366	0.0345	0.0459	0.1482	0.8518
Power nominal conditions – 1.4 kW [W]	294	344	324	431	1392	8000
Current nominal conditions [µA]	7.3	8.6	8.1	10.8	34.8	
Collimator percentage [%]	21.1	24.7	23.2	31.0		
Maximum Power - 3 kW [W]	632	740	697	930	3000	
Current for maximum power - 3 kW [µA]	15.8	18.5	17.4	23.2	75	

Table 6. Parameters defined for the various collimator segments

In order to dissipate the beam power, a cooling system has to be studied and designed. The first choice to perform is the method to cool the collimators: conduction or radiation.

The conduction method advantages are:

- Lower temperatures and deformations
- No effects to the other components due to the power deposited in the collimators
- Simpler mechanical design of the vacuum chamber

The conduction disadvantages are:

- The graphite has to be sustained by a good thermal conductor and electrical insulated material
- The thermal resistance on the interfaces has to be carefully studied to avoid unexpected temperature increases
- In order to increase the cooling surface, probably a welding or weld-brazing is needed on the vacuum side

The last point could be a serious problem for the safety point of view. ISOLDE experience [3.9] confirms that the weld-brazing of the copper in the very aggressive environment of an

ISOL facility could causes a water leak even if a quality control and an apparently perfect braze-welding has been performed.

On the other hand, radiation method advantages are:

- No presence of welding in vacuum
- Collimator almost insensitive to wall temperatures (more time to detect a water leak or cooling water interruption)

Radiation method disadvantages are:

- High temperatures need to dissipate power
- High thermal deformations
- Concerns on all the components in vacuum which could receive significant power even if shielded (due to light reflections)
- Graphite has to be sustained by an insulated material that supports high temperature

It has been decided to follow the second option. Since the collimators are an indispensable part for the target functioning and they have to work for years under severe conditions (1.4 kW in a high radiation environment), whereas the target is changed every 14 days, the safety of the system is the primarily aspect in the design.

Finally, in order to reduce as much as possible the total activity of the system, the vacuum chamber will be designed in aluminium, due to its much lower neutron activation compared with iron/steel, as some preliminary results point out. As a first information, a stainless steel component, impinged only by scattered protons, emitted a higher dose rate with respect to the collimators that are continuously impinged by a big amount of beam current.

3.2.2. The mechanical design

In this paragraph, the actual design and the components already manufactured will be here presented, whereas the FEA results will be exhibit in the next paragraphs. In particular, in Fig. 3.6 various pictures of the collimators are presented.

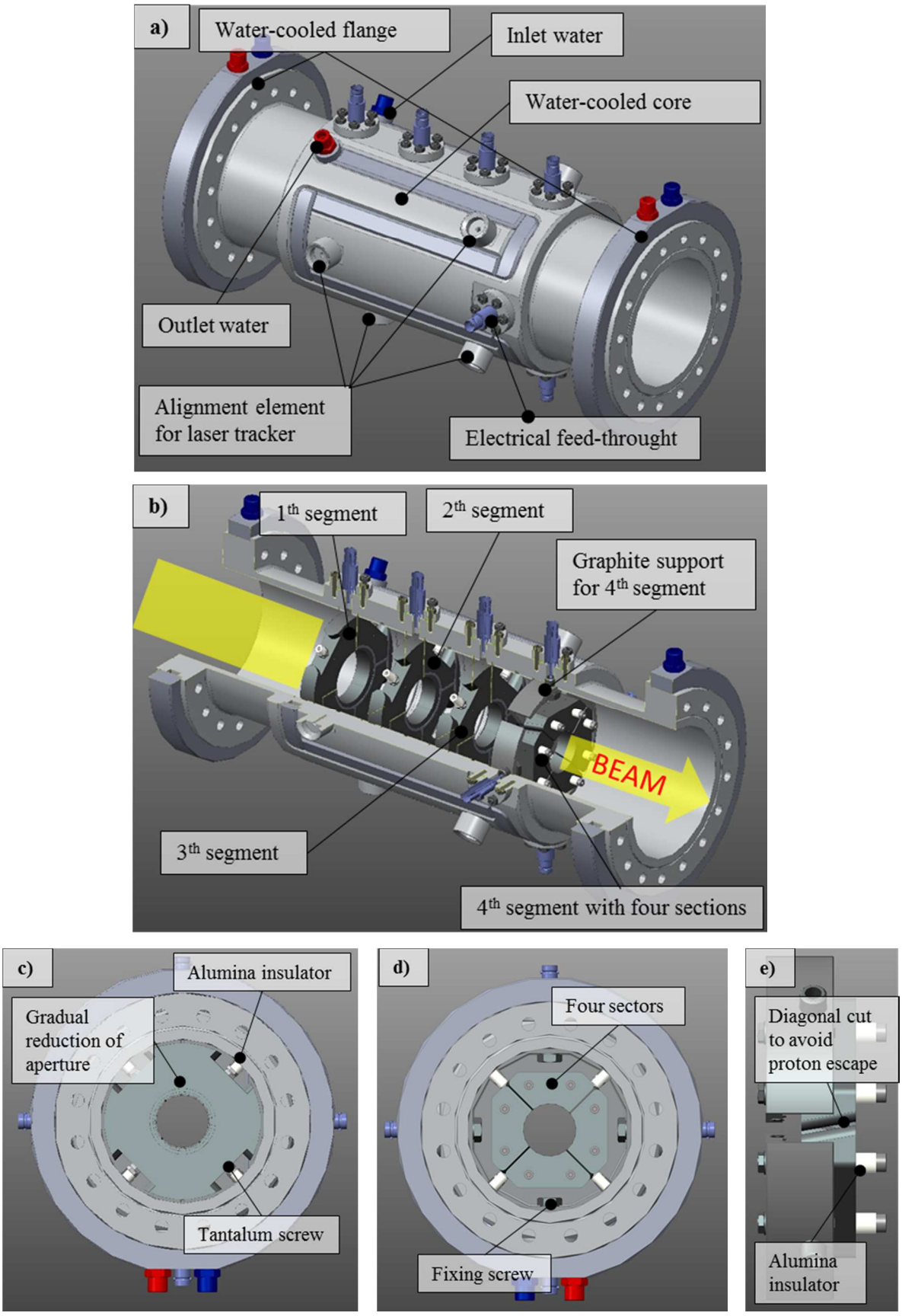

Fig. 3.6. Current CAD drawing of the collimators: a) water-cooled chamber. b) section of the water-cooled chamber with the four graphite sector. c) forward view of the collimators: here is possible to see the gradual reduction of the aperture made by the four sectors. d) backward view of the collimators. e) particular of the 4th sector with the studied diagonal cut to avoid proton escape

The water-cooled chamber, where the four segments are installed, has three different circuits. The main cools the core and it absorbs the majority of the proton beam power. The other two are designed to cool the flanges where the indium seals are placed. In particular, in paragraph 3.2.5, a discussion of the need of these two circuits is presented: in fact avoiding them, the possibility to use fast coupling flanges could be adopted, reducing the time for an eventual maintenance and decreasing the radiation dose absorbed by the operator. Some preliminary dose evaluations estimate the dose for this device due to proton and neutron activation on the order of hundreds of μSv/h, which is a dose rate quite high. Since the possibility to optimize the uncoupling time of the collimators is actually under study, the flanges of the water-cooled chamber, presented in Fig. 3.7, have not already been drilled and shaped.

Each collimator is electrically insulated by alumina cylinders that assures good insulation even at high temperature, more than 1000°C. The proton beam current dropped on them is, in this way, collected out by a tantalum wire and, by means of a standard alumina BNC feed-through, is taken in the air side. The last collimator has been divided in four sectors in order detect on each part the beam impinging there for alignment purposes. Thanks to a higher thickness and an opportune diagonal cut at a certain angle, there is not space between the sectors where the protons could escape, maintaining the total thickness higher than the proton projectile range.

Fig. 3.7. Water-cooled chamber of the collimators. The flanges have not been completed with the seal seats and holes in order to foreseen a possible fast coupling

The segments have already been manufactured and the pictures are presented in Fig. 3.8 and in Fig. 3.9. It is possible to see how the diameters of the various segments decrease from the first to the third in order to efficiently distribute the power.

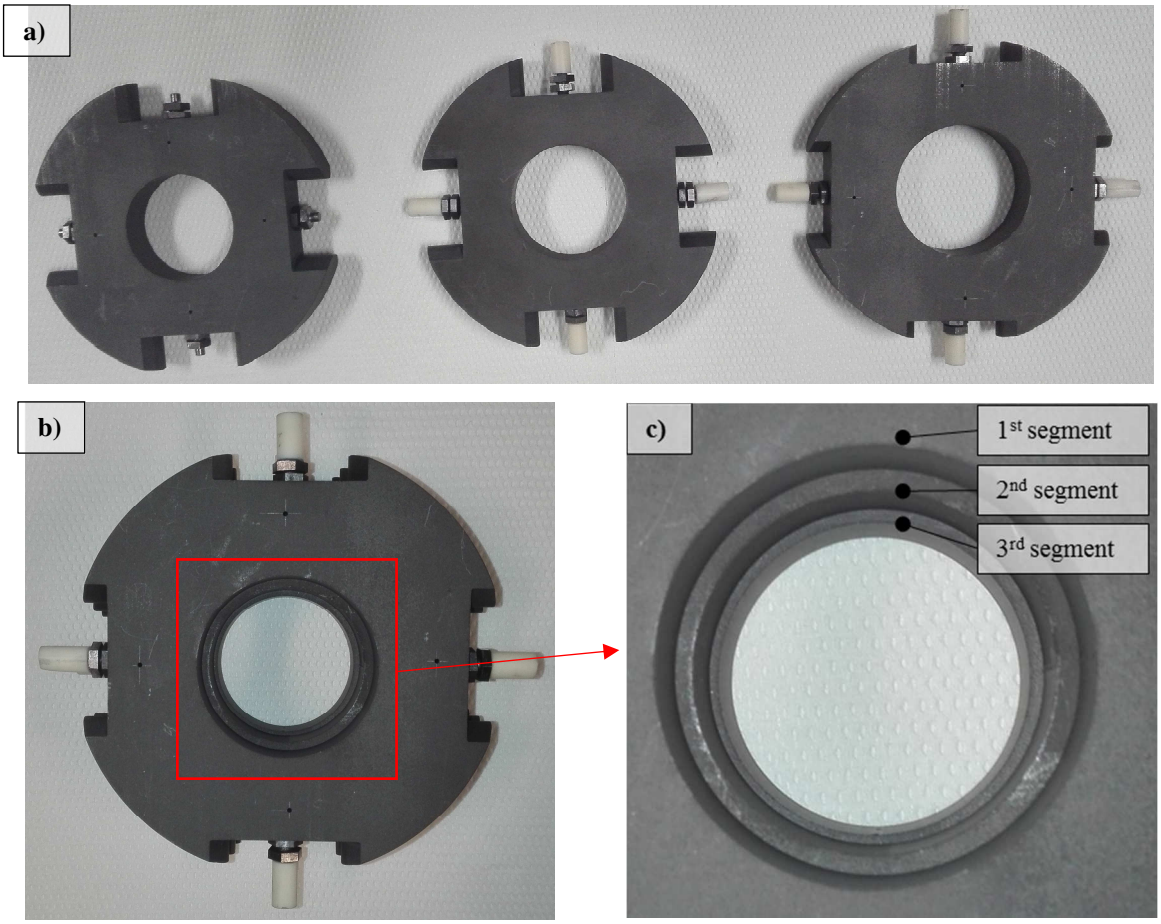

Fig. 3.8. a) pictures of the three segments; b) the three segments superimposed; c) particular of them.

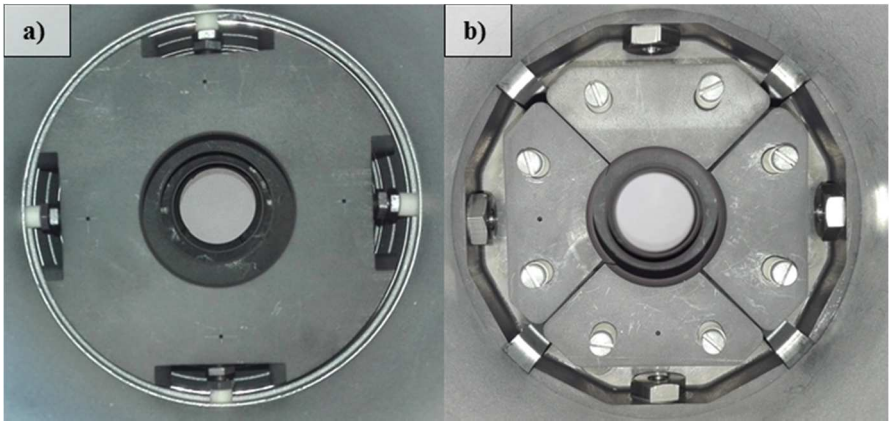

Fig. 3.9. Collimators assembled into the aluminium vacuum chamber: a) front view; b) back view.

3.2.3. *Thermal and structural analysis of the collimators*

In this paragraph, the various modification performed to improve the component will not be presented. Just the last version of the collimators and, as example, its simplified model in Fig. 3.10, with its thermal – structural (and later potential distribution) analysis will be discussed.

As already said, the inner diameter of the last segment has been fixed to 32 mm. In order to take into account the various beam impinging to the target, the beam properties to the target has scaled of a factor 0.8, which is the ratio between the beam diameters after the collimator

(32 mm) and to the SPES target (40 mm). The beam properties presented will be always related to the SPES target.

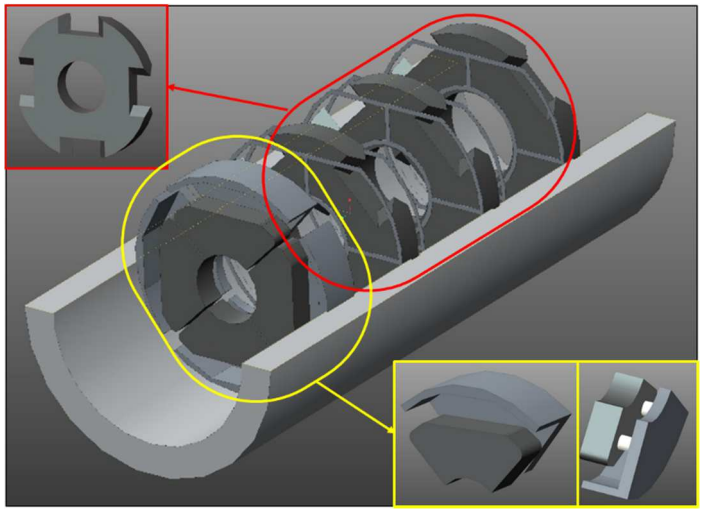

Fig. 3.10. Simplified model of the collimators for the FEA. In red the example of the 1st, 2nd and 3rd segment, in yellow one of the four sector of the last segment.

The first three segment (in red) are simulated suspended in vacuum without any contact, since the supports which will be adopted are probably negligible for the collimators thermal distribution. The last segment (in yellow) is sustained from the back by an alumina insulator and a graphite support. This support is then fixed to the aluminium chamber by means of a screw (M8).

In this case, the thermal contact resistance between the various components is not negligible. For more information, [3.10] provides a preliminary description concerning the modelling of the phenomena. In particular:

- The contact between alumina insulator and graphite is quite bad due to the high roughness of the cylinder alumina surface
- The contact between graphite support and aluminium chamber is very wide. In this case, the resistance is probably not negligible, but a perfect contact between the two materials is not for safety because it foresees lower temperatures

For this reason, three different simulations will be presented:

A. Perfect contact between the various elements
B. Absence of contact
C. Simulated contact between the graphite support and aluminium chamber. Absence of contact for the other components

In particular, for the last case, the M8 screw secures the graphite sector to the aluminium chamber. The tension of the graphite block in contact with the M8 washer (121 mm^2) is

assumed to be 5 MPa, which is a value lower than the fatigue limit of the ATJ graphite used [3.11]. The area in contact with the aluminium chamber is about 1240 mm^2, leading to a contact pressure of about 0.5 MPa. At this level, the specific thermal contact conductance has been measured in [3.10] with pieces manufactured by lathe (as in the collimators) to be about 8000 $W\ m^{-2}\ K^{-1}$. Due to the high measure errors, a value of $2 \cdot 10^3\ W\ m^{-2}\ K^{-1}$ (4 time lower) has been assumed. In the simulations, the temperature of the aluminium water-cooled chamber has been fixed to 50°C since it is a reasonable value and it does not influence the collimators temperature. Anyhow, its temperature will be deeply analysed in paragraph 3.2.5.

The results of the simulation are presented in Table 7 and Fig. 3.11.

Maximum	P [W]	I [μA]	Case A: Perfect contact	Case B: No contact	Case C: Contact resistance
Temperature segment 1 [°C]	632	15.8	916	923	917
Temperature segment 2 [°C]	741	18.53	1036	1052	1037
Temperature segment 3 [°C]	698	17.45	998	1047	1001
Temperature segment 4 [°C]	930	23.25	978	1099	1030
Alumina insulator			866	863	703
Graphite support			270	809	312
Potential shield			897	926	899
Radial displacement [mm]			0.039	0.136	0.056

Table 7. Thermal results of the collimators in the three cases taken into account.

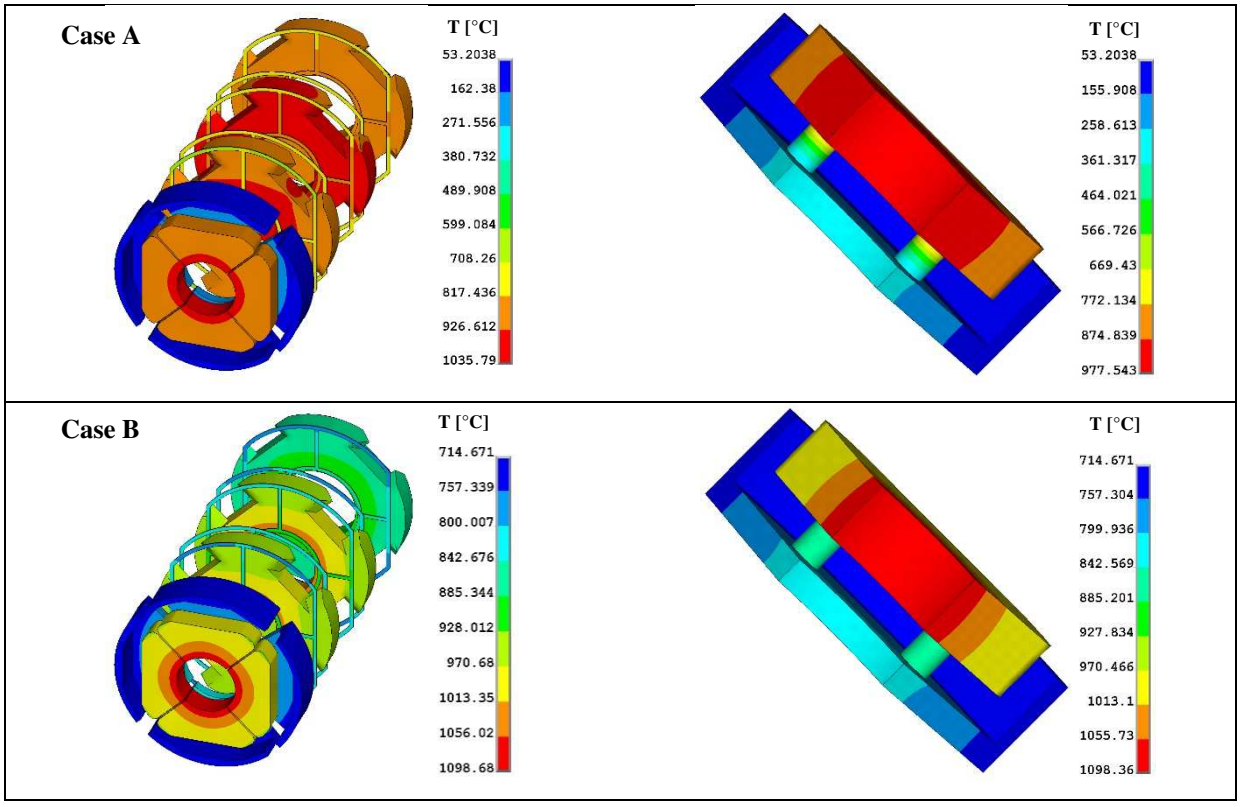

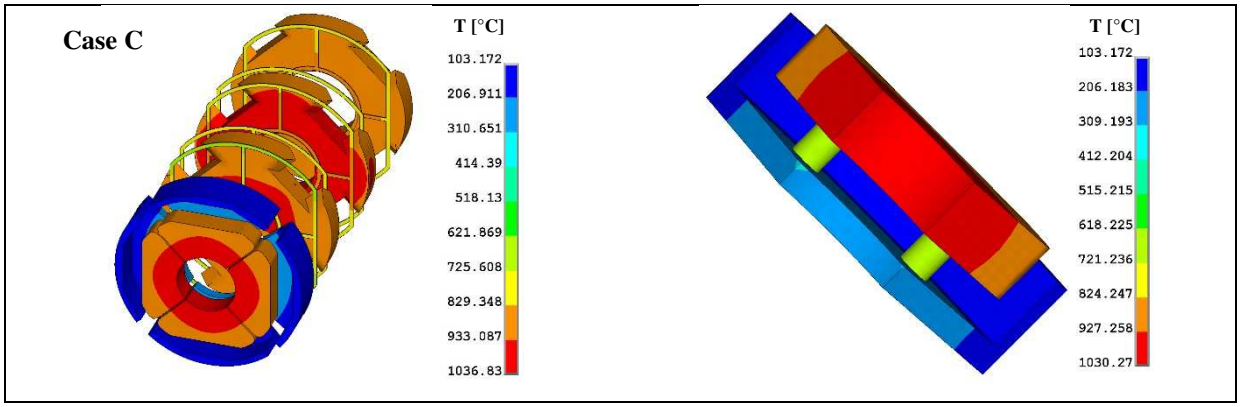

Fig. 3.11. Thermal results of the collimators in the three cases taken into account for the all segments (left) and for one of the four sectors of the last segment (right).

In all the cases, the maximum temperature reached by the segment impinged by the proton beam is between 980°C and 1100°C, which is absolutely safe for graphite [3.12] [3.13], common material used at high temperatures in furnaces or nuclear reactors. The very difference in temperature between the various cases is the temperature of the graphite supports and the alumina insulators in Table 8. In fact, on one side, the perfect contact is a good approximation for the prediction of the graphite support (only 40°C lower than the more reliable case C), but it is a bad evaluation for the alumina insulator.

Temperature of		Case A: Perfect contact	Case B: No contact	Case C: Contact resistance
Graphite support	Minimum	53	103	715
	Maximum	270	312	810
Alumina insulator	Minimum	229	854	693
	Maximum	866	863	703

Table 8. Thermal results for the graphite supports and the alumina insulators of the last segment.

The maximum displacement in the radial direction of the sector has been calculated to be about 56 μm (case C) which assures the insulation between the four sectors where the initial gap is 1 mm.

To complete the thermal characterization of the collimators, the temperature of the segments are presented for different beam profile, with 1.4 kW of proton beam dropped on them and 8 kW of beam impinging the target (target nominal conditions). In this paragraph, just the thermal results will be presented in Table 9, whereas more details will be presented in paragraph 3.2.6.

Beam properties	σ_{RMS} [mm]	4	7	10.2
	r_{WOB} [mm]	15.4	11	0
Maximum temperature [°C]	Segment 1	496	697	767
	Segment 2	718	788	785
	Segment 3	784	755	726
	Segment 4	904	775	721

Table 9. Collimators temperature for various beam profiles. Total power in the collimators: 1.4 kW, power to the target 8 kW.

The segments maximum temperatures are always lower than the results presented in Table 9. Anyway, the most stressing condition is with a mean square deviation radius of 4 mm and a wobbling radius of 15.4 mm.

3.2.4. Potential distribution for the secondary electron suppression

As presented in the paragraph 3.1 (introduction), the suppression of the secondary electrons is fundamental in order to evaluate the beam target impinging on a target. As seen, one hundred volts are enough in order to furnish a sufficient potential shield. In this case, the idea of maintaining the collimators at a positive potential has been adopted to simplify the mechanical design and the electrical connections. Consequently, the potential of the suppressor can be maintained at ground, with a strong simplification from the insulation of the electrical connections. A simple simulation of the potential distribution is needed to evaluate the minimum potential to suppress the secondary electrons. An axial symmetric geometry has been implemented and a potential of 1 V has been applied to the sectors. The results have been presented in Fig. 3.12.

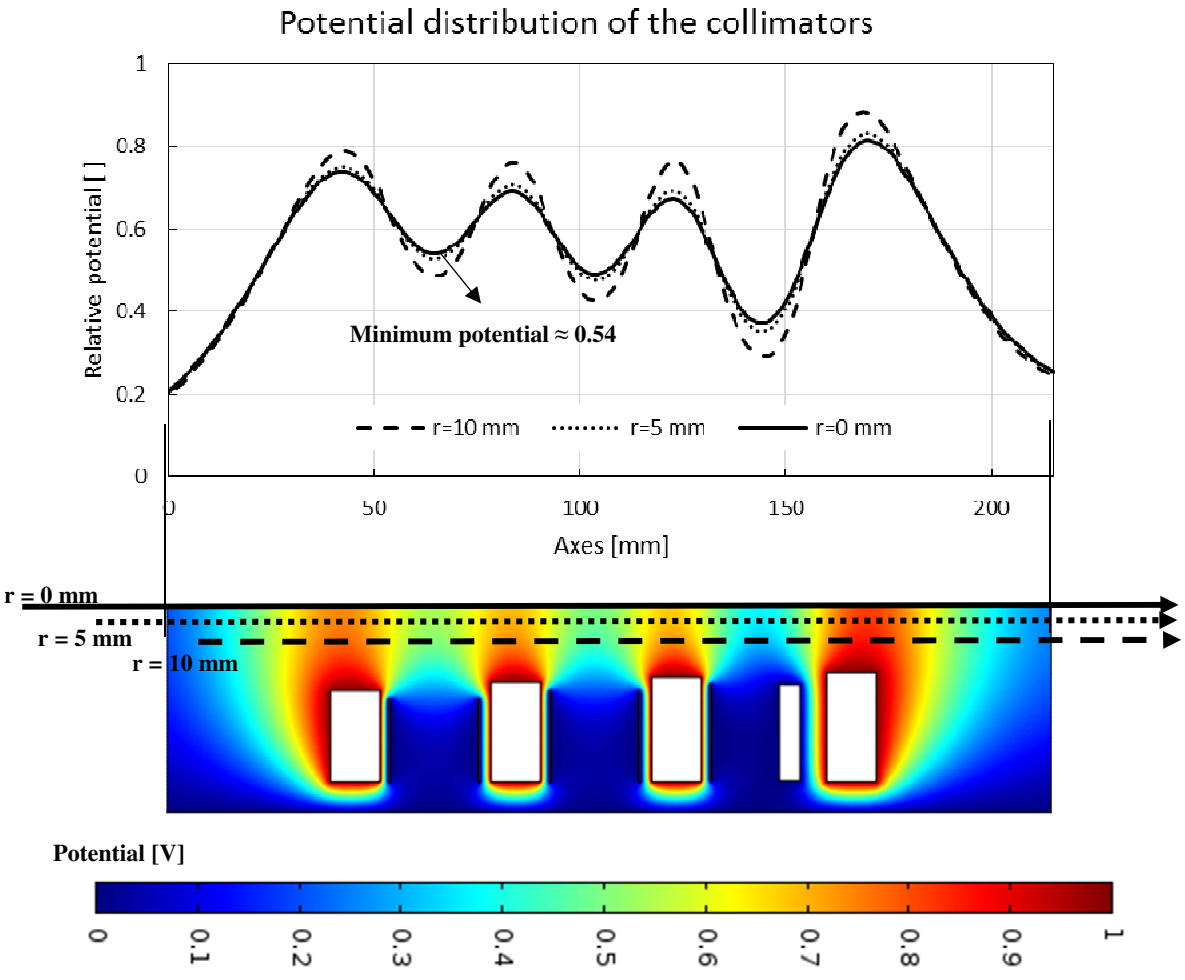

Fig. 3.12. Potential distribution of the collimators space.

The shielding efficiency of the secondary electrons is 0.46, thought as the difference between the highest "minimum potential" along the axis showed in Fig. 3.12 (0.54 V) and the potential applied divided by the potential applied (1 V). Consequently, assuming 100 V the minimum potential to repel secondary electrons, the minimum potential to apply to the collimators for a sufficient suppression is approximately 220 V. A double potential is suggested.

3.2.5. Thermal analysis of the water cooled vacuum chamber

In order to complete the component, the aluminium water-cooled chamber has to be designed. Assuming an increment of temperature of approximately 10-15°C for the cooling water, the main information concerning the design of the cooling circuit are presented in Table 10 for a power of 3 kW.

T_i [°C]	20	Inlet water temperature
T_f [°C]	33	Outlet water temperature
v [m/s]	1.1	Speed of water
Q [l/h]	200	Water flow rate
A [mm2]	50	Section Area
b [mm]	10	Section width
h [mm]	5	Section height

Table 10. Design parameters for the water-cooling circuit of the collimators

The consequent values for the cooling process are presented in Table 11.

Re [ ]	7820	Reynold number
Pr [ ]	5.81	Prandtl number
Nu [ ]	62.8	Nusselt number
α [W/m^2]	5760	Convection coefficient

Table 11. Water-cooling parameters for the collimator chamber

The analytical results predict a minimum length of the water-cooled circuit of about 0.24 m for a maximum wall temperature of 50°C. After the preparation of a simplified water circuit on a CAD model, a simulation has been implemented to verify the temperature distribution of the system with a higher detail. Moreover, on the external surfaces, the natural convection has been applied with an air temperature of 20°C and a convection coefficient of 5 W m^2 K^{-1}.

Three type of simulation has been implemented to evaluate the temperature increase on the flanges which has to be minimized for the presence of the seals:

1. Aluminium chamber with central core water cooled; stainless steel pipe attached

2. Aluminium chamber with central core water cooled; aluminium pipe attached
3. Aluminium chamber with central core and hottest flange water cooled; stainless steel pipe attached

In the flanges, an indium seal is foreseen and its maximum working temperature is 100°C [3.14]. As said in 3.2.2, the concern is about the possibility to foreseen special flanges with fast connections. The further simulations are focused on this problem, since the cooling of the core is surely efficient.

In particular for the point one, two different results are presented in Fig. 3.13 for a 3 mm thick wall pipe for chamber surface emissivity of 0.3 and 0.8; in fact, the emissivity value is not know since it depends from the quality surface and the possible presence of deposits or dirtiness. Anyhow, the emissivity is close to 0.3-0.4 for the treatment of sandblasting realized to the surfaces, as presented in [3.5], and 0.8 is the typical graphite emissivity, taken as maximum value in order to evaluate the dirtiness coming from the graphite collimators. This assumption will also be performed in other occasion of this chapter, where the emissivity is a very influencing parameter and it can change due to the surface status.

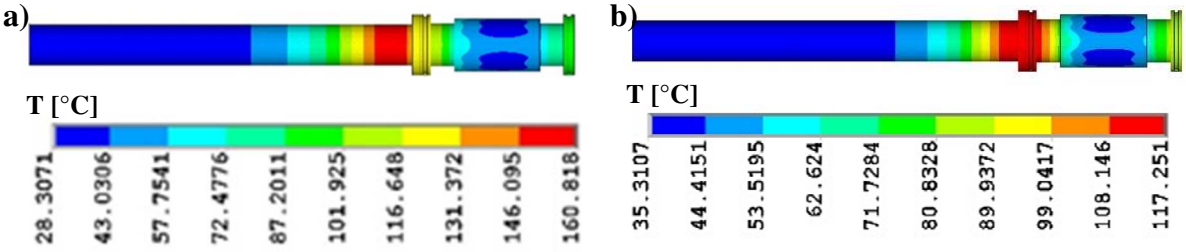

Fig. 3.13. Thermal results of the collimator vacuum chamber with a stainless steel beam pipe (3 mm thickness): a) wall emissivity: 0.3; b) wall emissivity: 0.8.

The results in Fig. 3.13 shows that a higher surface emissivity leads to lesser chamber temperature. This is due to a decrease effect of heat reflection on the inner walls: the walls are more efficient to absorb the heat coming from the hot collimators and a very small part is reflected to the other components. The temperature of the hottest flange (not water cooled) for both the cases remains over the limit of 100°C assumed: about 125°C for case a, 115°C for case b.

Concerning the second point, the same conditions as before have been applied, but with an aluminium pipe. The results are presented in Fig. 3.14.

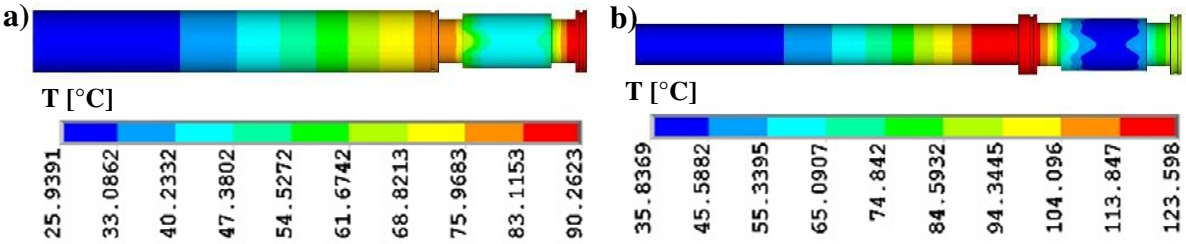

Fig. 3.14. Thermal results of the collimator vacuum chamber with an aluminium beam pipe with emissivity of 0.3: a) 28 mm pipe thickness; b) 3 mm pipe thickness.

In this case, the study was focused on the pipe thickness that can be increased due to the lower density and relative minor problems of activation. Moreover, scattering of proton, for example due to bad vacuum or the collimators, will cause a much lower activation in the case of an aluminium pipe and it is preferable for the proton beam line. The emissivity has been fixed to 0.3 since it is the most critical value. The results clearly show that a thicker aluminium pipe is sufficient to decrease the flange temperature below 100°C: in the case *a*, the flange temperature is about 80°C, in the case *b* 120°C. According to a final simulation, a thickness of 15 mm should guaranteed a maximum temperature of 100°C to the flange.

Finally, the results of the third case, presented in Fig. 3.15, will be here investigated: both the core and the hottest flange are water-cooled.

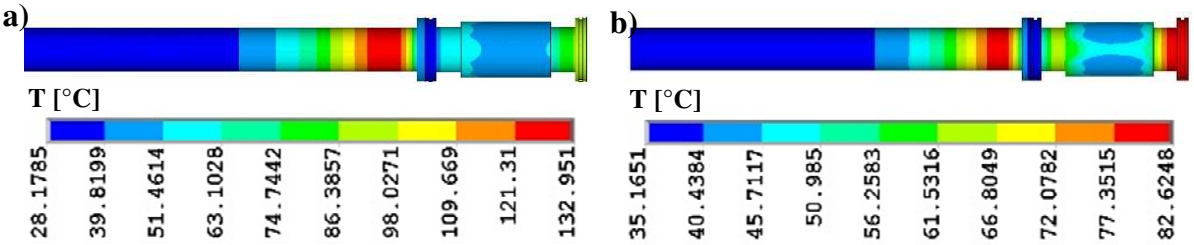

Fig. 3.15. Thermal results of the collimator vacuum chamber with a stainless steel beam pipe (3 mm thickness): a) wall emissivity: 0.3; b) wall emissivity: 0.8.

Both the cases fulfil the limit of 100°C imposed, even if, for a wall emissivity of 0.3, the maximum temperature of the stainless steel pipe is about 130°C, which is surely not a problem for the integrity of the system.

In conclusion, the actual version of the water-cooled collimator chamber could surely dissipate the 3 kW of beam power. The possibility to improve the system, foreseeing fast clamps and avoiding the two water cooled flange simplifying the component, has been investigated and it can be performed satisfying one of the following conditions:

- Studying metallic seals, different from indium, with working temperature higher than 120°C
- Foreseen an aluminium pipe of minimum 15 mm thickness

3.2.6. *Control of the proton beam parameters by the collimators*

As said before, one of the main function of the collimators is to estimate the proton beam properties. Assuming a perfect Gaussian profile and about 14% of total power dropped on them, for a beam power into the target of 8 kW, the beam fraction, power and current is presented in Table 12 and the beam fraction in Fig. 3.16 for the various profiles and segments. The beam fraction has been defined as the ratio between the beam current dropped on the collimators over the total beam before the collimators.

σ_{RMS}	r_{WOB}	Beam fraction on segment [%]				P_1	P_2	P_3	P_4	I_1	I_2	I_3	I_4
[mm]	[mm]	1	2	3	4	[W]				[μA]			
4	15.4	0.75	2.82	4.15	7.08	70	265	390	665	1.75	6.62	9.74	16.62
5	14.0	1.53	3.37	3.96	5.98	144	317	372	561	3.59	7.92	9.31	14.04
6	12.6	2.35	3.60	3.69	5.17	221	338	347	486	5.52	8.44	8.67	12.14
7	11	3.12	3.66	3.45	4.59	294	344	324	431	7.34	8.59	8.09	10.79
8.6	8	4.07	3.59	3.13	4.01	382	337	294	377	9.55	8.43	7.36	9.42
9.6	5	4.41	3.53	3.02	3.83	414	331	284	360	10.36	8.28	7.09	9.00
10.1	2.5	4.48	3.52	3.00	3.81	421	330	282	358	10.52	8.26	7.05	8.95
10.2	0	4.47	3.51	3.00	3.81	420	330	282	357	10.50	8.24	7.04	8.93

Table 12. Beam fraction, power and current dropped on the various segments for different beam properties, assuming a power dropped on the collimator of 14% (nominal conditions) and 8 kW of beam power to the target.

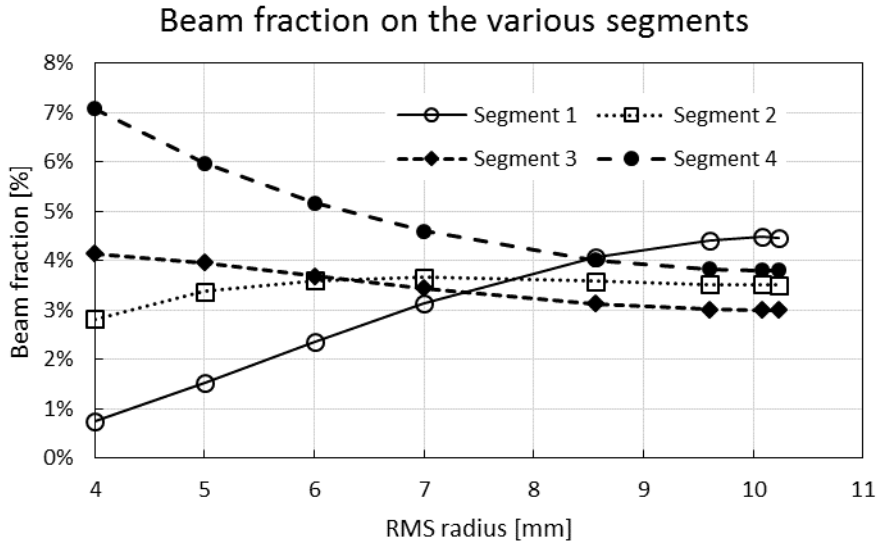

Fig. 3.16. Beam fraction dropped in the various segments for different beam properties fixing 14% of the power to the collimators and 8 kW of beam power to the target (nominal conditions).

From these data, it will be possible to control the beam properties and, consequently, the working conditions of the target. It is underlined that the maximum power dropped in the various segments with 1.4 kW (8 kW of power in the target in nominal condition) is always lower than the boundary condition used to design the collimators already presented in Table 6.

3.3. Design of the PB Faraday cup

3.3.1. Preliminary description

In general, a Faraday cup is a device that is insulated and completely stops the beam. Here the beam current is deposited and, thanks to an electrical connection to an ammeter, the beam current could be measured. As before, a shielding potential has to be applied in order to suppress the secondary electrons. As already stated in 3.2.1, even the Faraday cup will dissipate the beam power by means of radiation to the water-cooled vacuum chamber. In this case, the maximum power to dissipate is about 8 kW; on the other hand, the Faraday cup will not be used continuously, but just for beam preparation. Another important information is that it will not be a device used to stop the beam in case of malfunctioning since the intervention time is not as fast as it needs.

The geometry of the Faraday cup will be a "reversal" cone as in Fig. 3.17. This shape has two main advantages:

- The main part of the secondary electrons are emitted toward the other face
- The angle increases the surface where the power is dissipated

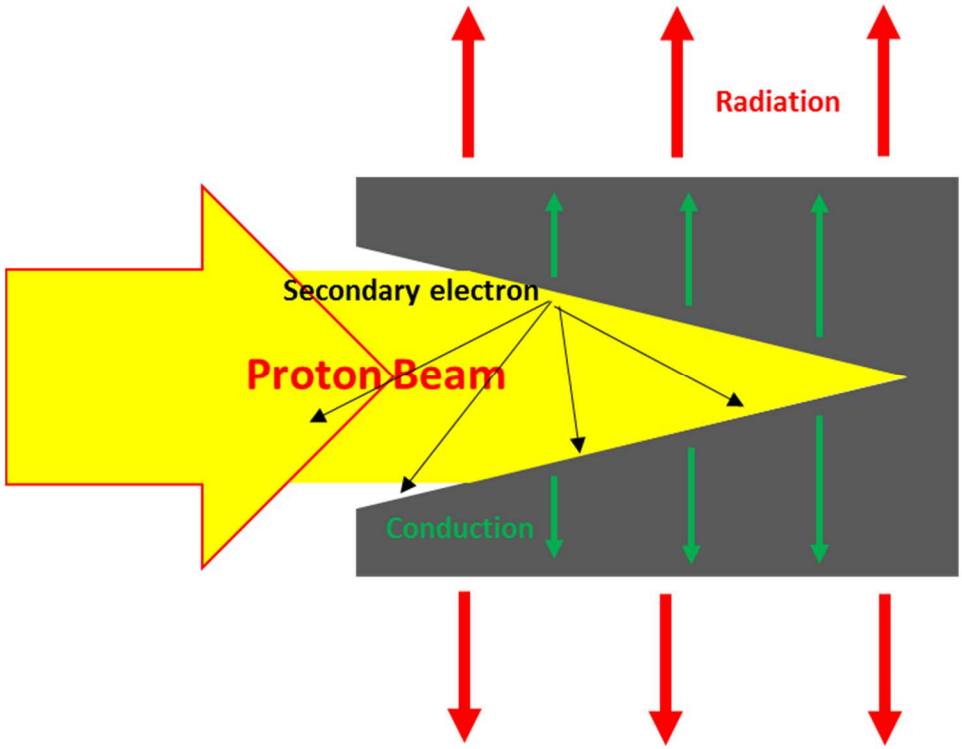

Fig. 3.17. Simplified geometry of the high power Faraday Cup

The beam diameter is approximately the same of the last collimators, about 32 mm and, as for the collimators, the graphite has been decided as material for the Faraday cup. A simple

analytical model can be implemented to estimate the temperature of the component in order to obtain some preliminary dimensions for the following design. The two mechanisms to take into account are:

- Conduction from the surface, which is impinged by proton, and the lateral radiative area
- Radiation from graphite cylinder to water-cooled chamber

The geometry can be easily thought as infinite axial-symmetric cylinder. The conduction will be represented with:

$$q = \frac{2\pi L\lambda}{ln\left(\frac{r_1}{r_0}\right)}(T_1 - T_0) \tag{3.1}$$

And radiation:

$$q = \frac{2\pi r_1 L\,\sigma \cdot \left({T_1}^4 - {T_2}^4\right)}{\frac{1}{\varepsilon_1} + \frac{{r_1}^2}{{r_2}^2}\left(\frac{1}{\varepsilon_2} - 1\right)} \tag{3.2}$$

Where the q is the power to dissipate, σ is the Stephan-Boltzmann constant, L the length of the cylinder, r the radius, ε the surface emissivity and T its temperature, as represented in Fig. 3.18.

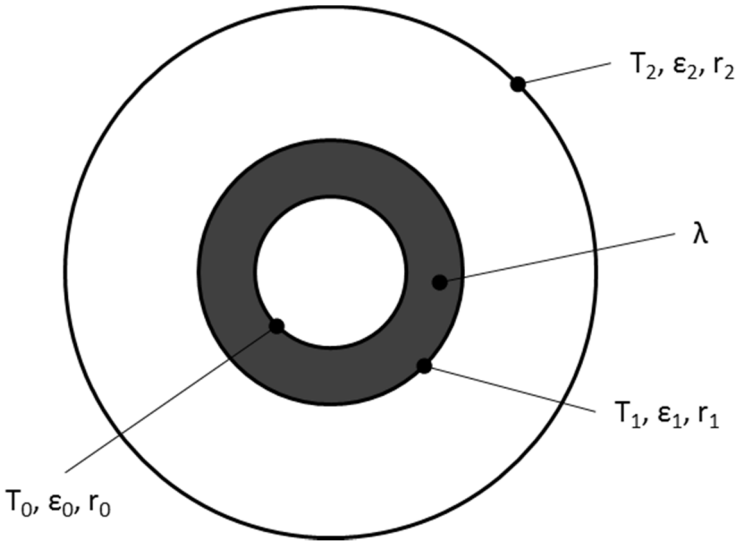

Fig. 3.18. Figure representing the analytical model implemented

Since $r_2 >> r_1$ and $T_2 << T_1$, (3.3) can be simplified as below:

$$q = \sigma\varepsilon_1 2\pi r_1 L \cdot {T_1}^4 \tag{3.3}$$

Some preliminary results are presented in Table 13. The material properties are typical of the graphite at about 1500-2000°C, r_1 has been fixed as the external radius of the SPES target, r_0 the half of r_1 and L a reasonable length of the Faraday cup. In particular, r_0 has not a "real" meaning but it is just to give an idea of the increment of the temperature due to conduction.

Material properties		Geometrical measures		Temperatures	
ε_1 [ ]	0.8	r_0 [mm]	12.5	T_0 [°C]	1762.581
λ [W m^{-1} °C^{-1}]	43	r_1 [mm]	25	T_1 [°C]	1557.339
		L [mm]	100		

Table 13. Preliminary parameters for the thermal and structural simulations of the high power Faraday cup.

In the further CAD model and FEA, the length L has been incremented according to the space available on the water-cooled cross presented in paragraph 3.3.5.

3.3.2. The mechanical design of the Proton Beam Faraday Cup

As mentioned in 1.4.3, the power deposition could be modelled as a Gaussian, but in this case the power is approximately decreased of a factor of *sin(θ)*, where *θ* is the angle of incidence. In fact, in Fig. 3.19, two different angle of incidence are foreseen, corresponding to two different power depositions. Where the power is lower, in the outer radius due to the Gaussian tails, the angle is higher. In particular, at the end of the Faraday cup cone, a fillet radius of 2 mm has been foreseen in order to avoid concentration stresses due to the notch (lower radius are difficult to made by a lathe on such a geometry). The beam should have in this position a diameter slightly higher than 32 mm since it is quite close to the collimators (260 mm distance), so the entrance diameter of the cup has been augmented to 38 mm.

Then the Faraday cup is sustained by a tantalum support, so the high temperatures of the graphite working conditions will not be a problem. The insulation of the support is performed by alumina cylinders, a material that supports high temperatures and it is radiation hard.

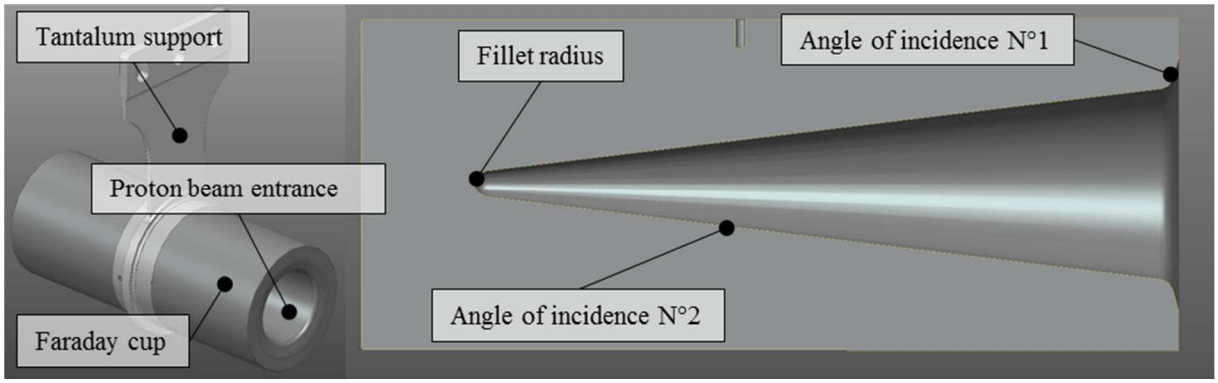

Fig. 3.19. CAD drawings of the high power Faraday cup.

As the collimators, even the Faraday cup is maintained at a positive potential to suppress the secondary electrons. For this component, an additional suppressor at a negative potential can be installed to get a more accurate current measure if necessary (see Fig. 3.20 and paragraph 3.3.4). In addition, before the FC is foreseen an insulated graphite shield (see Fig. 3.20a) to check the functioning of the previous collimators. If a rupture on the last collimator segment happens, the graphite annulus is impinged by the proton beam and the current will be measured.

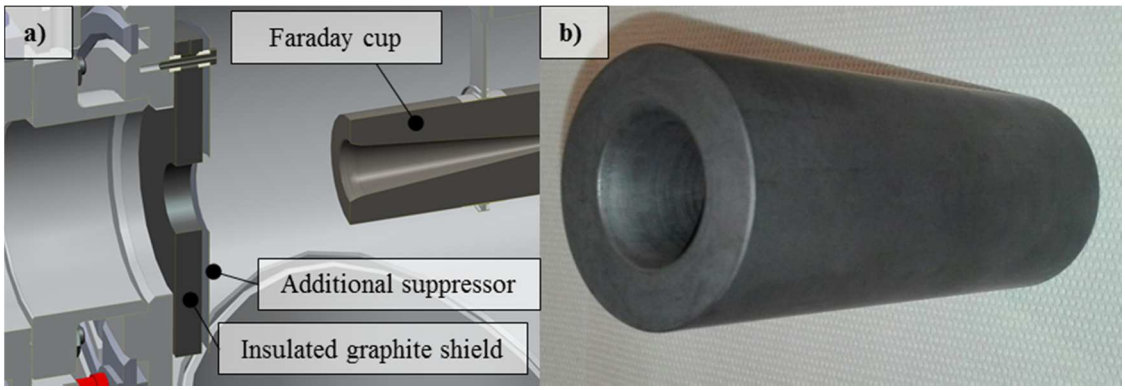

Fig. 3.20. a) Faraday cup in position, with the additional suppressor and a graphite shield; b) the manufactured Faraday Cup

3.3.3. Thermal and structural design of the Proton Beam Faraday Cup

As showed in 3.3.1, the analytical model predicts temperatures below 2000°C. Due to the cone geometry, the power deposition has to be simulated appropriately. The proton penetration for a 40 MeV proton energy is about 10 mm and a preparatory analysis has been performed on a reasonable geometry in order to well understand the effect of a simplified heat generation. In fact, the proton beam power can be assigned in two different ways:

1. As a heat generation on a volume: it is possible to take into account the power profile along the proton beam direction. Better for long proton project range. More complex.
2. As a heat flux on a surface: better for short proton project range. Simpler.

In this case, since the graphite power range is about 10 mm, probably the heat generation on a volume has to be used. Moreover, an eventual constant power deposition along the axis would be preferable in order to simplify the applied boundary conditions. The advantages of each method are:

1. Heat generation on a volume: the heat is deposited closer to the impinging area and has to travel to the external surface to be dissipate
2. Heat flux on a surface: the heat is deposited in a zero length volume and it can simulate the Bragg peak [3.15].

An axial-symmetric model, presented in Fig. 3.21, has been implemented to characterize the differences between various power depositions. In particular, two important dimensions are presented: depth p and thickness s. The first is related to the distance between the volume and the area where protons impact, the second is the thickness of the volume where an uniform heat generation is applied. Both of the two dimensions are related to assignment case N°1 (heat generation on a volume). In case of assignment case N°2 (heat flux on a surface), the surface distance from the area where protons impact will be the sum of thickness s and depth p. The study is presented in Table 14 for the last version of the Faraday cup which will be presented

later in this section. It has to be underline that σ_1 and σ_3 are the maximum principal stresses and they occur on different points of the Faraday cup as presented in Fig. 3.22. For all the following simulations, the Gaussian profile presented in Fig. 2.9 have been assumed, scaled of a factor 0.8 which is the ratio between the beam collimator diameter (32 mm) and the target diameter (40 mm) as it was done in paragraph 3.2 for the collimators.

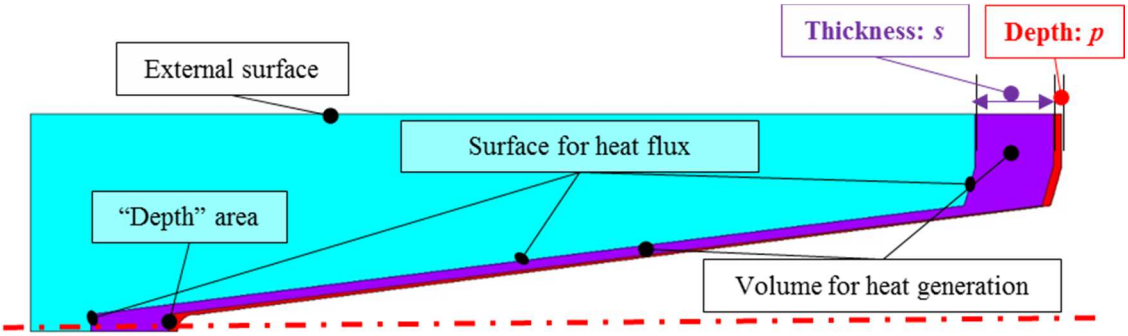

Fig. 3.21. Geometry of the axial-symmetric model implemented to verify the power deposition application.

	σ_{RMS} = 7 mm; r_{WOB} = 11 mm				
	Assignment case N°1		Assignment case N°2		
	p=1 mm; s=9mm	p=2 mm; s=5mm	p+s=2 mm	p+s=5 mm	p+s=10 mm
T_{MAX} [°C]	1744	1745	1749	1745	1742
σ_1[MPa]	10.1	10.0	9.8	10.0	10.4
σ_3[MPa]	-20.5	-20.2	-22.0	-21.3	-20.5
	σ_{RMS} = 10.2 mm; r_{WOB} = 0 mm				
	Assignment case N°1		Assignment case N°2		
	p=1 mm; s=9mm	p=2 mm; s=5mm	p+s=2 mm	p+s=5 mm	p+s=10 mm
T_{MAX} [°C]	1763	1763	1872	1886	1929
σ_1[MPa]	10.5	10.5	10.3	10.5	14.2
σ_3[MPa]	-32.7	-32.4	-38.7	-37.4	-36.0

Table 14. Effect on temperature and principal stresses for different power depositions and beam characteristics.

In case of nominal beam for the target (RMS radius of 7 mm, wobbling radius of 11 mm) the change on the power assignment is essentially negligible for temperature and maximum first principal stress, whereas there is a maximum difference of 9% on the σ_3. In case of the absence of wobbler (RMS radius of 10.2 mm, wobbling radius of 0 mm – beam properties already presented in 2.2.3), the values of temperature and stresses change a lot. In particular, the case with *s+p=2mm* is the most critical for the stresses point of view, whereas the case *s+p=10mm* for the temperature. For the design of the Faraday cup, the power deposition of the assignment case N°2 with *p+s=5 mm* has been used because it seems that it can take into account the critical phenomena of both the two methods.

The three points of the Faraday Cup where stresses are higher are shown in Fig. 3.22. Since the highest value of σ_{VM} (point 3) is in presence of a two negative principal stresses (the first is null), both smaller than the stresses at the point 2, point 3 has not been taken into account for

the design. On the other hand, the stresses in point 1 and 2 vary from zero (no proton beam) to the maximum (8 kW of proton beam), for this reason the mean stress of the fatigue cycles is the half of the maximum value. Assuming that the principal stresses σ_1 and σ_3 causes the fatigue rupture, the following limit are imposed:

$$\sigma_1 < 2 \cdot \sigma_{1\,LIM} \tag{3.4}$$

$$|\sigma_3| < 2 \cdot |\sigma_{3\,LIM}| \tag{3.5}$$

Where

$$\sigma_{1\,LIM} = 7.84\ MPa \quad for\ R = 0$$

$$\sigma_{3\,LIM} = -19.3\ MPa \quad for\ R = -\infty$$

Where R is the cycle ratio and the limits are obtained from dashed line of the Goodman diagram in [3.11] (figure 7).

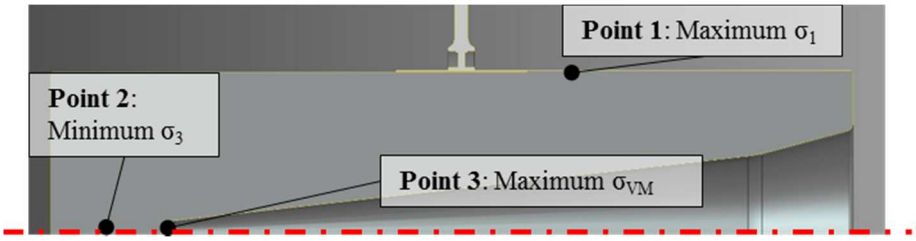

Fig. 3.22. Highest stresses on the Faraday cup.

The criterion implemented to optimize the geometry is presented below in Table 15:

Case	$\sigma_1 < 2 \cdot \sigma_{1\,LIM}$ $\quad |\sigma_3| < 2 \cdot |\sigma_{3\,LIM}|$	$\sigma_1 > 2 \cdot \sigma_{1\,LIM}$ $\quad |\sigma_3| < 2 \cdot |\sigma_{3\,LIM}|$	$\sigma_1 < 2 \cdot \sigma_{1\,LIM}$ $\quad |\sigma_3| > 2 \cdot |\sigma_{3\,LIM}|$	$\sigma_1 > 2 \cdot \sigma_{1\,LIM}$ $\quad |\sigma_3| > 2 \cdot |\sigma_{3\,LIM}|$
Value	$\frac{\sigma_1}{2\sigma_{1\,LIM}} \cdot \frac{\sigma_3}{2\sigma_{3\,LIM}}$	$\frac{\sigma_1}{2\sigma_{1\,LIM}}$	$\frac{\sigma_3}{2\sigma_{3\,LIM}}$	$\frac{\sigma_1}{2\sigma_{1\,LIM}} \cdot \frac{\sigma_3}{2\sigma_{3\,LIM}}$

Table 15. Definition of the criterion for the optimization process.

In this way, the value is less than one only if both of the principal stresses are lower than the limit imposed. The optimization process has been performed on the two variable *r* and *z* of the geometry presented in Fig. 3.23. In particular, the process has been performed for four of eight different beam properties already reported in 2.2.3. The results are presented in Fig. 3.24.

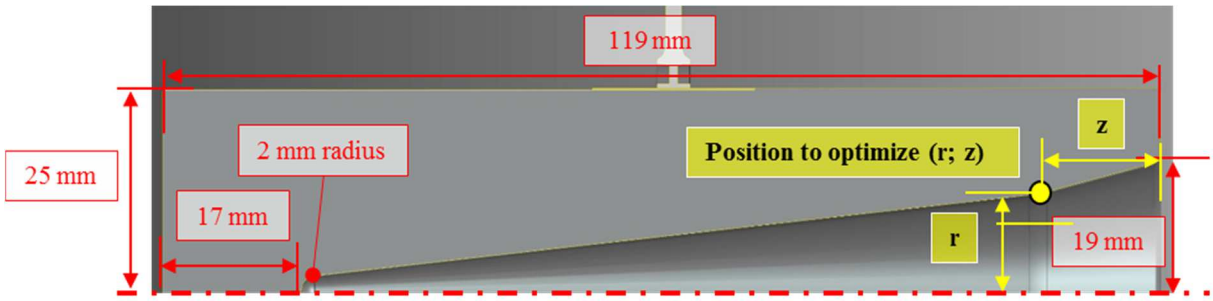

Fig. 3.23. Measures implemented in the Ansys geometry and position to optimize.

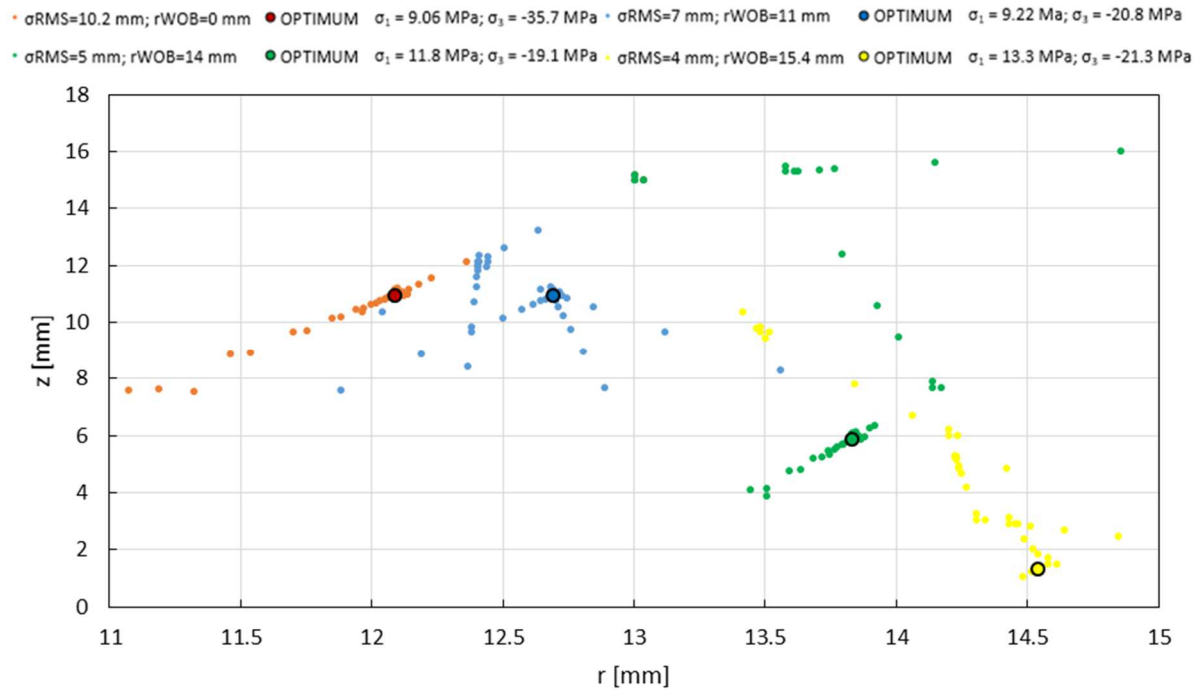

Fig. 3.24. Results of the optimization process with four different beam characteristics.

It is obvious that each beam has a different optimum geometry. In particular, higher the wobbling radius and smaller the RMS radius is, higher is *r* and smaller *z*. Then a simulation for the other beam properties has been performed for each optimum geometry, except the case of σ_{RMS} = 10.2 mm since its optimum was very close to σ_{RMS} = 7 mm.

	v1 – Optimum for σ_{RMS} = 7 mm; r_{WOB} = 11 mm				v2 – Optimum for σ_{RMS} = 5 mm; r_{WOB} = 4 mm				v3 – Optimum for σ_{RMS} = 4 mm; r_{WOB} = 15.4 mm			
r [mm]	12.7				13.8				14.5			
z [mm]	11				5.9				1.3			
σ_{RMS} [mm]	10.2	7	5	4	10.2	7	5	4	10.2	7	5	4
r_{WOB} [mm]	0	11	14	15.4	0	11	14	15.4	0	11	14	15.4
T_{MAX} [°C]	1857	1805	2035	2220	1880	1745	1913	2088	1886	1745	1838	1998
σ_1 [MPa]	9.8	9.3	14.2	19.1	10.3	9.9	12.0	16.4	10.5	10.0	11.8	13.5
σ_3 [MPa]	-36.6	-20.8	-29.1	-39.2	-37.2	-21.2	-19.1	-26.3	-37.4	-21.3	-19.3	-21.3

Table 16. The three optimum geometry applied to the other beam characteristics.

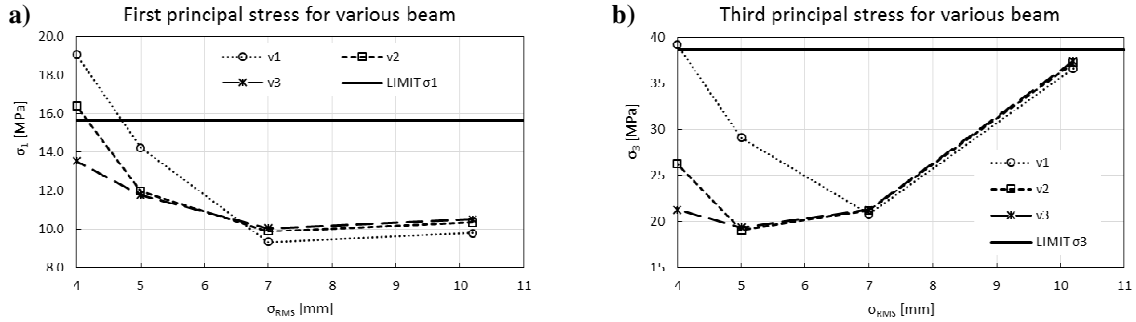

Fig. 3.25. First and third principal stress (absolute value) of the optimum geometries for various beam characteristics.

The results presented in Fig. 3.25 and Table 16 shows that only the optimum v3 satisfies the limits for all the beam characteristics. In particular, for small beam radius σ_{RMS}, both limits are quite restrictive, whereas for higher σ_{RMS}, just the third principal stress could be critical. In conclusion, the high power Faraday cup has been designed according to the geometry v3, which can accept all the beam deliverable to the target. It is important to underline that the limit imposed for the principal stresses have been evaluated at room temperature in [3.11], but it is well known that graphite improves its mechanical properties with the temperature [3.12], [3.16]. Just to complete the description, the thermal result distributions for the last version is presented in Fig. 3.26 for the various beam characteristics.

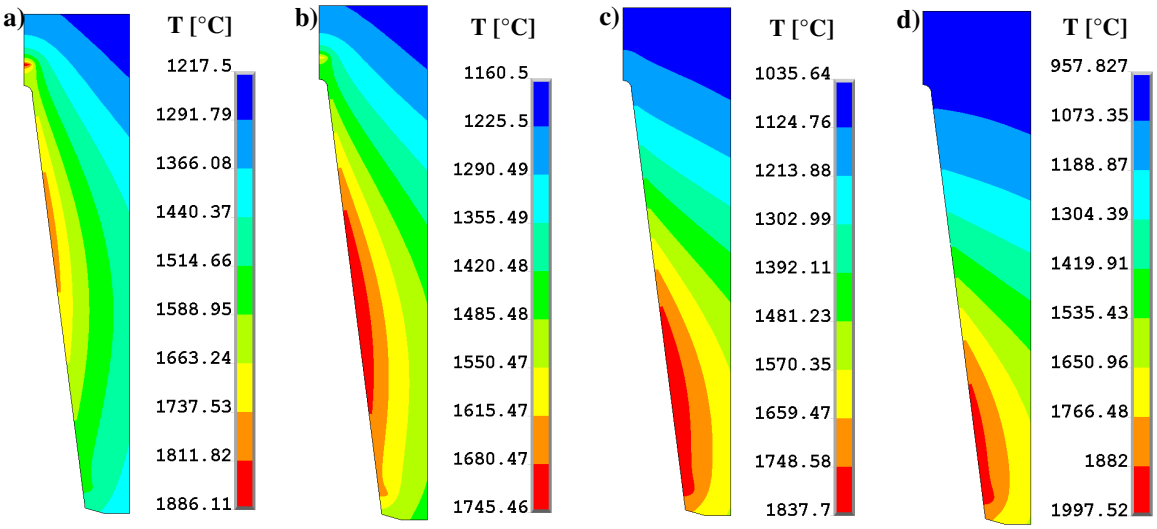

Fig. 3.26. Thermal distribution on the last geometry adopted for different beam characteristics to the target: a) σ_{RMS}=10.2 mm; r_{WOB}=0 mm; b) σ_{RMS}=7 mm; r_{WOB}=11 mm; c) σ_{RMS}=5 mm; r_{WOB}=14 mm; d) σ_{RMS}=4 mm; r_{WOB}=15.4 mm;

It is very clear how the beam properties influence the temperatures. In fact, in Fig. 3.26a, the beam maximum power is in the axis centre, as the maximum temperature value, while, proceeding with the pictures, the beam maximum power deposition moves on the outer radii incrementing consequently the maximum temperatures.

3.3.4. Potential distribution of the Proton Beam Faraday Cup

As for 3.2.4, the potential distribution along the Faraday cup axis has to be evaluated to assure a sufficient potential shield to suppress the secondary electrons. For this reason, two different simulations has been implemented:

1. With an additional negative suppressor (potential applied equal to -1 V)
2. With a simple ground suppressor

The results are presented in Fig. 3.27. It is clear that a negative suppressor almost double the suppression efficiency because the minimum potential between FC and suppressor goes up

from about 0.6 to 1.12. Assuming a potential of suppression of 300 V, a shielding potential of 336 V is ensured, which is fully sufficient.

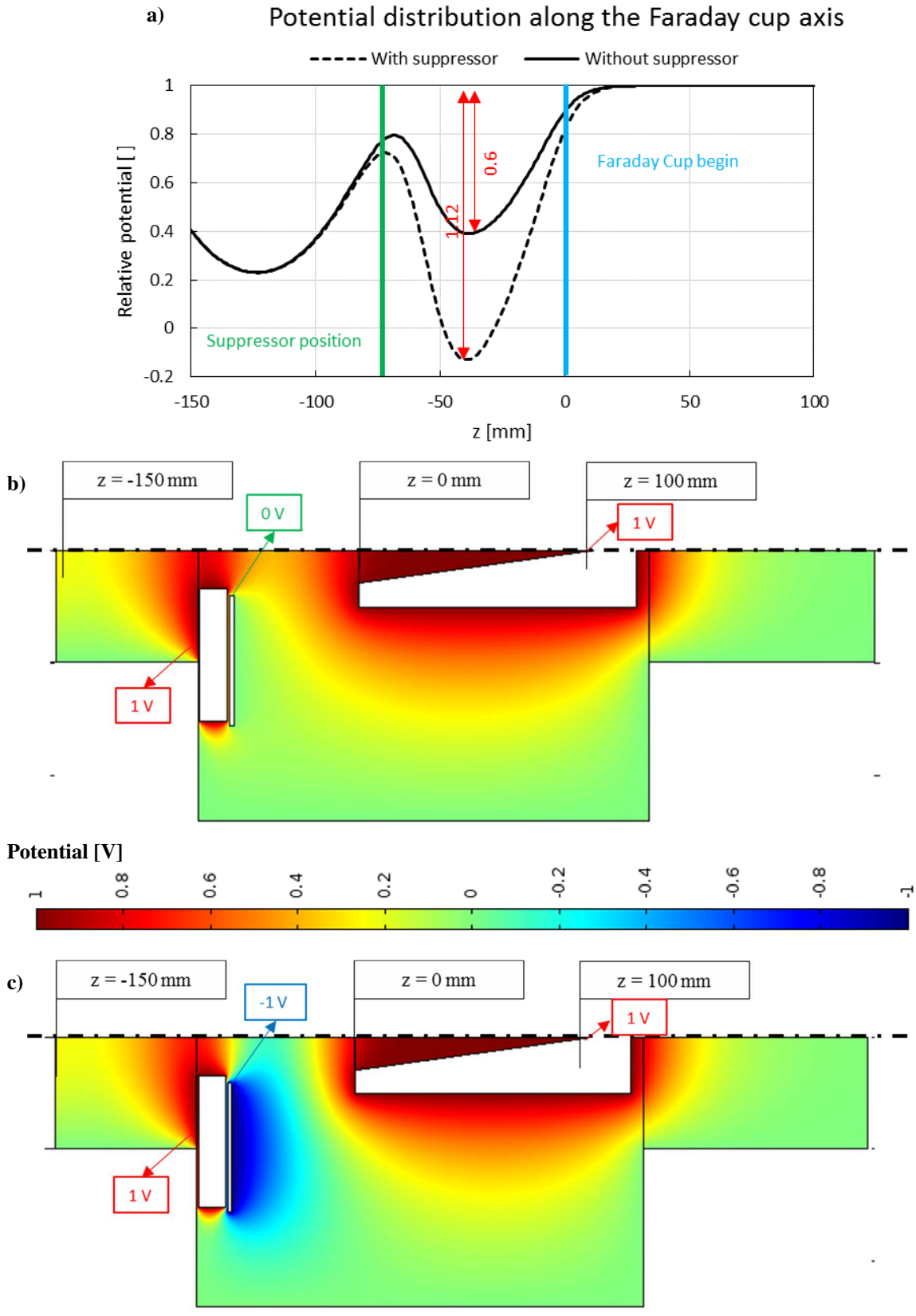

Fig. 3.27: a) Differences of the potential of the Faraday cup diagnostic box with and without suppressor; picture of the potential distribution: b) without suppression potential; c) with suppression potential

3.3.5. Thermal analysis of the water cooled vacuum chamber

In order to complete the analysis, the aluminium water-cooled chamber for the Faraday cup has to be designed. Assuming an increment of temperature for the cooling water of approximately 20-30°C, with a power of 8 kW, the main information concerning the design is presented in Table 17.

T_i [°C]	20	Inlet water temperature
T_f [°C]	47	Outlet water temperature
v [m/s]	1.4	Speed of water
Q [l/h]	250	Water flow rate
A [mm2]	50	Section Area
b [mm]	10	Section width
h [mm]	5	Section height

Table 17. Design parameters for the water-cooling circuit of the Faraday cup.

The consequent values for the cooling process are presented in Table 18.

Re [ ]	11560	Reynold number
Pr [ ]	5.42	Prandtl number
Nu [ ]	75.0	Nusselt number
α [W/m^2]	6920	Convection coefficient

Table 18. Water-cooling parameters for the Faraday cup chamber.

The analytical results predicts a minimum length of the water-cooled circuit of about 1.6 m for a maximum wall temperature of 60°C. After the definition of a simplified CAD model for the water-cooled cross, then a simulation with Ansys has been implemented to verify the temperature distribution of the system with a higher detail. Moreover, on the external surface, the natural convection has been applied with an air temperature of 20°C and a convection coefficient of 5 W m^2 K^{-1} as already done in 3.2.5. For a simpler simulation, the cross is divided in three section not in contact each other: the central core and the two flanges with tubes, as it is presented in Fig. 3.28.

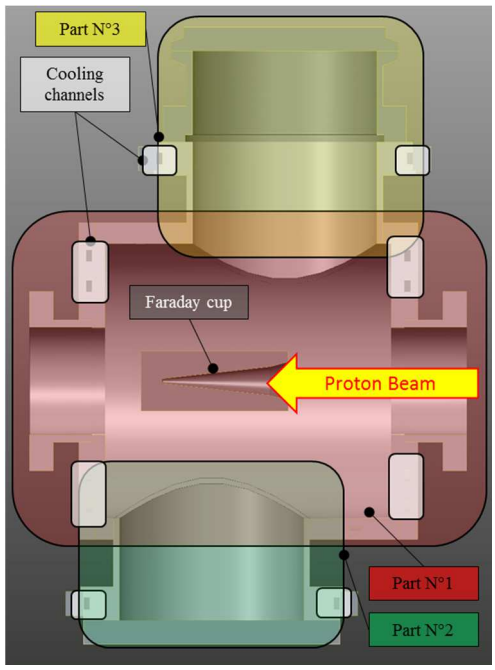

Fig. 3.28. Simplified model of the water-cooled cross divided in three main parts: N°1 core; N°2 and N°3 flanges with tubes.

The results presented in Fig. 3.29 clearly shows that the three parts are not connected since the tubes of the flanges reach higher temperatures than the close core. Anyhow, the maximum temperatures of the flanges are below the limit of 100°C already assumed in 3.2.5. Moreover the connection flange for the collimators is not so warm, about 65°C.

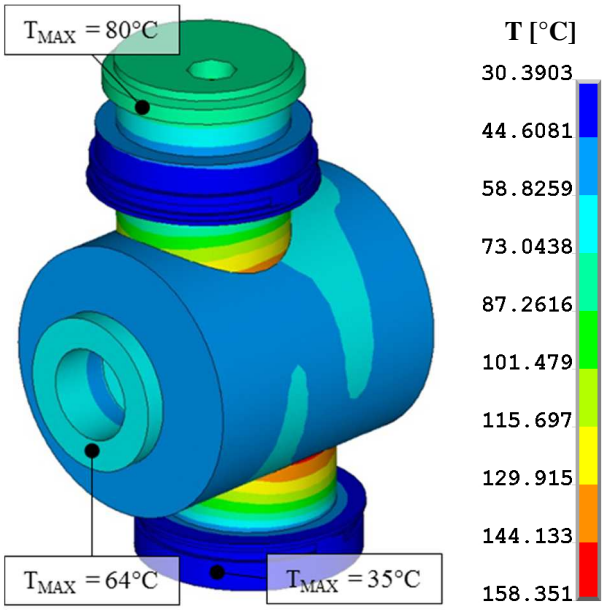

Fig. 3.29. Thermal distribution on the proton beam water-cooled cross.

A more complex evaluation of the thermal distribution, with a continuity between the three parts, is not required since no problems are foreseen.

The final water-cooled diagnostic cross design is presented in Fig. 3.30. In the yellow circle is showed the flange that could be modified in order to increase the changing speed of the collimator chamber (already presented in paragraph 3.3) that is here connected. The red circles are indicated some threaded holes foreseen to support eventual graphite annuli. They has to stop scattered protons that, according to recent calculus, significantly increase the activation of the proton beam line. Fig. 3.30c showed the actual status of the diagnostic cross: to complete the component, the seal seats, the flange holes and the alignment seats on the cross side have to be realized.

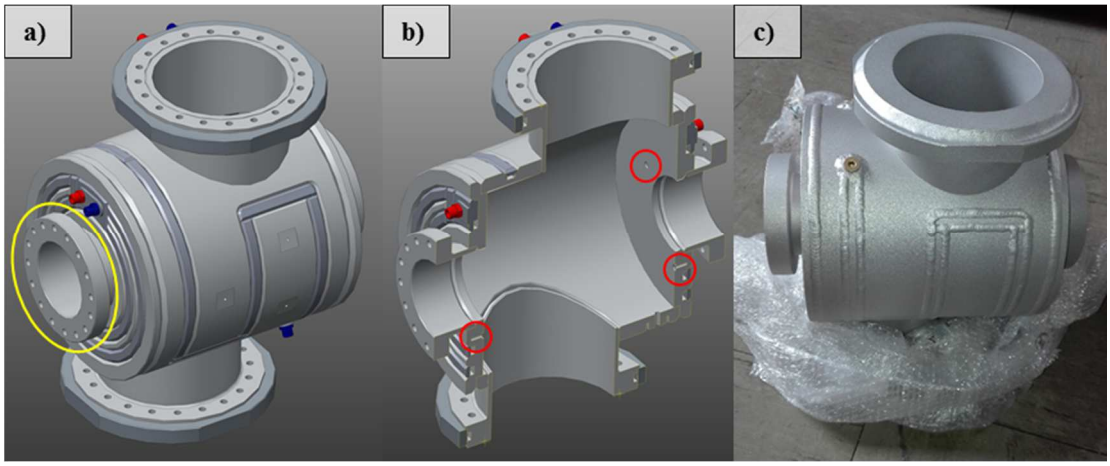

Fig. 3.30. Final mechanical design of the water-cooled diagnostic cross for the proton beam line.

3.4. Design and test of the PB Beam Profiler

3.4.1. Preliminary description

A beam profiler is a device which is able to determine the beam profile of a beam. Depending on the cases, the work principle and the type can be very different as it was already reported in 3.1. In particular, for the proton beam deliverable to the bunker, two types are the most used:

- Harp beam profiler
- Wire scanner

In both the devices, the mechanism to dissipate the huge beam power is by radiation and, consequently, the can reach very high temperature (order of 2000°C).

For the dedicated case, the scattering of the particle impinging the wires are not such an important problem as in a synchrotron accelerator. After some discussions, even if the number of components is higher and the design of the overall assembly could be more complicated, the harp type been profiler has been chosen because:

- Can be very compact and the space available on the diagnostic cross is enough to measure both the x and y plane
- The electronic necessary to control and to process the measures has been already developed and it is currently operating since it can be used the same of the RIB beam profilers

Usually such type of devices are made of wires in tungsten due to:

- Stability at high temperatures without an excessive grain enlargement
- Higher emissivity compared with other refractory metals
- Low expansion modulus
- High rigidity
- Metallic properties (not fragile)

In particular, the last one is very important. In fact, the most performing beam profilers are made of graphite or carbon wires, which are obvious more fragile. In this case, there was not such a need. The major problem to deal with was essentially the presence of devices, like the Faraday cup and collimators, at high temperatures, and the very small dimensions available for the system.

3.4.2. An analytical description of the main properties of the Beam Profiler

Concerning the first dimensioning, some analytical expression can well reproduce the working conditions of the wires. Using the code SRIM, already presented in 2.2.1, it is possible to evaluate the energy deposited on a determined thickness of tungsten, indicated as E_{T_W}. Since the wire has a circular section, the energy has to be corrected multiply by the ratio between a circular area and a square area. Finally, the factor of power *g* released in the wire can be calculated with:

$$g = \frac{E_{T\_W}}{E_0} \cdot \frac{\pi}{4} = f \cdot \frac{\pi}{4} \qquad (3.6)$$

Where E_0 is the initial proton energy. Finally, assuming a Gaussian profile wobbled around its axis, the mean power can be calculated with (1.4). An important simplification can be adopted using a standard Gaussian profile (not wobbled) since the maximum power density that is presented in the beam axis (r = 0) can be calculated with (3.8).

$$p(x,y) = \frac{P}{2\pi\sigma^2} \cdot exp\left(-\frac{x^2+y^2}{2\sigma^2}\right) \qquad (3.7)$$

$$p_{MAX} = p(0,0) = \frac{P_{TOT}}{2\pi\sigma^2} \tag{3.8}$$

Where P_{TOT} is the total power of the beam without collimations, σ the RMS radius and p the surface power density. The power dq released in an infinitesimal piece of wire dl can be calculated with:

$$dq = p \cdot g \cdot 2r \cdot dl \tag{3.9}$$

Where p is the density of power calculated with (3.7). Assuming the heat emission to an open space ($r_1/r_2 \approx 0$), equation (3.2) is simplified as

$$dq = 2\pi r\varepsilon\,\sigma \cdot \left(T^4 - {T_0}^4\right) dl \tag{3.10}$$

Where σ_B is the Stephan-Boltzmann constant, r and T respectively the wire radius and temperature, T_0 the environmental temperature and ε the surface emissivity. Finally, assuming that radiation is the only method responsible of the beam power dissipation, the maximum temperature T_{MAX} of the wire impinged by the beam is:

$$T(x,y) = \sqrt[4]{\frac{p(x,y)}{\pi\sigma_B\varepsilon}g + {T_0}^4} = \sqrt[4]{\frac{p(x,y)}{4\sigma_B\varepsilon}\cdot f + {T_0}^4} \tag{3.11}$$

$$T_{MAX} = \sqrt[4]{\frac{p_{MAX}}{4\sigma_B\varepsilon}\cdot f + {T_0}^4} = \sqrt[4]{\frac{P_{TOT}}{8\pi\sigma^2\sigma_B\varepsilon}\cdot f + {T_0}^4} \tag{3.12}$$

If T is high (due to high P_{TOT} or small σ), T_0 is negligible as presented in 3.3.1 and the maximum temperature T of the wire impinged by the beam is:

$$T(x,y) = \sqrt[4]{\frac{p(x,y)}{4\sigma_B\varepsilon}\cdot f} \tag{3.13}$$

$$T_{MAX} = \sqrt[4]{\frac{P_{TOT}}{8\pi\sigma^2\sigma_B\varepsilon}\cdot f} \tag{3.14}$$

The description of the factor f, which is the power ratio between the energy released on a certain thickness and the beam energy, is fundamental in order to estimate the temperature. Its value, for the tungsten, is evaluated in Fig. 3.31 using the code SRIM. It was also possible to estimate it by the integral of a proton stopping power in the tungsten.

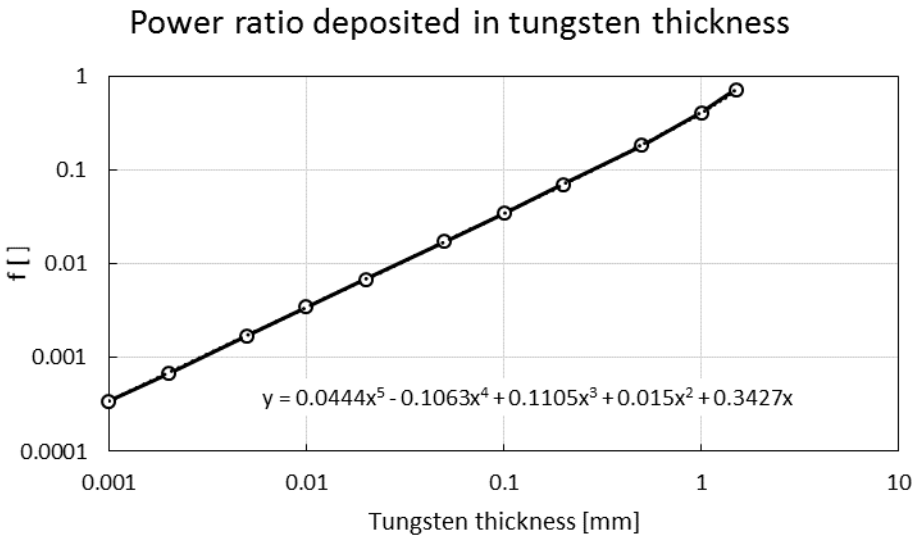

Fig. 3.31. Evaluation of the power ratio released in a certain tungsten thickness.

At low wires thickness, the energy released in the wire is almost proportional to the thickness. In fact is the only parameters of (3.13) related to the geometry: smaller is the wire radius, lower is the temperature. From the beam characteristics of Fig. 2.9 that could be delivered to the target, the beam of σ_{RMS} = 10.2 mm without wobbling will be analysed since it has the highest peak of power surface density and, consequently, the highest temperatures. As for the Proton Beam Faraday Cup and collimators, the RMS radius will be scaled of a factor 0.8, ratio between collimator diameter (32 mm) and target diameter (40 mm). For a beam of 8 kW to the target, P_{TOT} is 9.4 kW (as showed in paragraph 3.2, the collimators absorb about 1.4 kW during nominal operation). The maximum temperature calculated in the wire is showed in Fig. 3.32.

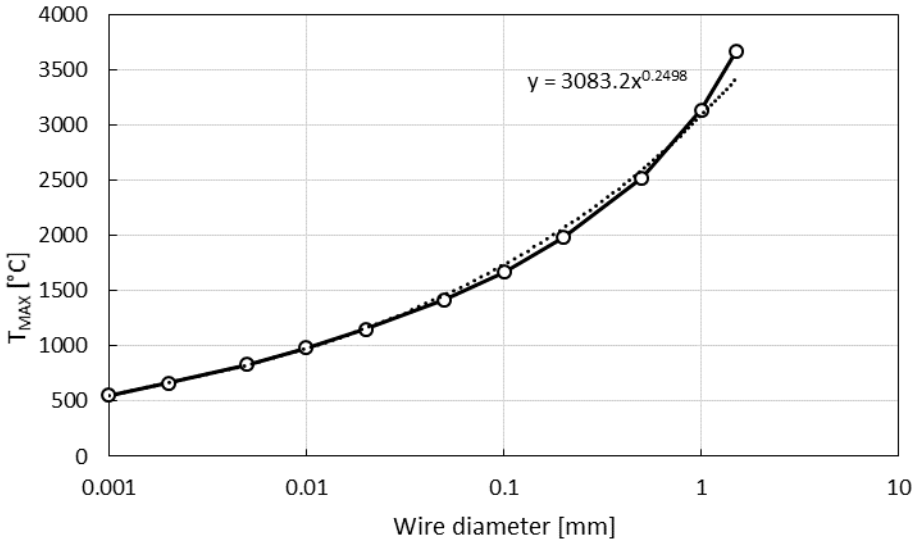

Fig. 3.32. Maximum temperature for different wire diameters for a 8 kW, 10.2 mm RMS radius proton beam delivered to the target.

Assuming that the wire disposes heat just by radiation (almost true at high temperatures), the temperature distribution is not influenced by conduction. For this reason, the temperature profile can be estimate by equations (3.7) and (3.13), which gives:

$$T(x,y) = \sqrt[4]{\frac{p(x,y)}{4\sigma_B \varepsilon} \cdot f + {T_0}^4} = \sqrt[4]{\frac{P_{TOT}}{8\pi\sigma^2\sigma_B\varepsilon} \cdot f \cdot exp\left(-\frac{x^2+y^2}{2\sigma^2}\right) + {T_0}^4} \qquad (3.15)$$

$$T(x,y) = \sqrt[4]{\frac{P_{TOT}}{8\pi\sigma^2\sigma_B\varepsilon} \cdot f} \cdot exp\left(-\frac{x^2+y^2}{8\sigma^2}\right) \quad if \;\; T_0 \approx 0 \qquad (3.16)$$

The hottest wire is in the central position (higher power density) and we can get the temperature profile on the x axis (y = 0):

$$T(x) = \sqrt[4]{\frac{p(x,0)}{4\sigma_B \varepsilon} \cdot f + {T_0}^4} = \sqrt[4]{\frac{P_{TOT}}{8\pi\sigma^2\sigma_B\varepsilon} \cdot f \cdot exp\left(-\frac{x^2}{2\sigma^2}\right) + {T_0}^4} \qquad (3.17)$$

$$T(x) = \sqrt[4]{\frac{P_{TOT}}{8\pi\sigma^2\sigma_B\varepsilon} \cdot f} \cdot exp\left(-\frac{x^2}{8\sigma^2}\right) \qquad (3.18)$$

The increase of the temperature produces the elongation of the wire, which is fundamental to evaluate in order to avoid wire bending during operation. The ΔL elongation of a length L is:

$$\Delta L = \alpha L \Delta T = \alpha L (T - T_0) \qquad (3.19)$$

Where ΔT is the increment of temperature (T final temperature, T_0 initial temperature) and α the expansion coefficient. So the elongation can be calculated with:

$$\Delta L = \int_{-\frac{L}{2}}^{\frac{L}{2}} \alpha (T - T_0) dx \qquad (3.20)$$

A very important simplification is assuming α and ε constant. In particular α can be moved out of the integral and a constant emissivity transforms the function to Gaussian. It is underline that the tungsten emissivity doubles passing from 1000°C to 2000°C. With this assumption:

$$\Delta L = \alpha \int_{-\frac{L}{2}}^{\frac{L}{2}} T dx - \alpha \int_{-\frac{L}{2}}^{\frac{L}{2}} T_0 dx = \alpha \left(\sqrt[4]{\frac{P_{TOT}}{8\pi\sigma^2\sigma_B\varepsilon} \cdot f} \cdot 2\sqrt{2\pi}\sigma - T_0 \cdot L \right) \qquad (3.21)$$

$$= \alpha \left(T_{MAX} \cdot 2\sqrt{2\pi}\sigma - T_0 \cdot L \right)$$

Where

$$\int_{-\frac{L}{2}}^{\frac{L}{2}} exp\left(-\frac{x^2}{8\sigma^2}\right) dx \approx 2\sqrt{2\pi}\sigma \qquad if \; L > 6\sigma \qquad (3.22)$$

(3.21) is a very simple equation that can easily estimate the elongation of the wire. It is better to remember that T_{MAX} was obtained assuming T_0 null (true if $T >> T_0$). At distances x>L the

power deposited is almost null and the temperature according to (3.21) will be almost zero Kelvin, consequently the hypothesis $T >> T_0$ is not more true. For this reason, even if $L>6\sigma$, the L value to insert is anyway 6σ because in the external region, the temperature is almost the ambient temperature. Then, if this elongation is not compensated, it provokes a deviation of the wire that can be calculated thinking that it deflects as in Fig. 3.33. The case *a* in Fig. 3.33a is easier to calculate but probably less accurate, whereas the second is represented by an equation that needs to be numerically solved. For both of them, the results are presented in Fig. 3.34 for a wire length of 70 mm.

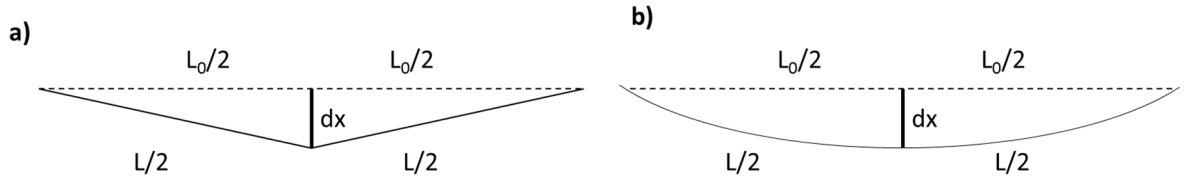

Fig. 3.33. Two different models in order to evaluate the deviation of the wire

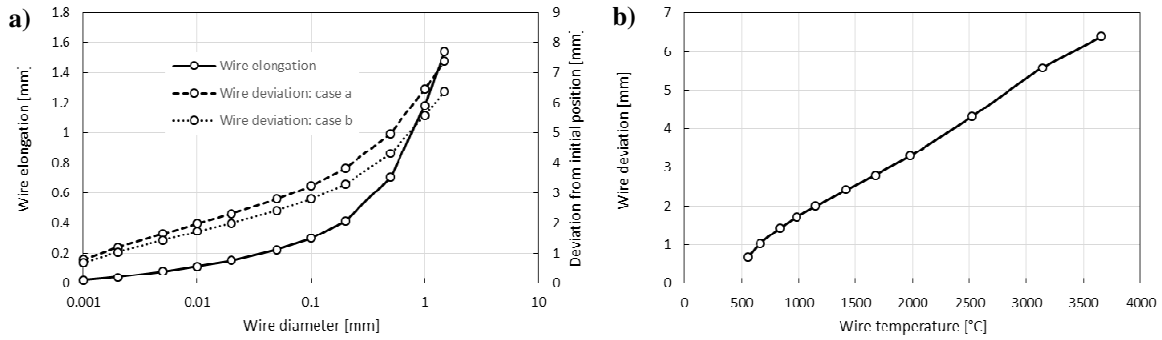

Fig. 3.34. a) Wire elongation and deviation for different wire diameters; b) wire deviation versus temperature

It is clear that, even for a very small wire elongation, the deflection is very important. Anyway, as a first results, the wire deviation from the initial position calculated in the first case is accurate enough.

In order to dimension the wire diameter, the temperature has to be maintained as low as possible to reduce creep and material evaporation: indeed the beam profiler, when is used, is continuously impinged by the proton beam. On the other hand, very small wire diameters are difficult to handle and assembly. A good approximation is a wire diameter of 50 μm because the maximum temperature is around 1400°C, which seems the value limit after that a decrease of the creep resistance of the tungsten [3.17] is showed. Table 19 summarizes the results.

Wire diameter	50 μm
Power ratio deposited (f)	0.0172 [ ]
Maximum temperature (T_{MAX})	1421°C
Maximum elongation	0.22 mm

Table 19. Wire parameters for the proton Beam Profiler

In order to maintain the wire tension, two springs are foreseen at each side of the wires. The choice was the spring CIM010ZD 04S of Lee Spring which properties are presented in Table 20. The compression of each spring has been fixed to 1.1 mm, for a total stroke of 2.2 mm. The tension in the tungsten wire is calculated about 75 MPa without taking into account any friction in the system.

Code	CIM010ZD 04S
External diameter	0.889 mm
To work in hole diameter	1.10 mm
Spring wire diameter	0.101 mm
To work over rod diameter	0.50 mm
Free length	4.597 mm
Minimum length (block)	1.549 mm
Spring rate	0.13 N/mm
Maximum force (at block)	0.413 N
Material	AISI302

Table 20. Properties of the chosen spring.

3.4.3. The mechanical design

The first Beam Profiler part to take into account is the wire system of tensioning that is represented in Fig. 3.35. In particular, during the assembly, the wire has to be previously clamped by two stainless steel capillary tubes. This process is fundamental in order to give the correct tension to the wire. Then the wires will be welded by tin to a PCB, in order to take out the signal.

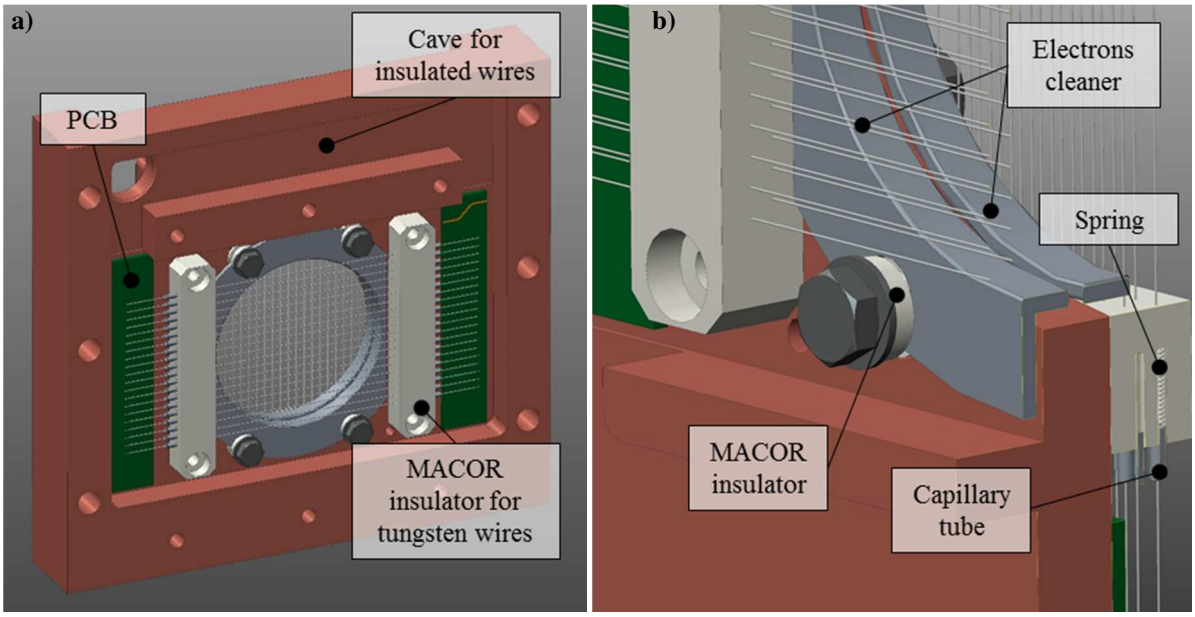

Fig. 3.35. a) wire system tensioning system; b) particular of the spring seat and the metallic cylinders for the electric field clearing

After, the system assembly will be installed as in Fig. 3.36. In particular, the front view can be observed in Fig. 3.36a with two stainless steel flexible pipes that are easier to be assembled and allow the movement of the system. The wire assembly, showed before, is housed between two copper blocks. In the front side, the first block looks the graphite collimators about 100 mm far from it, whereas the second one, on the back, has the hot Faraday cup very close to it (7 mm). For this reason, this part is water-cooled. A very important aspect is that the water connection are placed in the air side, consequently a leakage of water can not compromise the vacuum and the safety of the system. A tantalum screen shields the edge-welded bellow and an aluminium tube where the Kapton wires, coming from the PCB, are housed. The thermal simulations describing the proton beam profiler are presented in paragraph 3.4.6.

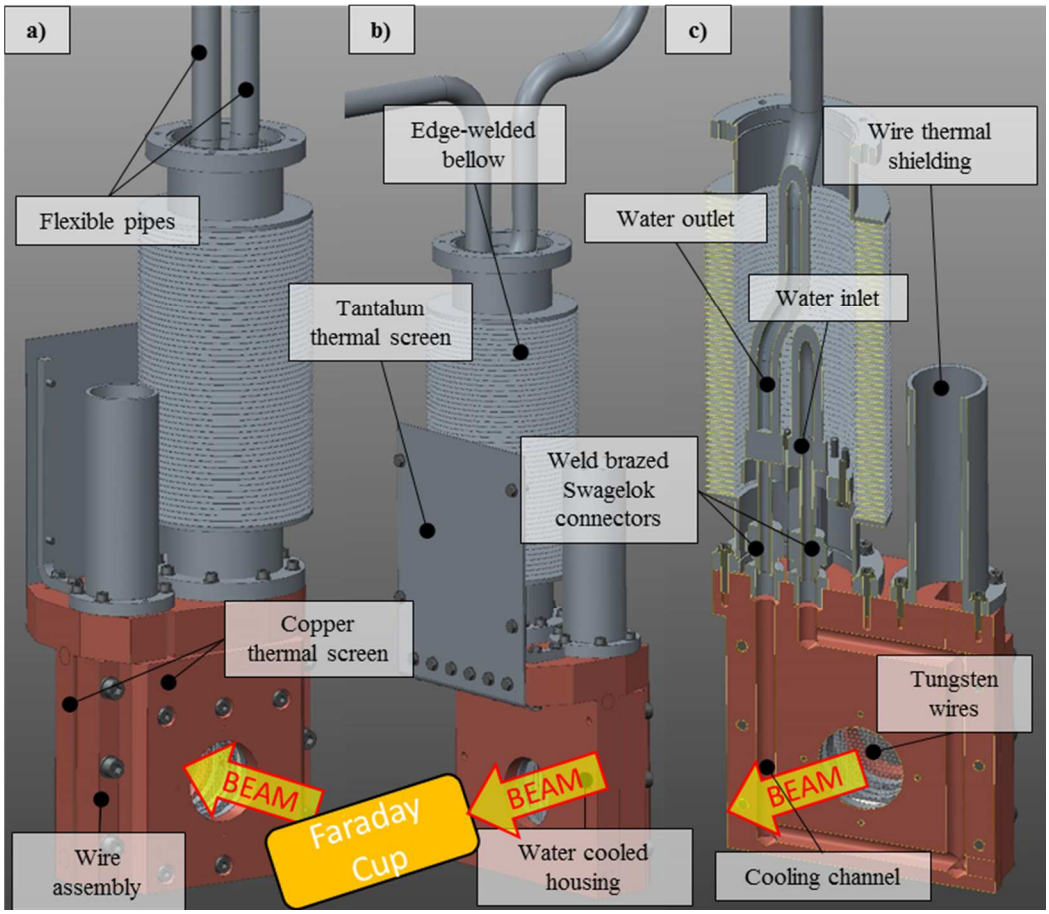

Fig. 3.36. Wire assembly mounted to complete the beam profiler: a) beam profiler front view; b) beam profiler back view; c) section of beam profiler back view

3.4.4. Thermal simulations of the wire tensioning system

A wide description of the temperature distribution has been presented before in 3.4.2. In this paragraph, the previous results will be analysed in more detail. In particular, the wire connection and the PCB temperature will be taken into account.

In order to reduce the number of elements, only half of the CAD model has been imported in the FEA. A volume heat generation depending on the beam axis distance has been implemented in order to simulate the 8.16 mm RMS radius Gaussian profile, corresponding to a 10.2 mm RMS radius at the target. In particular, the beam power has been deposited only on a 32 mm diameter, corresponding to the diameter of the collimator.

The welding of the wire on the PCB has been simulated, assuming a release of 0.2x0.5x1 mm lead block. The PCB tracks has not been taken into account, but they will surely decreases the temperatures. The PCB material, after some iterations, has been fixed to polyimide Kapton® of DuPont™ [3.18], which main properties are presented in Table 21. In the simulation, a 2 mm thick PCB has been assumed, which is a value quite high for this device.

The wire length is 80 mm and the environmental temperature has been fixed to 50°C. The picture is presented in Fig. 3.37.

Tensile modulus	3172 Mpa
Poisson's ratio	0.34
Density	1.42 g/cm^3
Conductive heat coefficient	0.12 W m^{-1} K^{-1}
Coefficient of linear expansion (30-100°C)	17 ppm °C^{-1}
Coefficient of linear expansion (100-200°C)	34 ppm °C^{-1}
Specific heat	1090 J kg^{-1} °C^{-1}

Table 21. Main properties of DuPont™ Kapton® [3.18].

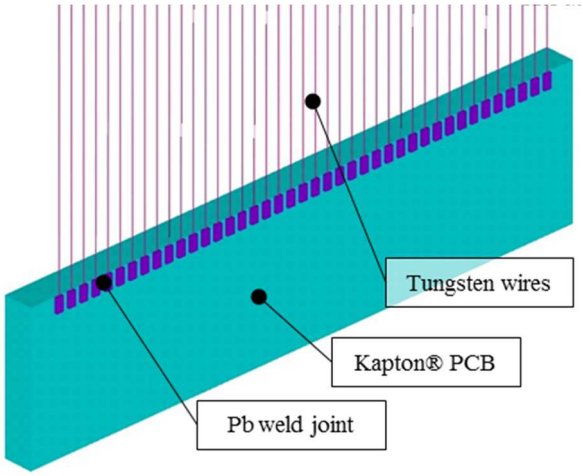

Fig. 3.37. Volumes with the different materials of the FEA analysis

Two aspects of the results has to be analysed. The first one concerns the wire temperature (Fig. 3.38) which can be compared with the various model implemented. In particular, the results of the various equations are compared in Fig. 3.39 with the FEA results.

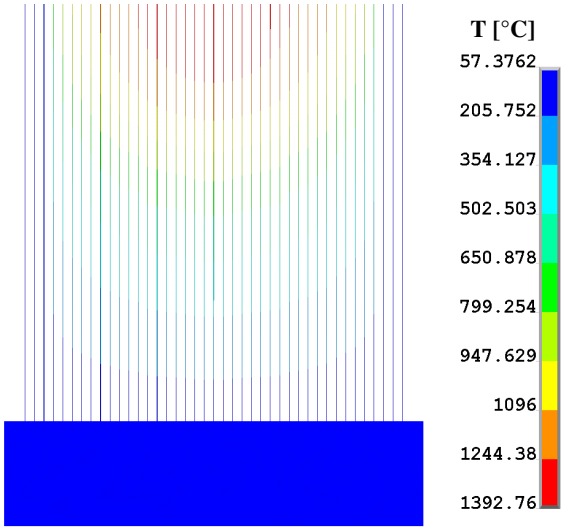

Fig. 3.38. Thermal distribution on the tungsten wires

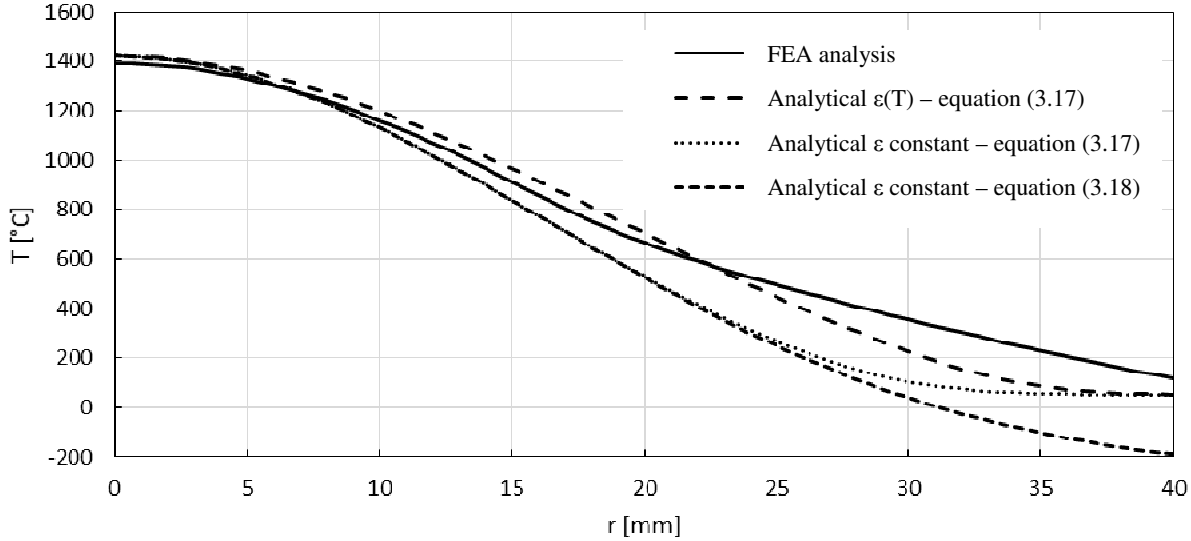

Fig. 3.39. Comparison between various results of the temperature wire distribution

The maximum temperatures calculated analytically are all very close to the FEA analysis as expected. The differences start to appear at a distance of about 1 σ from the centre axis, in particular the last two trends are the most different from the FEA results. This is due to the ε value assumed constant. Then simplification of assuming $T_0 \approx 0°C$ of equation (3.18) starts to be wrong at a distance of about 2.5 σ from the centre axis, where the temperature is less than 250°C. Finally, the most complete analytical curve (second) is very close to the FEA results. At a position of about 2.5 σ from the centre axis, the distance with the first curve starts to increase, probably due to the conductive effect which maintains the wire warm even without any power deposition (after 16 mm in the FEA analysis there was no power deposited as mentioned before). From the slope of the FEA analysis curve, the heat power flowing along the last part of the wire has been calculated to be about 7 mW, which is a very small value, but quite high for the wire dimension. Anyhow, in this zone, the conduction can not surely be neglected even if its cooling effect is small.

The elongation of the wire has been numerically calculated with (3.19) for the first three curves, whereas for the last (3.21) was directly used. The results are showed in Table 22.

Case	Elongation [mm]
FEA analysis	0.299
Analytical ε(T) – equation (3.17)	0.292
Analytical ε, α constant – equation (3.17)	0.269
Analytical ε, α constant – equation (3.18) + (3.21); L = 80 mm	0.248
Analytical ε, α constant – equation (3.18) + (3.21); L = 6σ	0.306

Table 22. Elongation calculated with the various cases

The results are all very close, except the (3.21) equation with L=80 mm: at distances from the centre axis higher than 30 mm (≈ 4σ), the temperature is lower than 0°C, which is less than

the initial temperature. According to this equation, here the wire shrinks and it is irrational. For this reason, as already said, in the formula a good solution is to reduce the maximum wire length to 6σ, where theoretically there is still there is a small quantity of beam power dropped. It is underlined that it was expected just the same order of magnitude, not such a good according between the cases that is probably due to the chance: the assumption of α constant at the highest values compensates the lower temperatures at high radius.

The second results to discuss are the temperature increase due to heat coming from the wires. Even if the amount of power is very small (7 mW), the poor conductivity of Kapton and in general, of polymers and insulating materials, causes a considerable increment of temperature, as it is showed in Fig. 3.40. The maximum increment of temperature is approximately 60°C, from 60°C to 120°C. The copper tracks will probably decrease the maximum temperature for the high conductivity of copper that can spread the heat in a higher surface. These results will be used later in the paragraph 3.4.6 where the overall beam profiler assembly is simulated.

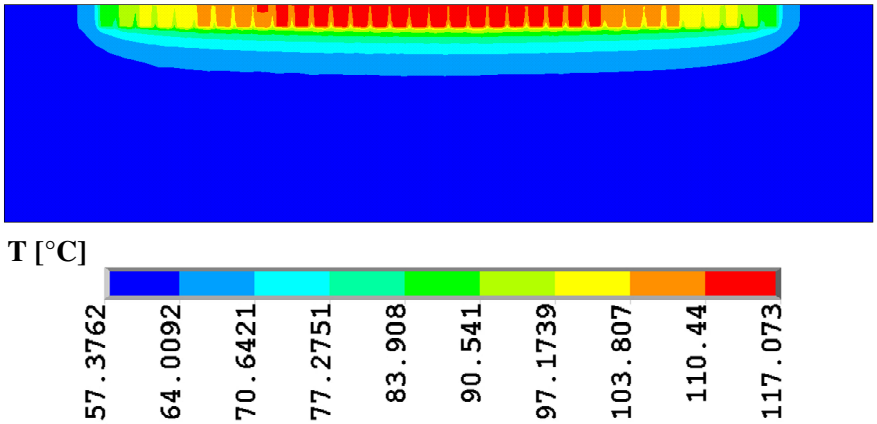

Fig. 3.40. Thermal results on the PCB

3.4.5. Experimental test of the wire tensioning system

The feasibility of the wire tensioning system design has been tested. The only wire available was made in Molybdenum, which is a refractory material more brittle at high temperatures than tungsten. The two concerns were the precision of blocking the wires to the correct length and the ability of the spring to maintain the tension of the wires at high temperatures. In particular, the wire tension could decrease for the friction between the MACOR, the capillary tube and the spring. At the beginning, the assembly precision has been tested and an example is presented in Fig. 3.41. The goal was to block the wire pressing the two capillary tubes to get a distance of 40 mm and the result was here acceptable. Some other tests have been performed and they shows the necessity to have an objective way to apply the correct force to squash the

capillary tubes. The interface between the capillary tube and the wire was so good that during a tension test, the wire rupture happens before the slipping of the interfaces.

Fig. 3.41. a) Example of the capillary tube with a 50 µm diameter wire; b) test of the wire block precision.

The second test concerns the ability of the system to compensate the wire elongation. For this part, copper capillary tubes have been used because there was not the availability of the stainless steel version. The interface force between the copper capillary tube and the wire is not so high as for the stainless steel because the interface slipping between the wire and the tube appears before its rupture.

In order to estimate the current needed to reach a determined temperature, the combination of (3.10) and (3.23) produces equation (3.24). This is the analytical formula to get the wire temperature with a circle section of r radius, emissivity and resistivity respectively ε and ρ, heated by an electric current I and a negligible environmental temperature ($T_0 \approx 0$ K).

$$dq = dR \cdot I^2 = \rho \frac{4I^2}{\pi r^2} dl \tag{3.23}$$

$$T = \sqrt[4]{\frac{1}{2\pi^2 \sigma_B} \cdot \frac{\rho}{\varepsilon} \cdot \frac{I^2}{r^3}} \tag{3.24}$$

To reach a temperature of about 2000°C, a current of 0.44 A has to be provided. The test setup is presented in Fig. 3.42, but it was not possible to measure the wire temperature due to the very small emitting surface.

The tests was divided in two parts: a continuous heating of the wire for about 16 hours divided in two days during which no evidences of damage appeared, then a cycles of turn on and off every 2 seconds to simulate the discontinuous use of the beam profile. It has to be underline that this test is graver than the operational conditions with proton beam because: the

maximum temperatures are much lower (2000°C instead of 1400°C) and, during the test, the overall wire is heated (see in Fig. 3.43). The last aspect is very important because at the connection, the heat can be transferred to the capillary tube and to the spring and this is probably the reason of the failure obtained after 7000 cycles: at this value, the deflection of the wire appears as it is possible to see in Fig. 3.44. At the aperture of the vacuum chamber, the wire was so fragile that it broke in a lot of pieces. It is surely due to the high temperatures, about 2000°C, that are not fully sustainable by molybdenum.

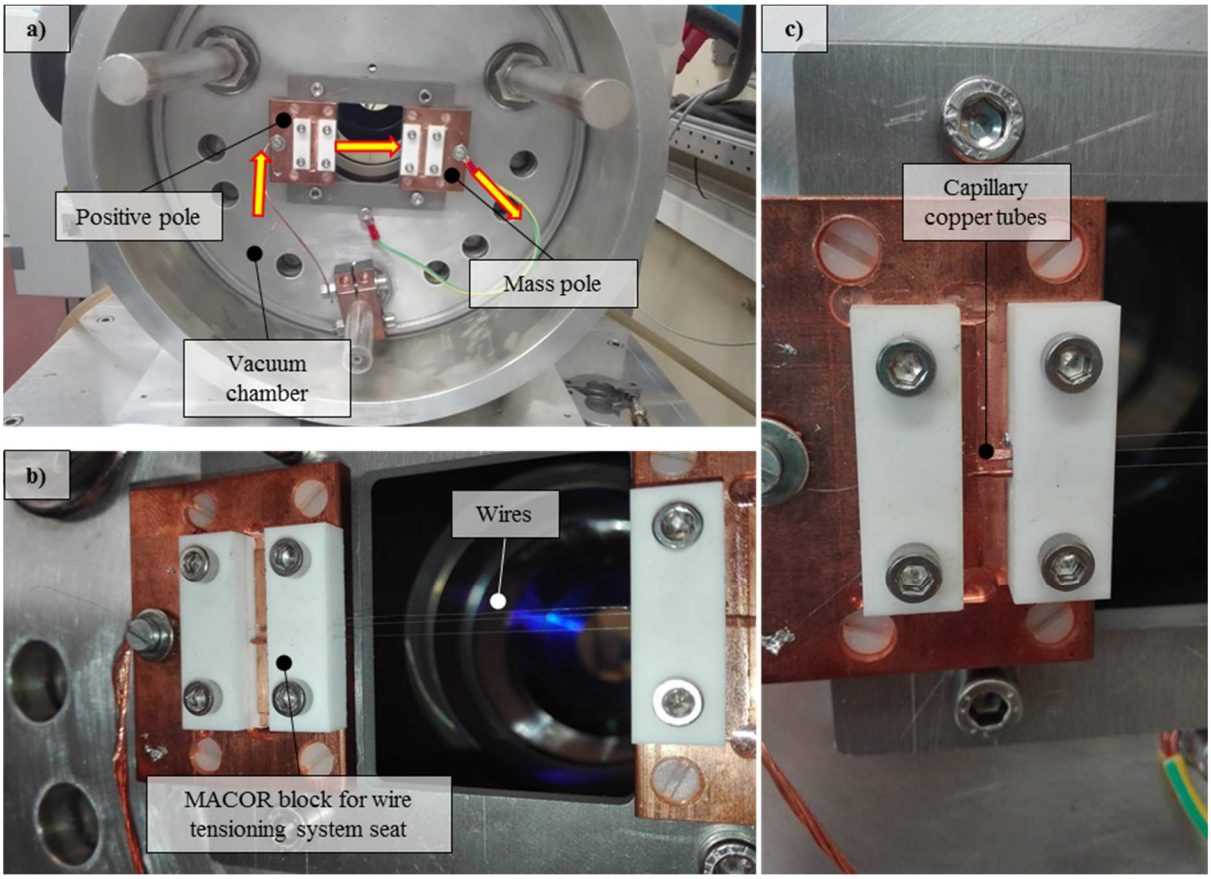

Fig. 3.42. Setup to test the wire tensioning system at high temperature.

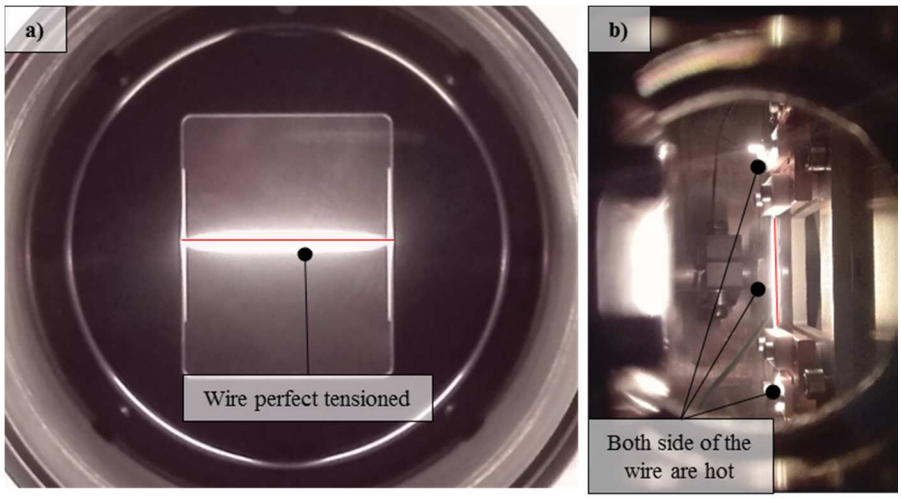

Fig. 3.43. Wire at high temperature during continuous operation. No bending on the wire are observable.

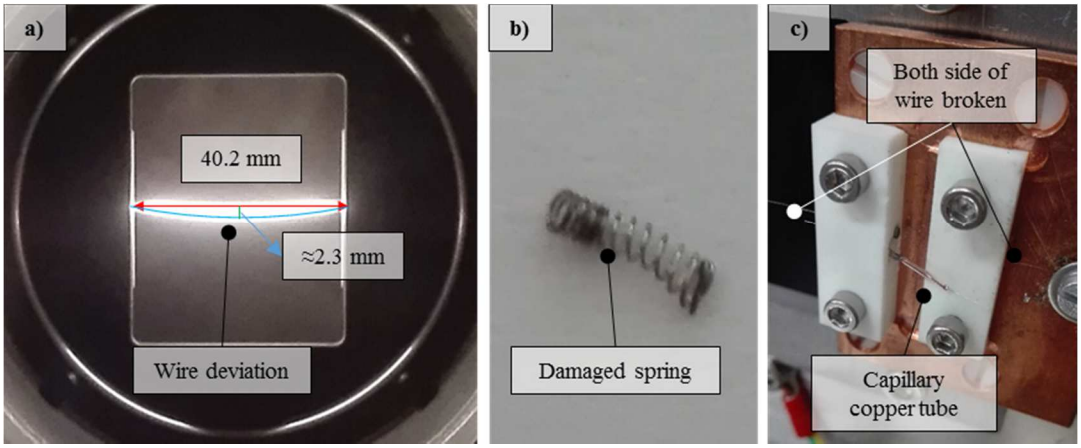

Fig. 3.44. a) bending of the wire at the end of the test; b) Damaged spring probably due to the high temperatures; c) unmounting process. The wire was so brittle that minimum movements broke it.

The SEM confirms that the material was pure molybdenum thanks to the analysis of the photon energy spectra emitted by the electron bombardment of the components. The pictures of the original and heated wire are presented in Fig. 3.45. It is very clear the grain coarsening of the heated wire, which causes the fragility, appears at the vacuum chamber aperture. Moreover, the diameter of the wire decrease of about 1.1 μm due to the evaporated material for the high temperatures.

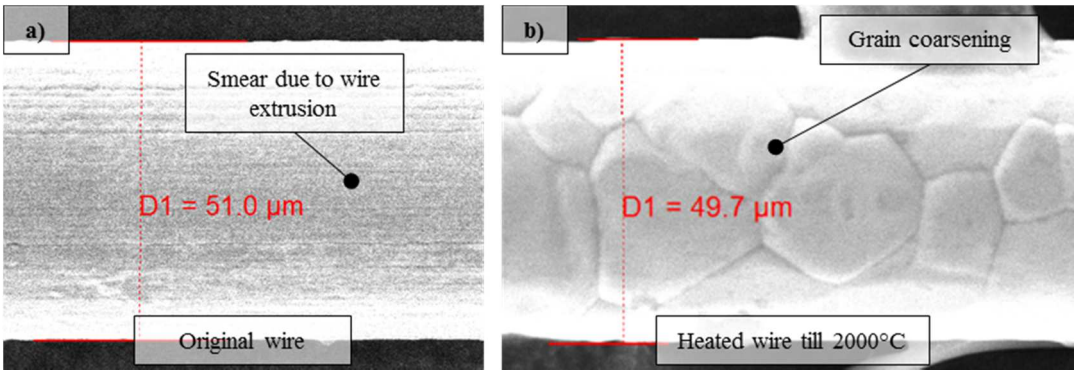

Fig. 3.45. Original and heated molybdenum wires.

Unfortunately, there were not availability of tungsten wire to repeat the test. Anyway, it was successful because it clearly shows the ability of the wire tensioning system to maintain the wire tension. Moreover, it was showed that copper capillary tubes, already available, can be used instead of stainless steel, which are more difficult to produce and to assembly.

3.4.6. Thermal simulations of the overall device

Many efforts have been spent to integrate the proton beam profiler in the actual version of the protonic diagnostic vacuum chamber. In fact, this component was the last element designed and it had to respect the constraints given by the other devices. In particular, two aspects were very restrictive:

- Very few space available in the diagnostic
- The hot Faraday cup close to it

The most problematic components are:

- The PCB used to connect the tungsten wires to the cable signals (T_{MAX} = 120-200°C) according to different materials
- The signal wires in the vacuum zone (T_{MAX} = 150-250°C) according to different materials
- The edge-welded bellow (T_{MAX} = 420°C)
- The metallic seals on the flanges (T_{MAX} = 100-150°C) according to different materials

In particular, the PCB temperature is the most limiting factor. Moreover, due to the very low material conductivity, it has to be conveniently shielded from the heat radiation of the hot Faraday cup. For this reason, it has been surrounded by copper, which can efficiently remove the heat. This was the first step taken into account in the design phases.

The hemispherical total emissivity of pure cleaned copper at 100°C is about 0.03, but this value is surely increased by the dirtiness that can deposit on it that, consequently, rises the heat absorbed by the beam profiler. Some measurements have been done on a copper connection in Fig. 3.46 that supported for many runs the SPES target heated by joule effect. The emissivity read by the thermal imaging camera IRISYS Multi-Purpose Thermal Imagers IRI 4000 Series was in the range of 0.3-0.5 for temperatures of 60-140°C, as it is showed in Fig. 3.47. Moreover, graphite, the material composing the hot FC close to the BP, is a very porous material and can release outgassing and impurities due to the production and manufacturing process [3.19] and even carbon atoms due to sublimation [3.20]. During the design phase, a very precautionary

emissivity of 0.8 has been assigned to all the components which could negatively increase the temperature.

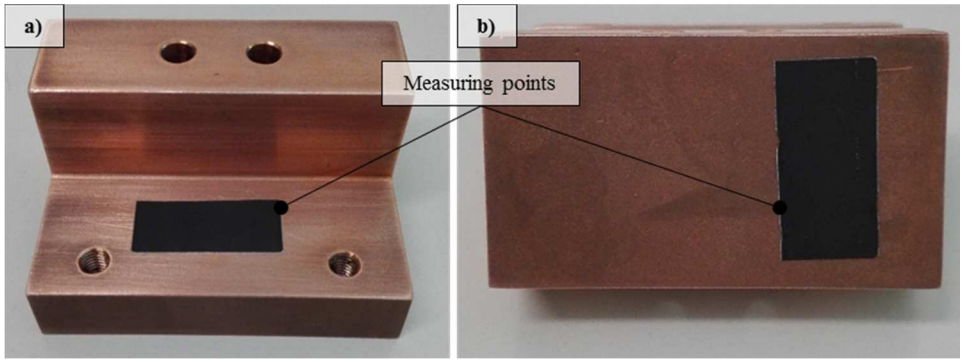

Fig. 3.46. Measuring point of a copper components.

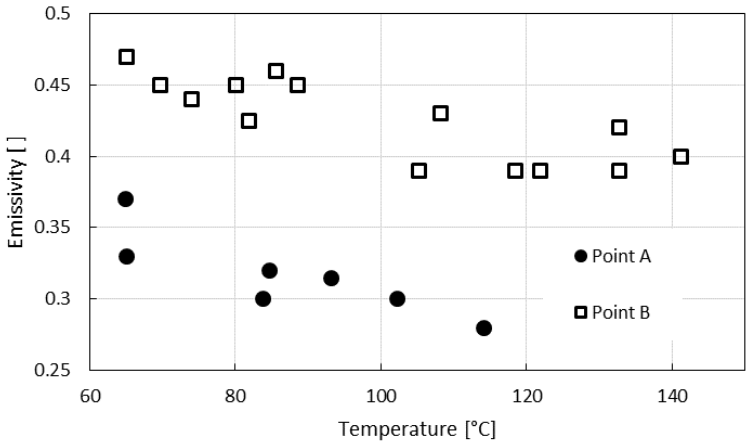

Fig. 3.47. Emissivity measured on the copper connectors.

P [kW]	3	Estimated power on BP
T_i [°C]	15	Inlet water temperature
T_f [°C]	28	Outlet water temperature
v [m/s]	1.1	Speed of water
Q [l/h]	200	Water flow rate
A [mm2]	50	Section Area
d [mm]	8	Section diameter

Table 23. Design parameters for the water-cooling circuit of the Beam Profiler.

The consequent values for the cooling process are presented in Table 24.

Re [ ]	8820	Reynold number
Pr [ ]	6.94	Prandtl number
Nu [ ]	75.0	Nusselt number
α [W/m^2]	5500	Convection coefficient

Table 24. Water-cooling parameters for the Beam Profiler.

The same simulation used for the FC of the paragraph 3.3.5 has been implemented inserting the beam profiler geometry. The wires have not been simulated since the effect on the thermal distribution is surely negligible, except for the temperature increment on the PCB which has already evaluated in paragraph 3.4.4. The edge-welded bellow has been simulated with a straight tube of 0.14 mm. This is a strong simplification, but a more precise effect on the thermal distribution will be presented later in this paragraph. A temperature of 28°C and a 5500 W/m^2 convection coefficient have been assigned to the BP water cooling circuit which has been simplified by 5 separated tubes. The results are presented in Fig. 3.48.

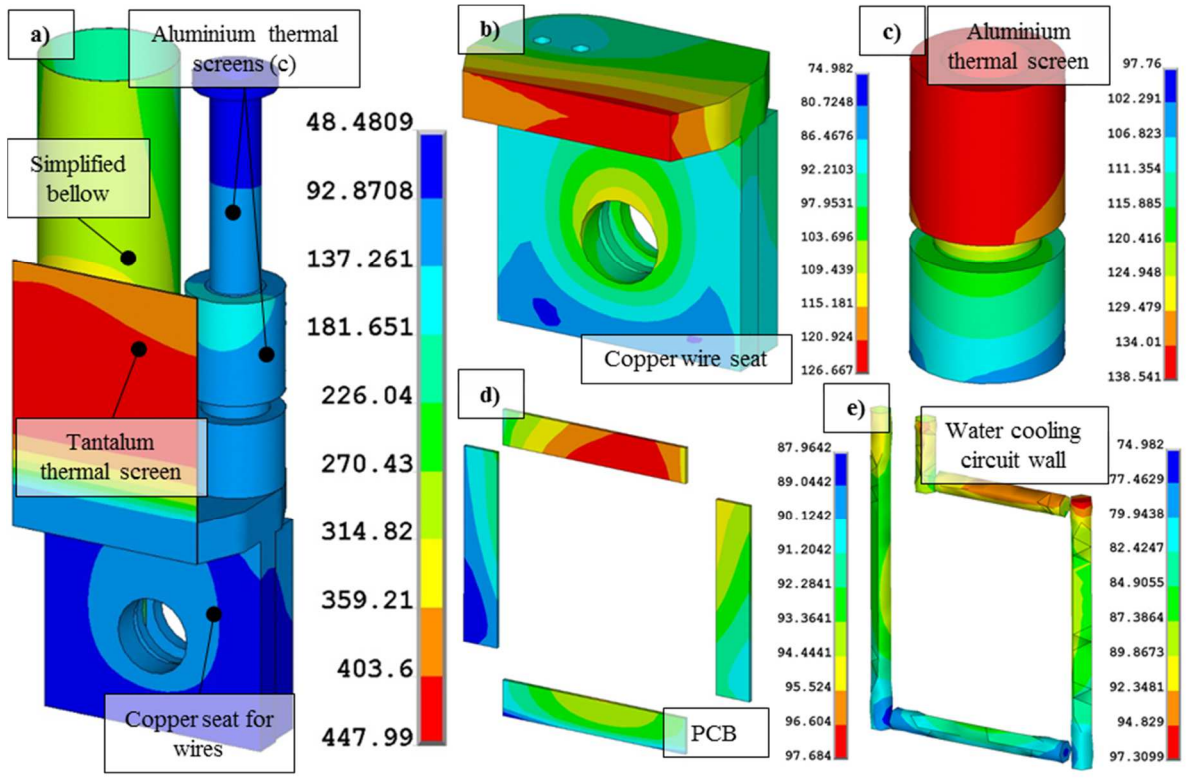

Fig. 3.48. Temperature distribution [°C] on the BP: a) all components in vacuum; b) copper seat; c) aluminium thermal screen; d) PCB; e) BP water cooling circuit walls.

Analysing the thermal distribution, the temperature on the copper seat is quite high, over 100°C, which could provokes some problems on the PCB. These components are also subject to the increment of temperature due to the heat coming from the wires; the final temperature has been evaluated to be about 160°C that is not bearable by standard PCB (in epoxy), but only by dedicated material like PEEK or Kapton.

The aluminium thermal screen, in Fig. 3.48c, has a maximum temperature of about 140°C. Kapton wires are suggested but experimental tests have to be carried out in order to confirm the feasibility of the design: in fact, Kapton insulator are quite rigid and they could be damaged by the insertion of the BP. A backup solution is the use of PUR (polyurethane), which can sustain a continuous temperature of 155°C.

The temperature on the water cooling circuit walls is few degrees below the water boiling temperature at one atmosphere. Moreover, a simulation with a 4500 W/m^2 convection coefficient foresees a maximum temperature of 110°C. A minimum water pressure of about 4-5 bar has to be provided in order to avoid bubble formation in it.

The various results, with different surfaces emissivity and water convection coefficients, are presented in Table 25.

Emissivity [ ]	Water convection coefficient [W m^{-2} K^{-1}]	PCB [°C]	Simplified bellow [°C]	Wire tensioning system in MACOR [°C]	Aluminium thermal screen [°C]	Maximum water cooling wall [°C]
0.8	4500	111	408	265	151	111
0.8	5500	98	406	253	139	97
0.5	5500	82	423	351	115	81
0.3	5500	68	428	450	92	66

Table 25. Summarize of the Beam Profiler temperatures of the most delicate components.

Finally, the temperature of the edge-welded bellow has been better evaluated. For this reason, dedicated simulations have been implemented with a simplified geometry, removing all the components excepted the bellow, the Faraday cup which provides heat by radiation, and the BP copper water cooled seat. The study was interesting because it is difficult to find some information in literature about the radiation heat effect on an edge welded bellow. First, the correct thickness of the bellow was simulated, which is 0.1 mm instead of 0.14 mm. Then, the variation of the bellow convolutions has been implemented (the convolution are the number of welded annulus that allows the axial dimension expansion or contraction). Therefore, the effect of the emissivity on the temperature distribution has been evaluated. The geometry with boundary condition and the results for a various emissivities, 50 convolutions (maximum number) and 0.1 mm thickness are presented in Table 26 and Fig. 3.49.

Convolutions	Thickness [mm]	ε [ ]	TMAX [°C]	Case
0	0.1	0.8	342	a
0	0.14	0.8	330	
10	0.1	0.8	321	b
20	0.1	0.8	304	c
50	0.1	0.8	278	d
50	0.1	0.5	253	
50	0.1	0.3	239	e

Table 26. Summarize of the results for the thermal distribution of the edge-welded bellow.

If in Fig. 3.48 the bellow temperature was about 410°C, without all the elements the temperature drops at 340°C, probably due to the reflection at the internal surfaces of the proton

beam diagnostic. Anyway, the increase of the bellow convolution in the mesh decreases the temperature due to the decrease of the power surface density. In particular, the differences between the most simplified case (a) and the real one (d) is about 60°C. Finally, the decrease of the emissivity from 0.8 (d) to 0.3 (e) decreases the temperature of 40°C. In conclusion, the maximum temperature of the bellow, estimated to be 350°C (350 = 410 – 60 °C), is well below the fixed limit of 420°C.

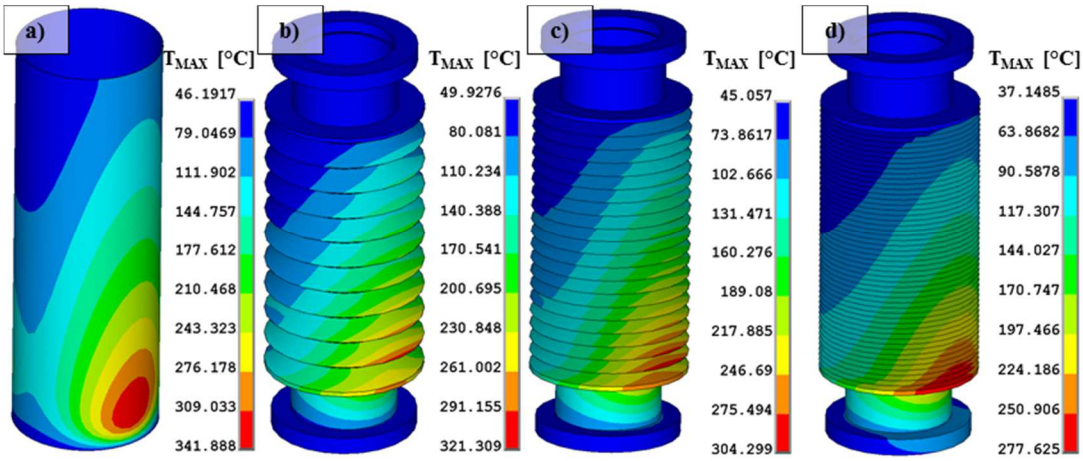

Fig. 3.49. Edge-welded bellow thermal distribution for different number of convolutions.

3.5. Design of the RIB diagnostic boxes [3.1]

3.5.1. Preliminary description

In this paragraph, the Radioactive Beam Diagnostics will be described. The paragraph will be not as extended as the others are since the problems related to these devices are not so critical. In fact, assuming a beam energy of 60 keV and a beam current of 10 μA, the power dropped by the beam is 0.6 W (both the previous numbers are surely oversize since, for example, it is not expected a beam power higher than 0.1 W). Assuming the vacuum chamber big compared to the Faraday Cup (60 mm diameter, 50 mm length) and an emissivity of its surface of about 0.3, if the heat is disposed just by radiation, applying formula (3.3), the temperature turns out 52°C, which is supportable by aluminium. In few words, the mechanical design from a thermal point of view can be neglected.

For this reason, the main part of the elements are constituted of an aluminium alloy in order to decrease the mass of the system. This has two main advantages: the reduction of the cost for its easy machinability and the reduction of the mass, which leads to an easy handling and maintenance.

3.5.2. The RIB Faraday Cup

The working principle of the Faraday Cup has been already presented in 3.3.1. Since the specification are not so restrictive, this component is designed as a standard Faraday Cup: a tube with an inner cone placed to decrease solid angle available for the electrons to escape. The component is insulated in order to collect the beam signal by means of a wire, and a frontal coaxial cylinder is maintained at a positive potential to suppress the other secondary electrons.

The inner diameter of the suppressor is determined by the maximum beam diameter estimated for that positioning in nominal conditions and during the beam tuning. As an example, a significant change on the current off-line diagnostic is the diameter of the first Faraday Cup. At present, the device installed in the Front-End before the Wien Filter has a diameter which does not allow to measure the total beam current when the beam is focused after the Wien Filter. This is very inconvenient because if it is required to measure the current before and after the Wien Filter, it is necessary to change the triplet settings.

For the two Faraday Cups, the maximum beam diameter has been evaluated to be about 56 mm (FC1 – maximum is on the x plane) and 36 mm (FC2 – maximum is on the y plane) for a 25 keV beam. This is possible to confirm looking in Fig. 4.35, where the final beam transport simulation is showed: at positions of about 1.9 (FC1) and 3.9 meters (FC2) on the z axis for a 42 keV beam, the beam has respectively 43 mm and 28 mm of maximum sizes. These dimensions correspond to the aforementioned value for a 25 keV beam, assuming them inversely proportional to the square root of the beam energy ratio. Finally, the inner FC diameter has been augmented in safety conditions to 64 mm for both the FC. On the contrary, the longitudinal length depends on the available space and the minimum potential to suppress the secondary electrons. In the second diagnostic boxes, the presence of the slits reduces the available space and the axial dimension has been fixed to 81 and 72 mm respectively for the first and the second FC. The CAD drawings are presented in Fig. 3.50, where the insulators (white component) and support system are clearly visible.

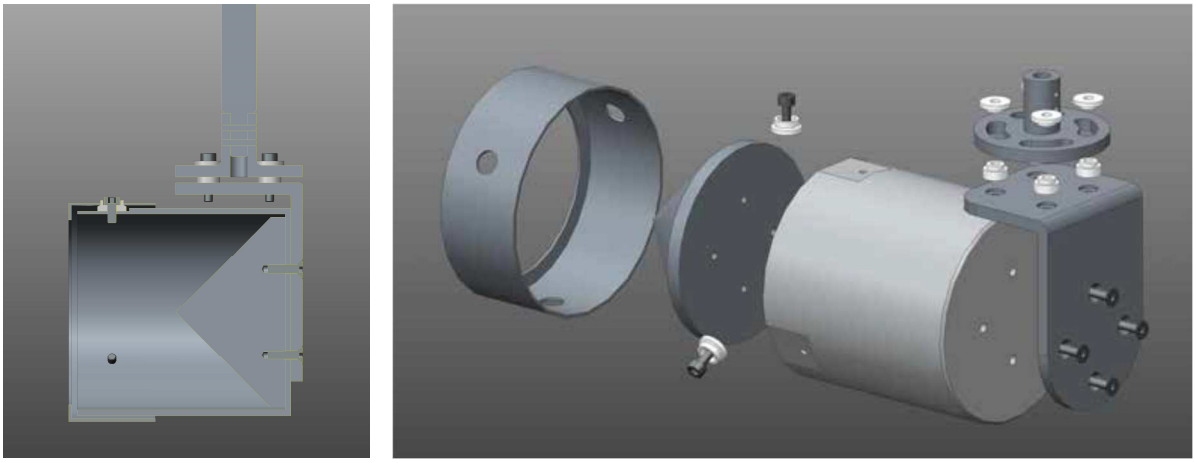

Fig. 3.50. CAD drawings of the RIB Faraday cup.

In order to complete the design, the picture of the potential distribution is presented in Fig. 3.51. The shielding efficiency of the suppressor has been calculated to 0.45 and, assuming a maximum electron energy of about 100 eV, the minimum suppressor potential to apply is about 220 V. A double value is suggested.

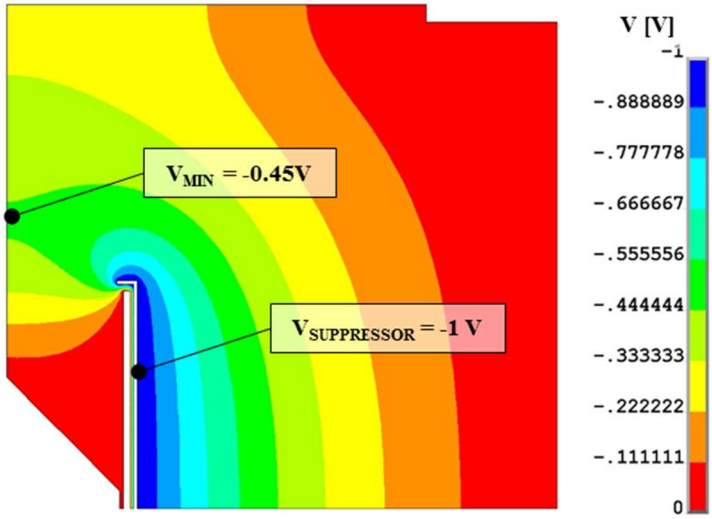

Fig. 3.51. Potential distribution for the FC2.

3.5.3. The RIB Beam Profiler

The RIB Beam Profiler (Fig. 3.52a) has not to dispose power as the version presented in 3.4. For this reason, instead of using wires, the Beam Profiler has been thought as a robust device composed of 0.4 mm thick stainless steel foils (Fig. 3.52d) cut by photogravure, a technique that is able to obtain high precision even in small thickness laminate. In this way, the rupture of the wire is absolutely avoided and the assembly of the beam profile can be easily done: all the foils are inserted in the seat on the PEEK insulator (Fig. 3.52c) which blocks them, and then the other insulator is fixed checking that all the foils are in the correct position. Finally, the foils bends are corrected in order to get them perfectly aligned. The number of foils for

each plane has been limited to 40 due to the ready electronic equipment that amplifies the various signals. It is interesting to observe that the external eight foils have a higher spacing (2 mm) in order to intercept the beam even far from the axis. The maximum beam diameter accepted is 60 mm, limited by the circular aperture of the beam profiler visible in Fig. 3.52a.

Since the space resolution required is not so high, 1 mm, it is a process easy to perform and the beam not intercept by each plane corresponds to the 60% of the total beam travelling (0.4 mm occupied by the foil over 1 mm of distance between two foil centres). Consequently, only the 36% of the beam passes undeflected through the BP.

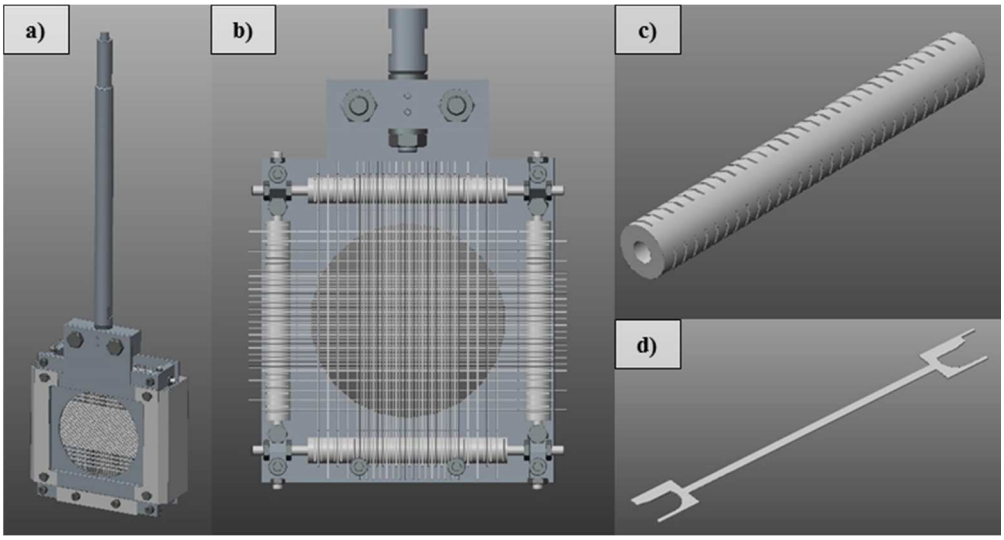

Fig. 3.52. Beam profiler CAD drawings: a) overall detector; b) backward view with the incremented distances on the external foils; c) insulated foil support; d) foils used as wires.

3.5.4. The mass separator slits

These components are used as a physical barrier to stop the undesired particles. In particular, they are usually positioned after a mass selector so the unwanted deflected beam is stopped on them as showed in Fig. 3.53. An additional function has been introduced for these devices: limiting even the aperture on the y-plane (50 mm, which is higher than the maximum beam size foreseen of 36 mm). In this way, the vacuum conductance has been decreased in order to help the maintaining on the target side the neutral volatile radioactive elements and decreasing the activation on the following beam line. Probably the effect is not so pronounced since the foreseen aperture of the slits on the x-plane is less than 10 mm, but this design has not any inconveniences.

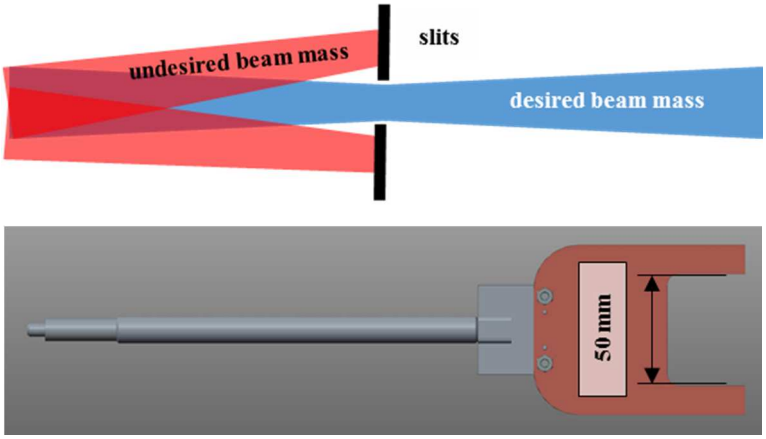

Fig. 3.53. Slits with the relative aperture on the y-plane.

3.5.1. Design of the standard handling system

This device, presented in Fig. 3.54, has to move all the previous detectors and it is thought to be the same for the previous apparatus. The advantages are:

- Reduction of the number of components
- Reduction of the number of the eventual problems

The main requisites of the system are:

- Radiation hard components: avoid polymers, suggested the use of metals
- Fast change of critical components, such as the pneumatic motor, end switches, potentiometers and the overall system if needed
- Backup solution in case of eventual failing of secondary components

The system is composed by a pneumatic motor (analysed in paragraph 3.6), coupled by means of a tongue to the bellow joint MBCK33-10-8-A (maximum static torque of 13.6 Nm). In particular, it could be very helpful during the replace of a malfunctioning motor: its change is very fast as it is possible to see in Fig. 3.54. Two screws have to be slightly unscrewed and the pneumatic motor is then free to be replaced. The bellow joint can recover the eventual small misalignments due to the hurry induced by the awareness of taking more and more radiation dose.

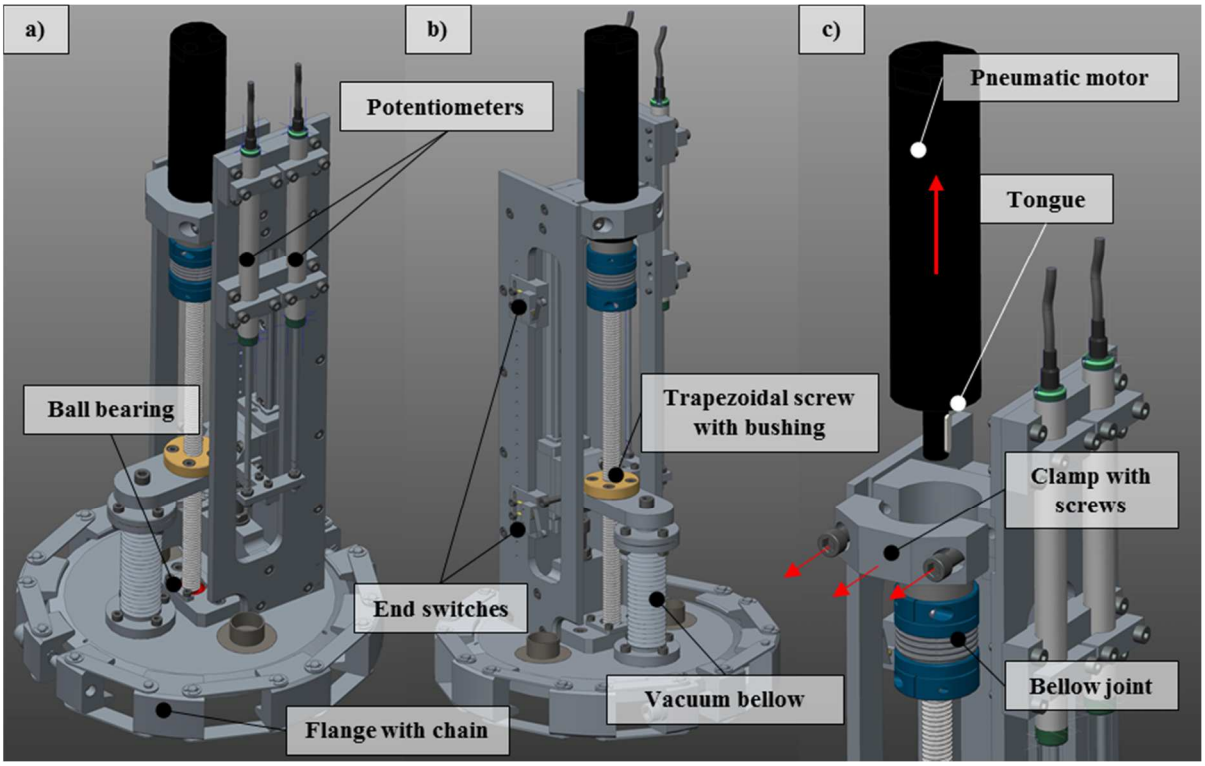

Fig. 3.54. Standard handling system with flange for the beam profiler.

The motor position will be controlled by two end switches, delimiting the total stroke, and one potentiometer to check the motor speed (and consequently having a feedback on the motor status). If one of the two systems fails, there is not the need to immediately change the component and the maintenance can be postponed at the end of the target irradiation time. Moreover, it is strongly suggested to connect all the three contact of the switch to have a redundancy on its functioning. Another redundancy is composed by the second potentiometer, because it is fundamental for the positioning check of the slits. In this way, if one of the two potentiometer fails, the second one lets to continue the run. Finally, a mechanical stop in both the direction has been foreseen to mechanically limit the stroke; in fact, the consequences of an over limit stroke could be the rupture of the most fragile component, the edge-welded vacuum bellow. This could cause the sudden entrance of fresh air in the vacuum channel and the burning of the hot uranium target, with the release of radioactive gases.

In case of an unknown malfunctioning, the overall system, handling plus detector, can be quickly and easily changed. The special stainless steel flange, equipped with chain and seal, can be unmount and replaced with a new one in less than half a minute; in this way the radiation dose absorbed by the personnel can be reduced of almost a factor 10 compared with a standard CF flange.

3.5.2. The diagnostic crosses

The last components of the assembly are the crosses, the vacuum chamber where the detectors are installed. The possible materials for its construction were:

- Stainless steel: it is easily weldable and standard flanges/seals can be used. Moreover it can assure a very good vacuum due to the low outgassing
- Aluminium: less weight and activation

In paragraph 3.2 and 3.3, the vacuum chambers were in aluminium alloy. The activation of the materials could be due both to neutron and proton activation and it can be very high since the proton beam travels through it. On the other hand, the RIB diagnostic crosses are quite far from the neutron sources (2 meters the first, 4 meters the second) and, consequently, the activation is probably negligible compared to other elements, such as the mass separator and extractor electrode, where the radioactive beam losses and the volatile elements strongly contaminate the components. Finally, it is very unlikely that their change is needed for a malfunctioning (simplified procedure with a smaller mass) due to the absence of critical aspects (no cooling circuits, no feedthrough, all metal components). For these reasons, stainless steel has been chosen as the material to produce these crosses, which lets to obtain good tolerances even after a welding process (not so for aluminium).

A small tolerance, about 0.1 mm, was assigned for the parallelism of the welded flanges in order to ensure that, if the overall detector and handling system has to be changed, the second one will be misalign of a maximum of 0.4 mm, which is considered acceptable. Finally, in the fast coupling flanges already presented in the previous paragraph, three pins ensure the correct detector orienting; on the other hand, two standard CF160 flanges have been maintained in the DB1 since here no detector are for the moment foreseen.

The picture of the first diagnostic box, assembled with beam profiler and faraday cup, is presented in Fig. 3.55 for the CAD drawings and Fig. 3.56 for the “real” device.

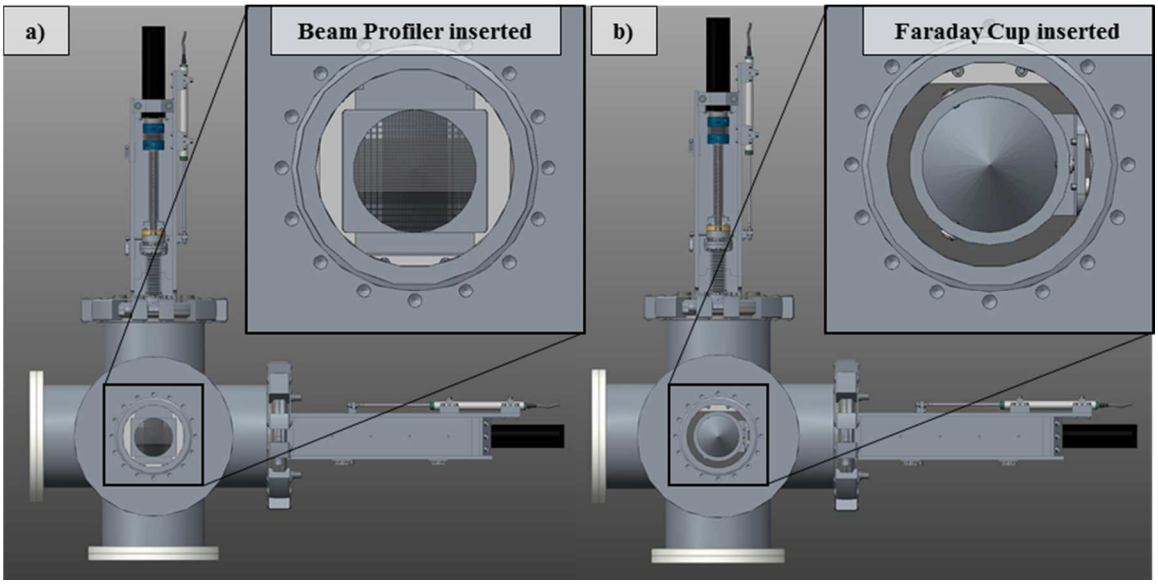

Fig. 3.55. First diagnostic box with: a) beam profiler inserted; b) Faraday cup inserted

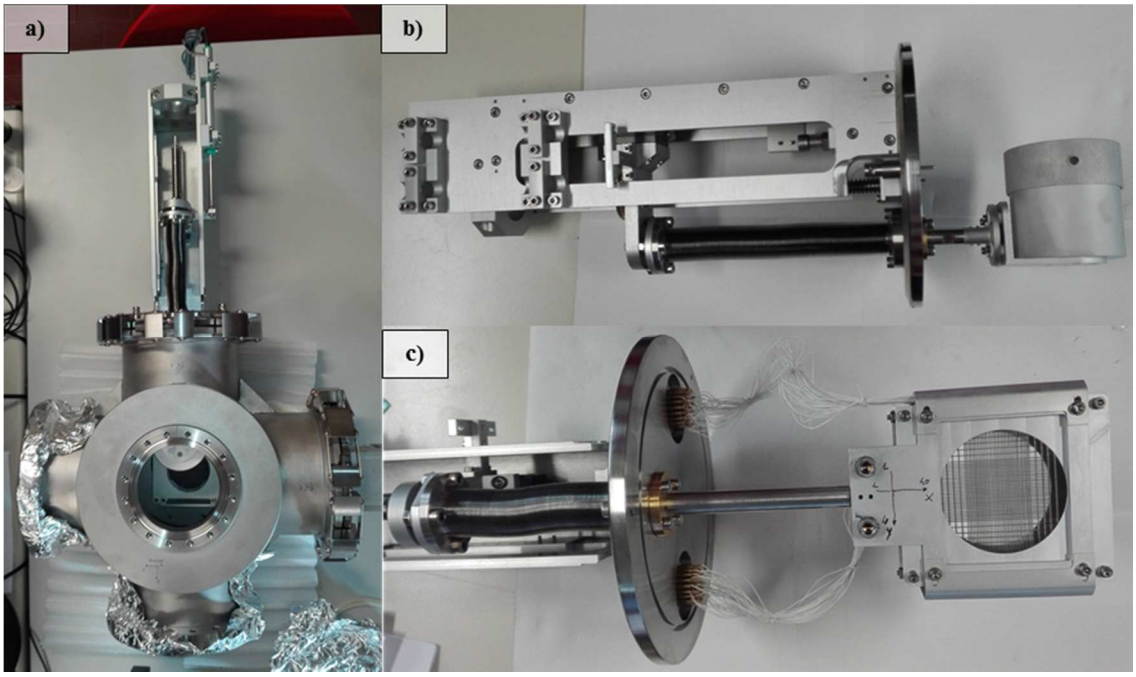

Fig. 3.56. a) View from the back of the first diagnostic box, with visible beam profiler and Faraday cup; b) Faraday cup assembly; c) Beam profiler assembly

3.6. Study and redesign of the pneumatic motor [3.21]

3.6.1. Preliminary description

In order to perform the various movement inside the SPES bunker, a pneumatic motor type was chosen as the standard actuator for four main reasons:

- The pneumatic motors in general can deliver very high torque and power in relative small sizes

- The motor can be positioned on a high voltage platform but the command at a ground potential. The electrical detachment is simply performed by insulated tubes needed to feed the motors with air flow
- The components are usually quite simple and robust. Moreover, there are few radiation sensitive parts
- The experience in ISOLDE is very bad with standard electric motors [3.22]

The choice of the motor was not performed during this thesis, but here the study of the main parts susceptible of radiation damage will be presented. In particular, the chosen motor is the standard 28M40R-D10 of FIAM [3.23] with few customized modifications introduced: the paddles are made in PEEK instead of a polymer very sensitive to radiation and the seal, which avoids the entrance of dirtiness in the motor, in EPDM instead of the common VITON. This modified motor was called 28M40R-D10-INFN. According to the datasheet, the standard motor has to provide at 6.3 bar of inward air pressure (nominal conditions) 210 W, with 190 rpm and 11.5 Nm.

In particular, the pneumatic motor can be divided in two main parts: the first part converts the air energy to mechanical energy, and it is composed by a rotor with paddles and a stator inserted into a metal jacket with air connections. The second part is a planetary gear which reduces of an approximately ratio of 27 the very high speed of the rotor. The pneumatic part has three ways for the air flow since it has to be reversible: inward flow, outward flow and dump. In order to protect the motor design, few pictures will be here presented.
The example of the motor functioning principles is presented in Fig. 3.57, taken from [3.24] where it is well explicated.

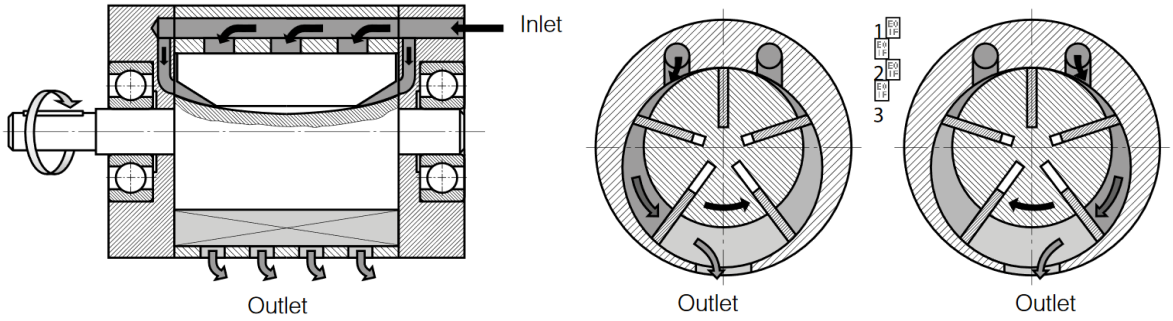

Fig. 3.57. Example of the principles of a reversible motor functioning, after [3.24].

The air enters from one of the entrances and, at the start, pushes up the paddle by means of a small aperture. Then, during stationary conditions, the centrifugal force maintains them out of the seat and provides the sufficient seal to decrease air leakages. The air expands during the rotation until the outlet, where air reaches ambient pressure. The remained air is now another

time compressed and released to the second entrance. For this reason, it is very important to maintain even the second way opened during operation.

An example of the characteristic curve is presented in Fig. 3.58. The torque is approximately linear with the speed, with a maximum at stopped rotor; this value strongly depends on the position where the paddles arrest. To prevent unstable working conditioning, the motor has not to be used at low speeds. The maximum power is foreseen at half of the maximum speed. Finally, the air consumption curve demonstrates that the air leakages are quite significant, especially at low speeds, since, even without power released, the motor consumption is for this case the 30% of the maximum speed.

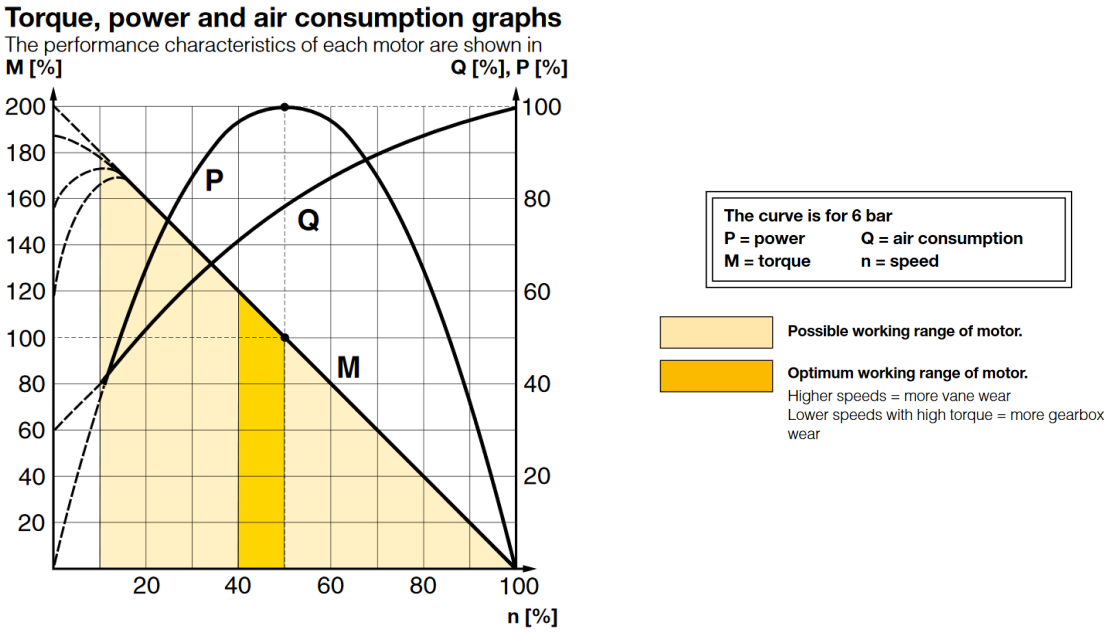

Fig. 3.58. Example of the characteristic curve of a pneumatic motors with paddles, after [3.24].

The regulation of the air pressure is very important. Two types of different regulation could be performed: pressure regulator (Fig. 3.59a) or by a throttle (Fig. 3.59b).

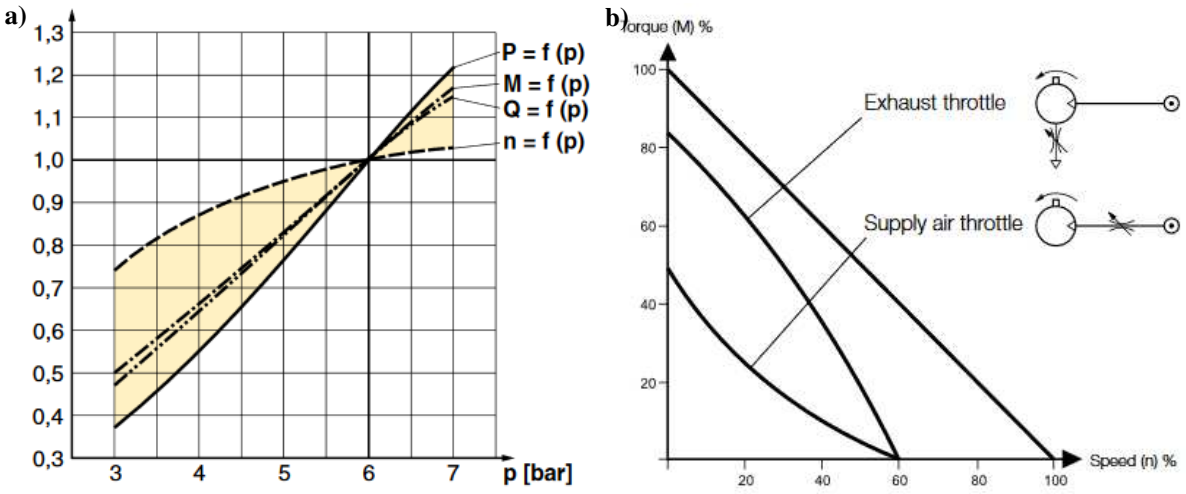

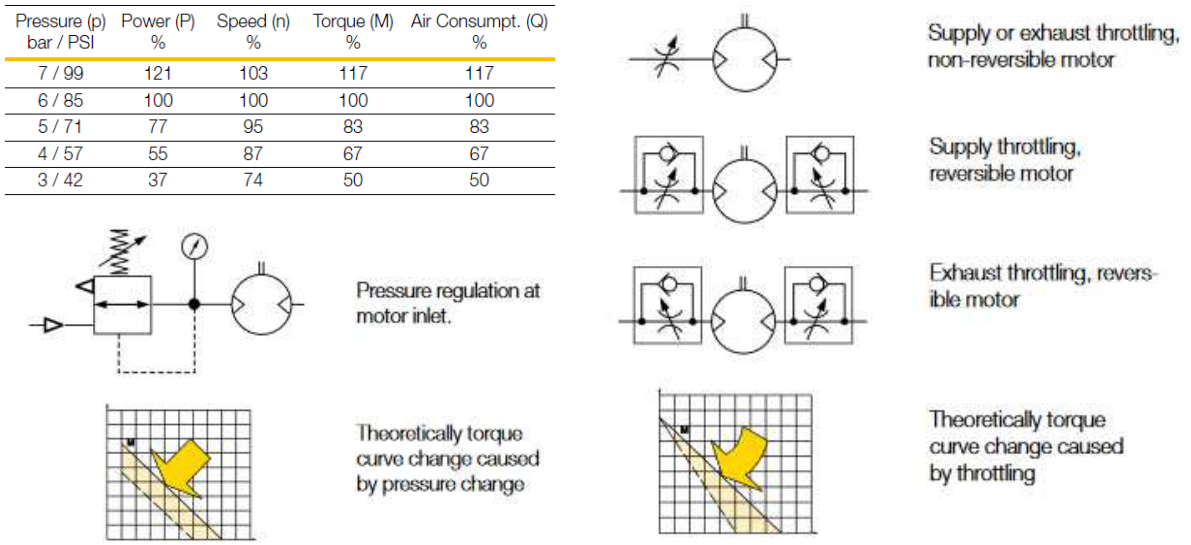

Fig. 3.59. Different way to regulate a pneumatic motor: a) air pressure regulation and conversion factor for different supplied pressure at the maximum power; b) throttling. After [3.24].

In the first case, the torque line is translated, whereas in the second one the line slope changes maintaining approximately constant the maximum momentum. The last type is the simplest way to control the motor.

Concerning the use on the SPES bunker, the motor positions are showed in Fig. 3.60. Two different working conditions have been identified:

- 4 motors that couple the target chamber to the Front-End (red coloured). They are used just in case of the chamber coupling. 84 uses have to be surely foreseen (12 runs each year for 7 years), but as a first estimation, 500 uses have to be assured. They are the closest to the target chamber and they surely suffer the radiation damage more than the others. They have to supply the highest torque, measured to be about 5 Nm on the stationary use, 11 Nm of peak for the coupling and 7 Nm of peak during the uncoupling [3.21] of the target chamber.
- 9 motors that move the diagnostics (green coloured). Assuming to insert the diagnostic twice each hour during a running, for 24 hours, 14 days, 12 runs per year for 7 year, about 50000 uses have to be foreseen. They are farther from the target chamber and the torque which has to be supplied is very low (less than 2 Nm), essentially just to overcome screw friction.

In this paragraph, the modifications applied to the pneumatic motor will be tested, with particular attention on the paddles materials: in fact, the motor with PEEK paddles was not already characterized. Moreover, the possibility to change polymeric paddles with different materials (such as graphite, bronze, anodize aluminium) will be investigated. Finally, the possibility to test irradiated paddles is presented.

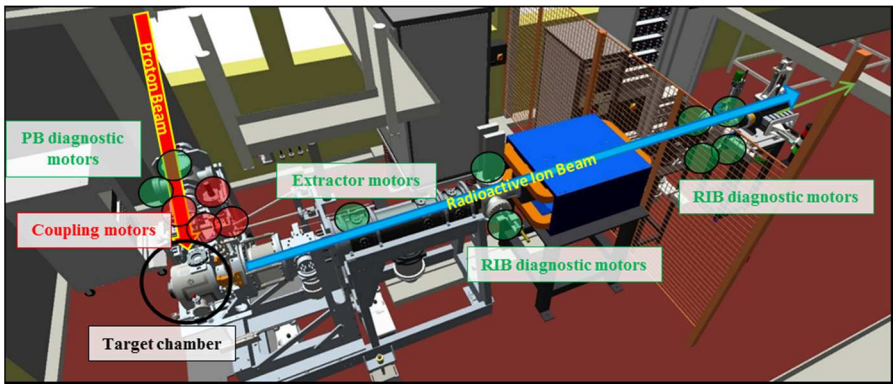

Fig. 3.60. Position of the various pneumatic motors on the SPES Front-End.

3.6.2. Realization of the test bench for the motor characterization

The first step of the study is the preparation of an easy transportable test bench to characterize the pneumatic motor. The most important measures to get are summarized in Table 27.

Physical characteristics	**Measurement device**	**Device**
Angular speed	Linear potentiometer	*GEFRAN* PZ-12-S-100
Output torque	Load cell	Home made [3.25]
Input / Output air pressure	Pressure switch	*Camozzi* SWCN-P10-P3-2
Mass flow	Mass flow meter	*M+W Instruments* D-6380-DR
Input / Output air temperature	Thermometer	Standard Pt100

Table 27. Physical characteristics with its device available on the test bench

Other ancillaries components are summarized in Table 28.

Component	**Use**
Clamp brake	Regulate resistant torque
N°2 Switch	Delimit stroke
Threaded bushing and nut	Transform motor from angular to linear
Electro valve 5/3 Camozzi 368-011-02	Command the reversible pneumatic motor
PLC Modicon M340	Programmable Logic Controller (PLC)
BMX AMI0410	Acquisition of analogic signals
BMX DRA0805	Series of relay (ex. control the electro valve)
BMX DDI1602	Current receiver from the sensors (ex. switches)
5 V power supply	Power supplier for load cell and Pt100
Amplifier circuit for Pt100	Home made amplifier circuit to provide signal to PLC
Amplifier circuit for load cell	Home made amplifier circuit to provide signal to PLC

Table 28. Other components needed for the test bench.

In particular, the amplification circuits for the Pt100 and for the load cell are very similar because they are based on the AD8237 integrate.

Concerning the Pt100, the amplifier circuit scheme is presented in Fig. 3.61. The Pt100 is in series with a 900 Ω resistor that is inserted on a Wheatstone bridge composed by other three 1000 Ω resistors. In this way, the current flowing on the sensor is limited to 2.5 mA which is considered acceptable.

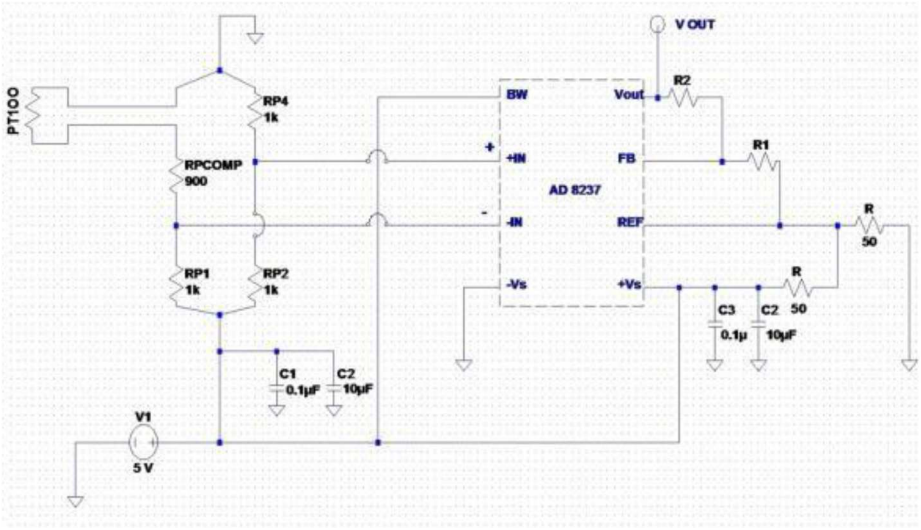

Fig. 3.61. Amplifier circuit scheme for the Pt100, after [3.21].

The output sensitivity of the bridge is:

$$\frac{dV}{dR_{Pt100}} = V_0 \frac{R_4}{(R_1 + R_4)(R_{COMP} + R_{Pt100} + R_4)} = 5 \cdot \frac{1000}{2000 \cdot 2000} = 1.25 \left[\frac{mV}{\Omega}\right] \quad (3.25)$$

The Pt100 sensitivity is:

$$\frac{dR_{Pt100}}{dT} = 0.3851 \left[\frac{\Omega}{°C}\right] \quad (3.26)$$

And the consequent bridge sensitivity:

$$\frac{dV}{dT} = \frac{\frac{dV}{dR_{Pt100}}}{\frac{dR_{Pt100}}{dT}} = 0.4814 \left[\frac{mV}{°C}\right] \quad (3.27)$$

Since the temperature of the output air could be quite low, the temperature range to measure is between -20°C to 50°C. A 0-5V of acquisition system is available and a good sensitivity could be:

$$\frac{\Delta V}{\Delta T} = \frac{5}{70} = 71.43 \left[\frac{mV}{°C}\right] \quad (3.28)$$

Using two resistance of 3.9 kΩ and 499 kΩ, the amplifier gain is:

$$G = 1 + \frac{R_2}{R_1} = 1 + 127.95 = 128.95 \quad (3.29)$$

Then the overall system sensitivity estimation is:

$$\frac{dV_{output}}{dT} = G\frac{dV}{dT} = 62.08\ \left[\frac{mV}{°C}\right] \tag{3.30}$$

which is acceptable. Finally, both the output voltages of the Wheatstone bridge (Fig. 3.62a) and the overall measuring chain (Fig. 3.62b) have been tested, obtaining the correlation between voltage and temperature - equation (3.31) and (3.32). The total resolution is 66.2 mV/°C, which is not so far from the estimation.

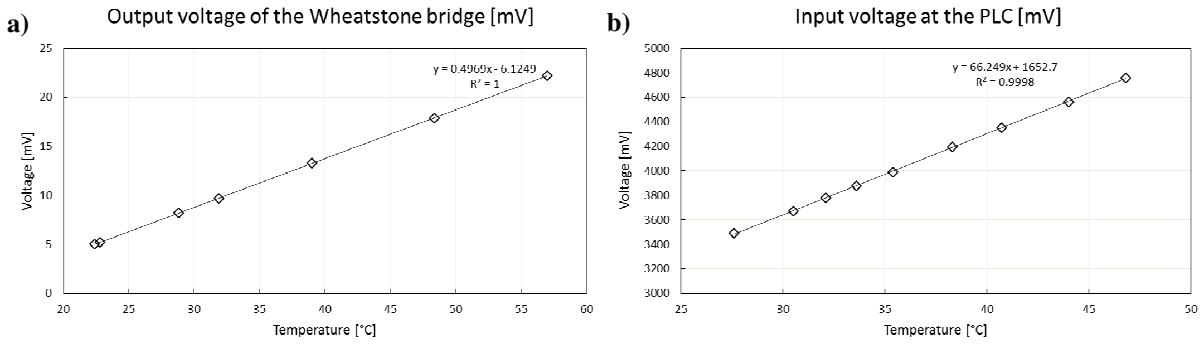

Fig. 3.62. Voltage: a) output of the Wheatstone bridge; b) input at the PLC after the overall measuring chain.

$$V[mV] = 66.249[mV/°C] \cdot T[°C] + 1672.7\ [mV] \tag{3.31}$$

$$T[°C] = 0.0151[°C/mV] \cdot V[mV] + 24.95\ [°C] \tag{3.32}$$

Concerning the torque measures, a load cell was manufactured [3.25] for momentum lower than 20 Nm, with a full bridge extensometer. Its calibration provides the deformation curve:

$$\varepsilon_{zz}(M_t) = 98.86\ M_t\ [\mu m/m] \tag{3.33}$$

With a power source of 5 V and an extensometer K=2.24 gauge factor, the output voltage is:

$$\left|\Delta V_{bridge}\right| = 11.2\ \varepsilon\ [V] \tag{3.34}$$

$$\Delta V_{bridge} = 1.107\ M_t\ [mV] \tag{3.35}$$

A very similar to the Pt100 amplification circuit is presented in Fig. 3.63 to amplify the output voltage of the full Wheatstone bridge. The AMI0410 PLC module has a resolution of 0.35 mV, whereas the range is 0-5 V. Since the motor is reversible, the maximum voltage range is decrease of a factor to read both the rotation direction. Assuming a maximum torque of 20 Nm, the best gain reachable is 125. To avoid any saturation problems, the resistor used are R_1 = 1.2 kΩ and R_2 = 100 kΩ, for a gain of $1+R_2/R_1$ = 84.3. The calibration curve is presented in Fig. 3.64 with a final sensitivity of 93.7 and momentum resolution of 3.73 mNm, which is considered good.

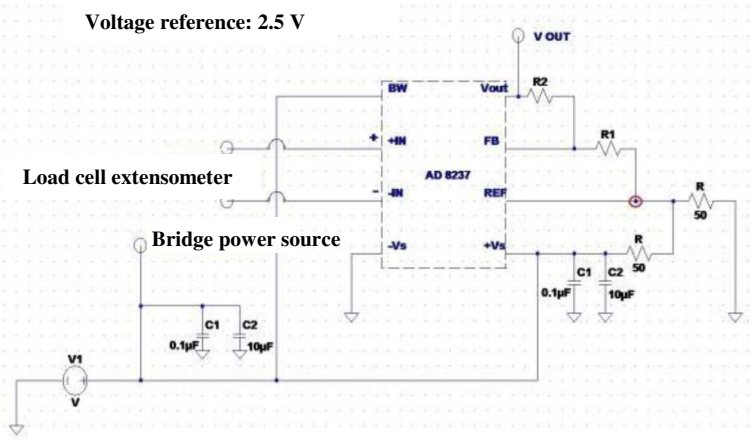

Fig. 3.63. Amplifier circuit scheme for the load cell, after [3.21]

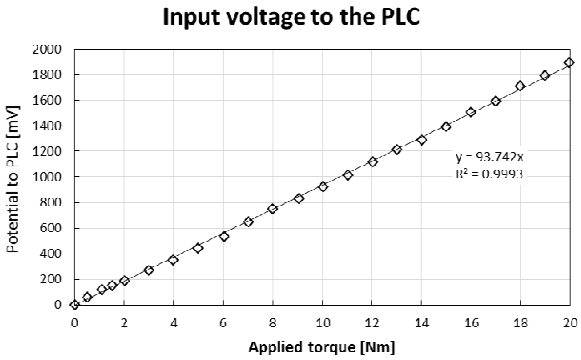

Fig. 3.64. Input voltage at the PLC during the calibration phase of the amplification circuit after zeroing.

$$\Delta V_{PLC}[mV] = 93.742[mV/Nm] \cdot M_t[Nm] \quad (3.36)$$

$$M_t[Nm] = 0.01067[Nm/mV] \cdot \Delta V_{PLC}[mV] \quad (3.37)$$

Finally, the resolution on the potentiometer is of the order of the one tenth of mm on a range of hundred, for a relative error of about 10^{-4}.

3.6.3. Preliminary test on the pressure drop for different pipe diameters

A very short description of the effect of the pipe length and diameter on the pressure drop will be presented. This is very important for the design phase of the pneumatic circuit. In fact, even if the motor is very powerful, it has to be feed with a significant air flow without compromising the pressure. As an example, in the first tests, not here reported, performed with PEEK paddles with a 4 mm diameter tube of few meters length, the motor performance at the maximum power were 40% of the datasheet values.

The setup used to measure the pressure drop is presented in Fig. 3.65, whereas the results for 4 and 6 mm diameter for a 4 meter length pipe are presented in Fig. 3.66. It is clear that the pressure drop decreases of a factor of ten incrementing the diameter of 50% and, consequently, the section of 125%. Therefore, even for very short pipes, a small diameter could decrease

significantly the motor performances as it was presented in [3.21] for the pneumatic motor studied.

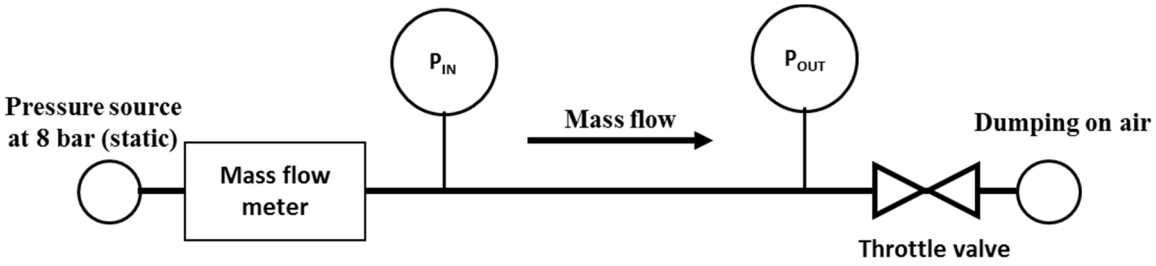

Fig. 3.65. Experimental setup to measure the pressure drop in the pipes.

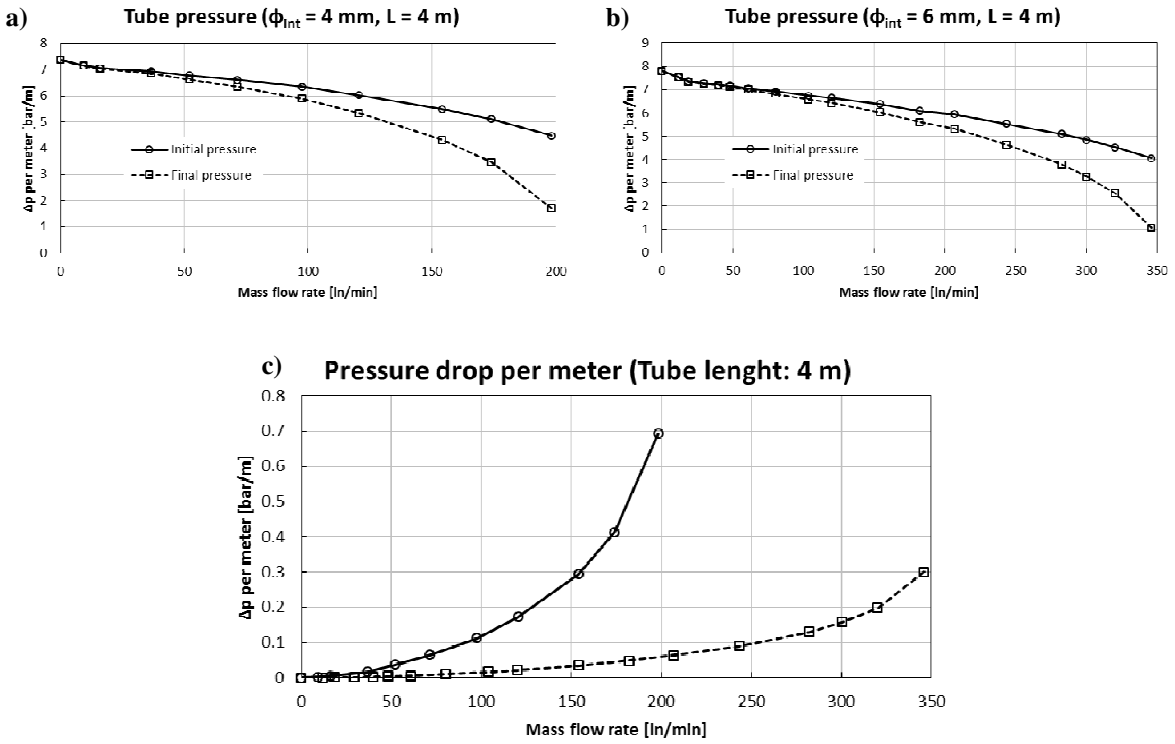

Fig. 3.66. Inlet and outlet pressure for two different pipes (a,b) and pressure drop (c).

3.6.4. Test of the motor with PEEK paddles

These tests have been performed with a static pressure of about 8 bar and for a tube diameter of 6 mm and the results are presented in Fig. 3.67. It is clear that, even if the static pressure is high, during the mass flow, the inlet pressure at the pneumatic motor decreases substantially, probably due to the pressure drop along the tubes.

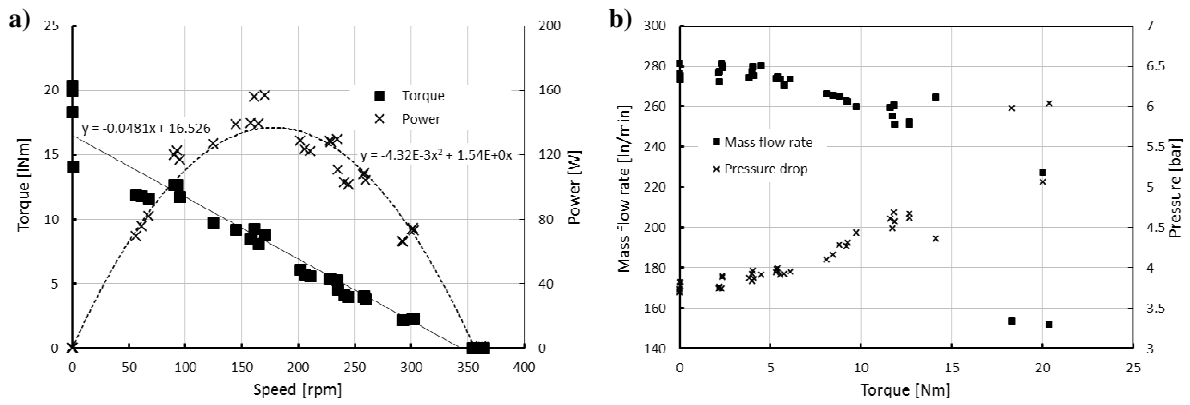

Fig. 3.67. Performances of the pneumatic motor for a static pressure of 8 bar on the power supply source.

Analysing the results, they respect the ideal characteristics curve: for example, the speed-torque graph is approximately a straight line until low speeds, where the motor becomes unstable, especially at blocked rotor. On the other hand, the power curve is similar to a parabola, as in the ideal case. The air flow rate is almost constant with the torque (change of 7.4% between 0 and 12 Nm), whereas the inlet pressure has an excursion of only 1 bar, with the data that are quite scattered. This is important to underline: by means of these measures, it is not possible to remotely analyse the motor performances cross-checking the value of the speed (measurable by a potentiometers) and the pressure or mass flow rate. The only important information that is possible to get data for the airflow and pressure drop when the rotor is blocked, as it is presented in Table 29.

M_T [Nm]	Q [nl/min]	Δp [bar]
18.3	153.4	5.99
20.4	152.2	6.04
14.1	264.9	4.36
20.0	227.3	5.07

Table 29. Measures at blocked rotor.

The data scattering for the momentum is justified by the position of the paddles respect to the inlet and outlet passages. A particular bad configuration can lead to the impossibility of moving the motor: if the break-out torque is a little higher (it was measured to be 11 Nm), the motor could not start even if the other times it worked. A “bad configuration” can be remotely monitored since the smallest torque M_T is always combined with the highest mass flow rate Q and the smallest difference of air pressure Δp. In this case, in order to unblock the motor, it is probably sufficient to turn a little the motor on the other side and then try to give again the pressure.

Finally, the comparison between the standard pneumatic motor and the modified version with PEEK paddles are presented in Table 30. The normalization process is only indicative

since it has been performed using the coefficient provided in Fig. 3.59 that are relative to a different motor company.

	Power [W]	Momentum [Nm]	v [rpm]	Inlet pressure [bar]	Q [ln/min]
Datasheet (6.3 bar)	210	11.5	190	6.3	348
PEEK paddles (5.3 bar)	148	7.95	178	5.3	270
PEEK paddles normalized	192	9.58	187	6.0 normalized	325

Table 30. Comparison between the motor datasheet, the modified version and the modified version normalized to the inlet pressure with PEEK paddles.

Anyhow is clear that the modified version (with PEEK paddle) do not significantly change the performances of the motor, consequently its use is strongly suggested.

3.6.5. Test of the motor with different materials for the paddles

In order to completely remove polymers from the motor, some tests with reasonable materials for the paddles have been performed. A table summarizing the advantages / disadvantages for the various materials is presented in Table 31.

Material	**Advantages**	**Disadvantages**
Graphite	• Low density • Low friction with stainless steel	• Fragile • Low wear resistance
Bronze	• Often use for bushes	• High density
Anodize aluminium (Al6082T6)	• Low density (higher than others) • Low friction with stainless steel	• Low density • Low depth penetration of anodization

Table 31. Summarization of the advantages/disadvantages of the different materials tested.

Concerning the graphite, the maximum static air pressure feeding the motor was fixed to 4 bar because, during previous tests, with 6 bar two graphite paddle broke. The performances of the motor were considerable lower compared to the standard motor, as it is demonstrated in Table 32.

	Power [W]	Momentum [Nm]	v [rpm]	Inlet pressure [bar]	Q [ln/min]
Datasheet (6.3 bar)	210	11.5	190	6.3	348
Graphite paddles (4 bar)	39	3	125	4.0	155
Graphite paddles normalized	70.9	4.5	144	6.0 normalized	231

Table 32. Comparison between the motor datasheet, the modified version and the modified version normalized to the inlet pressure with graphite paddles.

Then, a second study was performed using the motor at the maximum speed, without any torque applied. After 3 hours and 18 minutes, the motor blocked. Assuming a maximum speed of 230 rpm (water flow and pressures were essentially constant during the test), the numbers of rotor cycles are 1.2 million, for about 50000 turns for the motor shaft. For an excursion of 100 mm, the total number of cycles on the Front-End is about 1000. This is not satisfying

because it can not fulfil the requirements neither to couple the chamber due to the low torque that supplies, nor to move the detectors which have to be done for 50000 cycles.

Just for completeness, the probable rupture mechanism for the graphite is presented in Fig. 3.68. The stainless steel seat, during the paddle cycle of entrance and exit, dug into the paddle, increasing stresses and decreasing its resistance. This effect was present on all the paddles, but just two of them were broken. A possible solution to relax this process is increasing the paddle thickness limiting as much as possible the play with the seat.

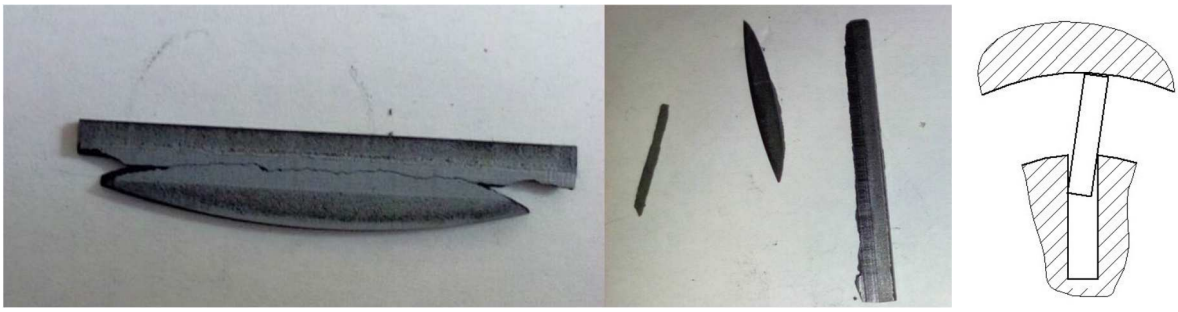

Fig. 3.68. Pictures of the broken graphite paddles and main wear mechanism leading to rupture.

Concerning the bronze, it was not possible to get a characteristic curve since the performances of the motor was changing during the functioning. The wear was so intense that the flash on the paddle due to material erosion blocked the paddles inside the seat as it is showed in Fig. 3.69.

Fig. 3.69. Picture of the bronze paddle, the stator chamber and the wear mechanism leading to the motor block.

Finally, the test on the anodize aluminium paddles was initially promising since the maximum torque and the maximum speed was as high as during the PEEK motor test. Then, after few tests, the torque dramatically decreased due to the removing of the anodize surface. The pure aluminium entered in contact with the stainless steel stator chamber compromising the motor. Even this material can not substitute the PEEK.

Fig. 3.70. Anodize aluminium paddle and ruined stator chamber after the tests.

3.6.6. Final considerations

Probably, the best material tested that satisfies the demands required by the pneumatic motor is PEEK. On the other hand, the tests on the other materials presented in paragraph 3.6.5 clearly showed that the most problematic aspect is the paddle wear resistance. In particular, the very high number of entrance and exit from the rotor seat that have to support during the functioning, compromises the performances and the duration of the motor itself with other paddles materials.

The dose absorbed by the PEEK paddles has been evaluated in Table 33 by MCNPX, analysing the motor closest to the target. The dose, compared to the irradiation tests presents in Fig. 3.71 taken from [3.26], are quite low and it seems that it can not affect the ultimate strength, deformation at rupture and Young modulus. On the other hand, the damage in the tests performed in [3.26] was essentially due to photon (gamma rays) and any information are provided concerning wear resistance: it is possible, for example, that the surface of the paddle could start to exfoliate or to lose some small particles that could cause motor block. For this reason, it will be very important to irradiate PEEK paddles and, even by means of the designed test-bench, analysing the overall performances of the motor. This probably will be done next months at the nuclear reactor sit in Pavia.

Dose	**Fluence** $[cm^{-2}\ s^{-1}]$	**Dose per hour**	**Per cycle (14 days)**	**Per year (12 cycles)**	**All life (7 years)**
Neutron	$8.53 \cdot 10^{8}$	30 Gy/h	10.1 kGy	121 kGy	0.847 MGy
Gamma	$3.35 \cdot 10^{8}$	12 Gy/h	4.0 kGy	48 kGy	0.336 MGy
Total		42 Gy/h	14.1 kGy	169 kGy	1.18 MGy

Table 33. Dose absorbed by the PEEK paddle during target irradiation.

Material: **PEEK** TIS No. **R 520**
Type **Natural polyether-ether-ketone**

Supplier: **Erta-Epec** UL 94: V-0
Remarks: via Angst and Pfister LOI: 35%

Radiation test results according to IEC Standard 544 (and ISO 178)

Dose rate (kGy/h)	Dose (MGy)	Ultim. strength (MPa)	Deformation ε (%)	Modulus (GPa)
0	**0**	**177**±3	**> 15**	**4.3**±0.1
1	**1**	**177**±5	**> 15**	**4.3**±0.1
180	**5**	**179**±0.3	**> 15**	**4.1**±0.1
180	**10**	**161**±35	**9.2**±4.5	**4.2**±0.1
1	**10**	**126**±7	**3.4**±0.3	**4.3**±0.3
210	**50**	**81**±41	**3.0**±1.1	**4.3**±0.1
220	**100**	**143**±22	**4.7**±1.2	**4.2**±0.1

Critical property = deformation
Radiation index (RI) = 7.1 at a mean dose rate of 220 kGy/h
Radiation index (RI) = 6.8 at a mean dose rate of 1 kGy/h

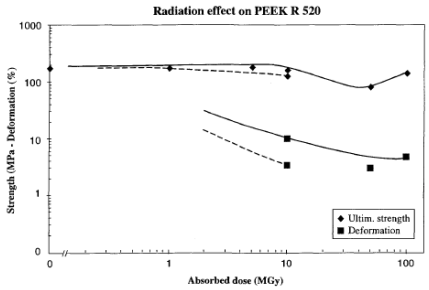

Comment: Dotted lines correspond to long-term irradiation.

Fig. 3.71. Damage test on PEEK essentially due to photon flux, after [3.26].

3.7. Conclusions

In this chapter, the various diagnostics developed for the SPES project have been presented. In particular, two big groups could be recognize: the proton beam diagnostic and the radioactive beam diagnostic.

The first group concerns the definition of the devices used to characterize and to determine the proton beam properties impinging the target. This is absolutely important for the irradiation of the target since, as it was showed, it is a very fragile component. For this purpose, the collimators have been developed. They are able to dissipate the proton beam part that has not to be delivered to the target. Moreover, this device can used to monitor continuously the beam properties during irradiation, constituting the first check on the proton beam. Then a Faraday Cup and a Beam Profiler have been developed. They will be essentially used during the preparation of the proton beam before its delivery to the target. Collimators and Faraday Cup dissipate the beam power only by radiation and, in this way, an eventual water leakage is not released in the vacuum side.

On the other hand, the radioactive beam diagnostic was dedicated on the secondary beam. The thermal and structural problems were essentially absent but many efforts were spent to use standardized components and to increase the facility and the speed during an eventual maintenance procedure.

Finally, the modified version of a standard pneumatic motor used to move the diagnostics has been studied. Firstly, a test-bench has been realized and, secondly, the motor has been tested. Various materials for the paddles have been taken into account but, unfortunately, only the PEEK version was satisfying. PEEK is a polymeric material and it is surely subjected to radiation damage. During the tests, it was demonstrated that the material wear resistance is the most critical aspect. So, thanks to a collaboration with the LENA nuclear reactor in Pavia, the PEEK paddles can be soon irradiated in a gamma and neutron field in order to take into account the radiation damage and then they can be tested by using the developed test bench.

References of Chapter 3

[3.1] L. Martin, *Progettazione meccanica delle box di diagnostica del Front-End del progetto SPES*, Tesi di Laurea Magistrale, Università degli Studi di Padova (2015).

[3.2] P. Forck, *Lecture on Notes on Beam Instrumentation and Diagnostic*, Joint University Accelerator School (2011).

[3.3] D. M. Douglas, *Secondary particle collection in ion implantation dose measurement*, Rev. Sci. Instrum **49**, 634 (1978).

[3.4] Ruggiero *et al.*, *Basic course on general accelerator physics*, CERN-2005-004 (2005).

[3.5] E. Boratto, *Progettazione ed ingegnerizzazione del Front-End protonico del progetto SPES*, Tesi di Laurea Magistrale, Università degli Studi di Padova (2014).

[3.6] J. Dietrich *et al.*, *Beam Position Monitor Development for iThemba LABS Cyclotron Beam Lines*, EPAC'2004, p. 2589, Lucerne, July 2004.

[3.7] M. Maggiore, *SPES target beam delivery analysis*, internal documentation.

[3.8] UCAR "Tecnical Data Sheet: 31": Grade ATJ Isomolded Graphite.

[3.9] A. P. Bernardes *et al.*, *Evaluation of a potential explosive Front-End*, CATHI Final Review Meeting (2014), CERN.

[3.10] G. Artuso, *Design and testing of a setup to evaluate the contact thermal resistances*, Bachelor thesis, Università degli Studi di Padova (2016).

[3.11] R. E. Bullock, *Fatigue behaviour of ATJ graphite*, J Mater Sci **12**, 1215-1224 (1977).

[3.12] L. Green *et al.*, *The behaviour of graphite under alternating stresses*, NAA-SR-115 (1951).

[3.13] W. L. Greenstreet, *Mechanical properties of artificial graphites – A survey report*, USAEC Rept. ORNL-4327 (1968).

[3.14] K. Sonderegger, *Vacuum Sealing Technology*, CAS Vacuum in Accelerator (2006), Spain.

[3.15] https://en.wikipedia.org/wiki/Stopping_power_(particle_radiation).

[3.16] L. Green *et al.*, *High temperature compression tests on graphite*, NAA-SR-165 (1952).

[3.17] S. Sharafat *et al.*, *Design window for tungsten alloys*, UCLA (1999).

[3.18] http://www.dupont.com/content/dam/dupont/products-and-services/membranes-and-films/polyimde-films/documents/DEC-Kapton-summary-of-properties.pdf

[3.19] J. P. Blakely, L. G. Overholser, *Outgassin behaviour of EGCR moderator graphite*, ORNL-3560, UC-4 – Chemistry, TID-4500 (26th ed.).

[3.20] É. N. Marmer *et. al*, *Investigation of the evaporation rate of graphite*, Sov Powder Metall+ **2**, 407-412 (1963).

[3.21] A. Sandrin, *Progettazione di un banco prova per test e sviluppo di motori pneumatici per il progetto SPES*, Tesi di Laurea Magistrale, Università degli Studi di Padova (2016).

[3.22] A. P. Benardes talk at INFN Safety review, LNL, November 2014.

[3.23] FIAM, http://www.fiamitalia.it/

[3.24] Parker Pneumatic P1V-S Vane air motor Stainless steel Series Catalogue PDE2554TCUK

[3.25] G. M. Colorio, *Sviluppo del progetto strutturale di un giunto di trasmissione flessibile, Tesi di Laurea Magistrale*, Università degli Studi di Padova (2014).

[3.26] M. Tavlet *et al.*, *Compilation of radiation damage test data*, CERN 98-01.

Chapter 4

The Wien Filter: study, redesign and tests

4.1. Introduction

The Wien Filter is a device which uses a perpendicular electric and magnetic field to select particles with different velocities. Its named is due to Wilhelm Wien that developed it in 1898 to study anode rays. It is clear that it is not a "recent" device and it is often assigned as a simple exercise of physics in the secondary school and university. Despite of this, there is very little information in literature concerning its design and construction, its selection capabilities and the correct procedure to sizing it. Moreover, there is even conflicting information on its design.

The first version installed in the Front-End was bought from an external company and it is shown in Fig. 4.1. After some tests, it was clear that the characteristics were not satisfying and the minimum power resolution requested to select the desire mass, decreasing the radioactivity along the following beam line, was not reached. For this reason, a deep study was carried on in order to increase its performances and this chapter is a description of the Wien Filter (both from an analytical and numerical point of view) and its engineering redesign. Finally, the validation of the calculations and, in general, of the correct approach to size a Wien Filter, is here defined and explicated.

About this device, three of the most important papers found are:

- [4.1]: it is the most complete analytical study of the Wien Filter. The object was separating the beam and, at the same time, focusing the beam equally in the x and y plane.
- [4.2]: it is presented an experimental Wien Filter not based on [4.1] and without any specific reference to [4.1]. Moreover, not enough information and explications are provided on how to size correctly it.
- [4.3]: it is presented an experimental test of a Wien Filter based on [4.1]

All the work performed in this chapter was mainly based on [4.2] since the other two papers were found very late. In particular, both the analytical and the following numerical studies were not influenced by any of the sentences presented in [4.1] and [4.3].

In this chapter, many terms and calculations belong to the physics sphere (essentially beam transport matter) but they are the basis for the engineering study. They will be limited as much

as possible, but the minimum descriptions can not be avoided in order to prove what in this thesis is sustained. Some important concepts will be described in the next paragraphs.

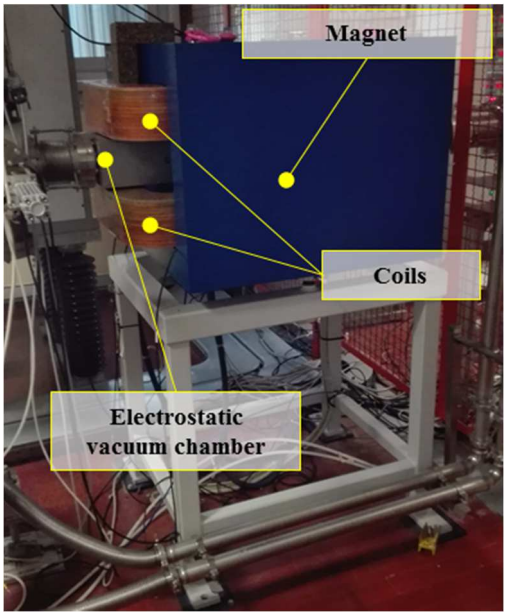

Fig. 4.1. First version of the Wien Filter, as received, bought from an external company.

4.1.1. The emittance

The emittance is the size of the beam in the phase space [4.4] and, in absence of non-linear effects or beam interaction, is constant due to the Liouville's theorem [4.5]. For the transversal planes, x and y, an easy way is to imagine the emittance as the product between beam size and beam divergence, which is the angle of the increase of the beam diameter in a unit distance. Various definition of the emittance are provided:

- Geometrical RMS emittance: is the product of the semi-axes of the ellipse in the phase space (x-x', y-y') calculated assuming a Gaussian beam particle distribution both for the position and the particle angle.
- Geometrical N% emittance: is the product of the ellipse semi-axes in the phase space (x-x', y-y') which contains the N% of the beam particle.
- Normalized emittance: is the geometrical emittance multiplied by the relativistic function β and γ. Essentially, the emittance is normalized on the beam momentum and, in absence of beam interactions and non-linear effects, it remains constant during an eventual acceleration.

4.1.2. The Twiss parameters [4.6]

The Twiss parameters defines the ellipse shape in the phase space, as shown in Fig. 4.2, and consequently they are able to characterize the beam properties. In particular:

- The β Twiss parameter defines the maximum beam size according to (4.1).

- The γ Twiss parameter defines the maximum beam divergence according to (4.2).
- The α Twiss parameter defines the position according to the focus.

In fact, the last Twiss parameter is very important to define the ellipse angle with respect to the abscissa: if it is negative, the resulting ellipse has an angle as in Fig. 4.2 and the beam is diverging (after the focus) because the particle with the highest x' has also a positive x, whereas if α is positive, the beam is converging (before the focus). Finally if α is zero, the beam is on the focus. This is explicated in Fig. 4.3.

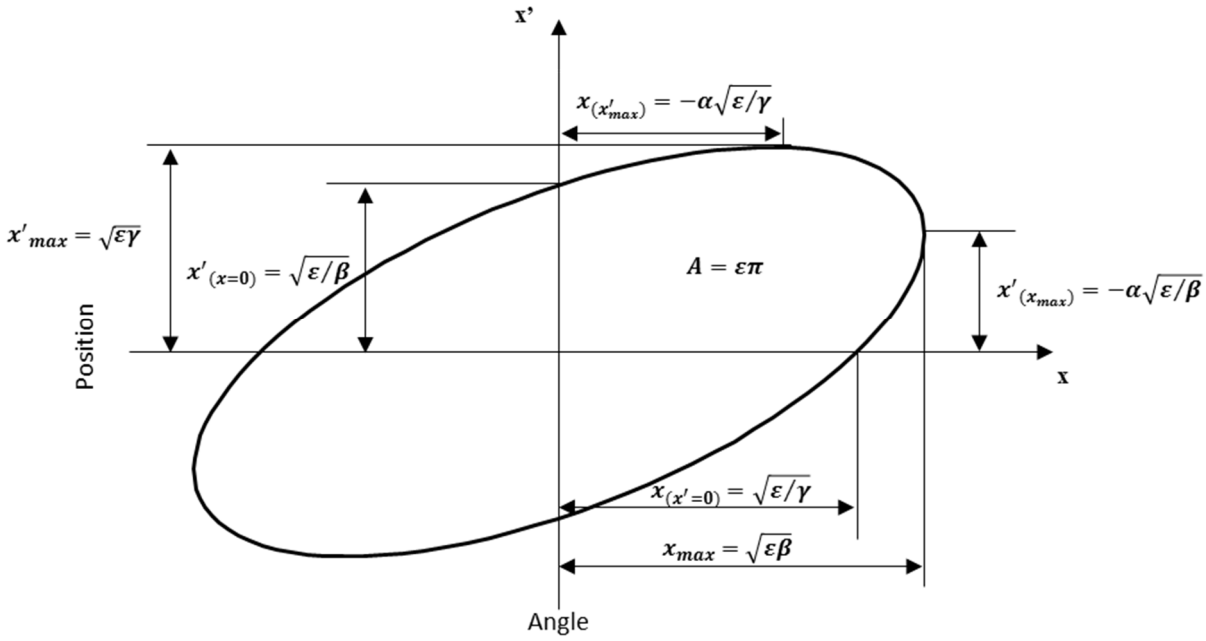

Fig. 4.2. Ellipse shape defined by the Twiss paramters.

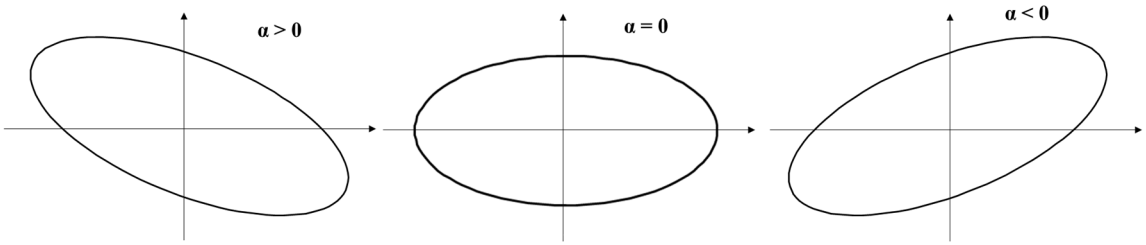

Fig. 4.3. Influence of α Twiss parameter to the ellipse shape.

Since the ellipse is mathematically characterize only three parameters (axes lengths and grade angle), assuming ε independent, the three Twiss parameters are related by an equation which is presented in (4.3).

$$x_{max} = \sqrt{\varepsilon\beta} \tag{4.1}$$

$$x'_{max} = \sqrt{\varepsilon\gamma} \tag{4.2}$$

$$\alpha^2 + 1 = \beta\gamma \tag{4.3}$$

4.1.3. The non-linear effects [4.6]

During the beam transport design, especially in the design phase of the various components involved on, one of the most important concern is to avoid the increase of the emittance, that leads to an essentially increase of the beam size. In fact, it is no more possible to recover the emittance except with a specific device, called beam cooler, which anyway inserts beam losses and high costs. The beam emittance increase is due to the non-linear effects which can be:

- Bad vacuum and, consequently, beam scattering
- Aberrations due to non-linear electric and magnetic fields
- Image effects
- Space charge
- Etc.

Among all these factors, the first two will be cited in this thesis. The first one is probably the cause of a strange beam shape found during the experimental validation of the Wien Filter presented in paragraph 4.7, whereas the second one is the main concern taken into account during the design of the beam transport device. Moreover, the non-linear effects can be evaluated without any beam transport simulation basing on the electric and magnetic field distribution which are matters belonging to the engineering sphere. Simply, if the electric or magnetic fields are not a linear distribution with respect to the nominal beam axis, applying a transformation to the ellipse, another function different from an ellipse is found; this effect results on the consequent emittance increase, as represented in Fig. 4.4.

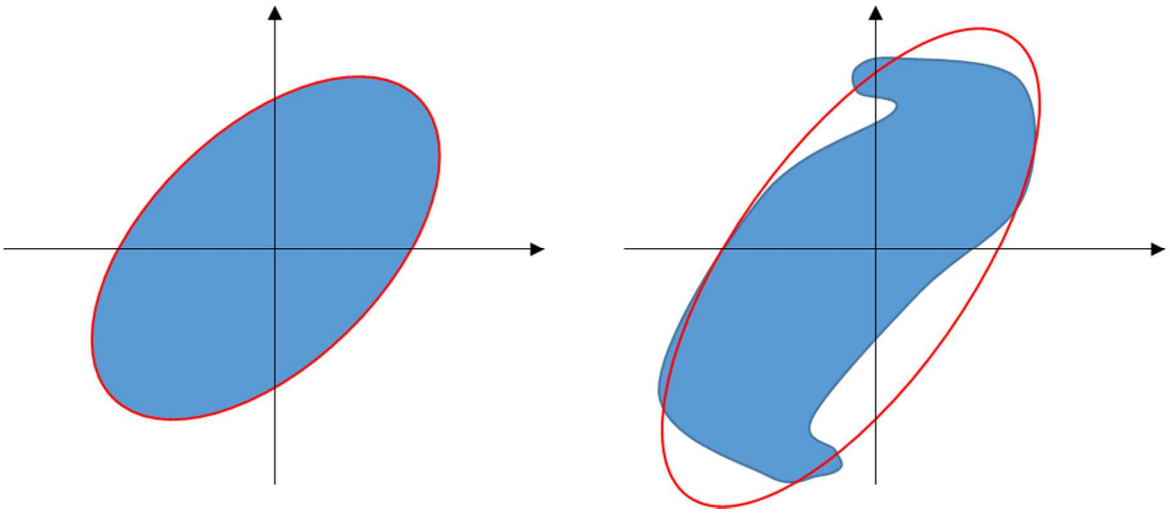

Fig. 4.4. Example of the non-linear effects on the beam particle distribution. The increase of the ellipse area is cleared even without the increase of the blue area representing the particles.

4.2. Analytical study

The Wien Filter is a velocity separator. Assuming a magnetic field *B* perpendicular to an electric field *E*, both uniformly distributed in the space, the particle that travels undeflected in the space has:

$$\vec{F} = q\left(\vec{E} + \vec{v} \times \vec{B}\right) = m \cdot \vec{a} = 0 \tag{4.4}$$

Where *v* is the particle speed and (4.4) is simply the Lorentz force. So:

$$v = \frac{\vec{E}}{\vec{B}} \tag{4.5}$$

If the beam of a certain energy is composed by different masses, the velocity depends by the mass and the Wien Filter can be used as a mass separator. In particular, the ability of separation, in this chapter called *ott*[1], can be defined as:

$$ott^1 = \frac{s}{d} \tag{4.6}$$

Where *s* is the distance between the two mass centre peaks and *d* is the diameter of the beam, as in Fig. 4.5. If *ott* is greater than one, the beam should be completely separated because the distance between the masses is greater than the beam composed by each mass.

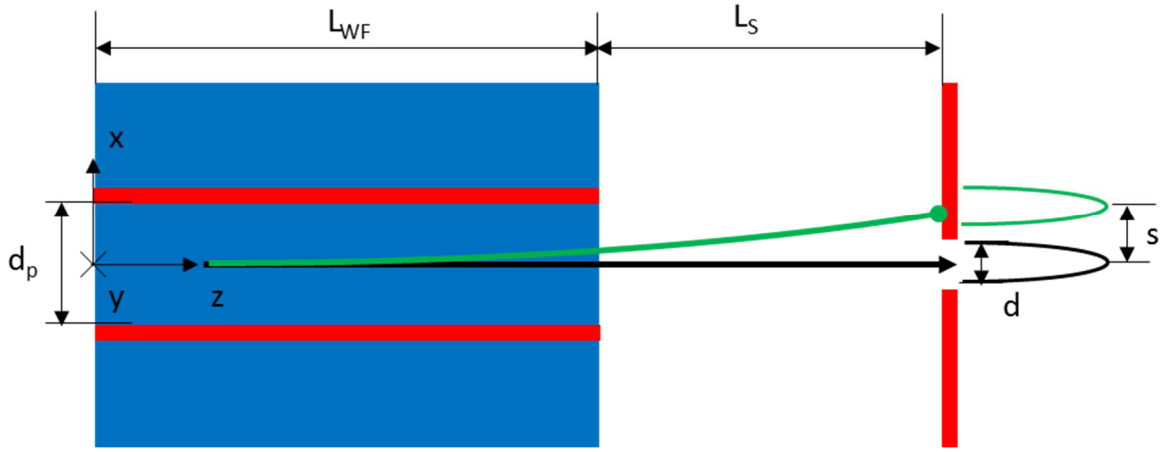

Fig. 4.5. Main dimensions characterising the Wien Filter. If s>d, then ott>1, the masses are separated, as here.

The highest value of *ott* determines the best Wien Filter design; in general, highest is the beam peak separation *s* or smaller is the beam diameter *d* better it is. Three different Wien Filter configurations can be found in literature:

- The classical version: the Wien Filter has a flat pole. It is the version usually provided by companies and installed in the Front-End before the modifications implemented during this thesis (Fig. 4.6a).

[1] *ott* has not a specific meaning, but simply it comes from the Italian word *ottimizzazione* (optimization)

- The most tilted version: the Wien Filter has tilted poles and the value of the tilted angle is determined by a formula developed in paragraph 4.2.3. It is probably the solution implemented in [4.2], but it is not very clear due to poor information and justifications presented there, while they will be provided in this chapter (Fig. 4.6b).
- The intermediate tilted version: it is a compromise between the previous two cases and the solution developed in [4.1] and [4.3] (Fig. 4.6c).

In this paragraph, a short analytical study will be presented using the notation of Fig. 4.7. Only part of this study was presented in literature ([4.1], [4.2], [4.3]), in particular the formula providing the separation *s*, whereas nothing was said about the beam dimension *d*, which is original in this thesis. Consequently, two main equations for each case will be always demonstrated, providing the maximum beam diameter *d* and the peak separation *s,* which determine the separation power of the Wien Filter.

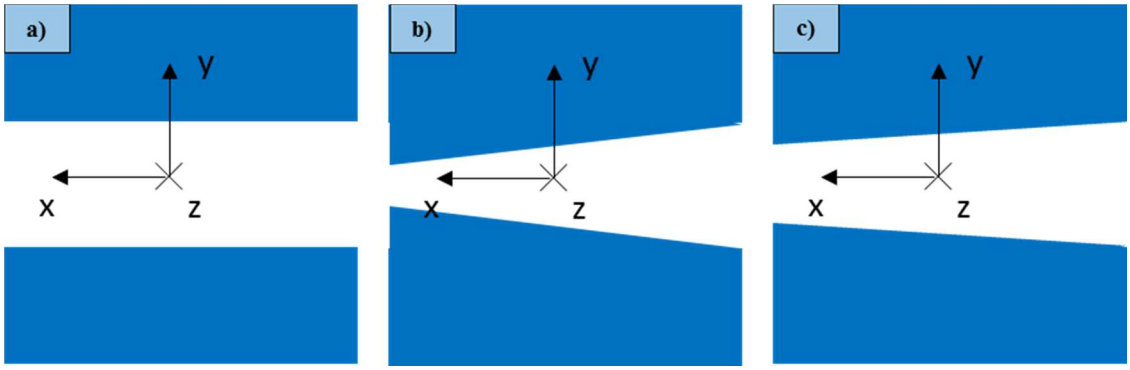

Fig. 4.6. The three version of a Wien Filter: a) case 1, flat pole; b) case 2, most tilted pole; c) case 3, intermediate tilted pole.

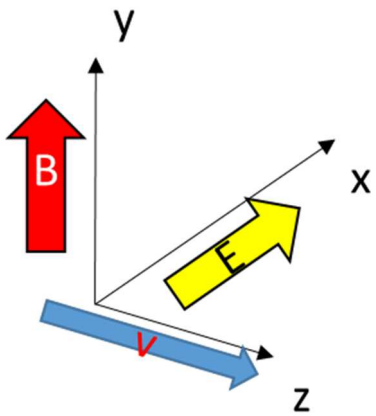

Fig. 4.7. Configuration used during the analytical study and in all this chapter.

4.2.1. General approach

The hypothesis for the general approach are:

- Uniform electric field *E* inside the Wien Filter, absence on the external region (absence of edge effect)

- Uniform magnetic field along the z axis, whereas an uniform gradient B_y' along the x axis is assumed. This leads to a gradient even for the y plane. Additionally, it is assumed absence of magnetic field on the external region (absence of edge effect).
- Gaussian beam

The second consideration defines the magnetic field inside the Wien Filter, which in general will be:

$$B_y(x) = B(x) = B_0 + B_0\, B_y' x = B_0(1 + B' x) \tag{4.7}$$

Where, if it is not specified, the magnetic field B and its gradient B', in this paragraph, is intended just along the y axis. B_0 is of course the magnetic field in the axis centre. The equation of particle motion are then:

$$m\ddot{x} = q\left(E - B_y \dot{z} + B_x \dot{y}\right) \tag{4.8}$$

$$m\ddot{y} = q(B_x \dot{z} - B_z \dot{x}) \tag{4.9}$$

$$m\ddot{z} = q\left(B_y \dot{x} - B_x \dot{y}\right) \tag{4.10}$$

A first approximation is the assumption that the speed on the x and y axis is negligible respect to the z axis. Without taking into account the motion along the y axis (not important for analytical case – speed along y equal to zero), the equations become:

$$m\ddot{x} = q(E - B\dot{z}) \tag{4.11}$$

$$m\ddot{z} = qB\dot{x} \tag{4.12}$$

B and B' starting from now are intended just the components along y axis.

Inside the Wien Filter, the potential is null only along the z axis, whereas off-axis the kinetic energy changes, according to

$$E_K = q(V_e + Ex) \tag{4.13}$$

Where V_e is the extraction potential. The consequently speed particle in the x position is:

$$v = \sqrt{2\frac{q}{m}(V_e + Ex)} = \sqrt{2\frac{q}{m}V_e} \cdot \sqrt{1 + \frac{E}{V_e}x} \tag{4.14}$$

Expanding at the first order of the Taylor series and assuming that the speed is essentially along the z axis (see Appendix A):

$$\dot{z} \approx v = \sqrt{2\frac{q}{m}(V_e + Ex)} = v_0 \cdot \left(1 + \frac{E}{2V_e}x\right) \tag{4.15}$$

Where it is considered that the particle speed before entering in the Wien Filter is:

$$v_0 = \sqrt{2\frac{q}{m}V_e} \tag{4.16}$$

Inserting (4.7) and (4.15) in (4.11), the equation resolving the particle motion in the x-axis for the Wien Filter is found:

$$m\ddot{x} = q\left[E - B_0(1 + B'x)\cdot v_0 \cdot \left(1 + \frac{E}{2V_e}x\right)\right] \tag{4.17}$$

And omitting the second order terms of x, the equation turns out:

$$\ddot{x} + B_0 v_0 \frac{q}{m}\left(B' + \frac{E}{2V_e}\right)x = \frac{q}{m}(E - B_0 v_0) \tag{4.18}$$

The solution of this equation describes the motion along the x axis of the particle of mass m and initial speed v_0 (calculated according to the extraction potential V_e) inside a uniform electric field E and a magnetic field B with gradient B'. The various pole geometries determine different solutions of this second order linear differential equation.

In all this study, along the z axis, the speed $\dot{z}$ will be considered essentially constant and equal to v_0.

4.2.2. Case 1: the classical Wien Filter with flat pole

In this case, due to the flat pole, no gradient B' is present inside the WF and the magnetic field is essentially B. Equation (4.18) becomes:

$$\ddot{x} + \frac{E}{2V_e}Bv_0\frac{q}{m}x = \frac{q}{m}(E - Bv_0) \tag{4.19}$$

Considering (4.5) true even for different masses for the left part of the equation (very small errors introduced for mass not so different from m), it turns out:

$$\ddot{x} + \left(B\frac{q}{m}\right)^2 x = \frac{q}{m}(E - Bv_0) \tag{4.20}$$

That is the classical harmonic equation. ω is defined as:

$$\omega = B\frac{q}{m} \tag{4.21}$$

The particle trajectory on the x plane is then:

$$x = A\cdot cos(\omega t + \varphi) + \frac{1}{\omega^2}\frac{q}{m}(E - Bv_0) \tag{4.22}$$

Where A and φ depend on the boundary conditions of the particle.

To calculate the separation of two different masses, the boundary conditions are relative to the particle that enters perfectly aligned at the Wien Filter centre: (x,y,z) = (0,0,0), $(\dot{x}, \dot{y}, \dot{z})$ = (0,0,v), leading to calculate parameters A and φ.

The result is the equation below, already presented in [4.2]:

$$x = \frac{m}{qB^2}(E - Bv)\left[1 - cos\left(\frac{q}{m}Bt\right)\right] \tag{4.23}$$

Where v will be simply the initial speed v_0. Calling x' the angle of the particle respect to x axis, at the Wien Filter exit we get:

$$t_{WF} = L_{WF}\frac{B}{E} \tag{4.24}$$

$$s_{WF} = x(t_{WF}) = \frac{m}{qB^2}(E - Bv)\left[1 - cos\left(\frac{q}{m}\frac{B^2}{E}l_{WF}\right)\right] \tag{4.25}$$

$$x_{WF}{}' = \frac{\dot{x_{WF}}}{v} = \left(\frac{E}{vB} - 1\right)\cdot \sin\left(\frac{q}{m}\frac{B^2}{E}l_{WF}\right) \tag{4.26}$$

The position at the slits of the mass m with initial speed v is:

$$s = s_{WF} + x_{WF}{}' \cdot L_S$$

$$s = \frac{m}{qB^2}(E - Bv)\left[1 - cos\left(\frac{q}{m}\frac{B^2}{E}l_{WF}\right)\right] + \left(\frac{E}{vB} - 1\right)\cdot \sin\left(\frac{q}{m}\frac{B^2}{E}l_{WF}\right)\cdot L_s \tag{4.27}$$

(equation of mass separation for case N°1).

To get the minimum beam spot d, an assumption has to be done: the particle that travels closer to the Wien Filter plate is the most divergent at the slits, where the beam is focused. In general, this is not mathematically true, but, especially if the beam spot at the slits is small compared to the maximum beam size in the Wien Filter, it can be well approximated in this way. The first boundary condition, which lets finding the parameters φ, is relative to the most divergent particle (A different from 0):

$$(x + L_s \cdot \dot{x})|_{@\,WF\,exit} = 0 \tag{4.28}$$

Reminding (4.5) for the reference particle, the consequence is:

$$\varphi = \text{atan}\left(\frac{v_0}{L_S\,\omega}\right) - \omega\, L_{WF}\frac{B}{E} \tag{4.29}$$

The second condition fixes the maximum position of the particle inside the Wien Filter, according to different φ:

$$A = \frac{D_{MAX}}{2f} \qquad if\ \varphi < 0 \tag{4.30}$$

$$x(0) = \frac{D_{MAX}}{2f} \qquad if\ \varphi > 0 \tag{4.31}$$

D_{MAX} is the maximum diameter accepted inside the Wien Filter and f the factor depending on the amount of particles composing the Gaussian beam that has to respect this condition. In general, this value will be assumed 3, consequently only 0.27% of the particles will be out of this value (the Gaussian tail). Two equations have been provided according to different lengths of the Wien Filter: in fact, if the length is short enough (φ higher than zero), only a small part of the cosines equation represents the particle trajectory inside the WF, as presented in Fig. 4.8.

Moreover, it is clear in the sketch that the particle, travelling inside the WF, is more and more focused. This effect was already reported in all the main citations.

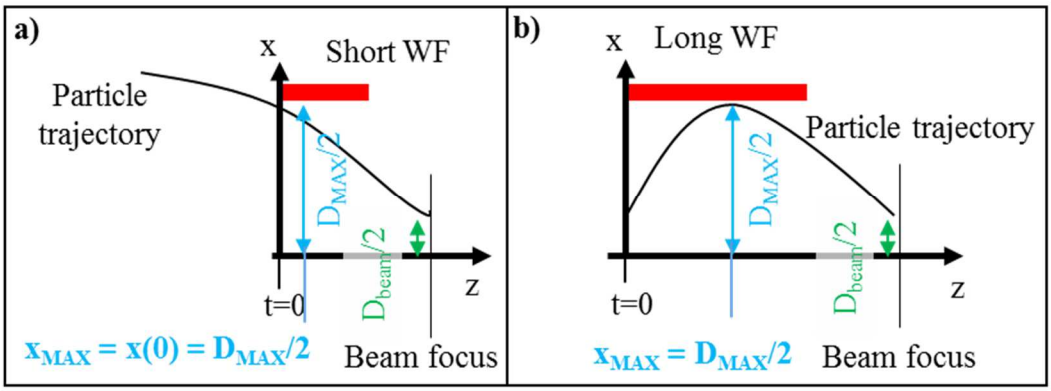

Fig. 4.8. Different particle trajectory for different WF length.

After some omitted calculi, the dimension of the beam corresponding to the total beam diameter D_{beam} is:

$$D_{beam} = 4f^2 \frac{\varepsilon}{D_{MAX}} \sqrt{{L_S}^2 + 4\frac{{V_e}^2}{E^2}} \quad if\ \varphi < 0 \tag{4.32}$$

$$D_{beam} = \frac{4f^2}{cos\varphi} \frac{\varepsilon}{D_{MAX}} \sqrt{{L_S}^2 + 4\frac{{V_e}^2}{E^2}} \quad if\ \varphi > 0 \tag{4.33}$$

(equation of beam x size for case N°1)

Where D_{beam} is assumed $2f$ the RMS beam radius. It is clear that the beam diameter does not depend on the beam mass.

4.2.3. Case 2: the most tilted pole Wien Filter

In this case, the poles of Wien Filter has to completely remove the focusing effect showed in the previous paragraph, as suggested in [4.2]. The focusing effect is essentially due to the change of the particle speed out of the axis in the x direction. For a simple explanation, the equation of the Wien Filter (4.5) can be changed as:

$$\sqrt{2\frac{q}{m}[V_e + x \cdot E(x)]} = \frac{E(x)}{B(x)} \tag{4.34}$$

In particular, q, m, V_e are constant. Moreover, it is much more simple to adapt the magnetic field B to a certain profile, instead of the electric field E. For this reason, in the three papers cited [4.1], [4.2], [4.3], E is always considered constant along x, whereas a tilted pole is studied to get the desired B profile. In this case, the B profile which resolves equation (4.34) is:

$$B(x) = \frac{B_0}{\sqrt{1 + \frac{E}{V_e}x}} \tag{4.35}$$

Where B_0 is:

$$B_0 = \frac{E}{\sqrt{2\frac{q}{m}V_e}} \tag{4.36}$$

Expanding in series Taylor:

$$B(x) = B_0 - B_0\frac{E}{2V_e}x \tag{4.37}$$

The gradient of the magnetic field results:

$$B'_{MAX} = -\frac{E}{2V_e} \tag{4.38}$$

Assuming that the magnetic resistance of the magnet is essentially due to the air gap g between the poles, calling I the current on the coil, N the number of spire, the magnetic field is:

$$B = \frac{\mu_0 N\, I}{g} \tag{4.39}$$

Consequently, the ideal function for the gap g is:

$$g = \frac{\mu_0 N\, I}{B_0}\sqrt{1 + \frac{E}{V_e}x} = g_0\sqrt{1 + \frac{E}{V_e}x} \tag{4.40}$$

Expanding in Taylor series:

$$g = g_0 + g_0\frac{E}{2V_e}x \tag{4.41}$$

The gap increase can be inserted tilting the Wien Filter poles and the angle α can be found as:

$$\theta = arctan\left(\frac{g_0}{2}\frac{E}{2V_e}\right) \tag{4.42}$$

Since the electric field is created by the potential V_p applied to the electrodes of the Wien Filter (positive on one electrode and negative to the other), the equation becomes:

$$\theta = arctan\left(\frac{1}{2}\frac{g_0}{d_p}\frac{V_p}{V_e}\right) \tag{4.43}$$

The angle does not depend on the beam mass and charge, but just on the geometrical dimension of the Wien Filter g_0 and d_p (distance between WF electrodes), on the extraction

potential V_e and on the potential to the electrodes V_p. If θ is fixed, even the ratio between V_p and V_p can not be changed.

Then, substituting (4.38) into the general equation of motion (4.18), the trajectory of the particle inside the WF becomes a standard parabola.

$$\ddot{x} = \frac{q}{m}(E - B_0 v_0) \tag{4.44}$$

In this case, the separation between two adjacent masses are derivable from (4.44) assuming:

$$\frac{\Delta v}{v} \approx \frac{1}{2}\frac{\Delta m}{m} \tag{4.45}$$

And the solution was already well described in [4.2]:

$$s = \frac{L_{WF}\left(L_s + \frac{L_{WF}}{2}\right)E}{4\,V_e}\frac{\Delta m}{m} \tag{4.46}$$

(equation of mass separation for case N°2).

What it misses in previous work was the beam focusing. Since no focusing effect should be present, the Wien Filter is just a long drift of length $L_{WF} + L_S$. This is confirmed reminding (4.5) for the reference particle and inserting it into (4.44) because it changes its solution to a straight line. Using the matrix of a common drift, the boundary conditions below were assumed:

$$(\alpha, \beta, \gamma)|_{@\ slits} = \left(0, \frac{{D_{beam}}^2}{4f^2\varepsilon}, \gamma_S\right) \tag{4.47}$$

$$(\alpha, \beta, \gamma)|_{@\ WF\ entrance} = \left(\alpha_0, \frac{{D_{MAX}}^2}{4f^2\varepsilon}, \gamma_0\right) \tag{4.48}$$

Where D_{MAX} is the maximum diameter accepted inside the Wien Filter and f the factor already defined in the previous paragraph, ε the beam emittance. Then, the beam diameter at the slits D_{beam} results:

$$D_{beam} = 2f\sqrt{\frac{2\varepsilon(L_{WF} + L_S)^2}{\frac{1}{\varepsilon}\left(\frac{D_{MAX}}{2f}\right)^2 + \sqrt{\frac{1}{\varepsilon^2}\left(\frac{D_{MAX}}{2f}\right)^4 - 4(L_{WF} + L_S)^2}}} \tag{4.49}$$

(equation of beam x size for case N°2).

It is underline that the beam diameter does not depend on the beam mass.

4.2.4. Case 3: the intermediate tilted pole Wien Filter

This is the most complete case since *B'* is present but it does not simplify the equation (4.18). In this case, the pole angle can vary between zero and the value defined in the previous

paragraph. A very similar approach to paragraph 4.2.2 will be performed, since the only difference is the definition of the parameter ω, which here is:

$$\omega = \sqrt{\frac{q}{m} B_0 v_0 \left(B' + \frac{E}{2V_e} \right)} \tag{4.50}$$

The beam particle trajectory is now represented by:

$$x = A\, cos(\omega t + \varphi) + \frac{\frac{E}{B_0 v_0} - 1}{B' + \frac{E}{2V_e}} = A\, cos(\omega t + \varphi) + \frac{1}{\omega^2} \frac{q}{m} (E - B_0 v_0) \tag{4.51}$$

Where A and φ depend on the boundary conditions assumed as before.

Imposing the boundary conditions $(x,x')=(0,0)$, the beam separation turns out:

$$s = s_{WF} + x_{WF}{}' \cdot L_S$$
$$s = \frac{1}{\omega^2} \frac{q}{m} (E - B_0 v_0) \left[1 - cos\left(\omega \cdot \frac{B}{E} l_{WF} \right) + \frac{\omega}{v_0} L_s \sin\left(\omega \cdot \frac{B}{E} l_{WF} \right) \right] \tag{4.52}$$

(equation of mass separation for case N°3).

As for paragraph 4.2.2, the first boundary condition lets to find the parameters φ, relative to the most divergent particle (A different from 0):

$$(x + L_s \cdot \dot{x})|_{@\, WF\ exit} = 0 \tag{4.53}$$

Reminding (4.5) for the reference particle. Consequently:

$$\varphi = \text{atan}\left(\frac{v_0}{L_S\, \omega} \right) - \omega\, L_{WF} \frac{B}{E} \tag{4.54}$$

That is the same equation found in 4.2.2, remarking that ω is evaluated in a slightly different way.

On the other hand, imposing even here (4.30) or (4.31) according to different φ values, the total beam diameter D_{beam}, assuming that it corresponds to $2f$ the RMS beam radius, is:

$$D_{beam} = 4f^2 \frac{\varepsilon}{D_{MAX}} \sqrt{{L_S}^2 + 4 \frac{{V_e}^2}{E^2} \frac{\frac{E}{2V_e}}{B' + \frac{E}{2V_e}}} \quad if\ \varphi < 0 \tag{4.55}$$

$$D_{beam} = \frac{4f^2}{cos\varphi} \frac{\varepsilon}{D_{MAX}} \sqrt{{L_S}^2 + 4 \frac{{V_e}^2}{E^2} \frac{\frac{E}{2V_e}}{B' + \frac{E}{2V_e}}} \quad if\ \varphi > 0 \tag{4.56}$$

(equation of beam x size for case N°3).

It is underline that the beam diameter does not depend on the beam mass. On the other hand, the increase of the magnetic field gradient *B'*, which is negative, decreases the focalizing force of the Wien Filter and, consequently, increases the beam diameter.

4.2.5. Discussion of the results

As an example, the beam particle trajectory will be presented in Fig. 4.9 for the parameters of Table 34 corresponding to the final case of paragraph 4.5.2.

Beam properties			
m	150	amu	Mass particle
Ve	42000	V	Potential of extraction
ε_{RMS} @ 25keV	5	πmm mrad	Emittance assumed at 25 keV
f	3	[ ]	Factor referred to Gaussian
D_{max}	45	mm	Maximum beam diameter tolerated
Geometric dimensions			
L_{WF}	875	mm	Wien Filter length
L_S	783	mm	Slits distance
g_0	108	mm	Magnetic gap at beam axis
D_p	50	mm	Wien Filter Electrode distance
Wien Filter "power"			
B	0.8	T	Magnetic field at beam axis
B'	-1.1	T/m	Magnetic field gradient (case N° 3)

Table 34. Characteristics assumed for the reference case.

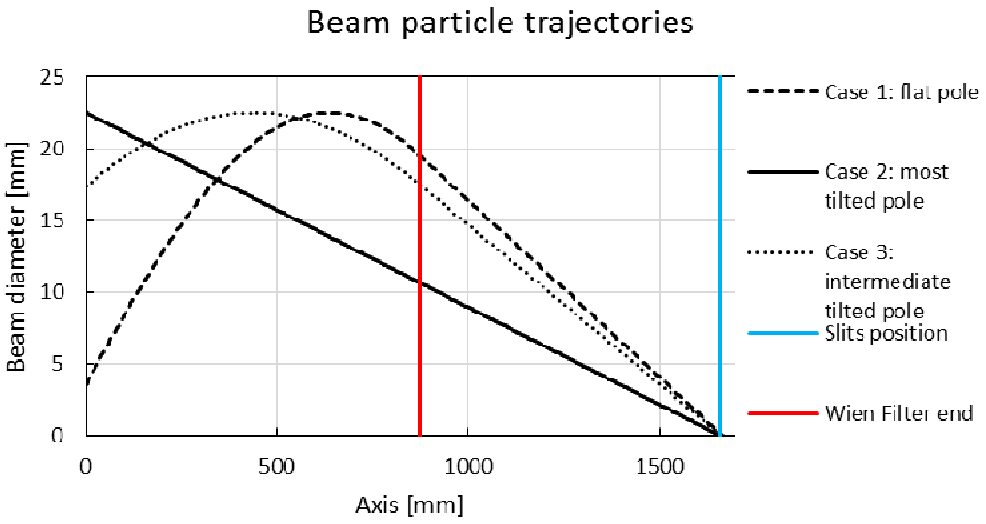

Fig. 4.9. Example of beam particle trajectories for the three cases according to Table 34.

It is clear that, in the case 1, the particle has an angle at the slits position higher than the others have. This reflects on the beam diameter at the slits which is small in this case. On the other hand, a case 2 Wien Filter has always a beam focus worse than the other cases.

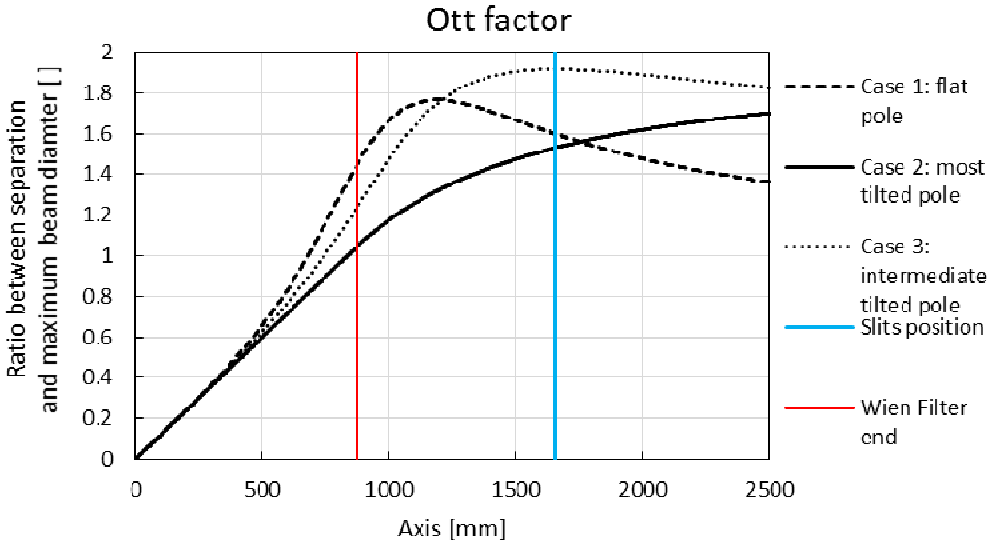

Fig. 4.10. Minimum beam diameter achievable according to different position on the axis.

The peak separation, in general, decreases with the increasing potential V_e and mass m. Anyhow, except for the case 2, this depends on the specific case.

Table 35, presented below, summarizes the various parameters influencing the Wien Filter performances.

Parameter	Description	Type	Characteristic of
m	Particle mass	Independent	Beam
q	Particle charge	Independent	Beam
V_e	Potential of extraction	Independent	Beam
v	Speed mass	Dependent (m, q, Ve)	
L_{WF}	Wien Filter effective length	Independent	WF Geometry
L_S	Slits distance	Independent	WF Geometry
D_{MAX}	Maximum beam diameter	Independent	WF Geometry
B	Magnetic field	Independent	WF Geometry
B’	Magnetic field gradient	Independent	WF Geometry
g	Pole gap	Dependent	WF Geometry
θ	Pole tilted angle	Dependent (B, B’, g)	WF Geometry
E	Electric field	Dependent (m, q, Ve, B)	
f	Number of Gaussian sigma	Independent	Quality design

Table 35. Summary of the dimensions determining the Wien Filter performances.

4.3. The boundary condition for the Wien Filter redesign

The object of this chapter is, beyond the study and the definition of the correct design procedure of a Wien Filter, to redesign the first version of the Wien Filter (bought from an external company) in order to increase as much as possible the resolving power, to manufacture and finally to test it.

The first version was presented in Fig. 4.1. It follows the recommendation of a classical Wien Filter according to the previous case N°1. The main parameters and information are provided in Table 36.

Parameter	**Value**	**Note**
Pole gap	130 mm	Magnetic circuit geometry
Maximum pole length	760 mm	
Pole width	326 mm	
Magnetic effective length	782 mm	
Electrode gap	50 mm	Electrostatic "geometry"
Electrode height	100 mm	
Electrostatic effective length	800	
N° of coils	2	Coil
Number of turns (total)	154x2 = 208	
Resistance 20°C	285 mΩ	
Maximum current	240 A	Current power supply
Maximum potential	72 V	
Maximum resolution (surely excessive)	< 0.5 ppm	
Maximum potential	5000 V	Electrostatic power supply
Maximum resolution	< 50 ppm	

Table 36. Main information of the first version of the Wien Filter.

During the redesign, the constraints are:

- Do not change the coil and the magnetic circuit (very expensive – tens of thousands of euros)
- Do not change the current power supply (very expensive – tens of thousands of euros)
- It has to fit inside the SPES bunker (slit distance is not completely free)

It is underlined that the product between current and number of turns is almost proportional to the product between magnetic field and pole gap. During the redesign, it is possible to change:

- The electrostatic part
- The magnetic poles
- The magnet thickness adding new pieces
- Slits distance

4.4. Optimization of the electrostatic chamber

4.4.1. The preliminary information for the electrodes design

In this paragraph, the various steps for the design of the electrostatic part of the Wien Filter are presented. The main dimensions are (see Fig. 4.11):

- Distance between electrodes d
- Electrode length L_E, thickness t_E and height h_E
- Distance between electrode and vacuum chamber d_{EC}
- Vacuum chamber dimensions (section height h_C, width w_C and wall thickness s)

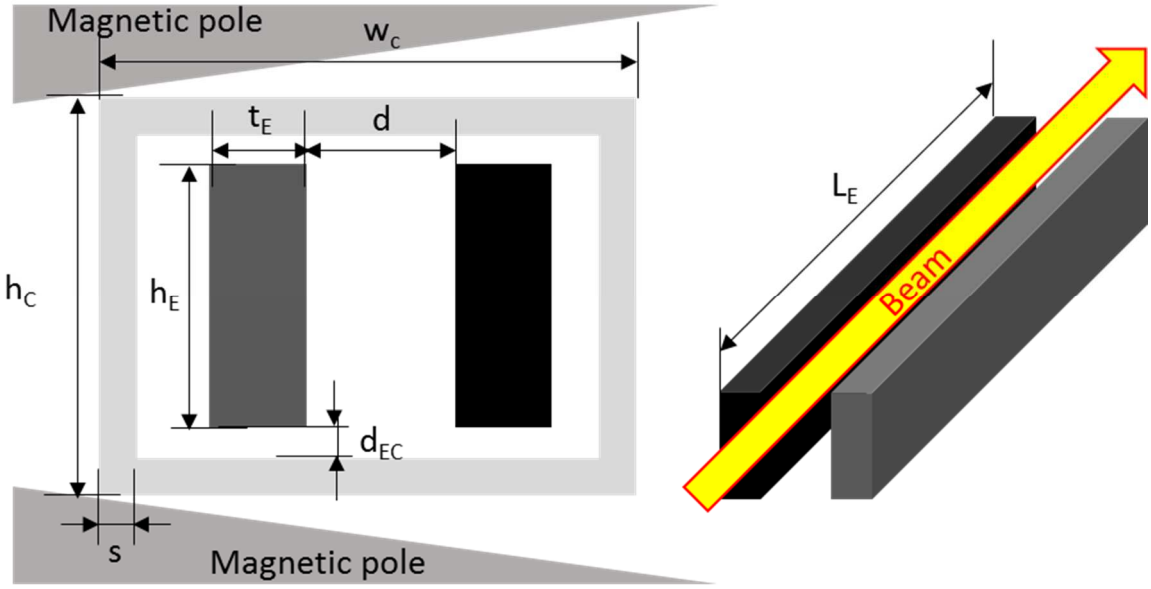

Fig. 4.11. Main dimensions of the Wien Filter section and on the 3D simplified drawing.

The influences on the various dimensions are presented below.

Parameter	***Type***	***Dependent on***	***Influence on***
d	Section	Beam emittance	• Maximum beam focusing • w_C • h_E
L_E	Longitudinal	Very close to L_{WF}	• Maximum beam focusing (only for case 2) • Beam separation • Wien Filter length, coil length, current power supply (only voltage)
t_E	Section	Manufacturing process	• w_C
d_{EC}	Section	Electric insulation of vacuum	• h_C • w_C
h_E	Section	d	• Electric field uniformity • h_C • Current power supply (current and voltage) to get determined magnetic field B • s • w_C (low effect and just for cases 2 and 3)
s	Section	Minimum chamber deflection tolerate h_E, d_{EC}	• Current power supply (current and voltage) to get determined magnetic field B • w_C
h_C	Section	d, (t_E), h_E, d_{EC}, s	• Current power supply (current and voltage) to get determined magnetic field B
w_C	Section	d, t_E, h_E, (d_{EC}), s	• Current power supply (current and voltage) to get determined magnetic field B (low effect and just for cases 2 and 3)

Table 37. Geometric parameters with dependences and influences.

The "independent" variables are the underlined parameters of Table 37, whereas the others depend on these. They have been called independent because their values are influenced just by external properties, like beam emittance, longitudinal length available, etc.

4.4.2. Definition of the "independent" dimensions

In this paragraph, the independent parameters are defined. In first place, the electrode length is almost independent from the dimensions of the section. For this reason, the study of its length can be postponed later.

The distance between electrodes *d* is the first dimension to be defined because it is the most influencing: it depends on it the electrode high h_c which determinates the pole gap, as it is possible to see in Fig. 4.11, and, consequently, the magnetic field. Moreover, it strongly influences the vacuum chamber width and, in second order, for the cases N°2 and N°3 again the pole gap due to the angle to provide to the magnetic pole.

In order to define the best distances between electrodes, some reasonable hypotheses have been assumed:

- The dependence of the pole gap on D_{MAX} according to the equation presented in the Fig. 4.12 (explication presented later in paragraph 4.4.3).
- The maximum magnetic field at the beam axis B_0 proportionally inverse to the magnetic pole gap g.

Using the beam properties of Table 34 and WF characteristics of Table 36, the separation performances of the final Wien Filter are presented here in Fig. 4.14 for a different maximum beam aperture D_{MAX}.

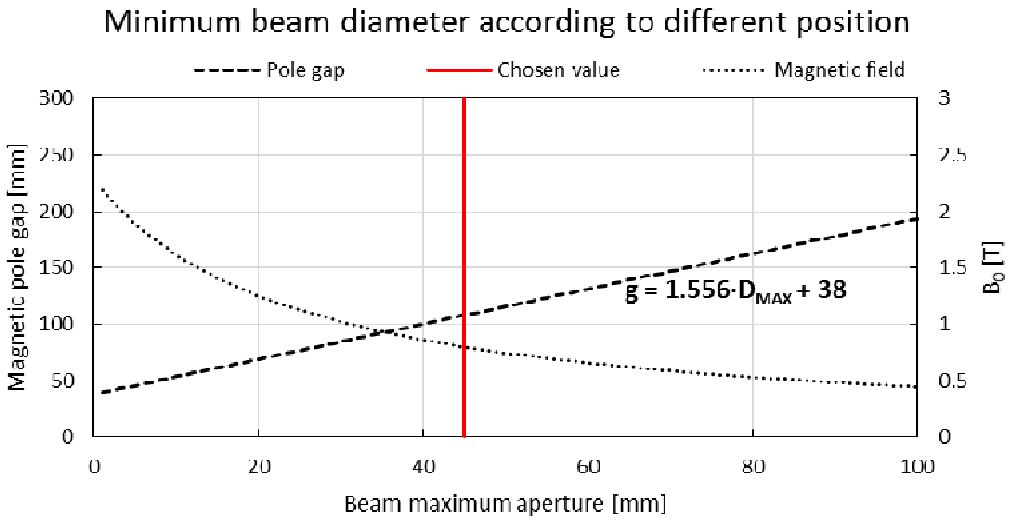

Fig. 4.12. Effect of the maximum beam aperture D_{MAX} on the magnetic pole gap g and magnetic field B_0 at the beam axis.

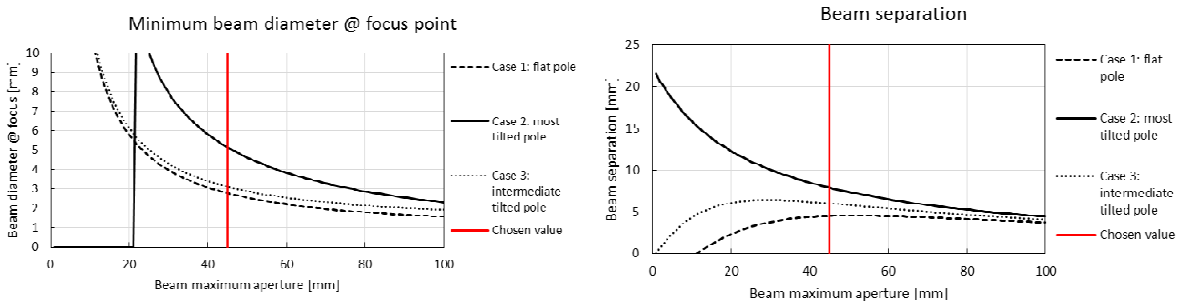

Fig. 4.13. Minimum beam diameter at the slits and beam peak separation according to different beam maximum aperture.

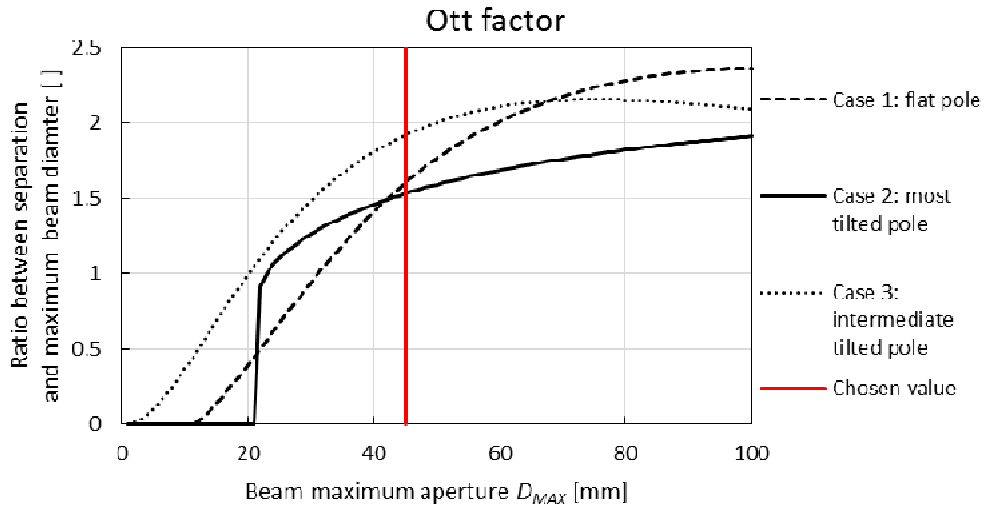

Fig. 4.14. Effect of the maximum beam aperture D_{MAX}.

It seems that higher is the beam aperture, better is for the *ott* factor. This is essentially due to a sharper focus even if the separation between two peaks of masses are smaller.

This study was possible to be performed only after the numerical definition of a first Wien Filter prototype. As a first step, 50 mm of distance was assumed, as the original version, for a maximum beam aperture fixed to 45 mm (10% lower) to avoid the beam passing too close to the electrodes. At a later time, it has not been taken into consideration the eventual increase of the beam maximum aperture (and consequently the distance between the electrodes) because:

- There was not enough time for another Wien Filter definition and the final version satisfied the requisites imposed for the redesign.
- The increase of the maximum beam aperture for the *case N°2* (the final chosen) leads to a bigger beam entering in the WF. This is not always possible because the triplet before the WF has to provide a bigger beam. As an example, a beam diameter over 60 mm is probably not deliverable by the present triplet without a consequent increase of the beam emittance due to non-linear effects.
- The increase of the electrode distances surely increases the fringe fields, both for the electrical and magnetic part.
- Higher is the beam radius, higher are the non-linear effects introduced for the most off-axis particles (showed later).

Some very preliminary experimental tests were performed on the extractor electrode and the SPIS in order to find the maximum electric field tolerated in our vacuum level (≈ 10^{-6} mbar). In theory, its value for a perfect vacuum is infinite, but in reality, it was found on the order of 3 kV/mm. To be sure that no discharges could happen between the WF electrodes and the

ground, a maximum nominal value of 1 kV/mm has been fixed. Originally, the maximum potential to apply was found 6.5 kV, then the dimension d_{EC}, distance between the electrodes and the ground, has been fixed to 6.5 mm. This potential was able to create the minimum electric field to "contrast" the magnetic field of 1.1 T.

t_E is the electrode thickness and it weakly influences the vacuum chamber width w_C. A minimum thickness is required to manufacture a very long electrode avoiding bending due to the manufacturing process and due to the stresses inserted during the extrusion process of the rough bar. Moreover, this is a fundamental dimension to design the components used to maintain in position the electrodes. Its minimum value has been estimated to be 6 mm.

4.4.3. Optimization of the electrode height h_E

As previously said, the electrode distances is the most influencing parameters of the Wien Filter electrostatic part. In particular, increasing the distance, in order to maintain the same electric field uniformity, even the electrode height has to be increased. The effect is a higher pole gap and, consequently, a smaller magnetic field (being equal the product between current and number of turns). It is underlined that a good electric field uniformity does not increment the beam emittance and, consequently, the beam spot at the focus and, in general, it does not make the beam line transport worse.

For this reason, it is very important to reach the best compromise between a good electric field uniformity, which needs high electrode height, with the highest magnetic field, easily obtainable with small electrode height. An optimization procedure has been implemented in order to find the best electrode geometry manufacturable. Two different shapes were suggested in literature:

- [4.2]: this geometry does not compensate the presence of the grounded vacuum chamber
- [4.3]: this has a good electric field uniformity but only along the beam axis.

A reasonable shape is showed in Fig. 4.15, where a parallelepiped is surmounted by a protrusion which is necessary to uniform the electric field and "shield" the presence of the grounded vacuum chamber. The beam essentially will travel through the yellow area, consequently the electric field has to be uniform just on that zone.

By means of the Ansys mechanical package, the geometry has been prepared according to Fig. 4.15 and the red parameters have been varied in order to find the minimum of the following value:

$$ris = \sqrt{\frac{\sum_{i=1}^{n}\left(E_{x,i} - m\right)^2}{n}} \tag{4.57}$$

Where $E_{x,i}$ is the electric field of a 1 mm grid of points inside the yellow square and m is defined as:

$$m = \frac{\sum_{i=1}^{n} E_{x,i}}{n} \tag{4.58}$$

Simply, the value *ris* is the mean square deviation of the electric field inside the yellow circular sector. It is underlined that the potential applied to the electrode is 1 V and a normalization has not in this way foreseen.

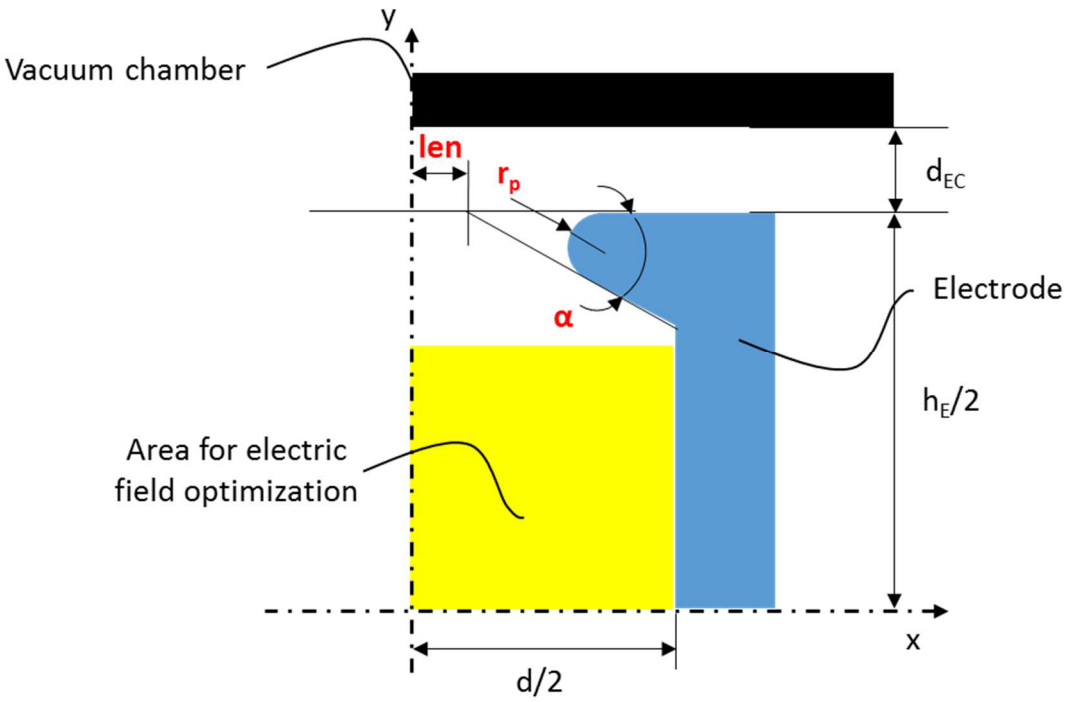

Fig. 4.15. Section of the Wien Filter electrode geometry to optimize.

The optimization process has been performed for various electrode height and, for each optimum geometry, the following parameters have been estimated:

$$E_{x,m,j} = \frac{\sum_{i=1}^{n} E_{x,i,j}}{n} \tag{4.59}$$

$$\sigma_{j,E_{x,j}} = \sqrt{\frac{\sum_{i=1}^{n}\left(E_{x,i,j} - E_{x,m,j}\right)^2}{n}} \tag{4.60}$$

Which are simply the mean electric field and the RMS error on the x component of the electric field for all the grid position at the y axis, as showed in Fig. 4.16. The results for all the optimized geometry are presented in Fig. 4.17.

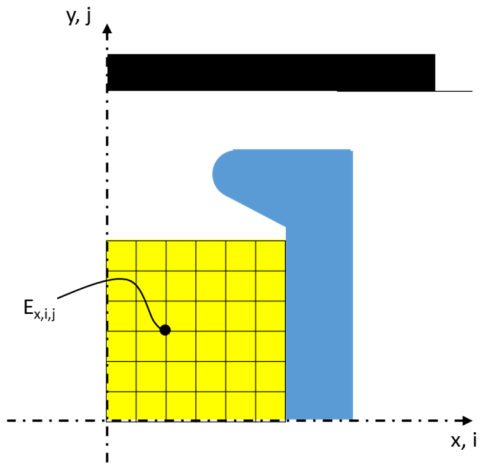

Fig. 4.16. Grid of point for the evaluation of the electric field uniformity.

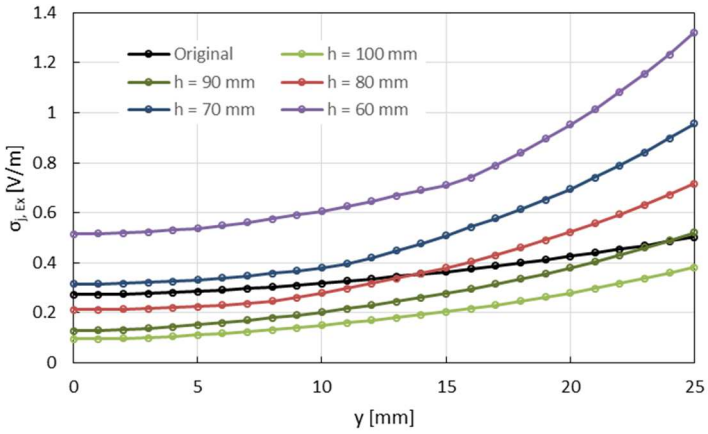

Fig. 4.17. Error on the electric field for the various optimized geometry.

It is clear that even with a 90 mm of electrode height, the uniformity of the electric field is better for the optimized version compared to the original one. Moreover, for a small *y*, the 70 mm optimized version is very good, whereas an important uniformity drop can be observed for the 60 mm electrode height.

To determine the minimum tolerated non-uniformity, some beam transport simulations have been implemented by TraceWin [4.7]. By this code, it is possible to characterize the beam transport both from a matrix and multi-particles point of view. In particular, the possibility to fly thousands of particle is very important: importing on the code the field map provided by external codes, such as COMSOL [4.8] [4.9], Ansys or other FEA codes which can simulate electric and magnetic fields, the trajectories of the ions can be accurately simulated. In this case, the electric and magnetic fields were simulated by COMSOL for all the "optimum" geometries found before introducing some reasonable fillets due to the working process. These small simplifications do not influence the electric field uniformity.

In particular, the analyses were performed for a higher magnetic field (about 1.1 T) since there was still the idea to change the current power supply, but the study is surely valid for smaller values. It is underlined that just the minimum beam transport simulations will be presented in order to focusing more on the engineering aspects.

The main properties of the simulations for the different optimized poles are presented below in Table 38. The increment of emittance in Fig. 4.18 is considerable for the case h = 60 mm (10%), whereas it is certainly acceptable for the case with h = 70 mm (2%). The effect on the phase space and beam profile is visible in Fig. 4.19: with the electrode of 60 mm height, the beam is quite spread on positive x due to the particle in the red circle (about 4%) that are the cause of the emittance increase. This comparison was the reason of the definition of the electrode height.

Mass particle *m*	150 amu
Extraction potential V_e	42 kV
Beam intensity	1 μA
Emittance @ 25 keV	25 π mm mrad
Maximum magnetic field B_0	1.1 T
Pole version (paragraph 4.5.2)	"v_3"
Pole length	760 mm
Pole angle (Case N°2)	9.5°
Pole gap	110 mm
Magnet thickness walls	150 mm
Maximum electric field *E*	0.248 MV/m
Potential applied V_p	6171 V
Electrode length	750 mm
Pre-electrode length (see paragraph 4.4.4)	130 mm

Table 38. Main properties of the beam transport simulation to fix the electrode height

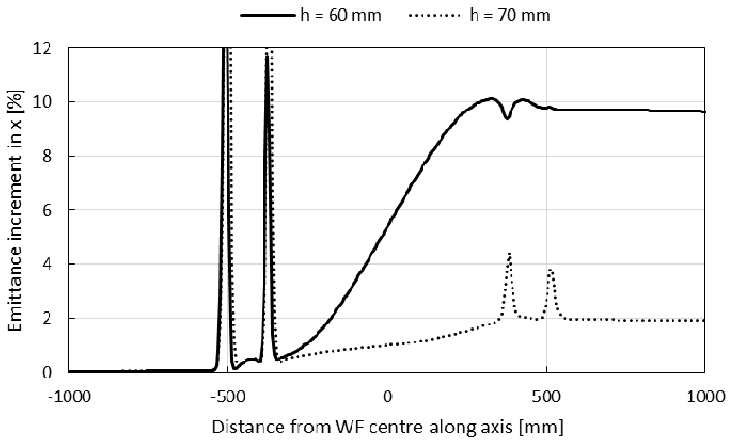

Fig. 4.18. Increment of emittance for the two electrode version.

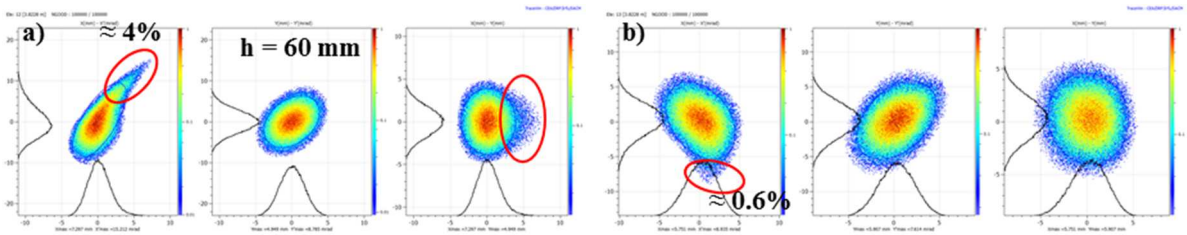

Fig. 4.19. Case of h = 60 mm (a) and h = 70 mm (b) height electrode. For each case, three picture are presented. In sequence: phase space on x-x' plane; y-y' plane; beam profile.

In the previous paragraph (4.4.2), the straight line slope of Fig. 4.12 was defined basing on this study. In particular, the best electrode height h_E has been here found 70 mm, for a distance between the electrode d of 50, leading to a ratio of 1.4. It was assumed that the maximum beam aperture D_{MAX} (taken 45 mm) is approximately proportional to the electrode distance d to avoid that the beam travels too close to the electrode. Consequently, the final slope is get by equation (4.61) that is the same of Fig. 4.12. On the other hand, the constant term of Fig. 4.12 simply depends on the minimum thickness needed to place the electrode, dependent on electrical insulation, wall thickness and alignment play. The second order term, due to the extra pole gap needed to maintain the pole angle, has not taken into account.

$$m = \frac{d}{D_{MAX}} \cdot \frac{h_E}{d} = \frac{50}{45} \cdot \frac{70}{50} = 1.556 \qquad (4.61)$$

4.4.4. The electrode length and the pre-electrode

As already said, the electrode length depends on the pole dimensions. In fact, since the Wien Filter is the result of the combination of the magnetic and electric field, their properties are deeply related. In particular, the electric and magnetic effective lengths, which is defined in (4.62) and it represents the length of an optic element seen by the ions, have to be very close, in order to avoid beam deviation from the axis as reported later.

$$L_{EFF}(x,y) = \int_{-\infty}^{\infty} t(x,y,z)\, dz \qquad (4.62)$$

(t is the electric field E or the magnet field B along the beam z axis)

The effective length usually provided for the optic elements corresponds to the values of L_{EFF} in (4.62) at x=0 and y=0 (beam axis), but the homogeneity on the x and y plane is the sign of a good field uniformity. In order to study the best distance between the electrode and the ground along the beam axis, the effective lengths on the x and y plane are evaluated for different distances *d* of the ground maintaining the same profile even for the grounded electrode, as in Fig. 4.20.

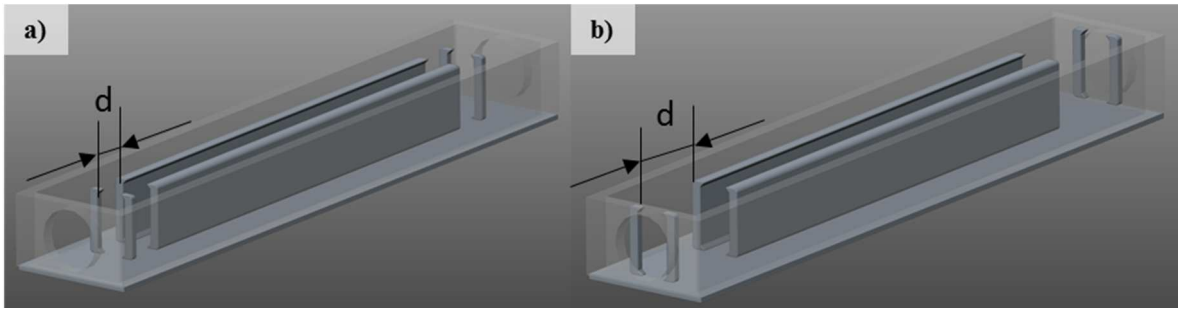

Fig. 4.20. Example of two different distances analysed: a) d = 20 mm; b) d = 100 mm.

The error on the effective length calculated for the axis x and y are presented in Fig. 4.21.

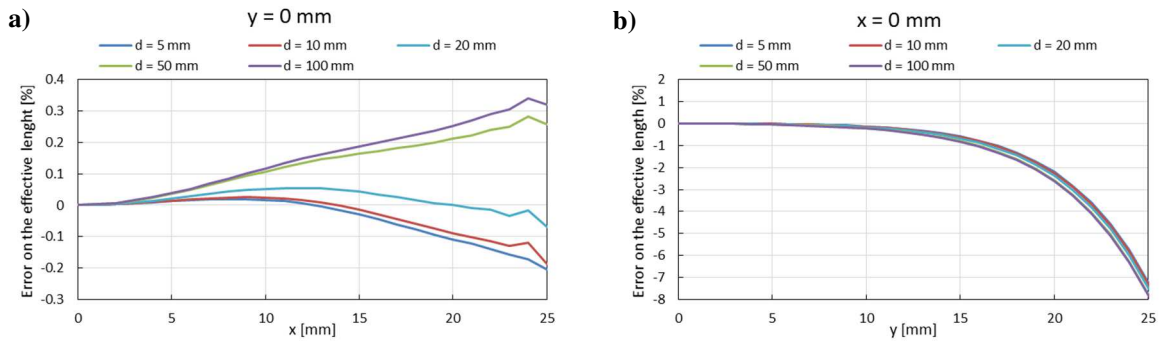

Fig. 4.21. Effective length calculated for the x and y axis. The position (0,0) is the beam axis.

Analysing Fig. 4.21a, it is evident that higher distances are not preferable since they cause an error on the effective length even at small x. On the other hand, a distance of 20 mm seems the best on the overall x position, but with a shorter distance, the electric field is better for small x. Anyhow, the error on the effective length for distances below 20 mm is low. Moreover, it is necessary longitudinal space to place far the grounded electrode and, in this case, a lot of space is not available. It is remarked that, it is very important to maintain the beam inside the Wien Filter small on the y plane in order to decrease as much as possible the errors due to the effective length visible in Fig. 4.21b, as it will be specified in paragraph 4.5.2.

The effect of the electric field on the longitudinal dimension is presented in Fig. 4.22. Its trend at the end of the electrode is not so sharp even with a small gaps *d*, but the effective length increment, due to the "protrusion" of the field in the space, is almost linear for short distances. This could be a good point to easy evaluate the effective length without any simulation. It is underlined that, after a certain value, approximately 25 mm, the increment on the electrode distance does not lead to an increment of effective length and, consequently, the protrusion of the electric field can not adjust as will. This protrusion is called "fringe fields" and it is present both for electric and magnetic fields.

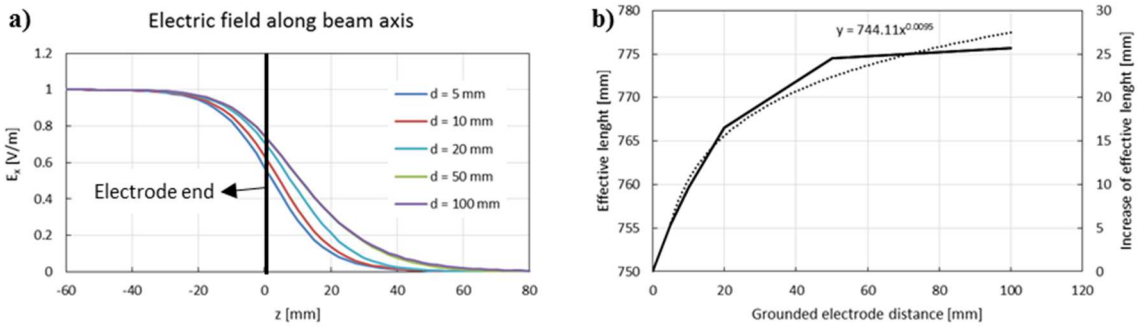

Fig. 4.22. Electric field along beam axis for different ground electrode distances.

Finally, the effect of the grounded electrode longitudinal dimension is presented in Fig. 4.23. All the previous results were obtained with a reasonable grounded electrode of 10 mm length. Here it is presented the comparison with a 130 mm length electrode: the curves are so close that are difficult to be distinguished. Essentially, there is not a change for different electrode lengths.

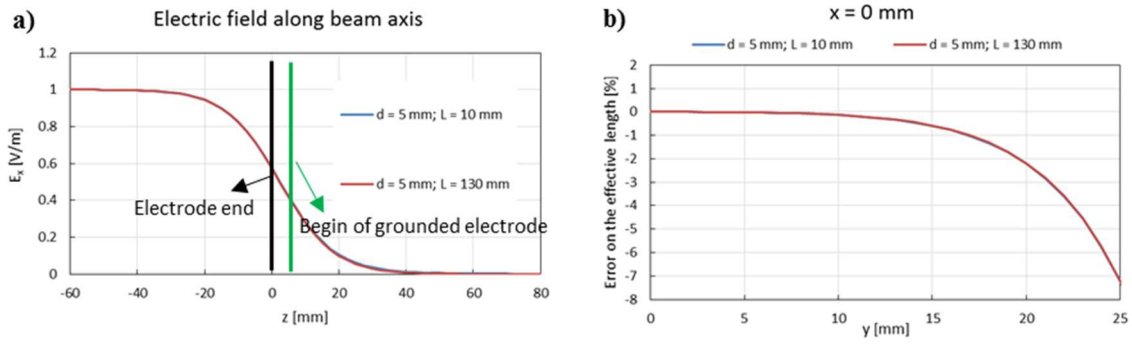

Fig. 4.23. Effect of the grounded electrode longitudinal dimension on electric field and on the error on the effective length.

In conclusion, in order to fix the electrode length, it is important to well know even the magnetic effective length. In general, higher it is, higher the resolving power of the Wien Filter is. Then, since the maximum pole length is a boundary condition of the study (760 mm), the relative maximum effective length is defined by it. In [4.10], some typical functions to

represent the magnetic field are presented. In this case, assuming the long tail curve, the effective length with a 760 mm pole length turns out 907 mm and the magnetic field (normalized) is presented in Fig. 4.24. It is evident that the fringe fields are decisively more pronounced than for the electric field since they are clearly visible even at more than 300 mm far from the pole end (electric maximum 40 mm).

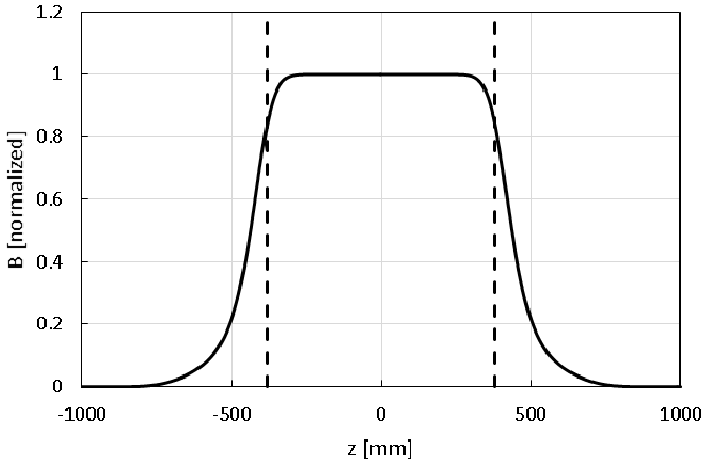

Fig. 4.24. Magnetic field along Wien Filter axis estimated by long tail formula in [4.10] - pole gap of 108 mm. The dotted lines are the pole starting and end points.

Since the electric and magnetic field profiles can not be the same due to the very different fringe fields, an estimation of this effect on the particle trajectories has to be performed. In order to simplify the problem, the electric fringe fields have been simplified with a straight line. Two cases have been taken into account corresponding to the wider cases: grounded electrode distances of 5 and 100 mm. The simplification is presented in Fig. 4.25a, whereas in Fig. 4.25b the comparison between the electric and magnetic field is performed. The electric field was the simplified version, with d = 100 mm, which is the most pronounced. Anyway, the magnetic field is decisively more spread.

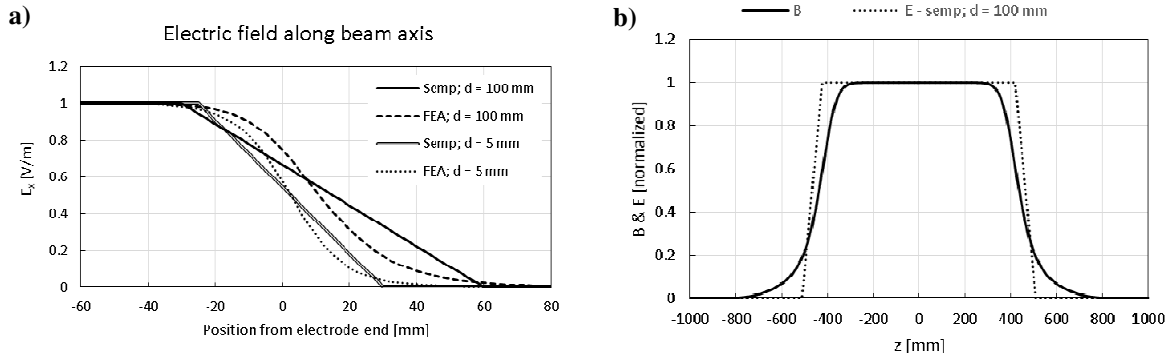

Fig. 4.25. a) Electric field along beam axis with ground electrode distance of 5 and 100 mm, for FEA results and simplified cases; c) comparison of the electric and magnetic fringe fields (simplified; d = 100 mm).

The effect on the beam is a movement off-axis of its centre. This can be estimated numerically integrating equation (1.2) by an Excel file, where q and m are respectively beam charge and mass, V_e the extraction potential.

$$\ddot{x}(t) = \frac{q}{m}\left(\sqrt{\frac{2qV_e}{m}} \cdot B(z(t)) - E(z(t))\right) \tag{4.63}$$

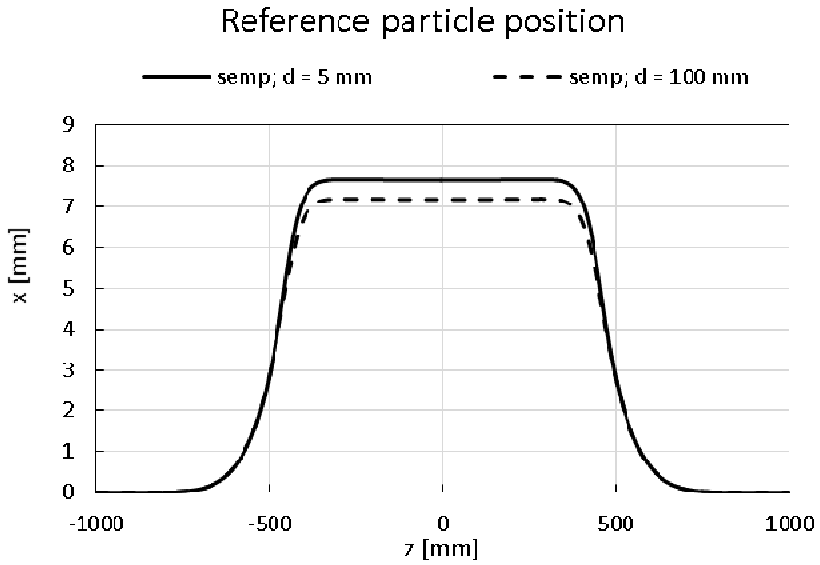

Fig. 4.26. Off-axis x reference particle position due to the different magnetic and electric fringe fields, for two different electric field profiles.

For a beam energy of 42 keV, mass 150 amu, 1+ charge and maximum magnetic field of 0.8 T (data from Table 34), the results are presented in Fig. 4.26. The differences between the two electrode distances are significants and the beam movement out of the axis, preliminary evaluated to 7 mm, is very high compared to the maximum electrode aperture of 50 mm. This cause a reduction of 30% on the maximum beam radius accepted, from 25 mm (50 mm of diameter) to 18 mm (36 mm of diameter). For this reason, in order to minimize this bad effect, two supplemental electrodes, called pre-electrodes, have to be installed before and after the main electrode. The length of the electrodes could be defined once the magnetic pole has been fixed.

It is underlined that at off-axis positions of Fig. 4.26, the beam has different energy and, consequently, speed. This effect has not been taken into account in this equation and the final beam movement is expected slightly lower.

For a more organic presentation of the work, the magnetic field profile along the beam axis found in the next paragraph will be here used. This is the input to define the length of the various electrodes. As said, the magnetic and electrostatic profiles have to be closest as

possible, to avoid the movement of the beam off-axis inside the WF. For this reason, the two functions presented in equations (4.64) and (4.65) have to be as close as possible.

$$L_{EFF-B}(z) = \frac{\int_{-\infty}^{z} B(s)ds}{B_0} \tag{4.64}$$

$$L_{EFF-E}(z) = \frac{\int_{-\infty}^{z} E(s)ds}{E_0} \tag{4.65}$$

The optimum corresponds to the minimum of the parameter e in (4.66).

$$e = \int_{-\infty}^{\infty} \left(L_{EFF-B}(z) - L_{EFF-E}(z)\right)^2 dz \tag{4.66}$$

This has been numerically performed by a simple Matlab code, assuming 4 mm the space between the main electrodes and the pre-electrode, and 2 mm the space with the grounded electrodes. Moreover, the electric field along the axis has been simplified as in Fig. 4.25. The two parameters to optimize are, then, the electrode lengths (main and pre-electrode) and the results are showed in Fig. 4.27.

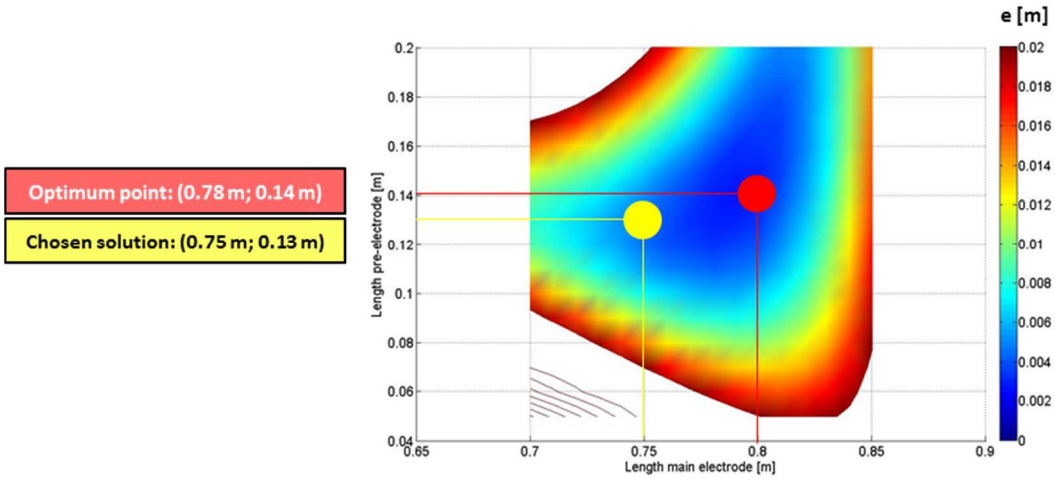

Fig. 4.27. Optimum found for the final pole configuration.

Analysing the optimum point, the two directly consequences of the electrode lengths are:

- The length of the vacuum chamber has to be about 1.1 m (1.06 m just for the three electrodes)
- The ratio between the potentials of the pre-electrodes and main electrodes is 0.313

A preliminary evaluation of the spaces available in the FE suggests to reduce the vacuum chamber length in order to increase the slits distance due to the maximum space available in the bunker. A good compromise is the couple (0.75; 0.13) since it combines the minor errors with the minor lengths. In this configuration, the potential to apply to the pre-electrode is about 45% of the main one and the two functions, that seems very close, are presented in Fig. 4.28.

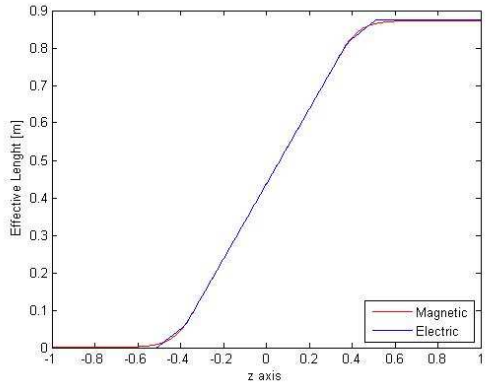

Fig. 4.28. Function of the first preliminary evaluation of the effective magnetic and electric length for the designed WF (the magnetic pole will be discussed in paragraph 4.5). z=0 corresponds to Wien Filter centre.

4.5. Redesign of the magnetic pole

4.5.1. Definition of the pole characteristics and effects

The WF magnetic pole geometry can be described by four main parameters:

1. The pole gap, which defines the maximum beam dimension on the y plane and the magnetic field obtainable with a certain product of coil turns and current. In the Wien Filter case, it depends also on the dimension of the electrostatic chamber.
2. The pole width, that usually depends on the required field homogeneity on the x plane. Higher it is, higher is the magnetic field homogeneity reached. For this particular case, the width is defined by the current Wien Filter version.
3. The pole angle: it is usually introduced when a beam required an extra focusing on the y plane. In the Wien Filter, for cases N°2 and N°3, the y focusing is a consequence of the wanted x plane defocusing (to compensate the x plane focusing due to the electric field). The angle will be defined in the next paragraph 4.5.2, but the effect on the beam in this one.
4. The pole dimension along beam axis. Usually, the Rogowsky profile is adopted in order to reduce the magnetic saturation that changes the dipole properties (effective length, edge focusing, etc.). Even this effect will be presented here

Starting to analyse the point three, it is underlined that it concerns only the Wien Filter cases N°2 and N°3, since the first one is a standard magnet with parallel poles. For the particular point, the magnetic field at the magnet centre will be analysed along the x axis (horizontal plane). The main characteristics are presented below in Table 39.

Mass particle m	150 amu	Independent
Extraction potential V_e	42 kV	Independent
Maximum magnetic field B_0	0.8 T	Independent
Pole gap g	108 mm	Independent
Magnetic field gradient (Case N°2) B'	-2.21	Dependent (B_0, V_e, m)
Pole angle (Case N°2) θ	6.8°	Dependent
Magnet thickness walls s	150 mm	Independent
Electric field E	0.186 MV/m	Dependent
Potential applied V_p	4650 V	Dependent

Table 39. Main characteristic of the pole characterization angle.

The ideal magnetic field has to follow equation (4.67), which is directly consequence of (4.35), and the comparison with a FEA magneto-static analysis is presented in Fig. 4.29 for a flat pole.

$$B(x) = \frac{B_0}{\sqrt{1 + \sqrt{\frac{2q}{mV_e}} B_0 x}} \tag{4.67}$$

The error introduced by the flat pole (instead of the ideal function) is quite small, but it increases significantly far from the axis. Moreover, the error is more significant at negative position, where the magnetic field is higher.

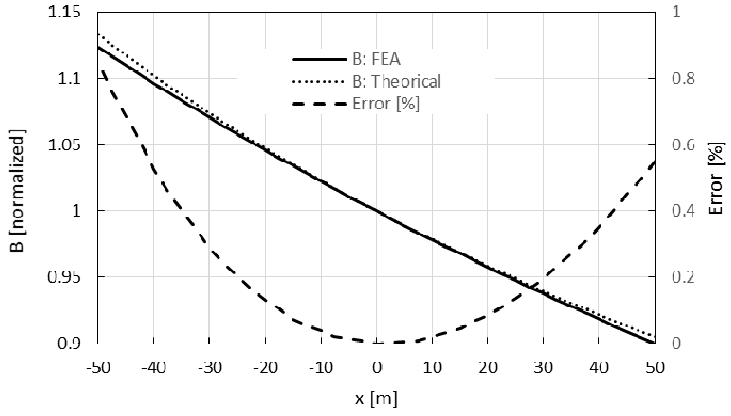

Fig. 4.29. Comparison between ideal magnetic profile at the Wien Filter centre and FEA results.

Finally, three different longitudinal pole profiles have been tested by TraceWin to characterize the best choice concerning the longitudinal dimension. In particular, the edges have different cut angle as it is showed in Fig. 4.30.

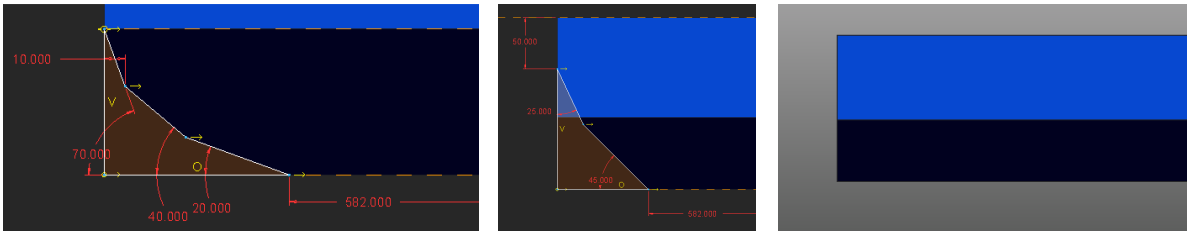

Fig. 4.30. Three different cut edge for the Wien Filter poles (v1, v2, v3).

The magnetic effective length changes are presented in Table 40, whereas the effect on the magnetic field are showed in Fig. 4.31. It is clear that the second version, due to higher angles, has an effective length shorter compared to the others, whereas the last one is the longer due to the maximum available length used. It is underlined that the effective length of the version 3 is not so far from that one calculated in paragraph 4.4.4 (907 mm – error of 4%).

Pole version	Effective length [mm]
v_1	855.2
v_2	817.7
v_3	868.4

Table 40. Effective length along the beam axis for different pole profiles.

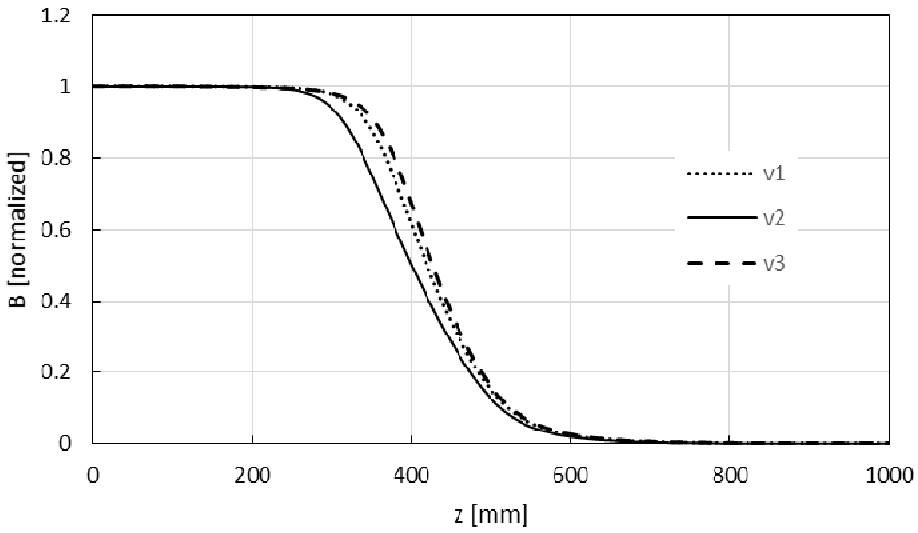

Fig. 4.31. Different magnetic profile due to the pole versions.

Assuming an electrode of length 740 mm, two pre-electrodes of 130 mm and gaps of 4 mm, with geometry as in paragraph 4.4.3, the results with a reasonable beam in Table 39 are presented. It is underlined that the magnetic field in this study is about 1.1 T because it was performed for a different power supply (and consequently higher currents available in the coil).

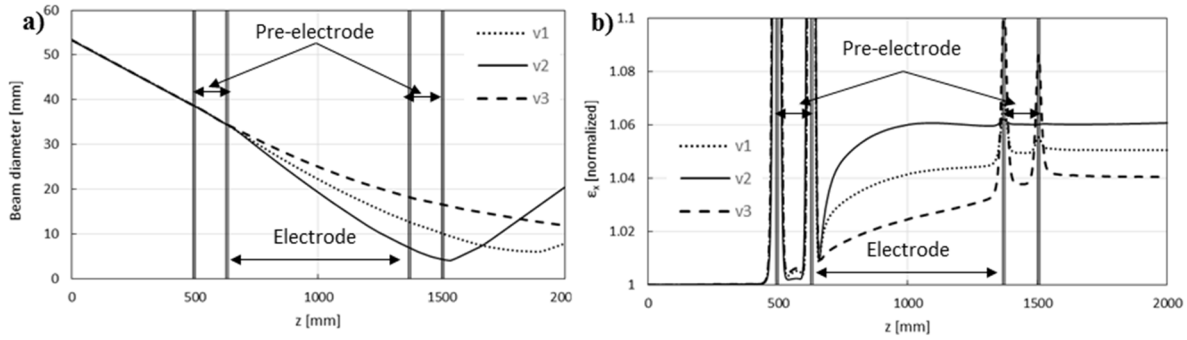

Fig. 4.32. Effect of the different pole edges on the beam: a) maximum diameter; b) emittance x-x' plane.

The change in the pole edge has two different effects:

1. On the beam diameter (Fig. 4.32a), due to different focusing: stronger for the shorter version (v_2), lower for the longer one (v_3).
2. On the emittance (Fig. 4.32b): its increase in the first part of the Wien Filter, where is present the effect of the different edges, is smaller for the version v_3 and higher on the v_2. This is the crucial point to define the best pole. Probably, in order to avoid any difference on the effective length, it is better to make it sharp instead of some others reasonably shapes. Moreover, due to the low magnetic field, the saturation effects that surely appears due to the sharp geometry, is confined at small areas as will be showed in paragraph 4.5.3.

Finally, the final geometry for the pole edge is assumed sharp, as in Fig. 4.33, due to the lower increment on the emittance, simplicity of production and the higher effective length that is available for a better separation of the peaks.

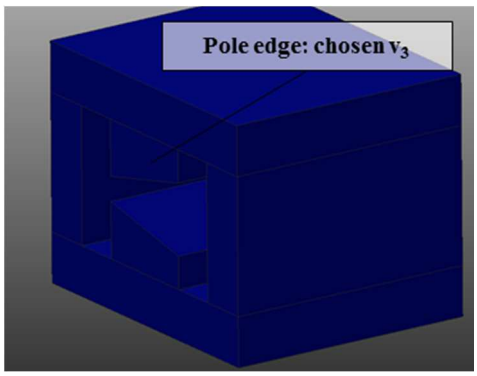

Fig. 4.33. Pole edge chosen: v_3.

It is underlined that in Fig. 4.32b the emittance for the version v_3 increases all along the Wien Filter (reaching anyway smaller values compared to the others), whereas the v_1 and v_2 seems to have a plateau at approximately the Wien Filter centre (z=1000 mm). This is probably due to the fact that versions v_1 and v_2 have smaller beam diameters there (Fig. 4.32a) and the

combination of non-homogenous electric field (Fig. 4.21) and non-ideal magnetic field (Fig. 4.29) at position far from the centre-axis increases the beam emittance.

4.5.2. The final pole

This paragraph will summarize all the previous results and it concludes the design phase of the device. In particular:

- The section of the electrode used according to paragraph 4.4.3 and all the consequent dimensions presented in 4.4 will be used.
- The distance between electrode, pre-electrodes and ground will be decreased as much as possible according to the maximum nominal electric field of 1 kV/mm. This reduces the longitudinal electrostatic dimension, maximizing the effective length.
- The pole longitudinal geometry according to paragraph 4.5.1.

The only dimension to decide is the tilting angle of the pole. This is essential in order to conclude the design. In particular:

- The Wien Filter provided by the external company has a flat pole (*case N°1*).
- [4.2] suggests that the pole angle has to completely remove the focusing effects. No formula are provided to calculate the tilting angle or the magnetic field gradient and, for this case, a non-critic reason why doing it was presented (*case N°2*).
- [4.1] and [4.3] suggested half of the pole angle of [4.2] in order to get the x and y plane focus in the same place and because it increases the performances respect to case N°1 (but nothing is said about case N°2) - (*case N°3*).

Since there were not any other specifications, all the three cases have been numerically tested. In particular, the definition of the other parameters leads to the dimensions presented before in Table 34 and the results in Fig. 4.10. It is clear that each case has his optimum slit distance, as presented in Table 41. Here, slit distance is intended the distance between the slit and the end of the Wien Filter effective length that is longer respect to the distance from the poles end. Moreover, the maximum beam diameter inside the WF has been inserted in the table. In fact, for each case, this parameter has been changed for reasons explicated below.

Case N°	**Slit distance**	**Maximum beam diameter in WF**
1	≈ 300 mm	33 mm
2	Maximum available: 783 mm	41 mm
3	≈ 783 mm	38 mm

Table 41. Slit distances according to the different cases.

The parameters in common are presented in Table 42 whereas the results in Table 43.

Beam properties			
m	150	amu	Mass particle
Ve	42000	V	Potential of extraction
ε_{RMS} @ 25keV	5	πmm mrad	Emittance assumed at 25 keV
f	3	[ ]	Factor referred to Gaussian
Wien Filter "power"			
B	0.8	T	Magnetic field at beam axis
L_{WF}	874	mm	Wien Filter length

Table 42. Parameters in common for the simulation

Case N°	Parameters		Analytical					Numerical					
	L_S [mm]	D_{MAX} [mm]	σ_N [mm]	β [mm]	D_{BEAM} [mm]	s [mm]	Ott [ ]	σ_N [mm]	β [mm]	D_{BEAM} [mm]	s [mm]	Ott [ ]	$\%\varepsilon_{inc}$
1	300	33	0.380	0.038	2.28	2.99	1.31	0.492	0.051	3.3	3.1	0.94	23.2
2	783	41	0.944	0.231	5.67	7.87	1.39	1.104	0.299	7.0	8.2	1.17	5.6
3	783	30	0.730	0.138	4.38	6.01	1.37	0.974	0.205	6.0	6.2	1.03	19.8

Table 43. Results of the analytical calculations and numerical simulations for the three cases.

Initially, it has to be underlined that the maximum diameter imposed D_{MAX}, which determined the minimum beam spot at the slits, has different values for each case. It has been fixed according to a reasonable increase of the emittance: higher is D_{MAX}, higher is the emittance increase. In particular for case N°1 and 3, it has been reduced respect to the case N°2 because the emittance increases considerably passing through the WF. This is clear looking to Fig. 4.34 and Fig. 4.36. The emittance increases is the highest on the last part of the Wien Filter, where, for cases N°1 and N°3 the beam has the biggest diameter.

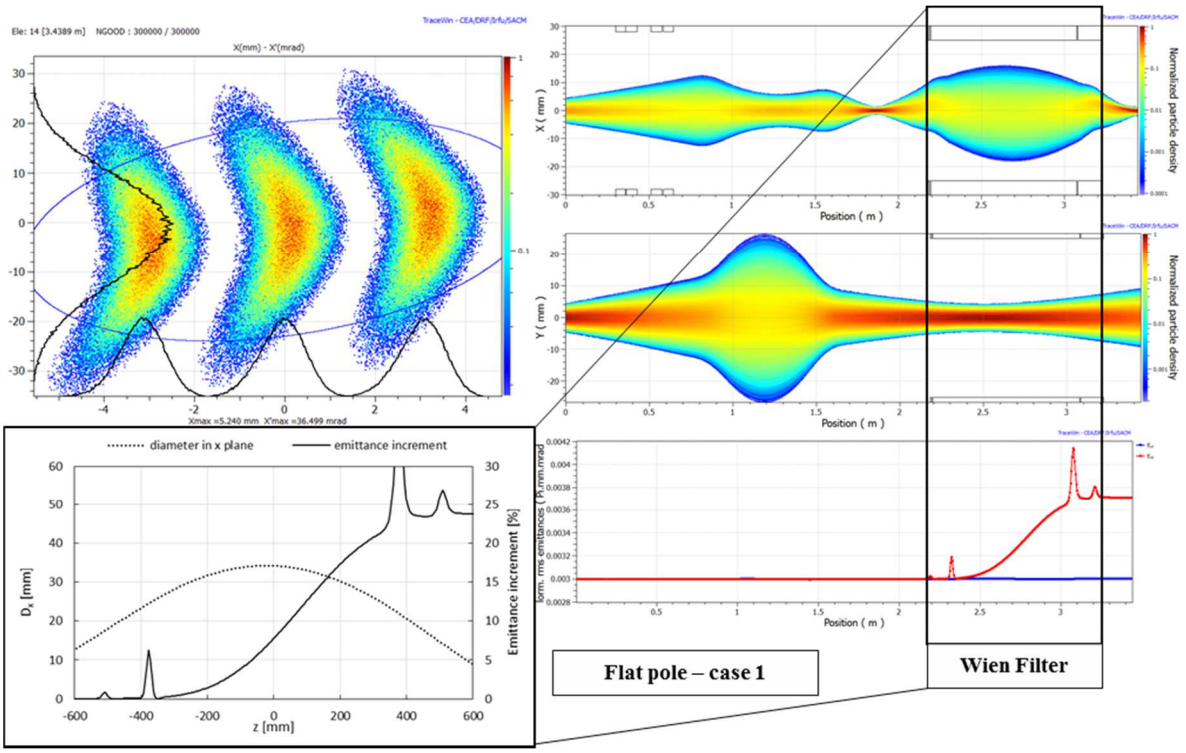

Fig. 4.34. Results for the optimum of the case 1; left: separation and beam on the x plane phase space and emittance increase and maximum diameter inside the WF; right: beam path on x and y plane, emittance increase in all the Front-End.

On the other hand, the case N°2, showed in Fig. 4.35, has the less emittance increase even if the beam diameter is higher. This has not been investigated at a later time to do not occupy too much time in a study that is not essentially pertinent to an engineering environment. The differences between the various cases is even clearer analysing Fig. 4.37: the emittance slope for the case n°2 is lower (and always constant) compared to the others, even if the beam size in the x plane is higher. Moreover, the emittance blows up for cases n°1 and 3 when the size in x increases, necessary step to get a sharp focus onto the slits.

Analysing the comparison between numerical and analytical results in Table 43, the distances between the mass peaks *s* are in good accordance, within an error of maximum 4%. On the other hand, the beam dimension on the x plane is larger of about 25% respect to the analytical part. Mainly this effect is due to the emittance increase that consequently increases the beam diameter.

Moreover, due to the focusing effect on the y plane induced by the tilted pole, the beam size on the y plane can be maintained small, less than 10 mm, even for long Wien Filters for case N°2 and N°3. In this way, the emittance does not increase due to the non-uniformity of the electric effective length far from the beam axis showed in Fig. 4.21b.

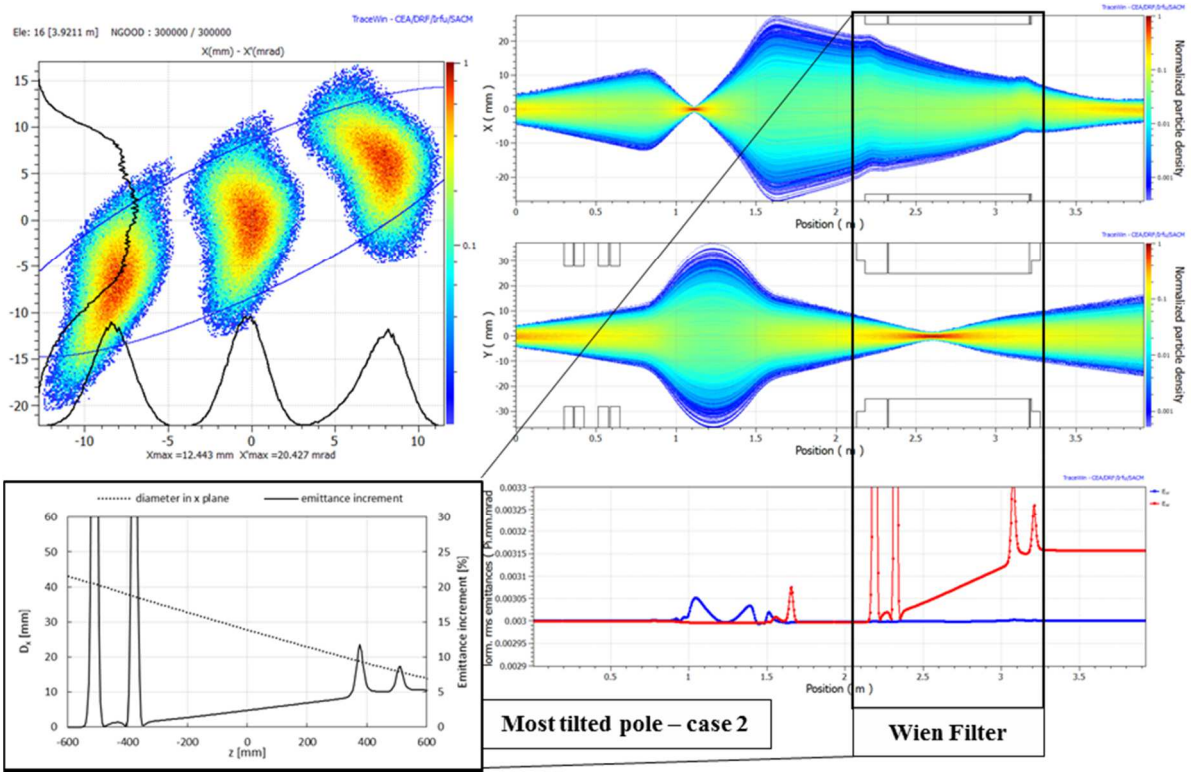

Fig. 4.35. Results for the optimum of the case 2; left: separation and beam on the x plane phase space and emittance increase and maximum diameter inside the WF; right: beam path on x and y plane, emittance increase in all the Front-End.

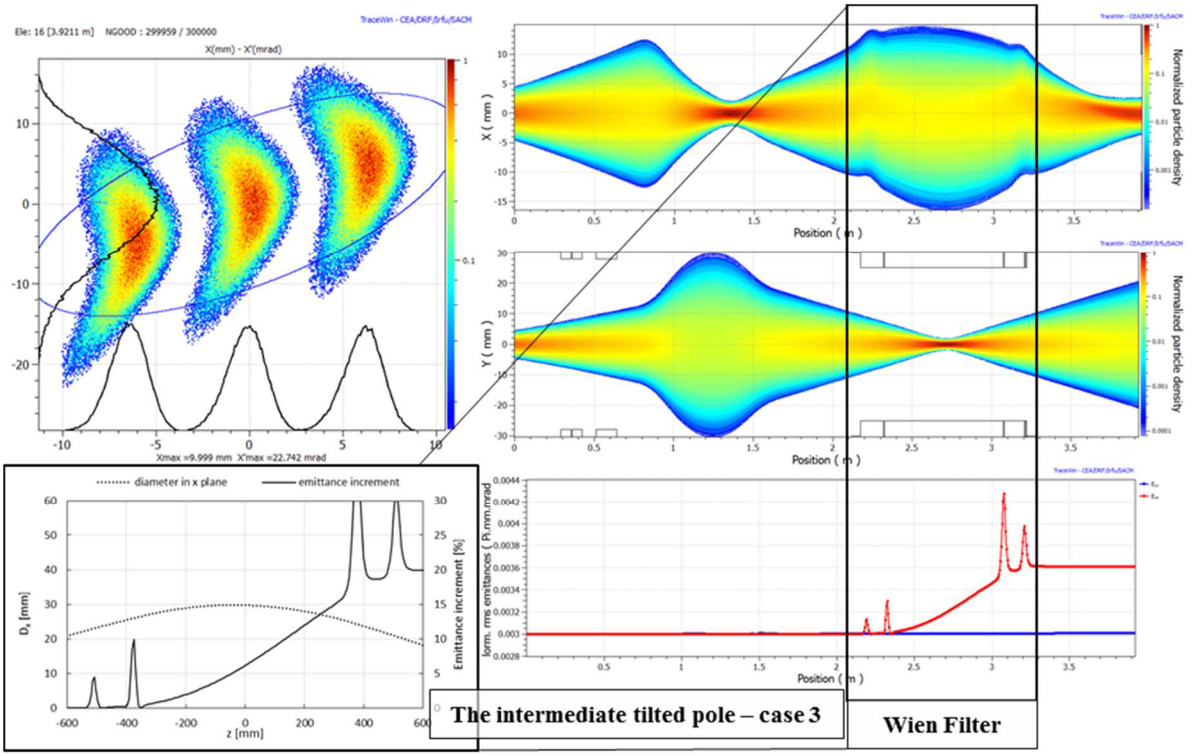

Fig. 4.36. Results for the optimum of the case 3; left: separation and beam on the x plane phase space and emittance increase and maximum diameter inside the WF; right: beam path on x and y plane, emittance increase in all the Front-End.

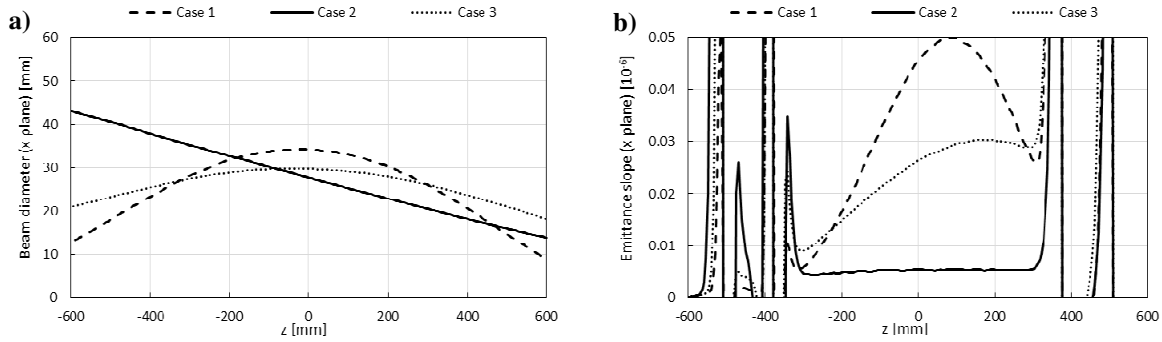

Fig. 4.37. Beam size and emittance increase for the x plane inside the WF for the various cases.

The consequences of this study are:

- The analytical approach, that suggests as the best configuration the case n°3, does not take into account the beam emittance increase which has a very important effect on the maximum beam diameter in the Wien Filter and the minimum beam spot at the slits.
- The best configuration has been found to be the case n°2: it has the highest numerical *ott* value (ratio between beam diameter and peak separation) coupled with the best beam transport properties, reflected on the smaller emittance increase. Case n°3 is anyway better than case n°1 (higher *ott* values) as reported in [4.1] and [4.3].
- The new Wien Filter will follow the specification of case n°2. The peak separation expected for the mass 150 amu is almost 100% (a very small fraction of mass 151, about 0.03%, can not be avoided) essentially zeroing the unwanted beam out of the bunker.
- The analytical study can be a very powerful method to size the Wien Filter. Since the beam diameter calculated in this way is about 20% higher, during the sizing process, the minimum *ott* factor has to be more than 1.25.

It is underlined that the potential applied to the electrodes are 4.61 kV and 2.19 kV, for a ratio of 0.475, which is very similar to the prediction performed in paragraph 4.4.4 (0.45) based on very simple assumptions.

4.5.3. Estimation of the saturation effect on the yokes and the poles

The longitudinal shape of the Wien Filter, here called "v_3", could generate a bad effect on the beam if the saturation effect of the sharp pole edges, that surely occurs, is wide on the pole. In particular, at the edge, the magnetic field is so intense compared to the other zones that reaches the plateau characteristic of the materials B-H curve presented in Fig. 4.38a for the poles (XC06) and the yokes (ST37); these curves have been furnished by the external company

that manufactured the WF. After about 2 T, the curve is interrupted and in COMSOL a linear extrapolation has been assumed. In order to try to represent even this part of the curve, a reasonable trend is the curve found in the CERN report [4.11] for a ST37-2 steel. The differences with the other curves are plotted in Fig. 4.38b.

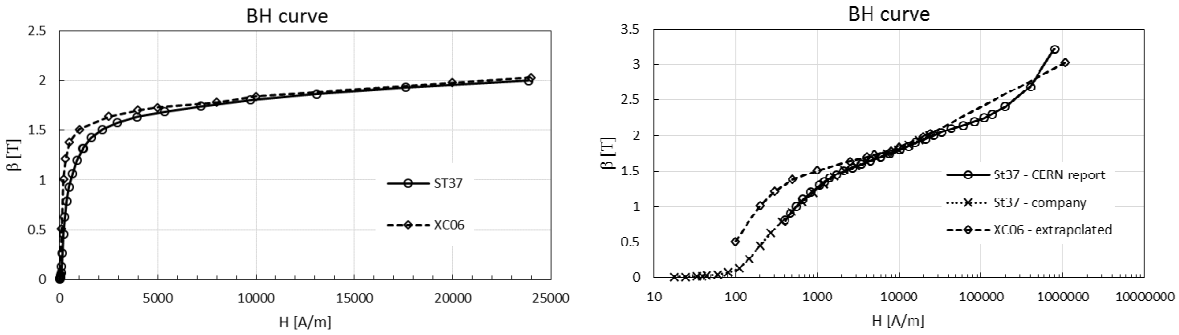

Fig. 4.38. BH curves of the magnetic soft iron used for the WF for logarithmic and non-logarithmic scale.

In general for magnets, it is important to avoid high magnetic fields which cause a less efficient magnetic circuit and a non-proportional magnetic field respect to the coil current. It is necessary, even for the Wien Filter, to verify:

1. The minimum yoke thickness required to avoid the increase of the magnetic resistance
2. The independence of the magnetic profile on the space for different coil currents

Concerning the first point, in Table 44 and Fig. 4.39a are presented the results for different yoke thickness. Obviously, higher is the thickness, higher is the magnetic field and, consequently, the magnetic circuit efficiency. On the other hand, the mass increases significantly, as the cost. A good compromise seems a yoke thickness of about 150 mm since the magnet mass has so far a reasonable value whereas the magnetic field is almost the maximum (only 1.8% lower with 0.1% of shorter effective length). Moreover, the magnetic field profile (normalized to their maximum value) along the beam axis has been compared in Fig. 4.39b with the results of 210 mm yoke thickness and no significant differences appear.

t [mm]	B_0 [T]	$L_{effective}$ [mm]	m [kg]
92	0.703	864.3	1952
110	0.765	868.9	2263
130	0.813	872.1	2626
150	0.837	873.6	3009
170	0.846	874.1	3411
190	0.850	874.3	3833
210	0.852	874.4	4273

Table 44. Magnetic properties for different yoke thickness @ maximum coil current (240 A).

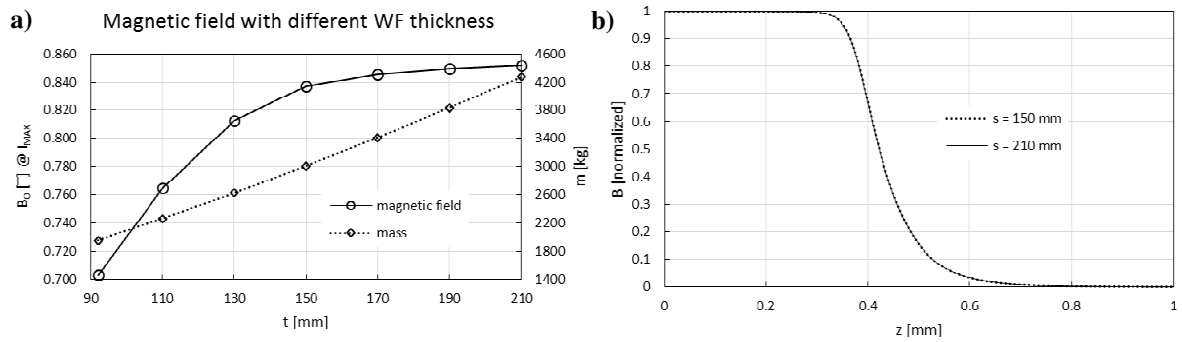

Fig. 4.39. a) Magnetic field in the WF centre and mass according to different yoke thickness; b) Magnetic field (normalized) for a maximum current of 240 A along the beam axis.

It is underlined that the maximum magnetic field required by the design is 0.8 T that it is surely satisfied by the magnet. The material to add is about 1 ton of soft iron (ST37 steel) that is one of the cheapest available in the market, whereas, for the new pole, XC06 is strongly suggested because it has a higher magnetic permeability and, consequently, it is more efficient.

Concerning the previous second point, the best way to verify that the magnetic field profile does not significantly change with the coil current due to saturation effect at the corners, is to perform a beam transport simulation. In fact, the particle trajectories are influenced all along their positions and a local difference influences the final results. For this purpose, a magnetic simulation has been initially performed without taking into account the BH curves but only an ideal material with the corresponding magnetic permeability. Then, the results have been applied to the beam transport simulation of the case N°2 presented in 4.5.2 and the beam Twiss parameters at the slits position are presented in Table 45 and Fig. 4.40.

	BH curve	BH curve modified	Magnetic permeability
ε_x [% increment]	5.20	5.72	5.57
α_x [ ]	0.077	-0.064	-0.050
β_x [mm/mrad]	0.316	0.297	0.298
ε_y [% increment]	0.07	0.03	0.05
α_y [ ]	-4.173	-4.282	-4.271
β_y [mm/mrad]	7.042	7.131	7.123

Table 45. Effect on beam emittance and Twiss parameters at the slits position due to the different magnetic field simulations.

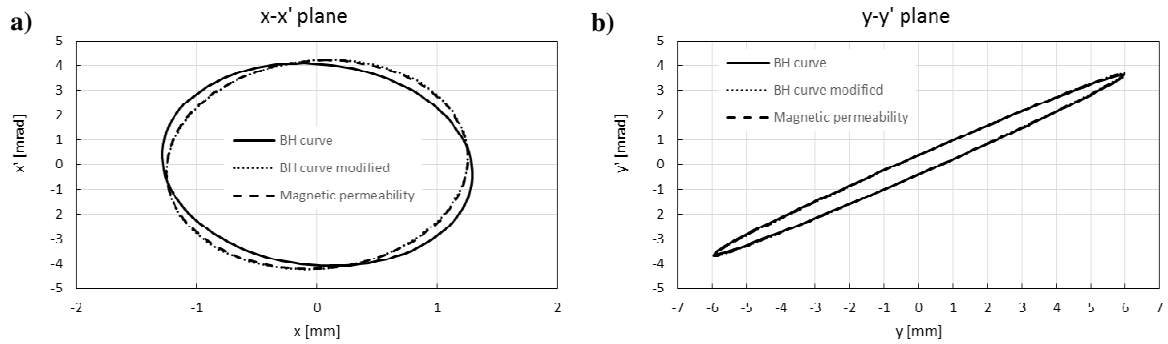

Fig. 4.40. Effect on the ellipse on the x and y phase spaces at the slits position due to the different magnetic field simulations.

The differences are negligible and, in these cases, the magnetostatic simulation can be performed using just the ideal material with a high gain on the magnetic field simulation time. It is underlined that, for this case, the magnetic field calculated with the BH curve is 3% lower compared to the simulation with the simple relative permeability.

Finally, the limits of the magnetostatic simulations due to the BH magnetic curve assigned to the materials are presented. At 50 mm off axis (Fig. 4.41a), where the magnetic field is higher due to the tilted pole, just a circle area of 10 mm radius has a magnetic field higher than the BH curve provided by the company (2 T), consequently here maybe some errors can be inserted due to the simplification. At 150 mm (Fig. 4.41b), the portion is bigger, but it is underlined that the maximum beam radius is 25 mm and, consequently, no effects are expected on the beam. On the other hand, using the BH curve found in the CERN report (which is probably very close to the reality), the area where the magnetic field is higher than the BH curve used (3 T) is limited to a radius of less than 1 mm even far from the axis (Fig. 4.41a). Then the error introduced will be probably negligible.

In conclusion:

1. The BH curve provided by the external company can be used to simulate the magnetic field inside the poles even at high currents.
2. No change on the focusing is expected at high currents since almost the same beam Twiss parameters have been calculated at the slits using an ideal material with constant magnetic permeability (no possibility of saturation effects).

These two considerations are surely consequence of the nominal magnetic field value 0.8 T, which is not excessively high.

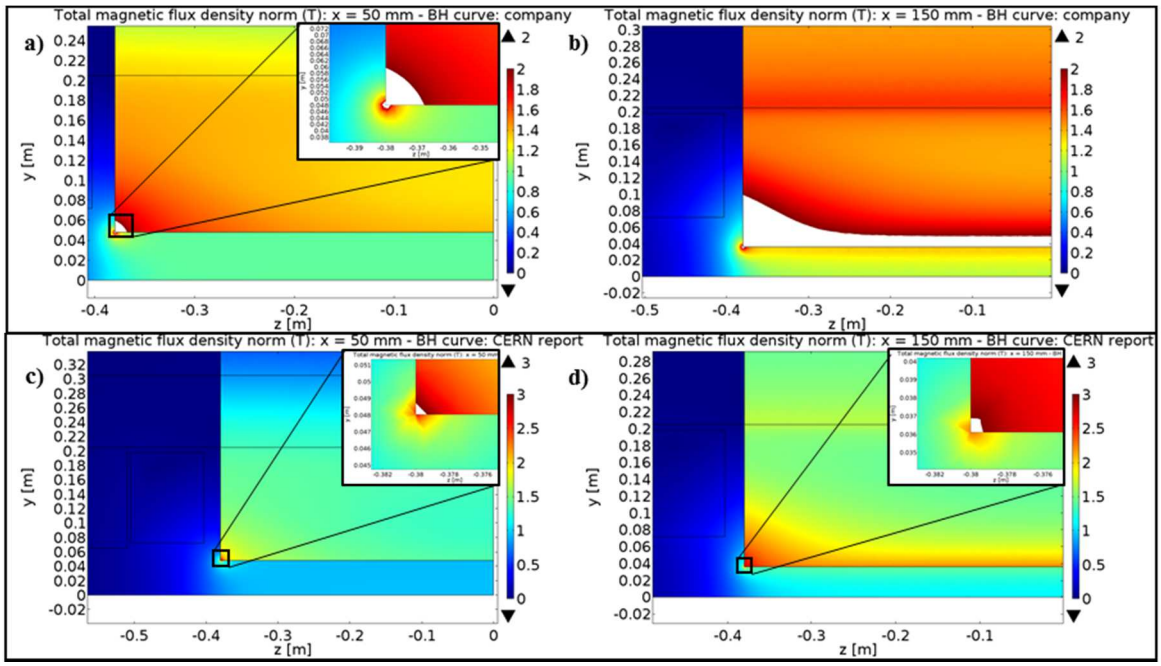

Fig. 4.41. Limit of validity of the simulation due to the extrapolation of the two BH curves given as input to COMSOL: (a,b) BH curve provided by external company – limit 2 T; (c,d) BH curve of ST37 in CERN report [4.11] – limit 3 T. Two different position on the x plane: 50 mm (a,c); 150 mm(b,d).

4.6. The mechanical design and the realization of the new Wien Filter

4.6.1. The mechanical design

Most of the work concerning the mechanical design has been spent on the definition of the electrostatic assembly of the Wien Filter. Particular attention has been paid on the minimization of the vacuum chamber height in order to maintain the magnetic poles closer as possible. The best choice is then to think the vacuum chamber as a box where inside an electrode is installed, whereas the other is fixed to the cap, as the sketch presented in Fig. 4.42; in this case, the manufacturing precision determines the tolerances between the two electrodes since very few adjustments could be performed during the assembly. In this way, the height of the chamber is minimize for two reasons:

1. The screws and the seal, which require a considerable space, will be placed on the side of the vacuum chamber that is not limited by the presence of the poles.
2. A chamfer on the vacuum chamber can be inserted without compromising the stability of the box since it is possible to increase the wall thickness on the other side

With the designed vacuum chamber, it is expected a maximum deflection in its centre of less than 10 µm and irrelevant stresses (less than 10 MPa) due to the air pressure.

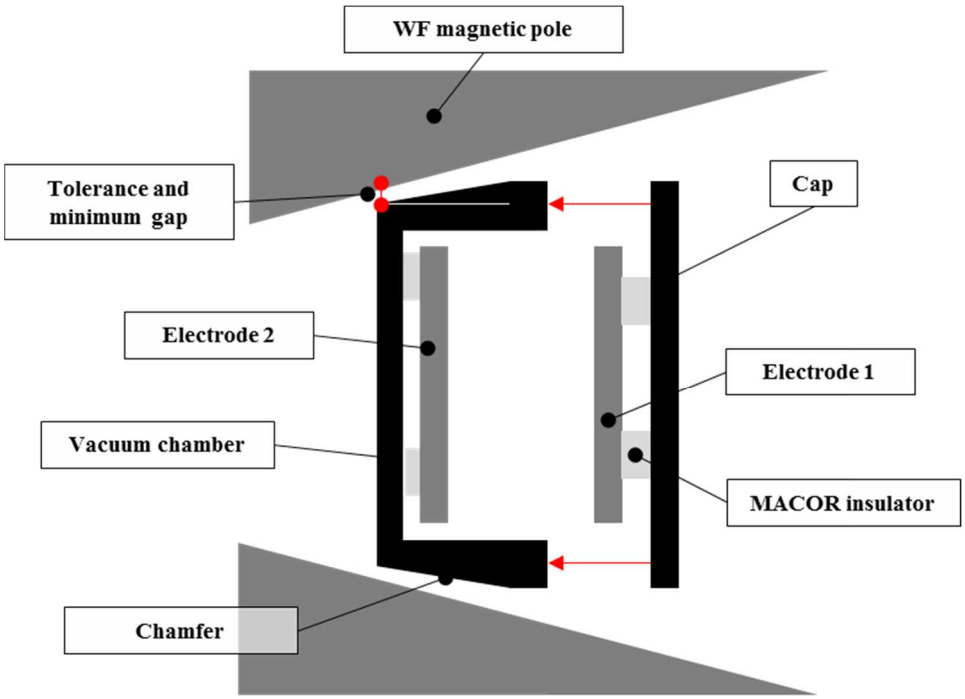

Fig. 4.42. Conceptual design of the electrostatic vacuum chamber.

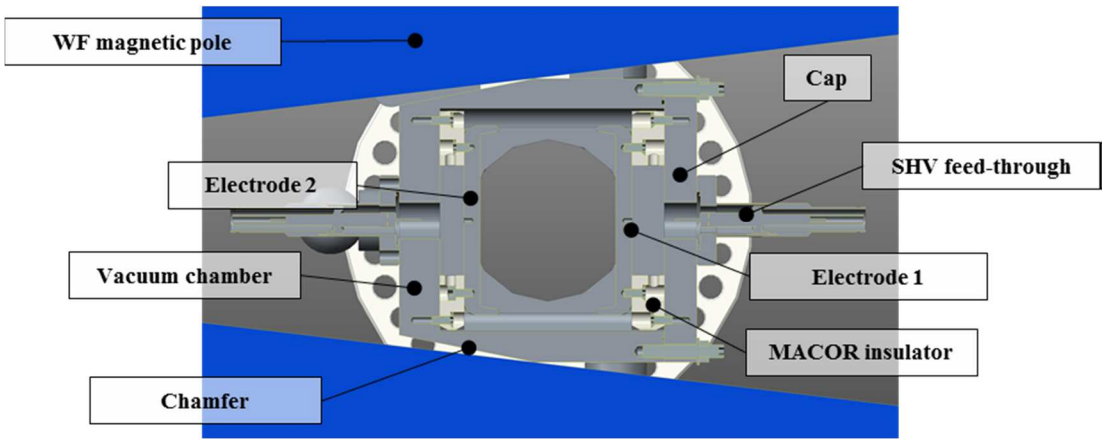

Fig. 4.43. CAD section on the x-y plane of the final assembly.

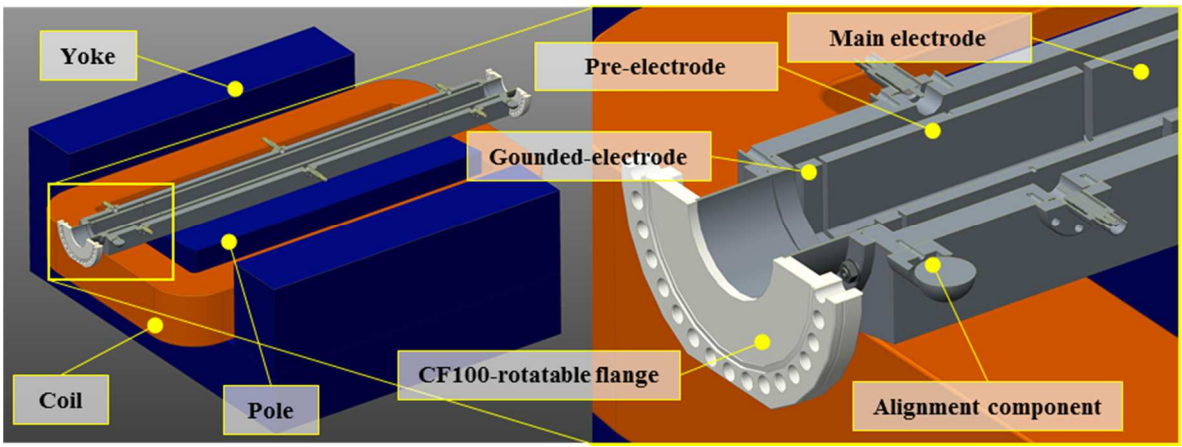

Fig. 4.44. CAD section on the x-z plane of the final assembly.

In order to have the best tolerances, it has been decided to produce the vacuum chamber starting from a rough bar and to dig it to create a box. Since no soldering has to be performed, the best material to work is aluminium (aluminium alloy) that is also lighter than stainless steel. Even the electrodes will be made in aluminium, whereas the insulator material will be in MACOR to assure the radiation resistance for tens of years. The insulators are probably the components which will insert the most important errors on the assembly for the poor machining properties of the MACOR due to its brittleness.

Two special stainless steel flanges are foreseen on both the vacuum bores. They have in one side the seat for an indium oring to assure the sealing with the electrostatic assembly, whereas the other side is a standard CF100 rotatable flange with both bolted and threaded holes. In this way, it will be possible to connect each type of CF flanges with standard copper gaskets. The CAD drawings representing the assembly are presented in Fig. 4.43 and Fig. 4.44.

Finally, the preliminary poles, used just to validate the numerical results, will be in ST37, which has as a good magnetic permeability.

4.6.2. The manufacturing process

As already said, the vacuum chamber has been realized from a rough aluminium bar, which has been twice heated up in order to relax the residual stresses due to the extrusion and manufacturing process. In this way, the best tolerances have been obtained, but, anyway, they had not been evaluated due to the lack of a coordinate measuring machine. The finishing process has been performed in only one clamp in order to reduce the alignment errors. Then the surface roughness has been manually completed by sandpaper.

Concerning the electrodes, various clamping needed to define both side of the component. Particular attention has been paid on the flatness and on the correct measures of the wings used to increase the electric field uniformity. For this purpose, a dedicated milling cutter has been modified by an EDM wire to get the desired electrode fillet.

Part of these manufacturing processes are showed in Fig. 4.45.

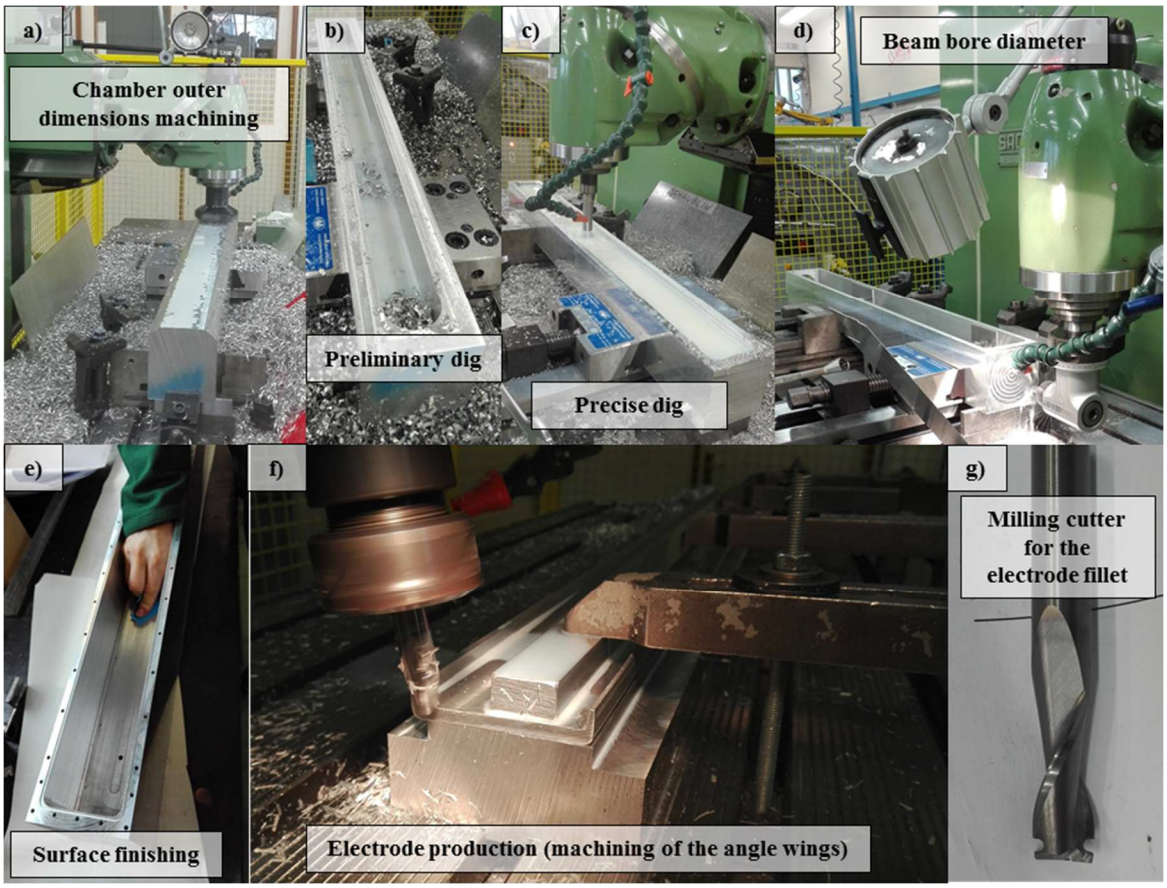

Fig. 4.45. Phases of the production of the electrostatic assembly main components.

Even a prototype of the new magnetic pole has been produced. It has not the best dimensions presented in paragraph 4.5.2, but it is shorter in order to adapt it to the current pole (Fig. 4.46). The material was ST37, a low carbon steel frequently used for the magnet yokes and poles. It has been heated up over 600°C to relax the residual stresses in order to avoid bending after the manufacturing process.

Fig. 4.46. First preliminary pole machined at the LNL.

4.6.3. *The assembly of the Wien Filter prototype*

Firstly, the electrostatic chamber was carefully assembled. Particular attention has been paid on the parallelism of the electrodes which could be ruined by the MACOR insulator components. In Fig. 4.47, the main parts of the assembly are presented.

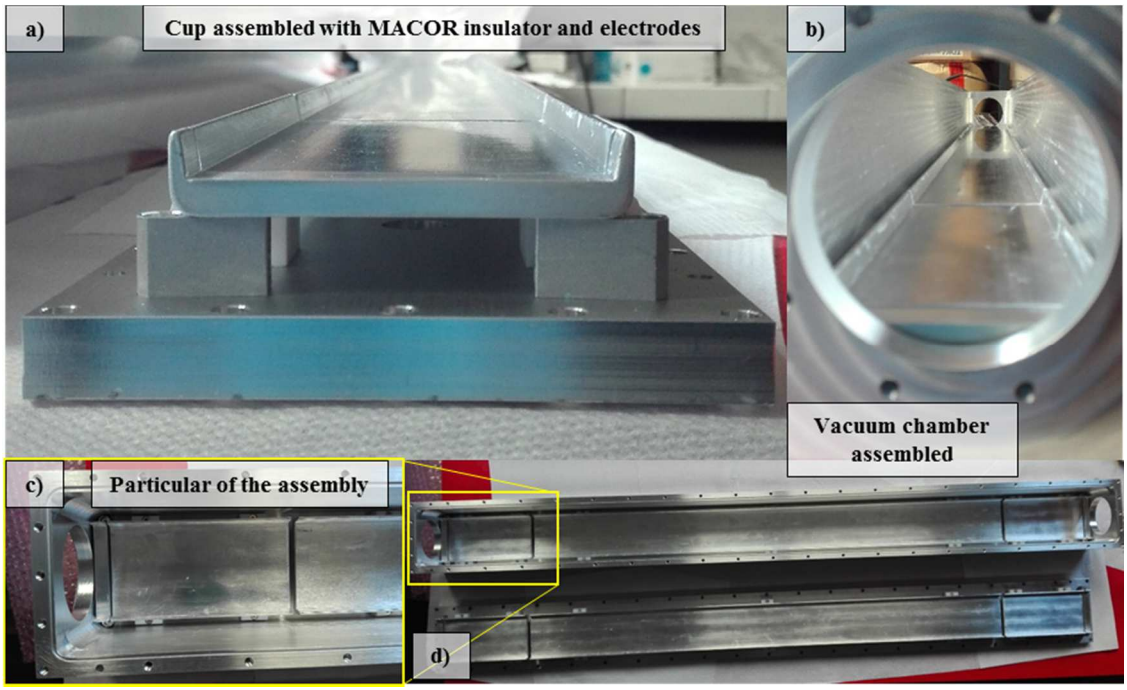

Fig. 4.47. Electrostatic chamber assembly.

After the closing of the electrostatic chamber, the special flanges have been coupled with the indium seal visible in Fig. 4.48a and then the vacuum of the system has been tested. No leaks were measurable, confirming the accuracy for this aspect of design, the manufacturing process and the assembly. Moreover, no electrical discharge were observed maintaining the central electrode at 5 kV (4 mm of minimum distance) or the four pre-electrodes at 4 kV (2 mm of minimum distance), for a maximum nominal electric field of about 2 kV/mm.

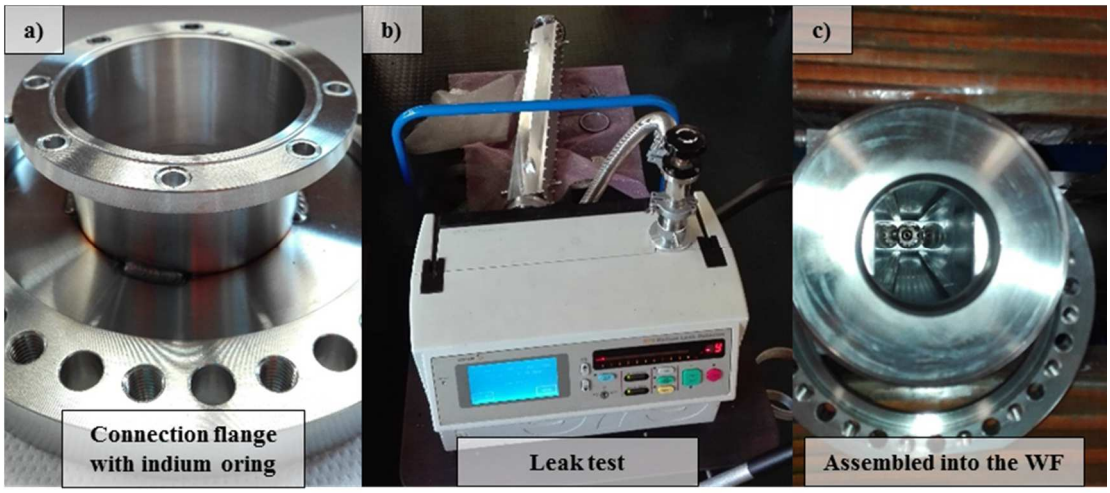

Fig. 4.48. Phase of the mounting process: connection flange (a); leak test (b); assembly into the WF (c).

After the removal of the old vacuum chamber by means of a lifter (Fig. 4.49a), the new assembly has been installed. It is underlined that with the new poles, the new electrostatic chamber can be changed, if necessary, without lifting the upper part for a much shorter intervention time and improved safety conditions.

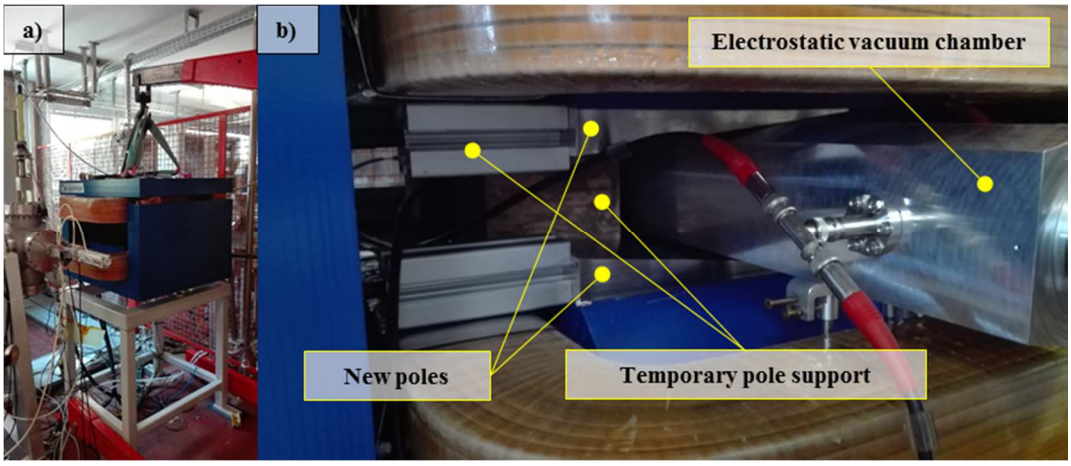

Fig. 4.49. Assembly of the new poles inside the WF.

After the first tests on the new electrostatic chamber presented in paragraph 4.7.3, the preliminary poles have been installed inside the WF. Particular attention has been used to fix the poles using some temporary supports in wood and aluminium because, turning on the Wien Filter, the forces acting on the poles could move them out of position.

4.7. Experimental test

4.7.1. The input beam for the analysis

The only possible way to validate all the previous considerations and simulations are to produce a preliminary Wien Filter, to inject a beam and to look the effects on it. In order to perform the validation, the FE has been used, its beam optic has been characterized and the source used (the SPIS) has been studied. Most of the simulations and tests will not be presented, but just a very short description reduced to the minimum will be showed.

The first step is to get the beam properties out of the extractor. Since it was not possible to directly measure them, the Twiss parameters after the triplet have been measured in three different quadrupoles configurations by an emittance meter. The Wien Filter was turned off by a small inverse current on the coils (less then 1 A) to remove the magnetic hysteresis zeroing the magnetic field. Then, a traceback has been performed with TraceWin for one of the three configurations in order to get the Twiss parameters of the input beam (Table 46). Finally, all the other two cases have been simulated. In the experimental tests, the beam current was maintained in the range of 300 nA in order to have the most stable beam, even if the maximum

RIB current expected with proton beam is of 1 μA. Anyway, no significant effects are expected for higher beam current. The deflectors after the source were used but in these cases their effect, which should be negligible on the Twiss parameters, are not taken into account.

Mass particle m	40 amu – (Ar)
Extraction potential V_e	25.15 kV
$\alpha_x = \alpha_y$ (1st Twiss parameters)	-0.929
$\beta_x = \beta_y$ (2nd Twiss parameters)	0.541
Extractor distance	≈ 60 mm
I_{BEAM}	≈ 300 nA

Table 46. Input parameters for the beam.

Since there are not evidences of non-linear effects both in the numerical and experimental results, they will be compared just looking to the RMS ellipse in the x and y plane.

Case	Q_1 [V]	Q_2 [V]	Q_3 [V]	Plane		α [ ]	β [mm / mrad]	γ [mrad / mm]
1	1160	660	1160	x	EXP	0.195	1.357	0.765
					TW	0.242	1.652	0.641
				y	EXP	-1.236	1.990	1.271
					TW	-0.912	1.765	1.038
2	1315	720	1326	x	EXP	-2.399	2.531	2.669
					TW	-1.886	2.456	1.855
				y	EXP	-2.951	4.757	2.040
					TW	-2.588	4.032	1.909
3	1181	688	1301	x	EXP	-1.705	1.500	2.604
					TW	-1.141	1.359	1.694
				y	EXP	-1.676	2.649	1.439
					TW	-1.249	2.202	1.163

Table 47. Comparison between numerical (TW – TraceWin) results and experimental (EXP) measures.

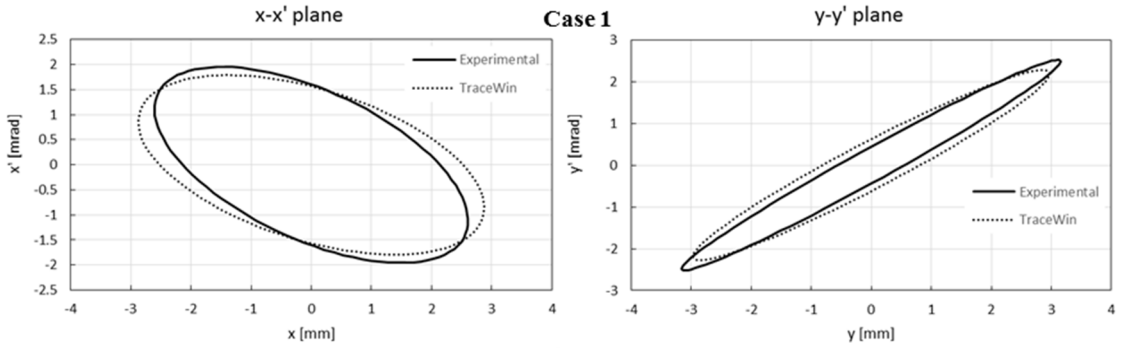

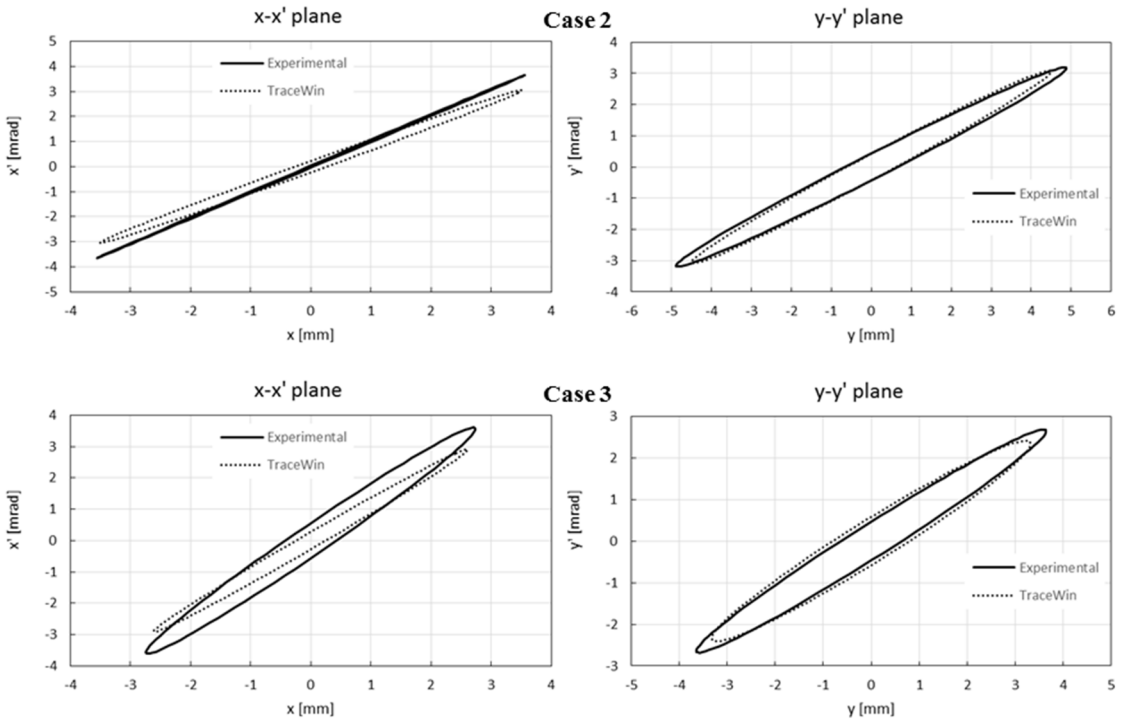

Fig. 4.50. Comparison between experimental and numerical results in order to validate the input beam and the triplet simulation for the further simulations

Even if the numbers sometimes seem quite far, the ellipse shape are very similar. Just probably on the case 3 – x plane the beams are a little different. Anyway, without taking into account the misalignment, the Twiss parameters are enough satisfying. This has two effects:

1. The input beam is good enough to let assume it as the initial conditions for the further simulation.
2. The triplet are correctly simulated and the procedure implemented has been validated.

4.7.2. The results of the first Wien Filter version

Here will be presented the tests performed on the first version of the Wien Filter available that corresponds to the device purchased from an external company. This was an essential step in order to have assurance on the later simulations. The same properties of Table 46 have been assumed, whereas the potential applied to the triplet was numerically found in order to have the minimum beam spot on the x dimension at the slits. All the five cases tested, corresponding to five different potential for the Wien Filter electrodes (and consequently different values to the triplet), are presented in Table 48 and Fig. 4.51.

Case N°	Q_1 [V]	Q_2 [V]	Q_3 [V]	I_{WF} [A]	B [T]	V_p [V]	Plane		ε_{INC} [%]	α [ ]	β [mm/mrad]	γ [mrad/mm]
1	1273	556	693	59.1	0.1771	1500	x	EXP	1.47	-5.871	5.258	6.744
								TW	1.04	-3.750	3.020	4.988
							y	EXP	0.98	-0.149	5.961	0.172
								TW	1.03	0.375	4.417	0.258
2	2133	748	1165	80.3	0.2389	2000	x	EXP	1.20	-4.768	4.369	5.434
								TW	1.04	-3.700	2.970	4.946
							y	EXP	1.31	0.146	3.131	0.326
								TW	1.04	0.462	2.919	0.416
3	1775	881	2493	100.9	0.29882	2500	x	EXP	1.08	-3.783	2.654	5.771
								TW	1.03	-4.090	3.200	5.540
							y	EXP	1.21	-1.062	5.402	0.394
								TW	1.03	-1.050	6.630	0.317
4	1208	808	2219	122.5	0.3607	3000	x	EXP	1.16	-4.895	3.884	6.427
								TW	1.04	-5.080	3.920	6.838
							y	EXP	1.02	-1.894	3.602	1.273
								TW	1.00	-2.000	4.240	1.179
5	709	641	1785	166.8	0.4857	3980	x	EXP	1.31	-5.146	3.832	7.171
								TW	1.22	-3.130	2.250	4.799
							y	EXP	1.41	-3.955	12.700	1.310
								TW	1.08	-3.190	12.900	0.866

Table 48. Experimental measures compared with TraceWin results for the first Wien Filter version (provided by external company) – flat pole.

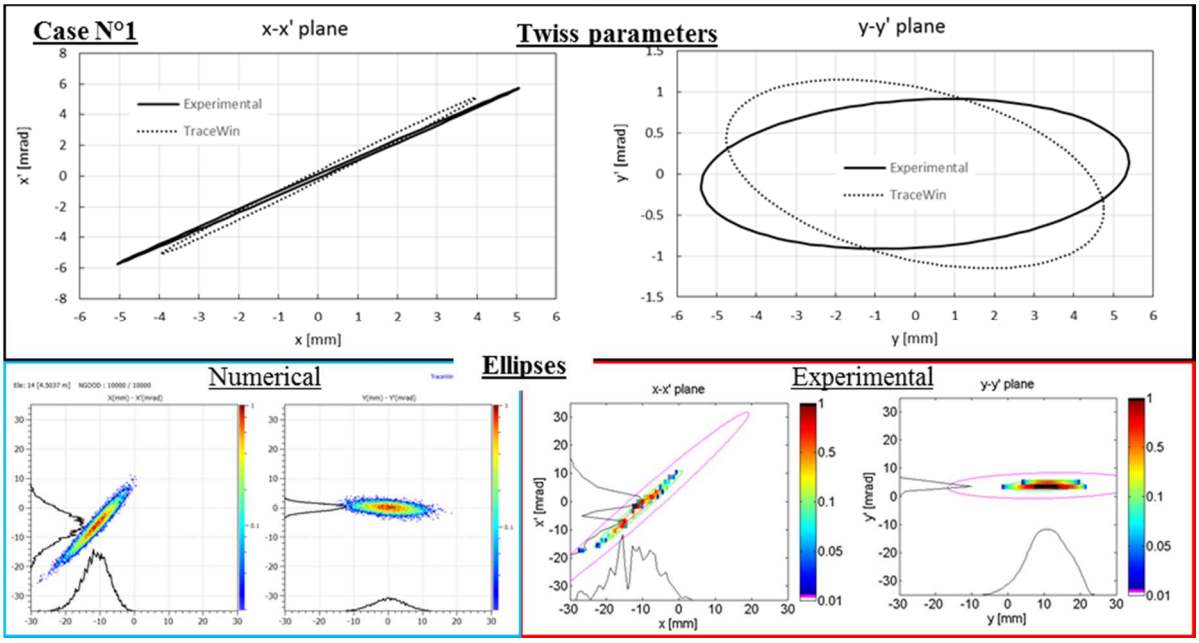

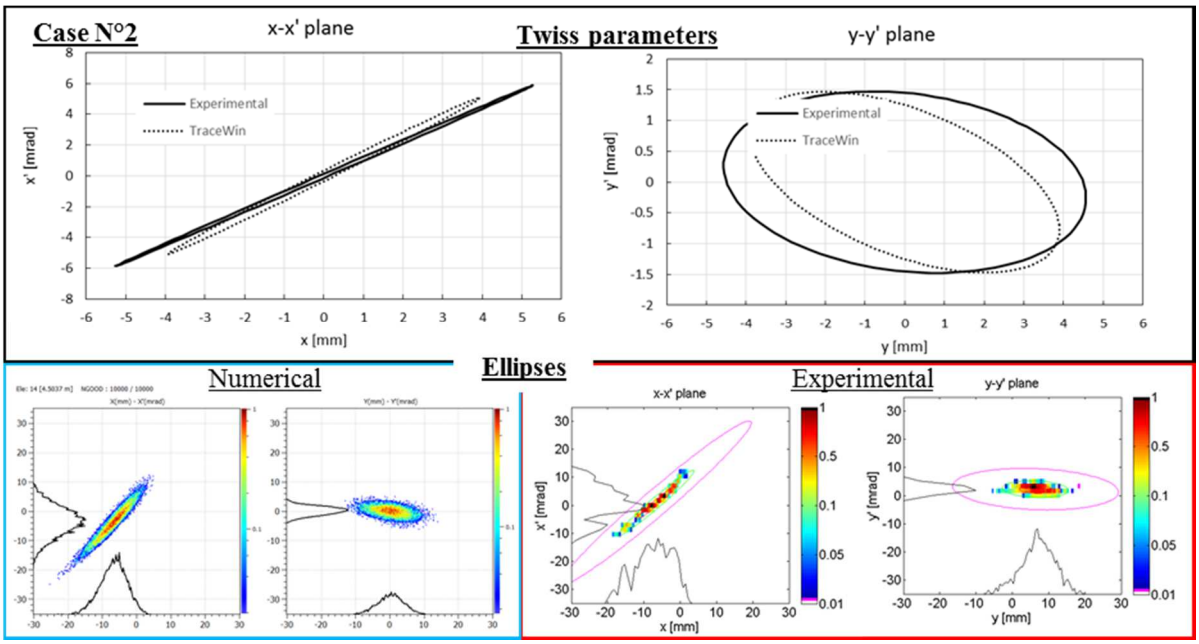
Case N°2
x-x' plane
Twiss parameters
y-y' plane
Experimental
TraceWin
x' [mrad]
x [mm]
y' [mrad]
y [mm]
Numerical
Ellipses
Experimental
x-x' plane
y-y' plane

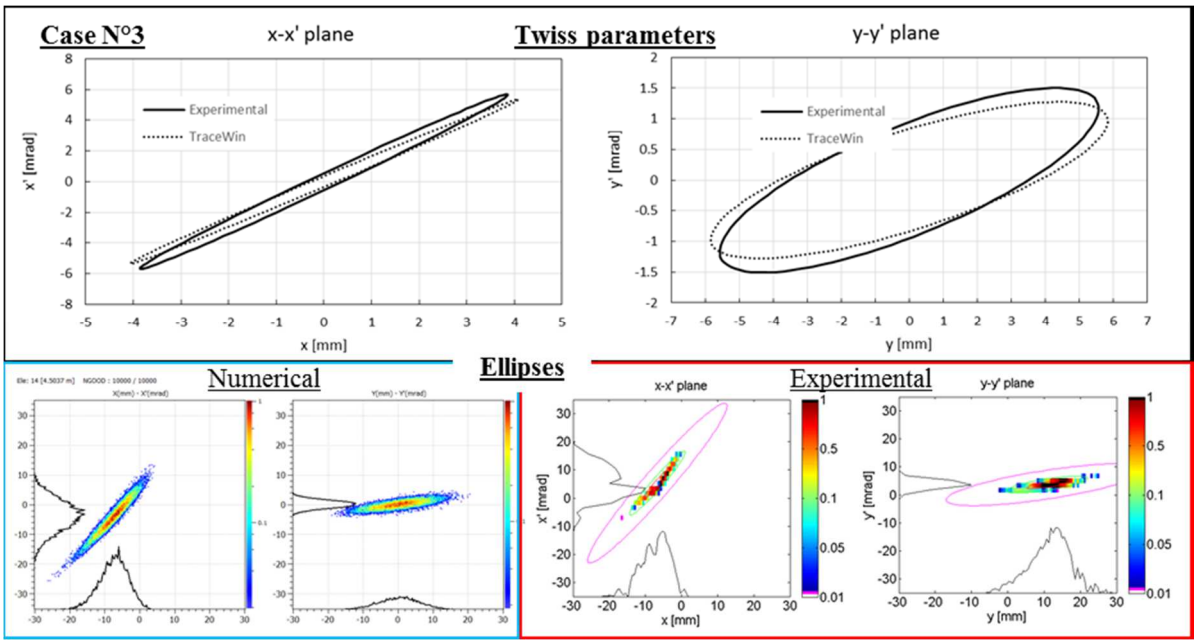
Case N°3
x-x' plane
Twiss parameters
y-y' plane
Experimental
TraceWin
x' [mrad]
x [mm]
y' [mrad]
y [mm]
Numerical
Ellipses
Experimental
x-x' plane
y-y' plane

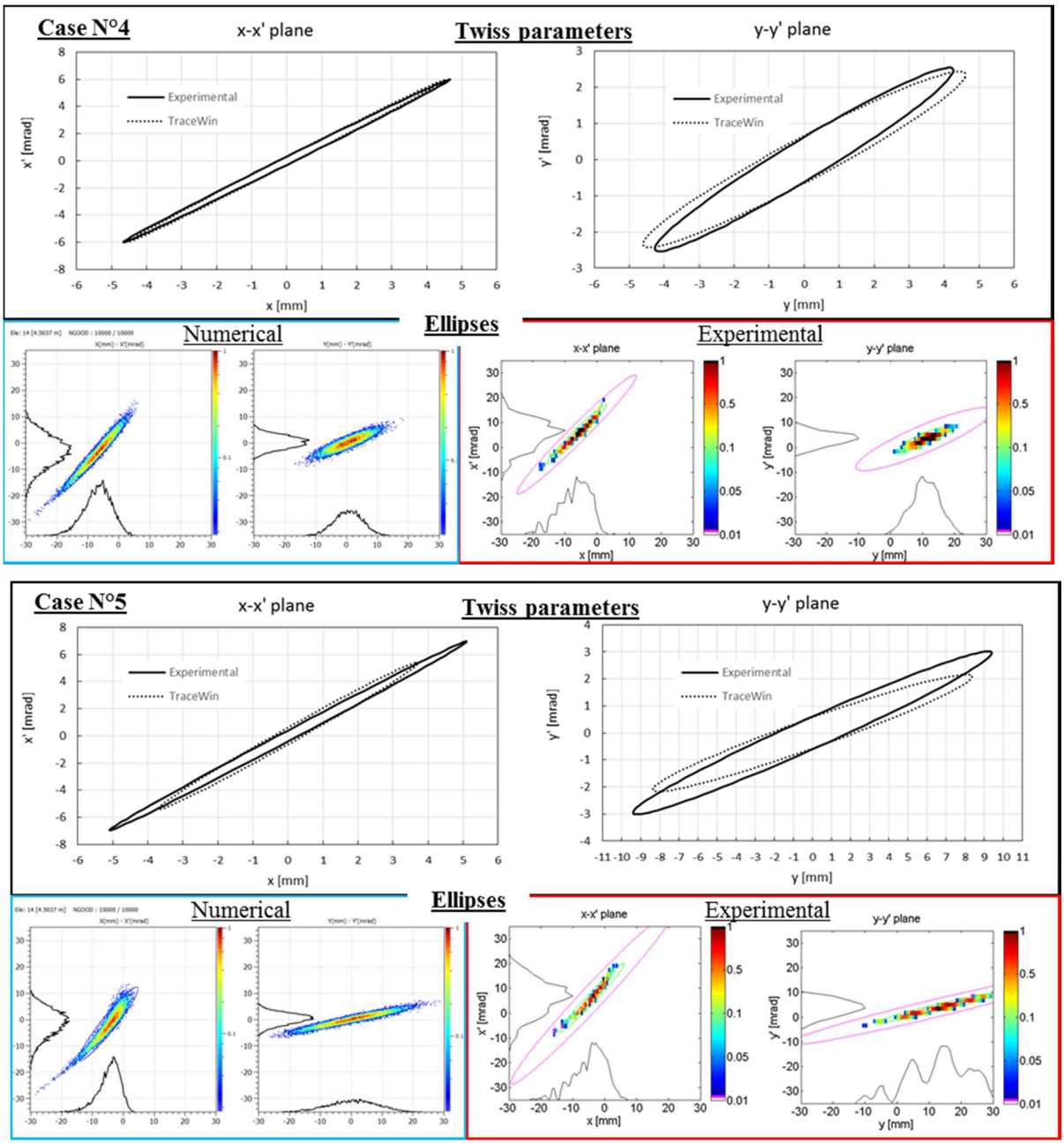

Fig. 4.51. Experimental measures (EXP) compared with TraceWin results (TW) for the first Wien Filter version (provided by external company) – flat pole.

The comparison is very good, especially at high electrode potential even if the experimental emittance increase is higher compared to the numerical results, probably due to a small misalignment of the beam. Moreover, the Twiss parameters, and consequently the ellipse figures were quite different for the case N°1 and N°2, anyway always into a satisfying error band. It is underlined that the increase of the emittance with a flat pole has been here verified, confirming what it was found in paragraph 4.5.2.

4.7.3. The validation of the new electrostatic part

In this paragraph, the experimental results concerning the new electrostatic part combined with the old magnetic poles are presented in order to validate the electrostatic device. The potential on the pre-electrode V_{pe} is proportional to the potential on the main electrode V_p to minimize the deflection of the beam inside the Wien Filter. The ratio has been fixed according to the numerical results, as the triplet potentials which have been found in order to minimize the beam focus on the slits. It is underlined that the beam entered a little misalignment in the Wien Filter and this is the cause of the high aberration measured and also calculated. This was not a problem since it was just a test to verify the quality of the manufactured pieces.

Case N°	Q_1 [V]	Q_2 [V]	Q_3 [V]	I_{WF} [A]	B [T]	V_p [V]	V_{pe} [V]	Plane		ε_{INC} [%]	α [ ]	β [mm/mrad]	γ [mrad/mm]
1B	1273	556	693	60.14	0.177	1510	393	x	EXP	1.26	-3.386	2.762	4.515
									TW	1.50	-2.080	1.797	2.964
								y	EXP	1.49	-0.189	3.195	0.324
									TW	1.47	0.120	3.131	0.324
2B	2133	748	1165	81.16	0.2387	2016	524	x	EXP	1.17	-1.219	1.056	2.356
									TW	1.44	-2.010	1.663	3.031
								y	EXP	1.34	0.024	1.143	0.875
									TW	1.61	0.026	2.204	0.454
3B	1775	881	2493	101.71	0.29883	2512	654	x	EXP	1.43	-0.471	0.722	1.691
									TW	1.54	-1.764	1.410	2.916
								y	EXP	1.59	-0.482	2.071	0.595
									TW	1.69	-1.086	4.669	0.467
4B	1208	808	2219	122.8	0.3608	3034	789	x	EXP	1.55	-0.210	0.525	1.988
									TW	1.26	-2.444	1.628	4.282
								y	EXP	1.00	-2.617	4.036	1.944
									TW	1.06	-2.139	4.305	1.295

Table 49. Experimental measures (EXP) compared with TraceWin results (TW) for the new electrostatic part and the old Wien Filter pole – flat pole

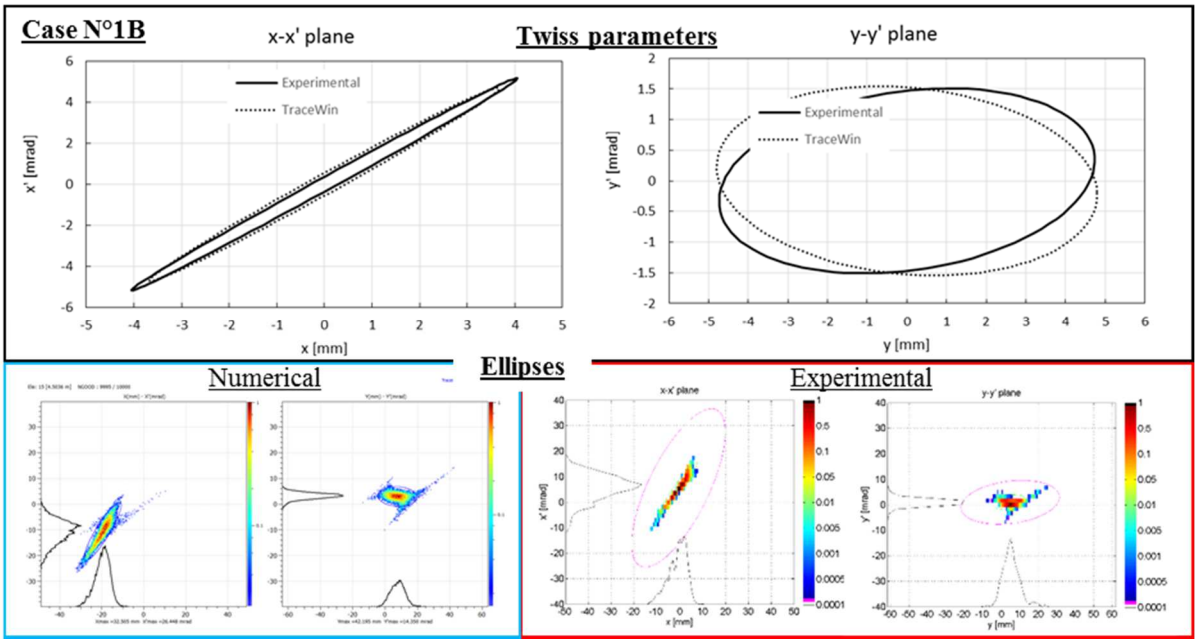
Case N°1B
x-x' plane
Twiss parameters
y-y' plane
Experimental
TraceWin
x' [mrad]
x [mm]
y' [mrad]
y [mm]
Numerical
Ellipses
Experimental

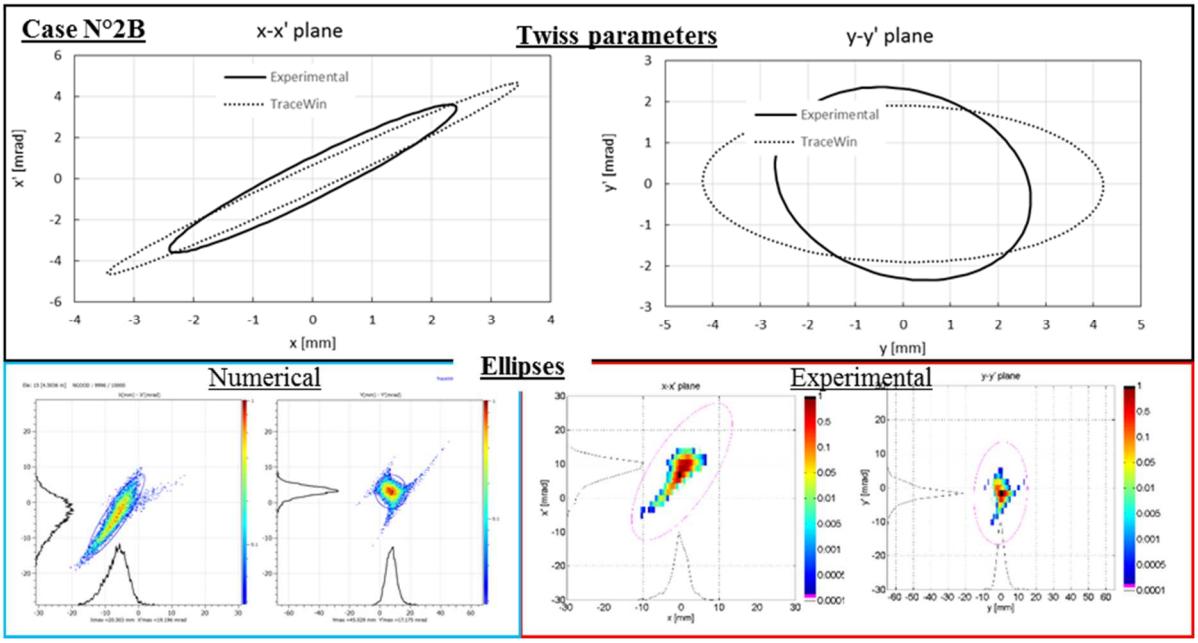
Case N°2B
x-x' plane
Twiss parameters
y-y' plane
Experimental
TraceWin
x' [mrad]
x [mm]
y' [mrad]
y [mm]
Numerical
Ellipses
Experimental

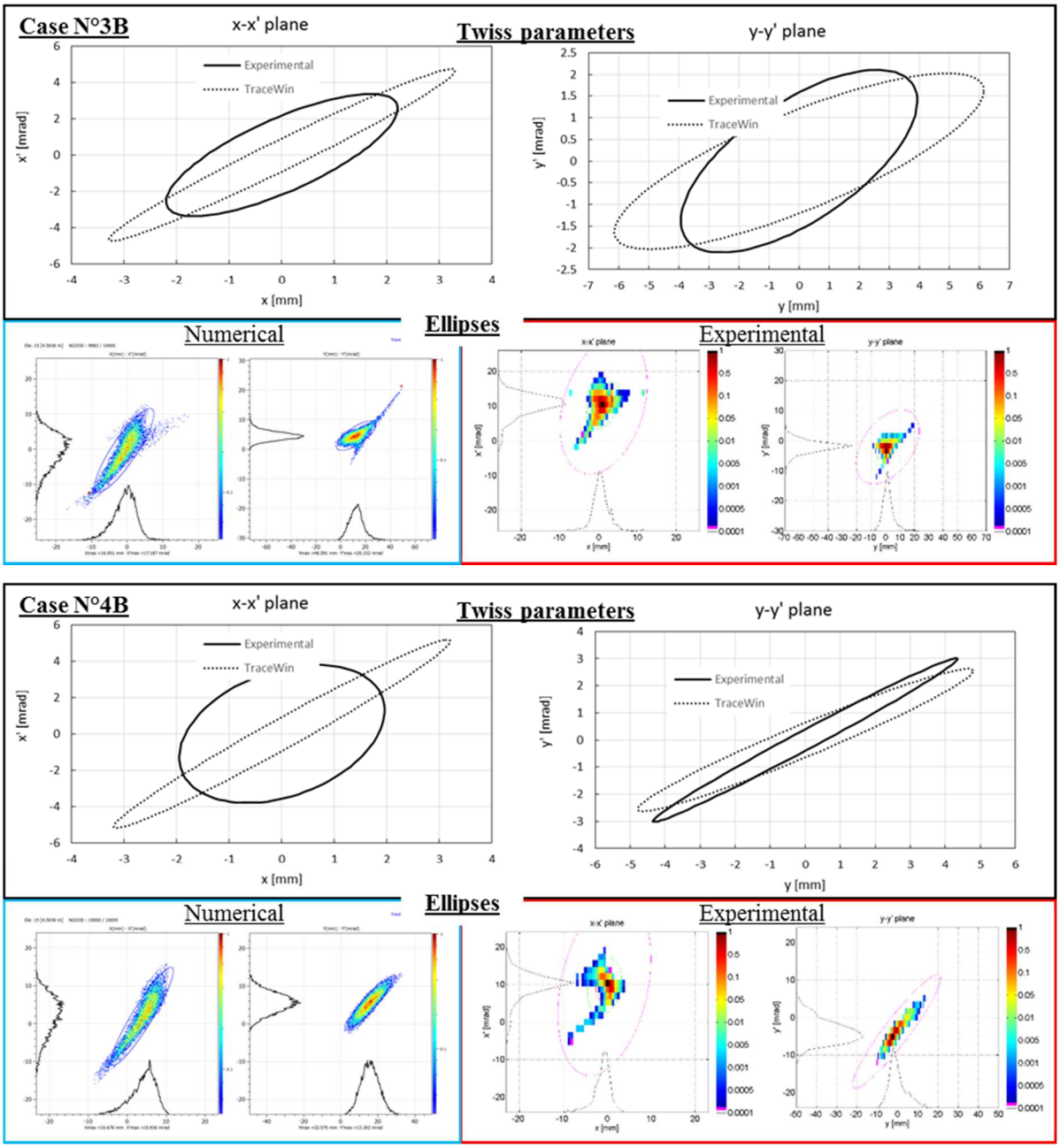

Fig. 4.52. Experimental measures (EXP) compared with TraceWin results (TW) for the new electrostatic part and the old Wien Filter pole – flat pole.

In this case, the experimental ellipse are not so close to the numerical results, especially for case 3B and 4B(x). In particular, the last one is very far from the numerical results due to the presence of very intense aberration that are not perfectly reproduced in the numerical results. A satisfying justification has not been found for case 4B. On the other hand, a very good point for the other measures is that, even if the Twiss parameters are not so close, the beam aberrations constituted by the protrusions for both the x and y planes visible on the coloured pictures, are well reproduced on the TraceWin results. This is also the key to justify the differences on the Twiss parameters: the emittance meter has not a sufficient resolution to

check all the possible beam aberration. It has been numerically verified that they are due to the passage of the beam very close to the electrodes due to the misalignment that surely is unwanted on the online version. On the other hand, here it was specifically not corrected by the deflectors after the extractor to amplify the aberrations and to demonstrate the quality of the simulations.

4.7.4. The validation of the new magnetic part

Finally, in this paragraph, the results of the first prototype of the Wien Filter, with a preliminary tilted pole, will be presented. As said in 4.5.2, the final pole version will be:

- As long as the magnetic longitudinal length in order to increase as much as possible the effective length.
- With a tilted angle covering the overall width.
- With an increased thickness of the yokes to reach higher magnetic field removing their magnetic field saturation.

Moreover, in these tests, the slits position was not at the final distance with respect to the Wien Filter but they were placed closer to it. All these conditions decrease the separation of the beam peaks and, consequently, the resolving power. For this reason, this paragraph is intended as the validation of the simulations of the new magnetic prototype to confirm the accuracy of the procedure implemented, and it is not intended as the test of the final Wien Filter that would be possible only after the aforementioned modifications.

It is even underlined that these were the first tests performed at extraction potential higher than 25 kV because the Front-End had to be adapted in order to maintain consistently the potential and some authorizations for radioprotection issues were needed to overstep the potential of 30 kV. No experience were present on the effect of higher potential extractions to the beam and three reasonable hypothesis were assumed:

1. The so-called normalized emittance is constant with the extraction potential (so the measured emittance will be proportional to the particle speed and, consequently, to the square root of the potential extraction).
2. The beam parameters, in particular the Twiss parameters, after the extraction electrode are constant.
3. The potential to apply to the optic elements (deflectors, quadrupoles, Wien Filter) are proportional to the extraction potential.

Firstly, the Hall effect sensor has been used to measure the magnetic field approximately at the Wien Filter centre with respect to the z axis, very close to the new poles. The position was not at the exact centre of the Wien Filter for x and y since the new electrostatic assembly was

already installed for the tests of the previous paragraph. The comparison between the numerical results and the experimental measures on the magnetic field are showed in Fig. 4.53. They are very close and, as an example, the difference at the maximum current of 240 A is 0.4% and the saturation of the magnet yoke is certainly well reproduced. This is a very important confirmation of the goodness of the magnetostatic simulations performed with COMSOL and the materials properties implemented on them.

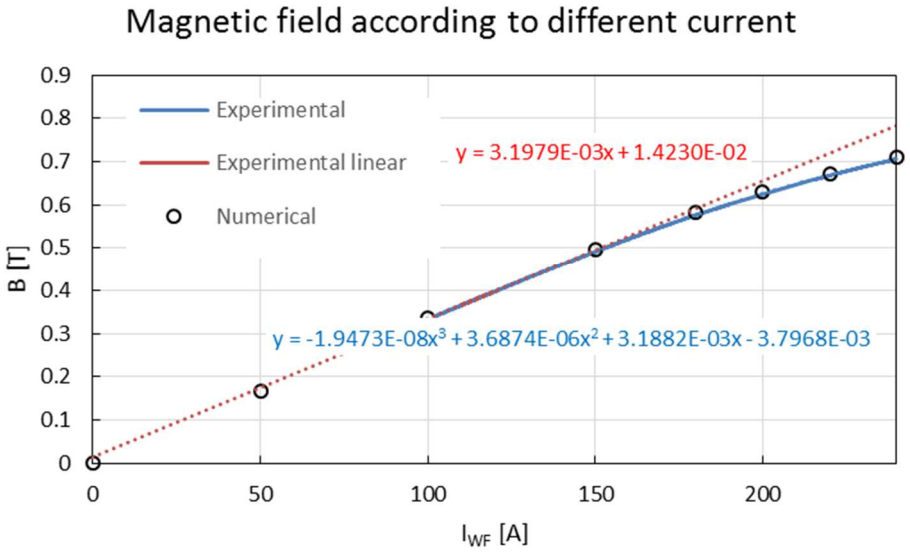

Fig. 4.53. Comparison between experimental measures and numerical results of the magnetic field approximately at the WF centre

Concerning the beam transport, initially various tests (from case 1 to 4) have been performed in order to characterized the Wien Filter at various electrode potentials and various focusing "strength". Then, the last one is the final version that will be always applied until the change of the preliminary poles (from case 4 to 8). During the most part of tests, a small part of the beam in the y plane was cut off at the emittance meter due to a small misalignment that was not possible to compensate. This is the confirmation of the need of the deflectors after the Wien Filter presented in paragraph 4.8.

Case	Q_1 [V]	Q_2 [V]	Q_3 [V]	I_{WF} [A]	B [T]	V_p [V]	V_{pe} [V]	Plane		ε_{INC} [%]	α [ ]	β [mm/mrad]	γ [mrad/mm]
1	581	627	1495	15.6	0.0538	468	86	x	EXP	1.03	-4.97	4.90	5.25
									TW	1.02	-2.32	3.84	1.66
								y	EXP	0.92	-2.19	3.24	1.79
									TW	1.00	-2.33	2.00	3.21
2	500	619	1517	48.76	0.1610	1403	257	x	EXP	0.94	-2.43	2.08	3.31
									TW	1.01	-1.56	1.39	2.47
								y	EXP	1.01	-4.32	6.30	3.12
									TW	1.00	-4.13	6.25	2.89
3	914	759	1521	63.39	0.2159	1874	343	x	EXP	0.87	-0.74	0.72	2.16
									TW	1.01	-0.45	0.83	1.44
								y	EXP	1.24	-0.51	2.80	0.45
									TW	1.00	-0.28	2.60	0.41
4	1465	771	1040	88.95	0.3027	2621	474	x	EXP	0.99	0.17	1.29	0.80
									TW	1.05	0.09	1.46	0.69
								y	EXP	1.02	-0.17	1.49	0.69
									TW	1.00	-0.23	1.68	0.63
5	1439	807	1277	88.65	0.3021	2621	474	x	EXP	0.91	-1.73	1.62	2.46
									TW	1.01	-1.35	1.63	1.74
								y	EXP	0.94	-0.38	0.70	1.65
									TW	1.00	-0.46	0.86	1.41
6	956	702	1361	88.65	0.3021	2621	474	x	EXP	0.92	-3.50	2.70	4.91
									TW	1.05	-3.16	2.61	4.21
								y	EXP	0.94	-4.08	7.62	2.32
									TW	1.00	-4.29	7.80	2.49
7	900	709	1384	88.65	0.3021	2621	474	x	EXP	0.97	-3.87	2.95	5.42
									TW	1.07	-3.53	2.87	4.69
								y	EXP	0.93	-2.21	4.70	1.25
									TW	1.00	-2.23	4.52	1.32
8	875	695	1398	88.73	0.3019	2579	590	x	EXP	0.89	-2.09	4.38	1.22
									TW	1.03	-3.14	2.58	4.21
								y	EXP	0.93	-2.42	1.61	4.27
									TW	1.00	-3.85	6.99	2.26

Table 50. Experimental measures (EXP) compared with TraceWin results (TW) for the new electrostatic part and first Wien Filter pole prototype

Except for the less interested case, with low voltage applied to the Wien Filter electrode (case N°1), the numerical and experimental Twiss parameters and the ellipse figures are very close. This constitutes the perfect validation of the simulation performed in paragraph 4.4 and 4.5 concerning the beam transport.

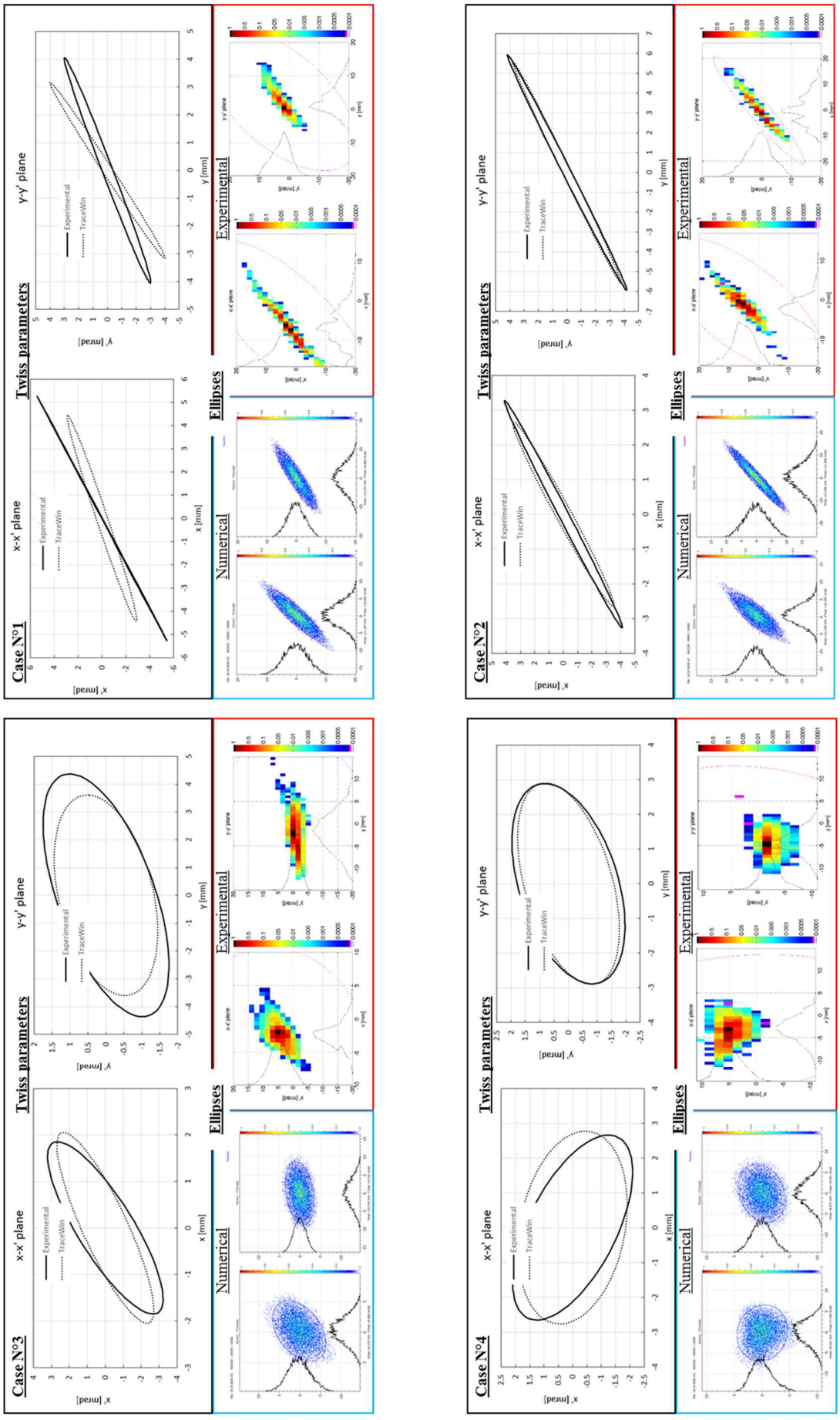
Case N°1
Case N°2
Case N°3
Case N°4
x-x' plane
y-y' plane
Twiss parameters
Ellipses
Experimental
Numerical
TraceWin
x [mm]
y [mm]
x' [mrad]
y' [mrad]

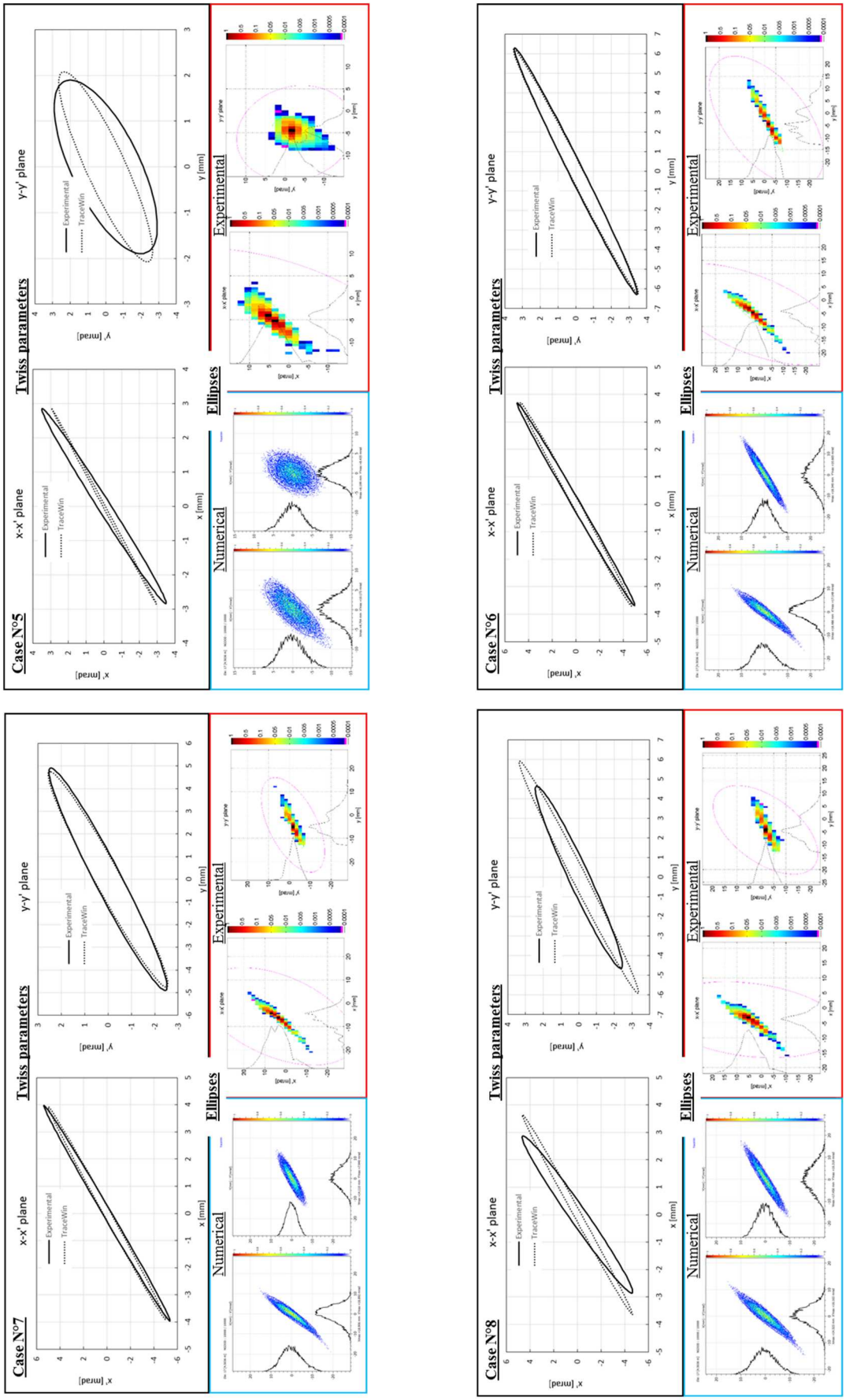

Fig. 4.54. Experimental measures (EXP) compared with TraceWin results (TW) for the new electrostatic part and first Wien Filter pole prototype.

The second step was to verify the minimum beam size on the x plane, the σ_{RMS}. This measure was taken even for other potential extraction, from 25 kV to 45 kV with steps of 5 kV because the accelerator has to work at different potentials according to different masses. In order to get the beam size, the slits have been moved along the x plane with a fixed aperture of 0.5 mm and a following Faraday cup measured the beam passing through the gap, as the scheme in Fig. 4.55. This method is much more precise compared to the use of a beam profiler.

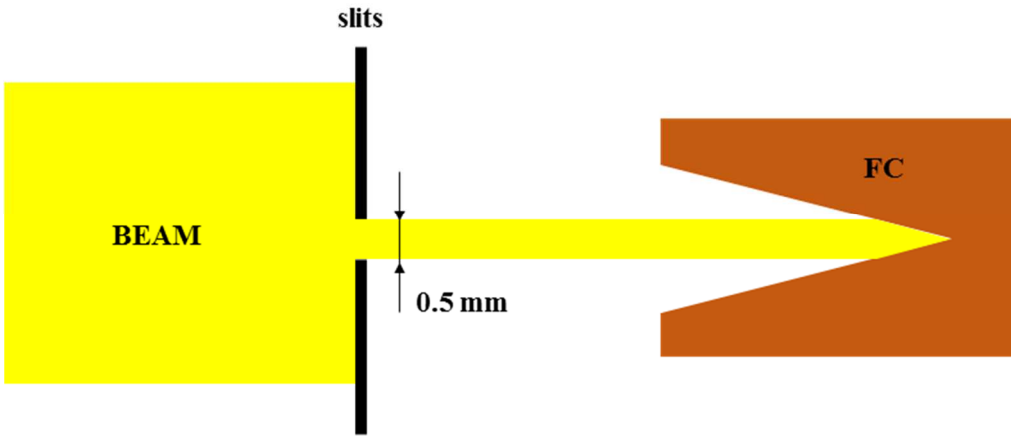

Fig. 4.55. Scheme used to get the beam size to the slits

The measures are then interpolated by a first Gaussian function calculating its average and its mean square deviation. Then, a second interpolation has been performed taking into account only the data within three standard deviation of the previous function. An example of the elaborated measures is presented in Fig. 4.56, where Fig. 4.56*a* shows that the second Gaussian seems to well describe the beam distribution. On the other hand, in the logarithmic scale, at positions of more than 3 σ_{RMS}, the experimental beam has a very wide plateau, called beam halo, corresponding in this case to about a 10% of total beam, which is a very significant part. It was demonstrated not caused by the Wien Filter and it was never observed in previous tests. Probably it is attributable to the poor vacuum close to the source for the missing of a broken pump and an air leakage discovered just recently. The vacuum level at about 1 meter from the source was slightly higher than 10^{-5} mbar, which is one order of magnitude higher than usual. In addition, in literature it is often described that a bad vacuum could generate beam halo [4.12], [4.13], especially at low beam energies as in the Front-End.

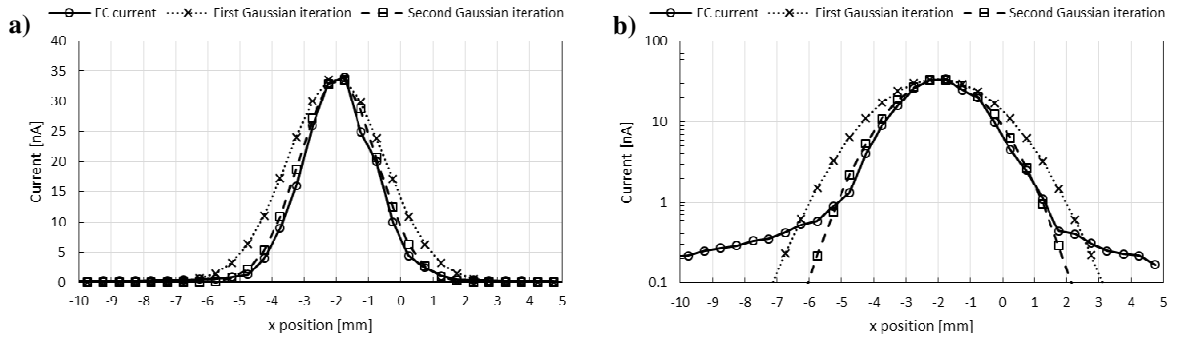

Fig. 4.56. Experimental measures of the beam profile and interpolation with the two Gaussians: a) linear scale; b) logarithmic scale.

The third step was to verify the mass peaks separation. Even for this purpose, the tests were performed at various potentials, from 25 kV to 45 kV with steps of 5 kV, and the distance between the peaks were taken by the beam profiler. The masses used were Kr and Xe isotopes corresponding to 80 and 130 amu. As an example, Fig. 4.57 shows the comparison for a 40 keV beam of Xe. It is underlined that the peaks seem separated but it is only due to the low resolution of this beam profiler and the relative low beam intensities (few nA for the most abundant mass). Moreover, mass-scans have been performed, consisting of the magnetic field variation and the consequent measure of the beam current at the slits closed to a minimum value (1 mm for this case). An example is presented in Fig. 4.58 for a 40 keV Xe beam (comparison between TraceWin results and experimental measures), where it is clear that the separation between the peaks corresponds to what was expected by TraceWin, with the differences due to the beam halo found even before (as between masses 132, 134, 136).

The beam diameter at the slits and the separation between peaks for all the extraction potentials and for the masses of Xe and Kr are summarized in Table 51. There is a very good accordance between the numerical and experimental peak separations and it is clear that it is almost constant with the extraction potential as equation (4.46) predicts (E, dependent on V_p, is proportional to V_e as said at the begin of the paragraph). This is not true for the beam RMS radius which does not decrease as expected. This effect it is not probably caused by an eventual increase of the normalized emittance (and a consequent increase of the beam diameter) at higher extraction potential since, for the case N°5, the normalized emittance is essentially constant (right of Table 51). Consequently, the only reason that justifies these effects are the slight change of the Twiss parameters out of the extraction with the acceleration potential, that causes a difference on the beam transport in the Wien Filter. In particular, this effect seems very pronounced from 25 kV to 30 kV of extraction potential as demonstrated in Table 52 by the change of the Twiss parameter values at the slits.

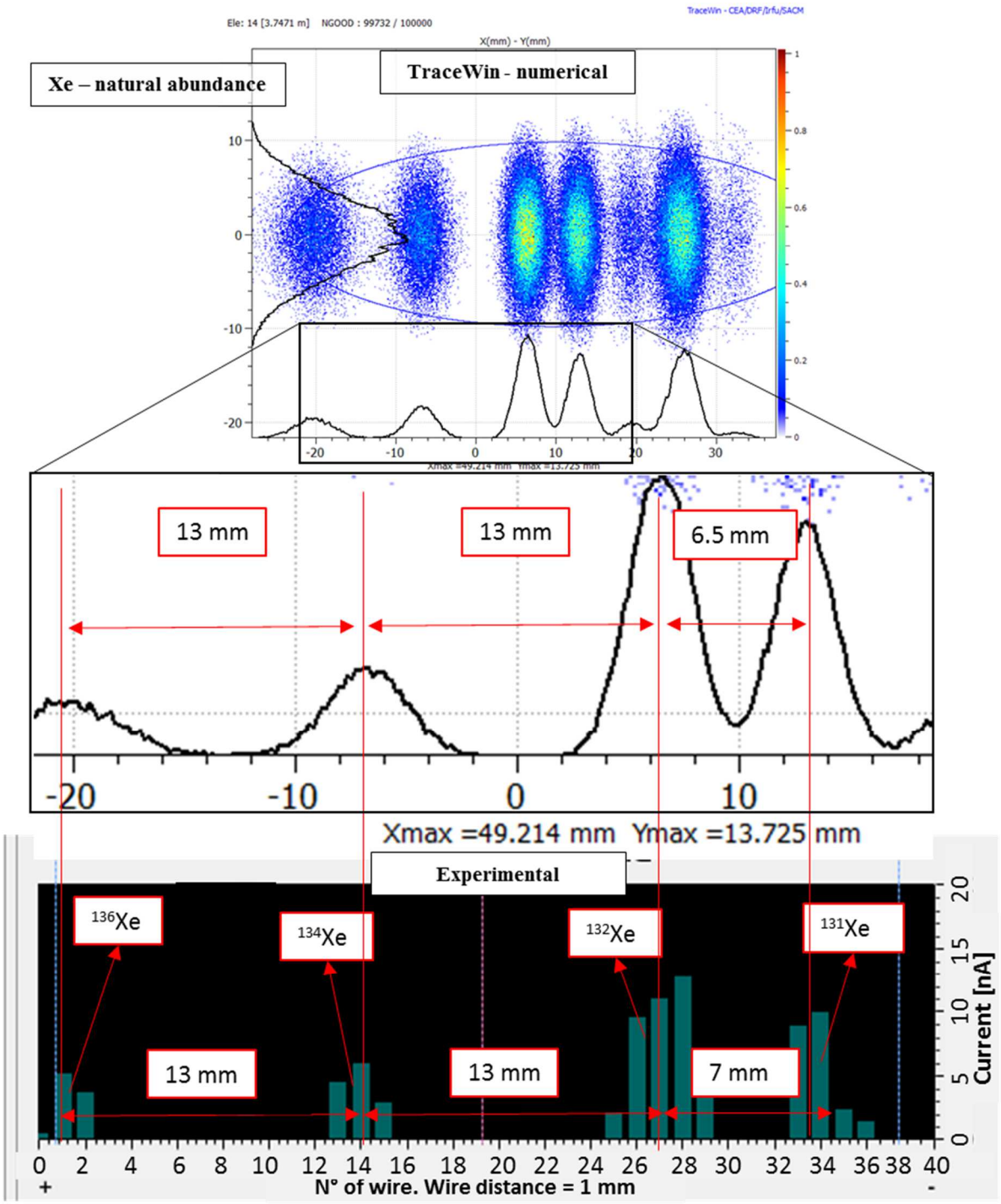

Fig. 4.57. Comparison between numerical peak separation and experimental for the Xe (V_e = 40 kV).

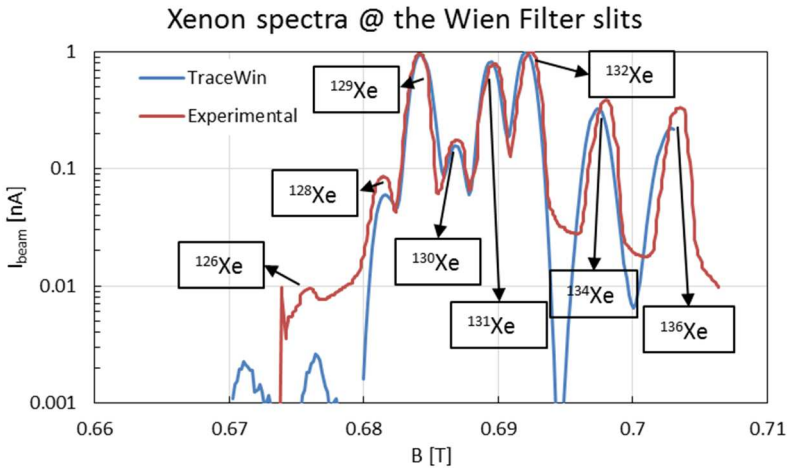

Fig. 4.58. Mass-scan for a Xe beam at energy of 40 keV

			Kr				Xe				Case N°8				Case N°5	
Ve [kV]	σ_{EXP} [mm]	σ_{TW} [mm]	d_{EXP} [mm]	d_{TW} [mm]	ott_{EXP} [ ]	ott_{TW} [ ]	d_{EXP} [mm]	d_{TW} [mm]	ott_{EXP} [ ]	ott_{TW} [ ]	ε_x	ε_y	ε_{Nx}	ε_{Ny}	ε_x	ε_{Nx}
											[π mm mrad]					
25	1.20	1.11	10	10	1.39	1.50	6.5	6.5	0.90	0.97	5.12	4.91	5.93E-3	5.69E-3	5.00	5.79E-3
30	1.26	1.05	10	10	1.32	1.59	6.5	6.5	0.86	1.03	5.18	4.98	6.57E-3	6.33E-3	4.53	5.75E-3
35	1.27	1.01	10.5	10.5	1.37	1.73	6.5	6.5	0.85	1.07	4.79	4.75	6.57E-3	6.52E-3	4.24	5.82E-3
40	1.23	0.98	9.5	10	1.29	1.71	7	6.5	0.95	1.11	4.46	4.45	6.54E-3	6.52E-3	3.93	5.77E-3
45	1.23	0.95	10	10	1.36	1.76		6.5			4.31	4.41	6.70E-3	6.85E-3	3.70	5.76E-3

Table 51. Summarization of the results for beam RMS radius and peak separation for Kr and Xe beams. No data are provided for Xe at 45 keV because it requires a maximum magnetic field not supplied without increase yoke thickness.

Plane	V_e [kV]	α [ ]	β [π mm mrad]	γ [π mm mrad]
x	25	-2.42	1.61	4.27
	30	-3.10	2.44	4.34
	35	-2.90	2.26	4.16
	40	-2.64	2.02	3.94
	45	-2.51	1.95	3.75
y	25	-2.09	4.38	1.22
	30	-3.54	6.45	2.10
	35	-3.41	6.04	2.09
	40	-3.49	6.09	2.16
	45	-3.57	6.10	2.25

Table 52. Twiss parameters at the slits for case N°8 at different extraction potential maintaining proportional the potentials applied to all the electrostatic devices (Ar^+ beam).

In order to determine the optimum triplet values to apply for the different extraction potentials, a traceback for each potential extraction has to be performed as presented in paragraph 4.7.1 for the case of 25 kV. For the purposes of this thesis, a satisfying validation of

the Wien Filter design has been completely performed in this paragraph and no further studies have been implemented.

4.8. The design of the steerers after the Wien Filter

4.8.1. Introduction

In general, each optical device along a beam line introduces a misalignment on the beam due to the impossibility to have a perfect shape and element position. For the Wien Filter, a preliminary evaluation of the misalignment induces to the beam has been performed and the most problematic effect is due to the misalignment of the planes due to a rotation along the beam axis. This effect causes a deflection on the beam in the y plane that is not compensated by any of the further elements for several meters (more than 5).

The errors during the assembly procedure could introduce a maximum angle around the beam axis of about 0.5°, which causes a beam exiting from the Wien Filter 11 mm far from its axis and with a divergence of about 8 mrad on the y axis. For this reason, deflectors has to be designed and installed in order to re-align the beam. It is underlined that during the experimental tests showed in 4.7.4, the beam was found at the emittance meter a little misaligned on the y plane (-4.5 mm and -2 mrad), but no intervention was possible to correct it.

4.8.2. Mechanical design

The deflectors have been thought as a simple device made, if possible, of standard elements. In particular, a standard CF160 4-way cross has been used, coupled with two standard CF160-CF100 flange adaptors to decrease to the nominal flange used along the beam line (CF100). The upper flange is free for the installation of an eventual turbomolecular pump, whereas the lower one has to be used to sit the four 5 kV electrical feed-throughs needed to maintain the electrodes at the wanted potential. All the available space between the Wien Filter (and the consequent bellows) and the second diagnostic box (where the slits are placed) has been occupied by the standard cross.

The mechanical design of the assembly are presented in Fig. 4.59. The deflectors are fixed to the ground case by means of a MACOR support, maintained in position thanks to two screws (Fig. 4.59c). The MACOR will assure the radiation resistance of the insulation for tens of years. The deflectors will be externally aligned adjusting their position to the ground case and then the overall assembly will be inserted into the cross, where the position will be adjusted by eight screws (four per side) and fixed by double nuts and a lock washers. It is underlined the presence

of the circular sectors with 100 mm inner diameter which are the grounded shields for the deflectors. The minimum assembly diameter is consequently 100 mm, which increases the vacuum conductance along the beam line improving the vacuum level. The minimum distance between the ground and the electrodes is 2.5 mm, which is enough in order to avoid discharge until a maximum potential of 5 kV, as demonstrated in the test on the WF.

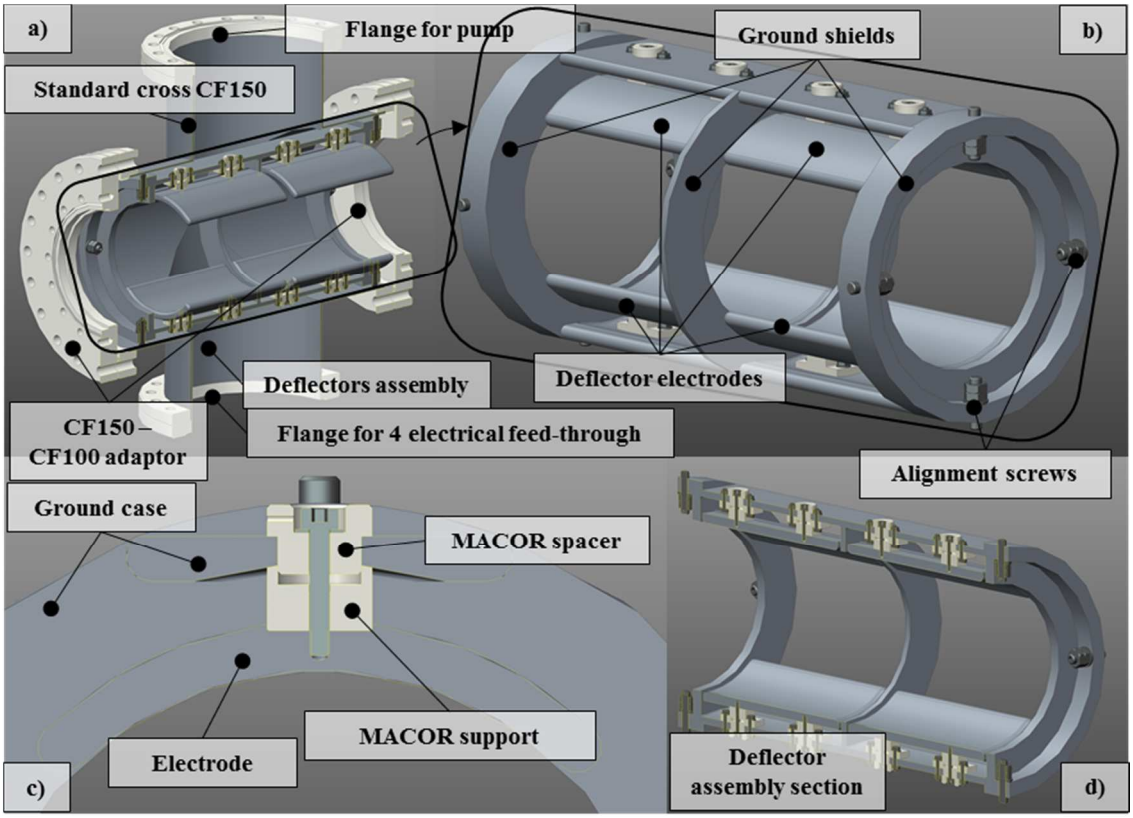

Fig. 4.59. 3D drawings of the deflectors after the Wien Filter.

The assembly is now under production at an internal INFN workshop and the delivery of the components is expected by end of 2016.

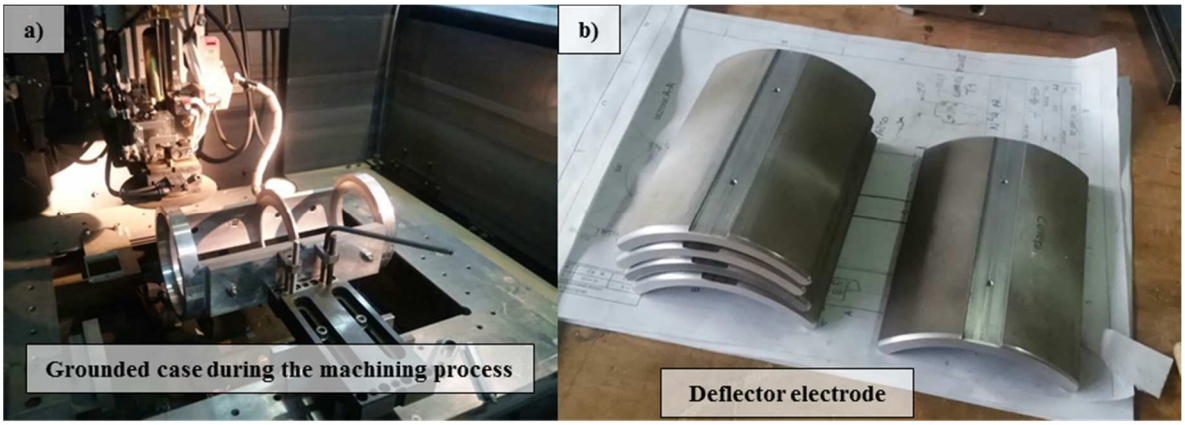

Fig. 4.60. Component machined at the internal INFN workshop: a) ground case; b) electrodes.

4.8.3. *Analytical dimensioning*

The input beam properties for the analytical dimensioning are summarize in Table 53. Only the beam centre characteristics have been provided since the deflectors should not affect the Twiss parameters.

Extraction potential V_e	42 kV
D_{MAX}	50 mm
y_0	11 mm
y_0'	8 mrad

Table 53. Input beam for the dimensioning procedure of the deflectors.

It is assumed that the beam trajectory inside the deflectors is a perfect parabola and no fringe fields are presented. A typical configuration is showed below in Fig. 4.61, whereas (4.68) and (4.69) are the equation representing the trajectory of a particle with energy V_e in the position y_0 and divergence y_0' inside the deflectors of length l, diameter d and potential applied V_s. On the contrary, (4.70) and (4.71) are the equation of the same particle in a drift with length s.

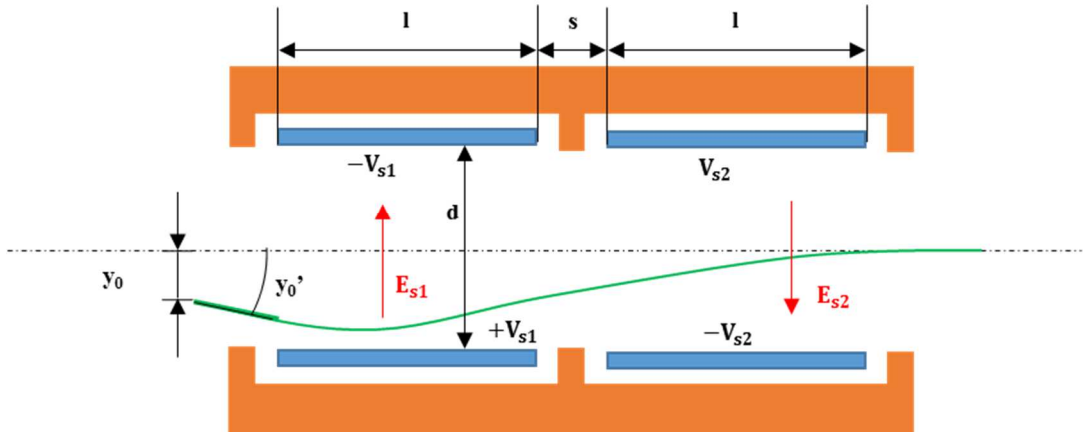

Fig. 4.61. Configuration used for the deflectors after the Wien Filter.

$$y = \frac{V_s}{2V_e}\frac{l^2}{d} + l\,y_0' + y_0 \tag{4.68}$$

$$y' = \frac{V_s}{V_e}\frac{l}{d} + y_0' \tag{4.69}$$

$$y = s \cdot y_0' + y_0 \tag{4.70}$$

$$y' = y_0' \tag{4.71}$$

The various parameters are indicated in Fig. 4.61 and the angle y_0' is small enough to assume equal to its sine. Imposing that the particle has to be aligned to the beam axis after the deflectors, the potential to apply are:

$$V_{S_1} = -V_e \frac{d}{l(l+s)}\left[y_0' \left(\frac{3}{2} l + s\right) + y_0 \right] \quad (4.72)$$

$$V_{S_2} = -V_{S_1} - y_0' \frac{d}{l} V_e = V_e \frac{d}{l(l+s)} \left(\frac{1}{2} l\, y_0' + y_0\right) \quad (4.73)$$

The dimension provided in the previous paragraph are:

Electrode length	l	120 mm
Electrode diameter	d	100 mm
Distance between electrodes	s	9 mm
Estimated effective length	l_{EFF} = l + s (as said in 4.4.4)	129 mm

Table 54. Main dimensions of the deflectors.

The consequent preliminary values to apply to the deflectors are about -3.4 kV and 3.1 kV respectively for the first and the second deflector using the electrode length, and -3.0 kV and 2.7 kV using the estimated effective length. Both of them are satisfying potentials to apply because they are below 5 kV and standard SHV electrical feedthrough can be used. In the real case, the potentials to apply are expected between the two cases. It is underlined that higher is *s*, the distance between the deflectors, smaller are the potentials to apply. In this case, as said in 4.8.2, the space available between the WF and the slits is fully utilized by the deflectors and there was not the possibility to increase it.

4.8.4. Electrodes optimization

As already said, the deflectors are thought as two pieces of tubes cut with an opportune angle. The inner tube has been fixed to 100 mm and the outer radius to 114 mm as it is a rough bar dimension available in the workshop. Moreover, it seems an appropriate dimension as the maximum beam diameter passing through is less than half. The inner diameter of the vacuum chamber has been fixed to 155 mm as it is relative to a standard cross CF160.

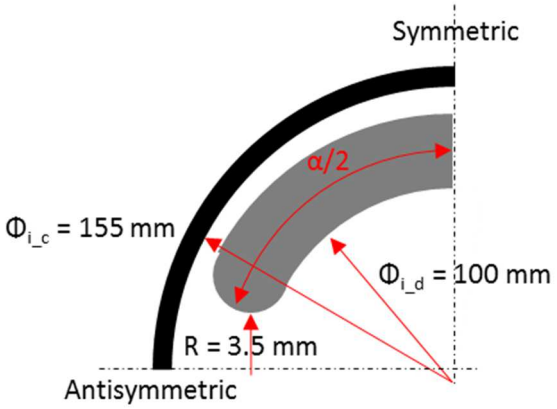

Fig. 4.62. Main geometries of the deflector. The angle α has to be determined.

In order to optimize the geometry concerning the beam transport point of view, the angle has been fixed finding the minimum of the mean square deviation of the electric fields evaluated in the grid points inside a circle of radius 25 mm (maximum beam radius expected), as presented in Fig. 4.63.

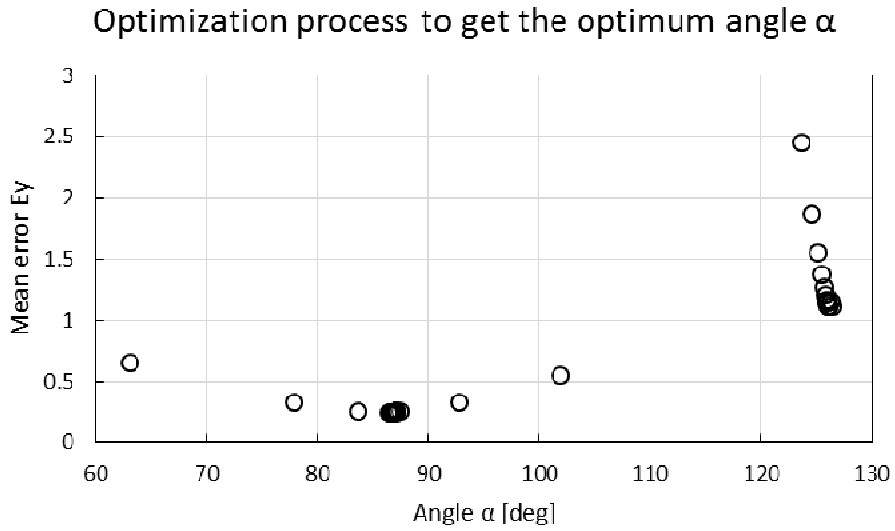

Fig. 4.63. Optimum angle α found during the optimization process.

The optimum value has been found between an angle of 85 and 90 degrees.

4.8.5. Numerical tests

The goodness of the design has been tested numerically. Therefore, the 3D geometry has been simplified, a potential simulation has been performed with COMSOL and the results have been imported to TraceWin, using the same procedure adopted for the Wien Filter.

It has been assumed the misalignment used before (y_0 = 8 mm, y_0' = 11 mrad), whereas, as input beam, the maximum size calculated at the end of the WF in Fig. 4.35, corresponding to a beam radius of 10 mm both for x and y. This corresponds to β Twiss parameter of 0.72 mm/mrad. For simplicity Twiss parameter α has been fixed to *0* for both the planes.

The potentials to apply have been calculated to 3.05 kV and -2.85 kV that are consistent with what has been analytically found since the values are between the analytical cases of electrode length and effective length. The emittance increase is essentially negligible.

The same procedure has been used for a 25 keV beam and 1.8 kV and -1.7 kV of potential for the electrodes has been calculated and even here the emittance increase is negligible. Consequently, once the deflectors are ready, they can be installed in the Front-End and tested.

4.9. Conclusions

In this chapter, it has been presented the study, the redesign process and the tests performed on a Wien Filter. Initially, the study was carried on both from an analytical point of view, only partially presented in literature [4.1], [4.2] and [4.3], and a numerical approach. The analytical study was important for a very preliminary evaluation of the Wien Filter power resolution, whereas the numerical one was essential as the confirmation of the approach. Then, the design has been fully presented, with very important information usable even during the design of other components on a typical beam transport, such as triplet and deflectors. No suggestions were provided in literature on the sizing process of the main parameters and, moreover, even the few papers on this device were not fully completed, especially from an engineering point of view.

After the definition of the final WF version, the mechanical design has been produced and the prototype has been manufactured in the internal LNL workshop. Since there was not the possibility to completely change the WF poles, just a preliminary version of this part has been tested. Finally, the experimental tests fully validated the various simulations, confirming the goodness of the approach and the correctness of the dimensioning procedure.

It is strongly underlined that the literature on the Wien Filter was clearly missing and very old. It was present just a not completed analytical approach to describe the effect of the Wien Filter and, for this reason, some imprecisions have been introduced. Here the use of numerical codes deeply supports the study, confirmed by the experimental tests. In this way, if somebody has to design for other purposes a new Wien Filter, he can base the sizing process on this chapter.

References of Chapter 4

[4.1] R. L. Seliger, *E×B Mass-Separator Design*, J Appl Phys **43**, 2352 (1972).

[4.2] K. Jensen and E. Veje, *Construction of a Wien Filter heavy ion accelerator*, Nucl Instrum Methods **122**, 511 (1974).

[4.3] E. Leal-Quiros and M. A. Prelas, *New tilted-poles Wien Filter with enhanced performance*, Rev Sci Instrum **60**, 350 (1989).

[4.4] https://en.wikipedia.org/wiki/Beam_emittance.

[4.5] https://en.wikipedia.org/wiki/Liouville's_theorem_(Hamiltonian).

[4.6] T. Kalvs, *Beam Extraction and Transport*, CAS 2012: Ion Sources, CERN-2013-007, pp. 537-564.

[4.7] http://irfu.cea.fr/Sacm/logiciels/index3.php.

[4.8] COMSOL Multiphysics® v. 4.3. www.comsol.com. COMSOL AB, Stockholm, Sweden.

[4.9] COMSOL Multiphysics® v. 5.1. www.comsol.com. COMSOL AB, Stockholm, Sweden.

[4.10] H. A. Enge, *Effect of extended fringing fields on ion-focusing properties of deflecting magnets*, Rev. Sci. Instrum. **35**, 278 (1964).

[4.11] W. Flegel *et al.*, *LHCb Magnet, Technical Design report*, CERN/LHCC/2000-007.

[4.12] S. Liu *et al.*, *In vacuum diamond sensor scanner for beam halo measurements in the beam line at the KEK accelerator Test Facility*, arXiv:1512.08024v1 [physics.acc-ph], 29 Decemer, 2015.

[4.13] Dou Whang *et al.*, Analytical estimation of ATF beam halo distribution.

Chapter 5

Conclusions

5.1. The overall work

This thesis is inserted into the framework of the study, the design and the construction of the SPES facility. It is one of the biggest challenges undertaken by the INFN at a national level and, especially, the most important project developing at the LNL. In the thesis, the developing process of the most important components installed in the most delicate area is presented. The title "Target-Ion source system" has been thought from the facility point of view, referring to all the equipment that has to be installed in the SPES bunker. If the first chapter is simply a brief description of the ISOL facilities in general and the SPES facility in particular, the second chapter is dedicated to the study concerning the SPES target, which is the heart of the facility where the radioactive isotopes are created. It is the most critical component since it has to work at very high temperatures and its functioning is necessary for the overall facility to work properly. Moreover its failure could compromise the safety of the accelerator and, consequently, all the project. In this chapter, the 40 MeV SPES target has been deeply study and redesign in order to take into account the real working conditions determined by the particular attention on the definition of the power deposition due to the proton beam. A procedure has been implemented to numerically calculate with a good confidence the final temperatures and stresses.

Then, this study has been applied to a 70 MeV proton beam in order to design another target which could use this beam energy. In this case, the first dimensioning procedure has been presented and, then, just the nominal proton beam profile has been studied. In fact, the main purpose was the definition of a target that could be tested at iThemba LABS, where a 66 MeV – 350 μA of proton beam could be deliverable by the installed cyclotron. Then, the on-line tests of 70 MeV target previously designed have been presented: before the description of the scattering chamber has been provided, then the other two paragraph are focused on the real tests performed in South Africa. Many efforts were spent in order to measure the temperature of the disks during irradiation and the results have been compared to the numerical expectations. The comparison was very good, validating the procedure adopted to simulate the target temperature distribution.

On the other hand, the third chapter is the presentation of the beam diagnostics developed. They are fundamental devices since they constitute the “eyes” of the operators on the correct functioning and setting of the facility. The most critical components were the proton beam diagnostics: collimators, beam profiler and Faraday cup. In fact, they have to sustain the high power delivered by the proton beam without being damaged. The study was both from a thermal and consequent structural point of view and it concerns materials able to support high temperatures. Moreover, particular attention was paid on the choice of the materials in order to minimize the activation: essentially graphite and aluminium (aluminium alloy) are the most used. Then, very important information has been provided concerning the collimators: they can be used as a stationary and continuous monitoring of the proton beam characteristics delivered to the target and, consequently, it is one of the most important diagnostic for the target functioning.

Even the radioactive diagnostics have been developed, such as Faraday Cup, Beam Profiler and slits. Most of the attention was paid in the use of standard components, radiation hard material and especially, facility of changing the most fragile components in order to reduce as much as possible the eventual maintenance time and, consequently, reducing the dose absorbed by personnel. Moreover, the modified pneumatic motor adopted to move all the systems inside the SPES bunker has been tested. No significant differences have been found respect to the standard motor but, unfortunately, PEEK has to be used for the most critical motor component: the motor paddles. In fact, some other reasonable materials have been tested, such as graphite, bronze, aluminium anodize, but none of them meets the minimum requirements. The test-bench developed in this chapter to study the pneumatic motor will be used soon in order to test some PEEK paddles that have been irradiated at LENA in a neutron and gamma field according to a dose corresponding to 7 years of the SPES bunker operation.

Finally, the last component inside the SPES bunker that had to be studied was the Wien Filter. It is the first stage mass separator chosen some years ago and, immediately after its installation during the last part of 2012, it was clear that it could not satisfy the minimum requisite, 1/150, in order to separate the different masses composing the beam and, consequently, reducing the radioactive contamination along the beam line due to unwanted particles. In the first part, a partially original approach has been developed in order to analytically describe the three different ways to design a Wien Filter. Then the electrostatic part composing the Wien Filter has been fully studied, designed and manufactured. Very important information has been provided even to design of some other typical electrostatic components, such as steerers and triplets. Then the best way to design a Wien Filter has been

numerically found, providing clear reasons and proofs which were not present in the literature found. A preliminary Wien Filter has been later manufactured and tested, validating the simulations performed and, consequently, the sizing process adopted. According to the numerical simulations, the new Wien Filter will satisfy the minimum requests of selecting the desired beam mass, reducing to the minimum the beam line contamination. Finally, even a pair of deflectors has been designed and are now under construction in order to correct eventual beam misalignments due to the Wien Filter.

It is underlined that, in all the designs, particular attention was paid on the materials: the components have to work in a high aggressive environment, where mainly radiations, but also corrosion, can quickly damage the materials. In order to minimize the risk of rupture, very common materials, mainly polymers, were not adopted or, at least, avoided.

5.2. Final tests to perform

During the entire thesis, many efforts have been spent in order to test most of the designed components: the target impinged by a real proton beam, the tensioning system of the high power beam profiler, the pneumatic motor, the RIB diagnostics and the Wien Filter.

On the other hand, the most delicate components composing the proton beam diagnostic have never been tested since they are now in the manufacturing phases and a proton beam is not at the moment deliverable. In fact, the cyclotron is still in the commissioning phase and the manufacturing priority has been given to some other components, such as WF and diagnostics.

A new way to test these components is accelerating an electron beam by means of an electron gun. This device is able to deliver very high beam power up to 10 kW without the radioprotection problems due to the radiation and activation induced by the proton beam. Consequently, it is strongly suggested to test the proton beam diagnostic from the thermal point of view by an electron gun. Moreover, the flanges used to couple these systems have already been defined, but a new idea has been proposed: use of the standard fast coupling geometry already presented in paragraph 3.5, and coupled them with metal seals such as indium or lead. In this way, it could be possible to decrease of a factor of more than ten the intervention time to remove the eventual collimators, Beam Profiler or Faraday Cup in case of malfunctioning or rupture. In addition, an eventual lead shield of a thickness preliminary evaluated on 10 mm, will be preferable to be inserted around the collimators in order to reduce the dose emitted by this component, decreasing the eventual dose absorbed by the personnel which has to do some maintenance close to it (ex: change pumps, connectors, etc.).

New tests occur even to complete the design of the Wien Filter. The majority of the work has already been performed in this thesis, but the final configuration will have a longer and sharper pole and an increased slits distance. Moreover, in order to better represent the beam transport along the FE, the initial conditions of the sources have to be found by a traceback at extraction potential higher than 25 keV. In addition, the new deflectors after the Wien Filter have to be tested since they will be completed very soon.

Since the beam pipe inside the bunker is 250 mm higher, new frames have to be designed and realized, with a more efficient alignment systems.

Certainly, both UC_x targets (40 MeV and 70 MeV) have never been tested with a proton beam and at high temperatures. This is one of the tests which needs a lot of care in order to do not compromise the use of the facility. A good idea could be to test the disks by an electron gun from the thermal and structural point of view, checking the maximum temperature and stress sustainable by them.

It would be very important to carry on the study of the components which are subjected to radiation damage. In our case, they mainly consist of polymers, lubricants and ceramic. In the framework of a collaboration between LNL, Padova university, Brescia university, Pavia university and LENA, the nuclear reactor sit in the INFN section of Pavia has been already used to irradiate in a gamma and neutron field some components, such as polymeric oring and, concerning this thesis, the PEEK paddle of the pneumatic motor. To complete this particular test, the PEEK paddle will be soon tested by the test-bench designed and presented in paragraph 3.6. On the other hand, new tests have to carry on for the other aforementioned materials, in particular lubricants which are present in all the Front-End to move the diagnostics and to couple or uncouple the test chamber.

Finally, it will be very important to estimate the various interventions times in order to plan the possible maintenance. Personnel has to be trained and has to keep calm during the intervention even if the dosimeter bells very fast. For this reason, new efforts have to be spent (and were spent) in order to improve the actual design making it as simple as possible from the maintenance point of view.

Appendix A

The general equation describing the particle trajectory in the Wien Filter

In paragraph 4.2.1, the speed along the z axis $\dot{z}$ has been assumed equal to the total speed v in the overall Wien Filter which is reasonably true only at the Wien Filter entrance. A clarification of this assumption is needed because, at first, it seems surprising that this assumption can be used for the overall Wien Filter since, for hypothesis, the electric field vector E is purely along the x axis which will change just the speed $\dot{x}$, leading to the increment of v but not of $\dot{z}$. This reasoning seems contradict the assumption $\dot{z} \approx$ v.

As aforementioned said, it can be assumed that $\dot{z}|_{t=0} \approx v_0$ because the angle between v and $\dot{z}|_{t=0}$ (Wien Filter entrance) is small. Then, if (4.12) is integrated once, it is obtained:

$$\dot{z} = \frac{q}{m} Bx + v_0 \qquad (1)$$

which substituted to (4.11) results to:

$$\ddot{x} = \frac{q}{m}\left[E - B^2 \frac{q}{m} x - Bv_0\right] \qquad (2)$$

Substituting equation (4.7) and omitting the second and third order terms of x, one gets:

$$\ddot{x} + B_0 v_0 \frac{q}{m}\left(B' + \frac{q}{m}\frac{B_0}{v_0}\right)x = \frac{q}{m}(E - B_0 v_0) \qquad (3)$$

Remembering (4.16) – initial condition of the particle - and (4.5) – the basis equation of the Wien Filter – the general equation (4.18) presented in paragraph 4.2.1 is obtained. It is underlined that equation (3) is more rigorous because equation (4.5) – the basis equation of the Wien Filter – is true only for the reference particle velocity. On the other hand, equation (4.18) well describes the link between the electric field E and the extraction potential V_e and for this reason it has been used.

Ringraziamenti

Alla fine di un grosso lavoro, è doveroso ringraziare le persone che anche in piccola parte hanno contribuito ad aiutarmi perché, nonostante mi sia impegnato con tutte le energie a portare avanti ciò a cui mi sono dedicato, il non riconoscere i meriti e, magari, i contributi di altre persone è un comportamento egoistico che mi ha sempre deluso.

Vorrei per prima cosa ringraziare i miei genitori: se sono riuscito a studiare, laurearmi e a conseguire il dottorato è grazie anche a loro che mi hanno trasmesso i valori con cui sono cresciuti. Vorrei ringraziare anche i miei due fratelloni a cui voglio un mondo di bene, anche se mi mancano un po' le baruffe chioggiotte di quando eravamo piccoli. Infine vorrei ringraziare tutto il resto della famiglia, cugine, zii, cognate, nipoti e infine nonni che, anche se non ci sono più, mi mancano tanto.

Ringrazio tutti i miei colleghi e responsabili: Giovanni Meneghetti, il quale non può che essere preso di esempio per la passione con cui porta avanti il suo lavoro, e Alberto Andrighetto, che durante questi tre lunghi anni in tanti modi ha compreso le giornate in cui ero intrattabile, cercando di aiutarmi a migliorare e sottolineando con molto tatto i miei grossi difetti in modo che potessi cominciare a correggerli. Non posso non ringraziare Mattia Manzolaro, Stefano Corradetti, Massimo Rossignoli e infine Daniele Scarpa; quest'ultimo, in special modo, per la sua immensa e proverbiale disponibilità. Credo che colleghi così non possano che essermi invidiati. Infine vorrei ringraziare tutti gli altri ragazzi del gruppo con cui in questi tre anni ho lavorato e che magari sono anche partiti: Michele B., Francesca B., Elisa V., Luca Safety, Christian G., Aldo M., Roberto S., Fabio DA., Davide T., Tony M., Gianfranco P., Fabio V., Chiara T., Valentina B., Jesus V., Giulia D., Giovanni C., Matteo V., Calderolla M., Giovanni A., Francesco R., Edoardo V. Giovanni B., Alessio V., Matteo F., Danilo B., Davide A., Gianluca V., Mattia A., Paolo T. Con tutti ho avuto momenti felici e nessun tipo di risentimento: è stato bello vivere con loro questa avventura. Vorrei ringraziare due persone che hanno realizzato gran parte del lavoro di questa tesi: Flavio Pasquato e Michele Lollo; Michele in particolare è sempre riuscito a ritagliarsi del tempo per discutere con me dei dubbi che avevo, fornendomi sempre ottimi suggerimenti. Infine ringrazio di cuore i ragazzi che ho seguito come correlatore: Alberto Sandrin, Alberto Raccanello, Luca Martin, Nicola Sattin ed Enrico Boratto. Senza di loro non sarei certamente stato in grado di riuscire a portare avanti tutto il lavoro che è stato svolto. Li ringrazio di cuore perché durante la loro tesi si sono impegnati a fondo e hanno subito e, magari compreso, anche le mie sfuriate.

Può non sembrare pertinente, ma vorrei ringraziare tutti i miei amici che hanno sopportato i miei periodi di assenza, ma che, nei momenti in cui avevo necessità di svago, non si sono mai tirati indietro. In particolare vorrei ringraziare Fabio, con cui in questi ultimi anni ho instaurato una bella amicizia. Purtroppo i miei più cari amici, Andrea e Federico, non sono geograficamente vicini perché la strada che hanno cominciato a percorrere li ha portati distanti; però, quando ci troviamo riusciamo sempre a fare gran festa rinsaldando quei piccoli segni che rendono grande un'amicizia. Spero con tutto il cuore che la via che stiamo percorrendo non ci cambi fino a non farci più riconoscere e apprezzare.

Infine vorrei ringraziare Irene, la mia splendida ragazza che ormai da quasi quattro anni mi accompagna. La vorrei ringraziare perché anche lei ha contribuito a questa tesi, sopportandomi con molto comprensione in quei momenti che, trasportato dalla passione per ciò che stavo facendo, lavoravo senza prestarle alcuna attenzione. Specialmente nell'ultimo periodo di scrittura, poi, è riuscita con la sua semplicità e con il suo sorriso misto a pazzia a farmi dimenticare in quei pochi momenti liberi che avevo, gli impegni che mi preoccupavano. Ti voglio bene Irene.